Lightweight positioning:
Design and optimization of an actuator with two controlled degrees of
freedom

PROEFSCHRIFT

ter verkrijging van de graad van doctor aan de
Technische Universiteit Eindhoven, op gezag van de
Rector Magnificus, prof.dr.ir. C.J. van Duijn, voor een
commissie aangewezen door het College voor
Promoties in het openbaar te verdedigen
op dinsdag 26 september 2006 om 14.00 uur

door

Juraj Makarovič

geboren te Košice, Slowakije

Contents

Preface

This work was carried out in the Group of Electromechanics and Power Electronics, Eindhoven University of Technology, within the framework of a IOP - Precision Technology project in cooperation with the Groups of Control Systems Technology and Precision Engineering at the same university.

I must first of all express my recognition to the Ministry of Economic Affairs for the material aid that it granted me through the IOP program, and to the Dutch Government for the advantages from which I profited during my stay in the Netherlands.

Professor Vandenput accepted me within his research group. The confidence that he always testified, was a continual encouragement. That he is ensured of my deep recognition.

Professor Compter, from Philips Applied Technologies, directed this work as second supervisor. I am grateful to him for the advices that he constantly gave me. Also my thanks for his kindness to borrow measurement equipment from his laboratory.

I express my sincere thanks to Professor Steinbuch from the Group of Control Systems Technology, Eindhoven University of Technology. Being always an inspiring teacher, he followed my work very attentively and gave me valuable comments.

Dr. Lomonova, assistant professor at the EPE group, acted as my assistent supervisor. She must be ensured of my recognition for the guidelines and the attention she paid to a great part of my work.

I also owe many thanks to Professor Hameyer from the "Institut für Elektrische Maschinen", RWTH - Aachen, Professor Brochet from the "École Centrale de Lille" and Professor Schellekens from the Eindhoven University of Technology for their interest in and appreciated comments on this work.

Thanks are also due to my colleague Maurice Schneiders and Jeroen van der Wielen for their friendly and fruitful cooperation within the IOP-project. I also would like to express my gratitude to the technical and administrative staff of

Chapter 1

Introduction

Already from the beginning of the human adventure, it surely became clear that straightforward mechanical tools are not the way to replace the necessity of an manual work. Therefore, to facilitate the execution of jobs, there have always been attempts to utilize energy resources in combination with tools. And since work is related to force $\vec{F}$ and displacement $\vec{s}$, as

$$W = \vec{F} \cdot \vec{s} \tag{1.1}$$

there has always been a quest for controlled motion and positioning systems.

Figure 1.1: Wind plough.

Consider, for instance, the "idyllic" situation in Fig. 1.1. The plough, as illustrated, uses wind as energy source, and the system of canvas is an actuator that drives the plough-share (load). The whole system is controlled by a person (control unit with sensors), who uses only a small force (signal) to determine the direction of ploughing.

Such an ancient system does not have high performance characteristics (as high speed, higher number of plough-shares, etc.), because the most important objective is to replace rough manual work. However, in later applications, as for example a sewing machine (Fig. 1.2), where the same relatively precise movement is repeated plenty of times, a higher velocity of the needle means a higher production rate. In most cases the maximum speed was determined by mechanical failures, part of which were caused by internal vibrations.

Since the epoch of the old sewing machines, positioning technology has advanced a great deal. Thanks to intensive research effort, the state-of-the-art of positioning systems is part of many areas of our lives. They have become more and more complex, reaching higher velocities and precision. Nevertheless, internal vibrations and eigenmodes have directed the design approach of mechanisms through
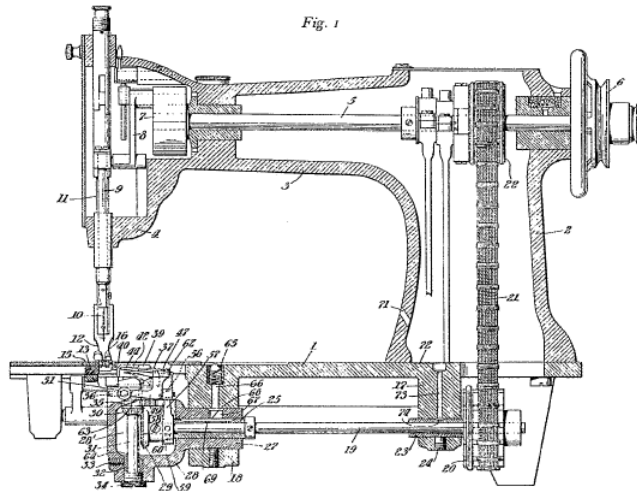
Figure 1.2: Sewing machine (Patent DE513906).
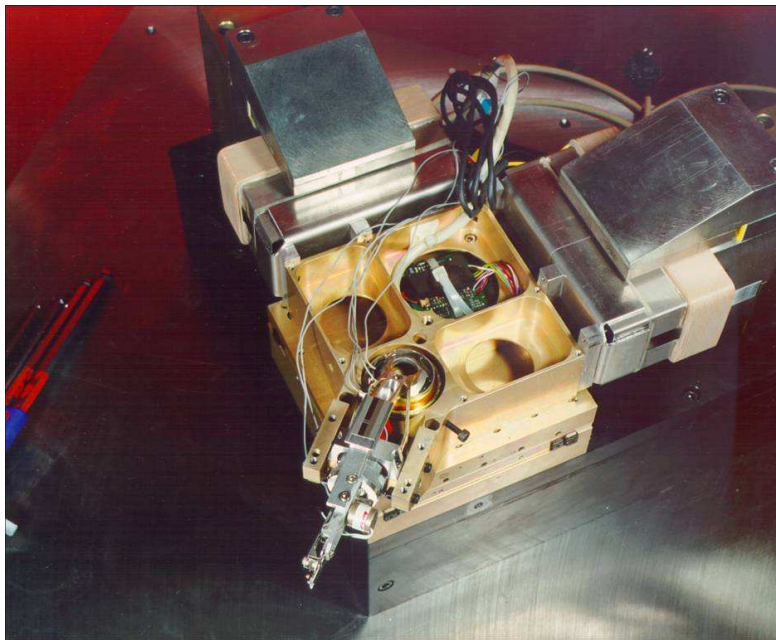
Figure 1.3: Wire-bonder with three degrees of freedom (Philips AppTech).

ages, and these are still phenomena that need to be addressed in the applications of present day.

Precision positioning systems as wafersteppers, scanners, pick-and-place machines for production of PCBs, wire-bonders (Fig. 1.3) etc. are probably the most sensitive applications to vibrations and disturbances. These applications are nowadays designed so effectively that they are almost reaching physical limits. Therefore, it is important to investigate ways of design that would be able to bring positioning systems beyond the limits of current design approaches.

The philosophy that is presented in this thesis, called Lightweight positioning, differs from the classical approach used to build, for example, a canvas plough, a sewing machine, or even a wire-bonder. The proposed approach treats the motion and vibration control problem at the same system level. The current work is part of a three-disciplinary approach consisting of:

- control,

- mechanics,

- electromechanics,

with the ultimate goal to supply knowledge to design lightweight overactuated positioning systems [1, 2, 3, 4]. Each sub-level is influenced by the system approach in its own particular way and consequently are described separately in three parts:

- Over-actuated motion control - a modal approach [5],

- Mechanical design of a lightweight positioning system [6],

- Design and optimization of an actuator with two controlled degrees of freedom.

The latter is the subject of this thesis.

In the next sections, the classical approach is shortly summarized. Together with practical examples, some drawbacks and advantages are presented. A general embodiment of the classical approach is introduced. Then, the lightweight design methodology is described and a general lightweight system, which realistically represents the challenges of internal vibrations, is defined.

1.1   System approach

1.1.1   Classical design methodology

The current design approach to precision positioning systems starts with the mechanical design based on kinematic principles [7]. The primal goal of the design is to reach a high servo bandwidth and repeatability of positioning. This is accomplished by designing the mechanical parts with dominant mechanical natural frequencies by a factor 2-3 higher than the required servo bandwidth. For high-precision systems further care is taken to reduce vibrations, i.e. balance masses and vibration insulation units. In some cases a passive [8] or active vibration damping [9] is applied in the form of special functional units (i.e. controlled actuator-sensor pairs [10]). However, this traditional approach has some drawbacks. When the control bandwidth has to be increased, the mechanical stiffness needs to be higher, and often the total mass of the system also rises. Consequently, the increasing moving mass, acceleration and velocity require higher force (current) and power for actuators and amplifiers. Moreover, the power of the actuator is bounded if thermal deformations, caused by losses in the actuator, must be kept within an acceptable range in order to prevent an insulation failure. This is to prevent isolation damage, which is the most dominant phenomenon. In practice, it means that the ratio of the moving mass of the system to the mass of a payload is about 450 up to 800.

1.1.2 Examples of classical positioning systems

Surface mount pick-and-place H-drive

As a typical representative of the classical design a surface mount pick-and-place H-drive by Philips AppTech (Fig. 1.4) can be considered. It is used for precise placement of surface mounted devices (SMD) on printed circuit boards (PCB). The main movements are in x- and y-directions. They are realized by two linear motors in y-direction and one linear motor in x-direction. The movement and rotation in and around the z-axis are performed by the placement heads, which supply SMD's. To reach the required 40 Hz system control bandwidth the mechanical structural
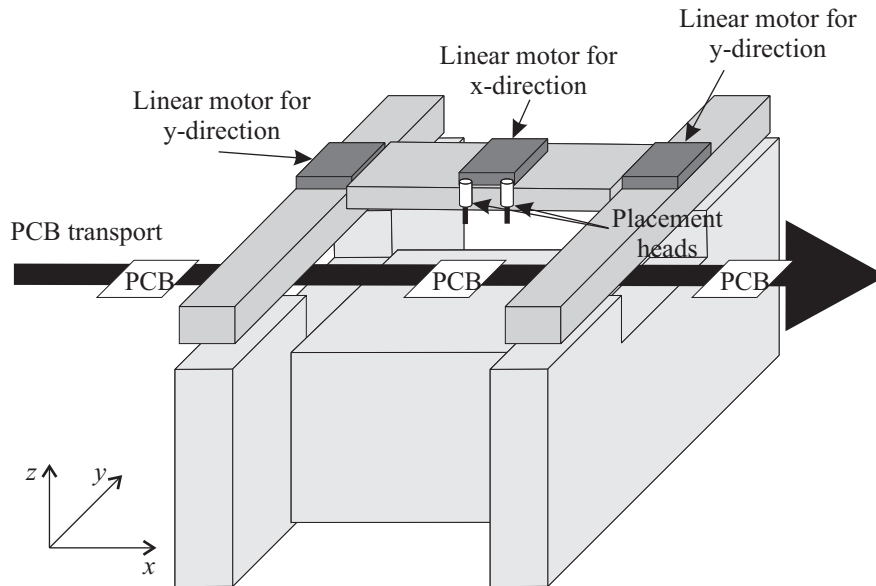
Figure 1.4: Surface mount pick-and-place H-drive (Philips AppTech).

resonances of the manipulator are made higher than 120 Hz, which is three times the required control bandwidth.

This system, with moving mass of several tens of kilograms, is designed to position with high acceleration and accuracy a SMD having a mass of a fraction of a gram.

Wafer scanner

Similarities in the design philosophy of mechanical structures can also be found in a more technologically advanced wafer scanner of ASML, intended for production of microchips from a silicium wafer. The wafer of about 300 gram is positioned in six degrees of freedom. The six degree of freedom positioning system is divided into two stages, a long and a short stroke.

Figure 1.5: Wafer scanner (ASML).

In this system, special function units, which cope with vibrations, internal as well as external disturbances are added to reach a few nanometers accuracy of the positioning. Vibration isolation units are implemented to prevent transfer of external disturbances, as floor vibrations, to a mechanical frame. The principle of balance mass [11] is used to reduce reaction forces of the linear drives. Then, the forces are not taken by the static mechanical structure and so the excitation of the

vibration modes is prevented.

The resulting positioning system reaches a weight of more than 125kg.

1.1.3 Benchmark of the classical design - Stiff beam

The two previous examples have different performance parameters. Thus, it is difficult to objectively compare these systems and consequently to evaluate the classical design approach. For this reason, a simple benchmark, which sufficiently captures the characteristics of classically designed systems, should be defined. The benchmark should also be suitable for a comparison of the classical and lightweight approach.

Therefore, a system with a stiff beam (Fig. 1.6) is chosen as a benchmark. It presents the main characteristics of precision positioning systems:

- The dominant vibration modes with the lowest frequencies of a mechanical structure are bending and torsion modes.

- The frequency of the first vibration mode is higher than the control bandwidth.

- The beam is positioned over a small trajectory (usually a few millimeters).
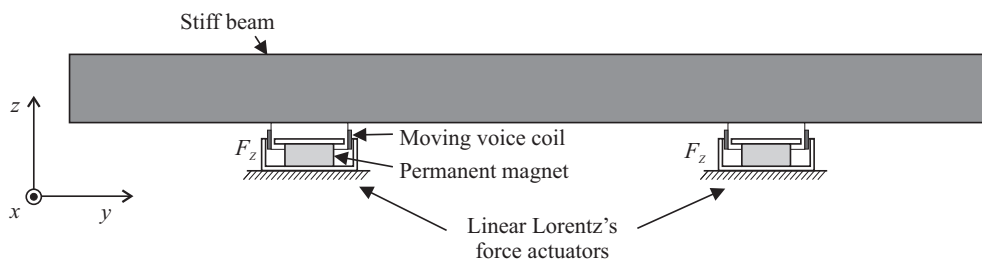
Figure 1.6: Stiff beam.

The stiff beam is supported by two voice coil actuators (short-stroke linear actuators), mainly characterized by very low cogging force, high acceleration, almost constant force-stroke characteristic. The heavy beam is positioned in two degrees of freedom, the translation in the z-direction and the rotation around the x-axis.

1.1.4 Lightweight positioning

The design philosophy, called lightweight positioning, focuses on mass reduction of the moving parts in a motion system. It also allows to design a lighter overall kinematic structure (force-path). The resulting mechanics have lower mechanical stiffness with lower dominant mechanical eigenfrequencies. This means that the internal dynamics of the structure are easier excited, which deteriorates the performance. To keep the required system performance, extra actuators and sensors are included in the design. The use of extra actuators must increase both tracking and regulation performance, which is lowered due to the weaker mechanics [5]. In other words, mechanical stiffness is exchanged by smart control and intelligent placement of additional actuators and sensors. Applying more forces than strictly needed for the control of the rigid body movements is called over-actuation.

As already mentioned, the lightweight design approach incorporates three areas of expertise: control, mechanics and electromechanics. Contributions from the three different areas are all focused on mass reduction in order to design an overall lighter motion system while reaching the same performance.

1.1.5 Benchmark of the lightweight design - Flexible beam

In a similar way as in section 1.1.3, the benchmark of the lightweight design is specified. A light and flexible beam (Fig. 1.7), which replaces the stiff beam, has much lower frequencies of the dominant vibration modes. The motion task in this case is to reach the same control bandwidth in closed loop as in the heavy beam system.
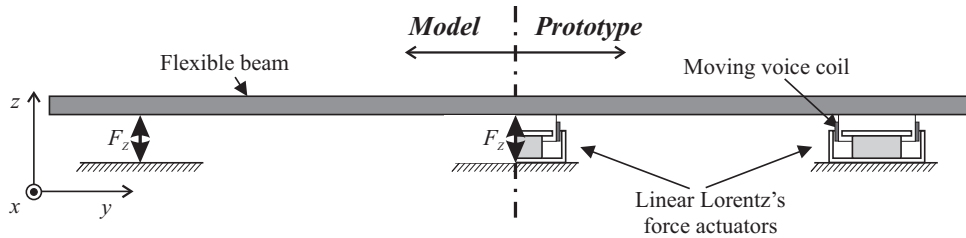
Figure 1.7: Flexible beam (setup 1).

It can be noticed that the light beam, with two degrees of freedom (z-translation and x-rotation), is now supported by three voice coil actuators according to the
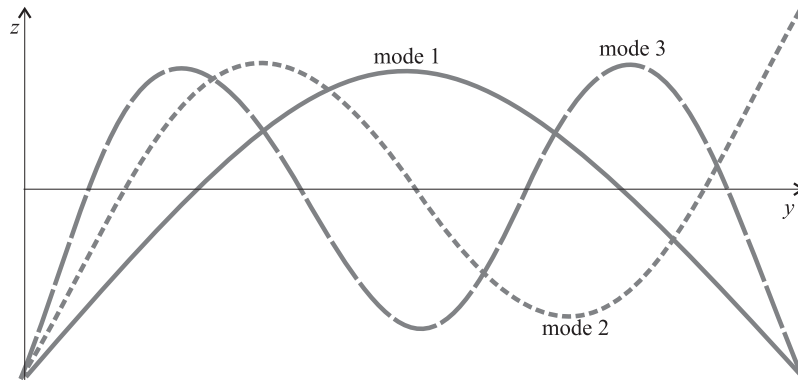
Figure 1.8: Shape of vibration modes.

overactuating principle. The placement of the actuators is governed by two rules:

- A vibration mode is not excited if the points of actuation (positions of the actuators) are exactly in the nodes of the mode.

- A vibration mode is controllable if the points of actuation are out of the nodes.

In this way, the dominant vibration modes (Fig. 1.8) with frequencies lower than the required control bandwidth can be controlled by not placing the actuators in the nodes.

The position of the actuator out of a node has also an adverse influence. If the actuator is out of the node the vibration mode has higher controllability but also higher sensibility to disturbances via the actuator. An alternative configuration is to apply an actuator producing force F_z and torque T_x in the node, as it is depicted in Fig. 1.9. The force is then applied to perform a motion task and the torque is used for vibration control.

Figure 1.9: Flexible beam with torque production for vibration control (setup 2).

1.2   Structure of the thesis

This thesis presents the results of research that has been done in the area of light-weight positioning, particularly the part focused on ways of actuation of lightweight positioning systems. It gives answers to the following questions:

- Is it possible to find a new electromechanical actuator topology with decoupled control of two degrees of freedom (force and torque) that would actuate the flexible beam in Fig. 1.9?

- How could this actuator be mathematically described and designed?

- What would be the way to minimize the total mass of such an actuator?

The challenges of precision technology positioning systems were studied in order to find suitable means of precise actuation. Based on these studies, the most promising topology of an electromechanical actuator was proposed, analyzed, designed and optimized. Towards this end, the thesis is structured as follows.

The first two chapters concentrate on the analysis of challenges related to precision positioning systems and state-of-the-art actuators, respectively. The main result of these chapters is the synthesis of a novel actuator.

Chapter 1 outlines the influence of internal vibrations on the performance of positioning systems. It sketches the way of dealing with vibrations in positioning systems used in precision technology, by classical and lightweight design approaches. A few classical examples are described and the main problems of high moving mass, actuation forces and currents are pointed out. It is also explained how the lightweight design will deal with the disadvantages of a classical design. Two benchmarks of the two approaches are introduced, one for each design method.

Chapter 2 concentrates on the electromagnetic actuators for precision technology, which are one of the sub-levels of the system design. Several state-of-the-art actuators are summarized, pointing out advantages and disadvantages of particular

designs. Based on two possible configurations of the lightweight design an innovative actuator with two controlled degrees of freedom is proposed (further referred to as 2-DoF actuator), which takes the performance requirements in consideration. The working principle of the novel actuator is explained.

The following three chapters describe comprehensively the analytical and numerical methods of analysis and design of the 2-DoF actuator, which was proposed at the end of Chapter 2.

Chapter 3 starts with a fundamental basis for the electromagnetic theory that is needed to derive the magnetic equivalent circuit of the actuator. This analytical model is built of lumped parameters (magnetic reluctances, magnetic flux sources), which are dependent on the geometric dimensions of the actuator and the characteristics of materials. Then, the theory of the finite element method is shortly presented and a finite element model is built for the purpose of identification of the magnetic reluctances and comparison of the analytical and numerical models. From the magnetic flux density values obtained by these two methods, forces and torques can be calculated by three approaches: Lorentz force equation, virtual work and Maxwell stress. Finally, simulation results are presented and compared.

Chapter 4 is dedicated to the thermal analysis. The chapter starts with a short basis of heat transfer, which is used to classify and analyse heat flows in the actuator. Because of the complex patterns of the heat flows, a way to simplify the thermal model is presented. Then, relevant parts of the actuator are separately analyzed and modeled. By connecting the actuator parts in accordance with the identified heat flows an equivalent lumped parameter model is derived. The chapter ends with the presentation and discussion of simulation results.

In Chapter 5, a design optimization approach is presented that deals with finding an optimal solution of the actuator. To do so, the design problem is transformed into a mathematical formulation of the optimization problem. Recognizing objective and constraints functions, the link between the analytical models of the actuator and the optimization problem is created. Further, it is necessary to select design variables and parameters. The end of this chapter is focused on an optimization method that brings all the results of the earlier chapters together. All these efforts yield optimal dimensions of the novel actuator.

An important and indivisible part of all scientific studies are experiments, presented in Chapter 6. Several experiments are carried out in order to confirm the analytical and numerical descriptions to model the actuator. The results demonstrate a good agreement with those of the theoretical models put forward in this thesis.

This dissertation summarizes the main contributions in Chapter 7, where several recommendations for future work are also made.

1.3   Contribution of the thesis

A novel lightweight design synthesis approach at a system level is elaborated in this thesis. It is the result of a common research effort in the areas of mechanics, control and electromechanics. The study emphasizes the mass reduction of the moving parts in positioning systems designed by the lightweight methodology.

Further, the design and optimization of an electromagnetic actuator for precision positioning systems is addressed in details. The major contribution is the innovative topology of an integrated 2-DoF actuator, suitable for multi-degrees of freedom positioning stages, capable of implementing the required precise movements and vibration control. Further contributions are consequences of the novel actuator topology:

- The adaptation of the analytical electromechanical description of the actuator based on the general theory of electrical machines and the dynamics of mechanical systems. The description expresses interconnections between electromagnetic, electromechanical and thermal design parameters, and performance characteristics.

- The elaborated optimization approach integrates the analytical description into a complete design procedure for optimization of the actuator.

Chapter 2

Dedicated actuator for the lightweight positioning system

Various topologies of standard as well as customized electromechanical actuators can be found in precision technology applications. The variation in actuator topologies arises from different requirements of particular applications. In other words, based on the requirements put on a particular drive system an appropriate topology of the actuator is selected in order to reach the best possible performance.

To make the best choice of actuator topology for the lightweight positioning system, and consequently to reach the best possible performance, an overview of state-of-the-art actuators is presented in this chapter. The overview shows important aspects of different designs, their connections to topologies and construction elements. Furthermore, pros and cons are discussed.

Based on the most important aspects of the design of electromechanical actuators, a novel topology of a two degrees of freedom actuator is introduced. The topology tries to reflect on the requirements of the lightweight positioning system in an optimal way, so that a good harmony among the requirements and the mechanical, electromagnetic and thermal characteristics of the actuator is achieved.

At the end of the chapter, the working principle of the 2-DoF Lorentz actuator is explained and one of the possible embodiments of the actuator is selected.

2.1   State-of-the-art of actuators

2.1.1   Voice coil actuator

The voice coil actuator or Lorentz force actuator is the oldest type of actuator used nowadays in precision technology. It evolved from a totally different application field. The word "voice" may suggest that the apparatus is used in sound reproduction. One of the oldest illustrations of the voice coil in the form as it can still be found nowadays dates back to July 1932 (Fig. 2.1).
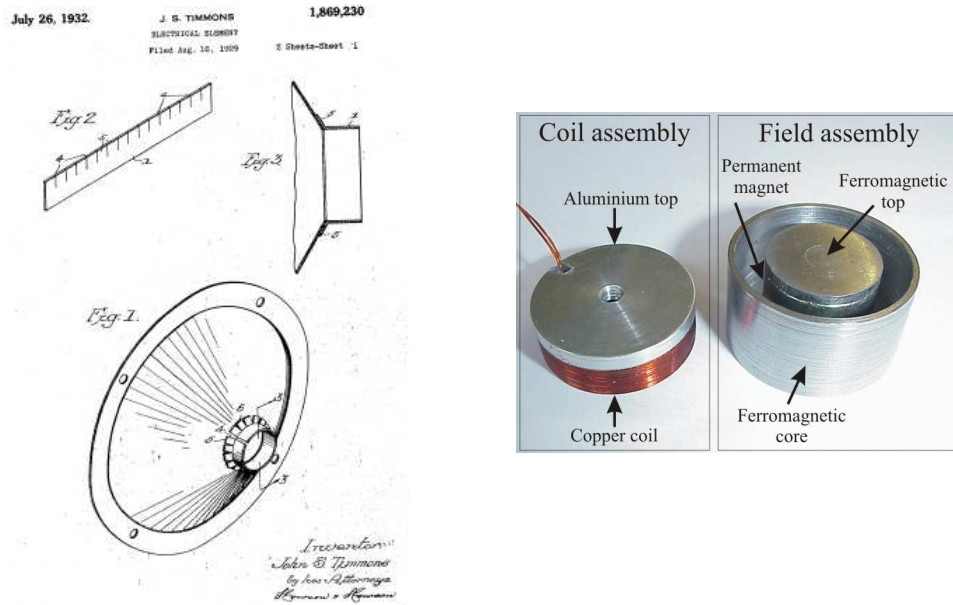
Figure 2.1: Past and present of voice coil actuators.

The actuator consists of a moving coil assembly (coil connected to a nonmagnetic cup) and a field assembly (ferromagnetic material and permanent magnet) creating a magnetic field that crosses the coil perpendicularly.

Performance requirements have led the voice coil actuator to go through many improvements causing that the actuator can nowadays be found in many different forms and topologies (see Fig. 2.1). Precision positioning performance requirements that can be efficiently met by a voice coil actuator are:

- low parasitic forces,

- low moving mass,

- high acceleration,

- almost constant force-to-current ratio,

- direct drive (no gear box).

Having low parasitic forces and also no preferred position (due to cogging force) this kind of actuator produces low disturbances and, therefore, it can be controlled with high accuracy. The low moving mass of the coil ensures high acceleration and small inertia, which is convenient for set-points with high dynamics. The dependency of the force-to-current ratio on position can be minimized by a convenient design of the actuator. If the ratio is made almost constant, the control strategy for the actuator can be implemented in a simple form. The direct drive is preferable if high positioning accuracy is required. Furthermore, it does not use a gear box and, as a consequence, the drive does not introduce additional tolerances, play and friction.

Actuators of this type are implemented in the setup 1 of the flexible beam system (Fig. 1.7), where they realize the translation in the z-direction. The actuators on the sides can also rotate the beam around the x-axis. However, the voice coil actuator is not necessarily found to be the optimal solution for positioning systems with more degrees of freedom or with a longer stroke. In such cases, a Lorentz force actuator with different topology may be chosen, as it is shown in the following sections.

2.1.2 Three degrees of freedom planar drive

The planar actuator [12] shown in Fig. 2.2 is able to create long-stroke linear movements in x- and y-directions and a limited rotational movement around the z-axis. In the case shown, the moving parts are permanent magnets with iron yokes connected into one assembly. The stationary part consists of a set of coils attached to a flat ferromagnetic plate.

Two kinds of forces are created by the actuator in Fig. 2.2:

- Lorentz forces in the xy-plane between the coils and magnets.

- Attractive reluctance forces in the z-direction between the magnets in the mover and the flat ferromagnetic plate of the stator.
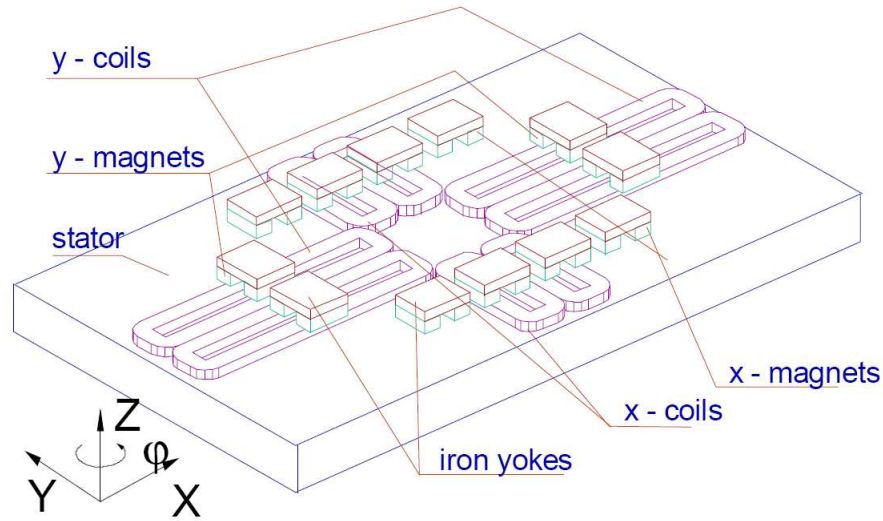
Figure 2.2: Three degrees of freedom planar motor [12].

The attraction force is used to pre-load air bearings by which the mover is suspended from the stator. Because the air gap between the stator and the mover is smooth, the actuator does not have any preferred position due to reluctance forces (no cogging).

A potential advantage of this topology is that the mover is a passive magnetic element and thus does not have any cable slab, which introduces additional parasitic forces. As a result, the actuator can reach higher accuracy than an actuator with a cable slab. Unfortunately, this advantage is not fully used because parasitic forces are introduced by the air intake hoses of the air bearings connected to the mover.

The negative consequence of the passive mover is a high mass of the mover and, so, lower acceleration, due to the mass of the magnets and ferromagnetic core, which is higher than that of the coils. Another disadvantage is that the coils are covering the whole length of the stroke, but the active volume (contributing to force production) is only under the permanent magnets. It means that the copper losses are high (low efficiency) and special attention has to be paid to the thermal management of the setup. Otherwise, thermal deformations of the materials may deteriorate the accuracy of the whole setup. It has to be mentioned that two types of damping appear in the structure. The first is due to hysteresis friction. The

second is due to eddy currents, since laminated back iron is hard to realize.

2.1.3   Planar magnetic levitator

In the previous example, the positioning accuracy is dependent on the flatness of
the air bearing surfaces (the flat ferromagnetic plate). This dependence may be
eliminated if the actuator can be controlled electromagnetically in all six DoFs.
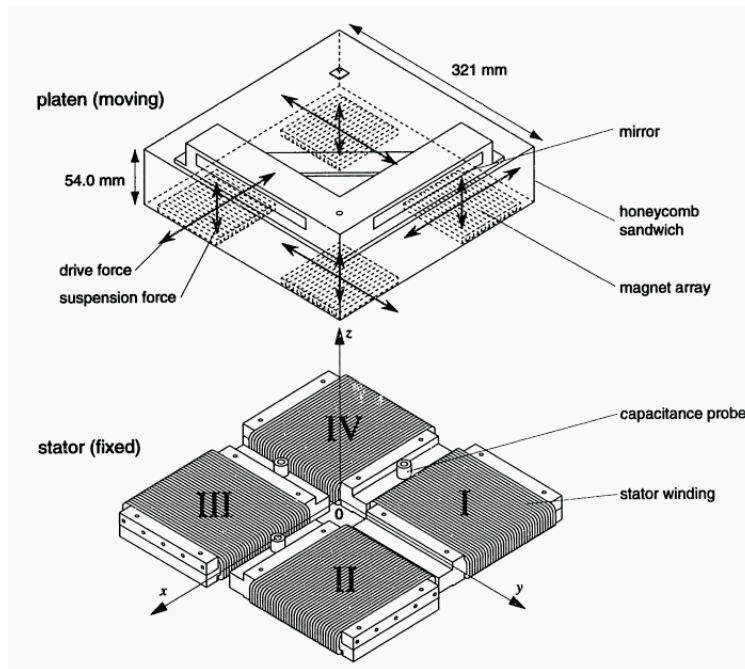
Figure 2.3: Six degrees of freedom planar magnetic levitator [13].

The 6-DoF actuator in Fig. 2.3 has a very similar topology as the 3-DoF
planar drive in Fig. 2.2. It does not contain any ferromagnetic material, so, there
is no attractive reluctance force. The Lorentz forces are produced by four units
comprising a mover with Halbach magnet array and three-phase stator windings.
Each unit can produce lateral and suspension Lorentz forces.

The Halbach magnet array is built from magnets where each successive magnet

has the magnetization vector rotated by 90° with respect to the preceding magnet (see Fig. 2.4). This type of array creates a stronger magnetic field than a magnet array made of only south-north combinations of magnets without any ferromagnetic core.
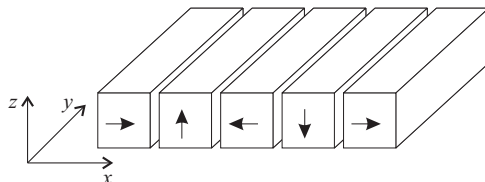
Figure 2.4: Halbach magnet array.

The electromagnetically suspended mover is advantageous for accuracy because it is not limited by bearing surfaces, does not need any lubrication (suitable for vacuum environment), and it does not produce wear particles. The mover has a low number of mechanical elements, so it achieves a higher reliability and low cost. As a heat source the winding is connected to the static world, consequently the cooling is easier.

The disadvantage of the actuator is its efficiency. It is lower than in the case of the 3-DoF planar drive because it uses a wrap-around winding with just the top side of the coils active.

In the next example of a 6-DoF actuator, the efficiency is increased by a better active-volume utilization of the coils.

2.1.4   Long-stroke planar motor

The planar motor in Fig. 2.5 has the inverted topology with respect to the previous two examples. This means, that the magnets are stationary and the coils are moving. It can be seen that the arrangement of the magnets forms a two-dimensional Halbach array. The coils constitute four propulsion units that are rotated by 45° with respect to the magnets.

Each unit is able to produce lateral and suspension forces (see Fig. 2.6). The lateral force is produced by interaction of the coils and the vector component of the magnetic flux density in the z-direction. The suspension force is created by reciprocal action of the coils and the magnetic flux density vector in the xy-plane.

In such a configuration of magnets and coils, the coil dimensions are not dependent on the stroke of the actuator. The dimension of the active part of the

Figure 2.5: Six degrees of freedom planar motor [14].

Figure 2.6: Principle of force production of the planar motor in Fig. 2.5 [15].

coils is determined only by the required force of the actuator. The dimensions of the end connections are related to the pole pitch of the magnets, which can be chosen

optimally with respect to the active length of the coil. Thus, a high force at high efficiency and low moving mass can be reached. Consequently, a high acceleration of the mover and therefore a high throughput of a positioning system is ensured.

On the other hand, the active mover experiences parasitic forces due to a cable slab and cooling hoses if forced cooling is applied.

It is also important to mention that the long-stroke planar motor as well as the planar magnetic levitator dissipates energy to overcome gravity and to keep the mover floating.

2.1.5   Moving iron actuator

The so-called moving iron actuator is a new alternative for implementing precision technology actuators, which avoids the moving coils or moving magnets. It appeared recently [16] and it is still in research phase [17].

The actuator consists of an I-shaped ferromagnetic mover and two U-shaped stator cores with suspension and propulsion coils. The stator cores are magnetically coupled by permanent magnets (see Fig. 2.7).
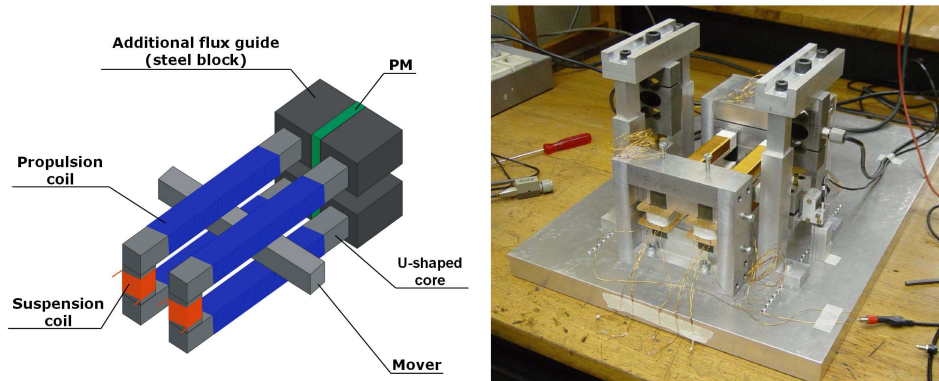
Figure 2.7: UI-shaped actuator topology and experimental setup [17].

The actuator utilizes reluctance forces for the suspension (short stroke) and Lorentz forces for the propulsion (long stroke). It has four controlled degrees of freedom, two rotational and two translational.

The suspension reluctance forces are realized by a bias magnetic field created by the permanent magnets. It means that the suspension requires low power

($0.8mW$ for the suspension of a $3.4kg$ mover [16]) that is needed only for cancellation of disturbances. Thus, the actuator is suitable for applications where gravity cancellation is required.

Because of the high mass of the mover the actuator is restricted to achieve low propulsion acceleration ($1.6m/s^2$) at quite high power consumption ($200W$). Nevertheless, according to the authors the acceleration and power consumption can be optimized by increasing the volume of the coils and by using coil segments [16].

2.1.6   Main issues of electromagnetic actuators

In general, electromagnetic actuators are used for positioning of a payload in the range of nanometers up to several centimeters. They are used to build high dynamic systems with high acceleration and low moving mass. The actuators reach a high repeatability of positioning and thus they satisfy the requirements of high throughput of mass production and big production series.

There are a few issues that have to be considered when choosing and designing electromagnetic actuators. The major issue is power dissipation since it is limited by the temperature insulation limit. Further, dissipation decreases the precision of positioning by producing thermal deformations. The negative influence of heat production can be reduced if the active volume of the coils is maximized, and if the heat transfer path is short and an effective cooling system is implemented.

The second issue are parasitic, position dependent and cogging forces. Parasitic forces or forces in other directions than the direction of interest need to be counter-acted by a guiding system, which, in turn, introduces tolerances, adds mass and decreases the accuracy of the positioning. Position dependent forces can be compensated by control, but usually at the expense of higher power dissipation. The cogging and hysteresis forces of iron core actuators are hard to correct and therefore they are avoided by choosing air coils actuators with lower force vs. mass ratio.

These issues can be solved in various ways; some of them are demonstrated by the presented state-of-the-art actuators. In most cases, particular solutions or topologies are chosen in order to satisfy specific requirements of applications.

In the next sections, the topology of a 2-DoF actuator is presented. The concept of the actuator is chosen to satisfy the main issues of the electromagnetic actuation in precision technology in order to create an universal actuator. Such an actuator can be used in the flexible beam system but it is also suitable for more general use.

2.2   Innovative actuator with two controlled degrees of freedom

In section 1.1.5, the lightweight positioning system benchmark (setup 2 in Fig. 1.9) is positioned on a distance of a few millimeters by the collocated force and torque acting in the nodes of the vibration modes. For this purpose, a novel short-stroke actuator, which produces the force needed for positioning and torque used for vibration control, is proposed.

2.2.1   Principle of force production by integral electromagnetic structure

The force and torque production in the innovative actuator is based on the principle of redundant force cancellation. It means that if an electromagnetic structure is controlled in two degrees of freedom, for example, more than two forces are created within the structure. Then, by interaction of the redundant forces (cancellation or superposition) two resulting forces can actuate the two degrees of freedom independently. The principle is also used in the planar magnetic levitator (section 2.1.3) as well as the long-stroke planar motor (section 2.1.4). In the next section, the principle of the force and torque production is explained on the example of the topology of the 2-DoF actuator .

2.2.2   General topology of the actuator with two controlled degrees of freedom

The 2-DoF actuator (see Fig. 2.8) consists of a set of force magnets (1), a set of torque magnets (2) and a set of coils (3). The magnets and coils build up two stages. In the first stage both the force and the torque magnets create a magnetic field that crosses the volume of the coil (3.1 and 3.2, respectively) on the sides of the coil, symmetrically around the axes of symmetry. When current I is flowing through the coil of one stage, the parts of the coil (3.1) in the magnetic field of the force magnets create redundant forces f_r that are acting in the same direction parallel to each other. Therefore, the resulting total force created by the parts of the coil (3.1) is in the direction perpendicular to the vectors of current and magnetization of the force magnets. The parts of the coil (3.2) in the magnetic field of the torque magnets create redundant forces in the opposite direction parallel to each other. Thus, the sum of all forces in volume (3.2) is a torque with the axis of rotation identical to the axis of symmetry and perpendicular to the direction of the forces.

The second stage is built up to create a resulting force and torque in a similar
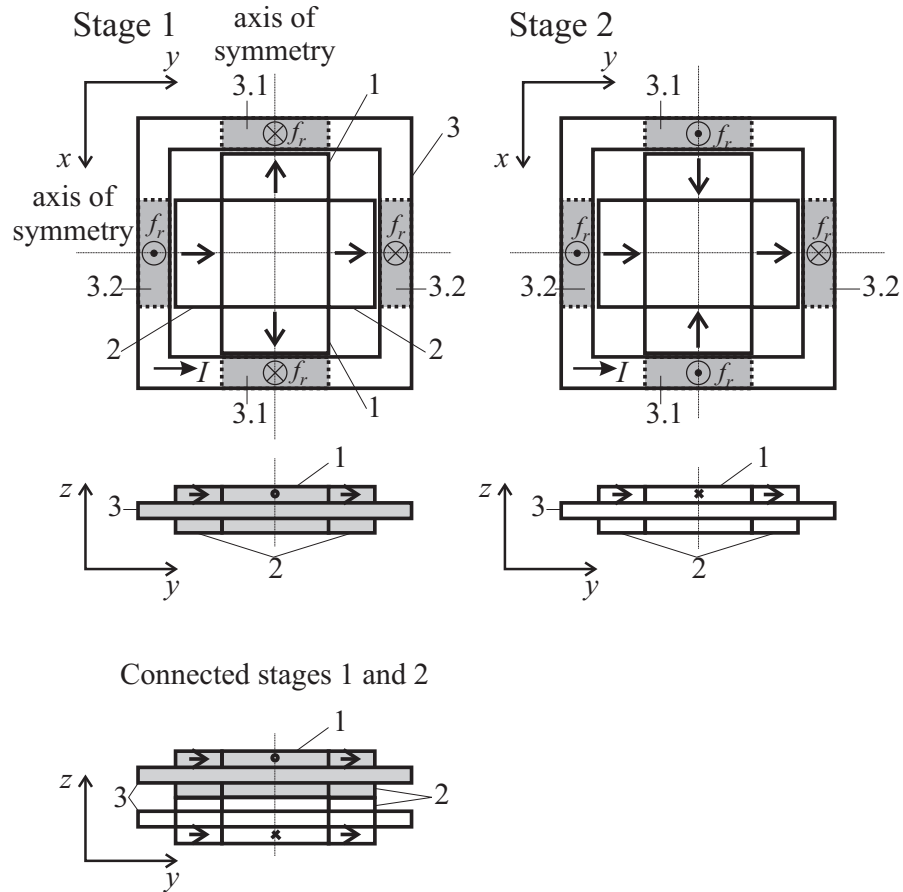
Figure 2.8: Working principle of a 2-DoF actuator.

way as the first stage. However, when the directions of the currents in both coils (in the first and second stage) are identical the total force of the second stage counteracts the total force of the first stage. At the same direction of the currents in the coils, the total torques of both stages act in the same direction.

If the force and torque of one stage would counteract the force and torque of the other stage at the same time, the independent control of the resulting force and

torque of the actuator (comprising the two stages) would not be possible.

The coils of the two stages are mechanically connected creating one coil assembly. The magnets of the stages are also mechanically connected forming one magnet assembly.

By this topology it is achieved that the dimensions of the coils are not dependent on the stroke (absence of end turns). As it will be seen in the next section (Fig. 2.9), almost the whole volume of the coils is active. A drawback is the principle of redundant forces cancellation. It causes parts of the coils (3.2 or 3.1 in Fig. 2.8) to be inactive and generating heat if only force or torque is produced.

The general topology can be modified to create various physical forms of the actuator. Each embodiment has slightly different performance characteristics. These different structures represent flexibility for adaptation in various applications and requirements. In the following section, a particular embodiment that is especially suitable for the flexible beam system is described.

2.2.3   Topology of the 2-DoF actuator for the flexible beam system

The chosen topology of the 2-DoF actuator for the flexible beam system is shown in Fig. 2.9. The actuator can realize a force in z-direction and a torque around the x-axis. Comparing to Fig. 2.8, the actuator in Fig. 2.9 has one torque magnet in
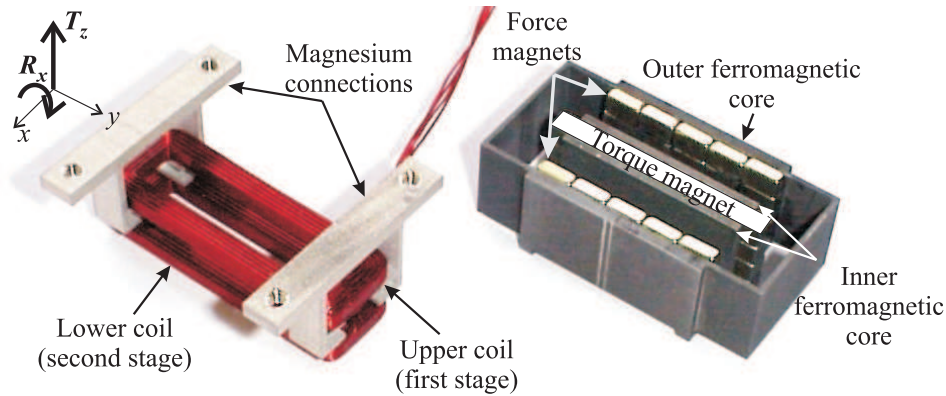
Figure 2.9: Coil, core and magnet segments assembly of the 2-DoF actuator.
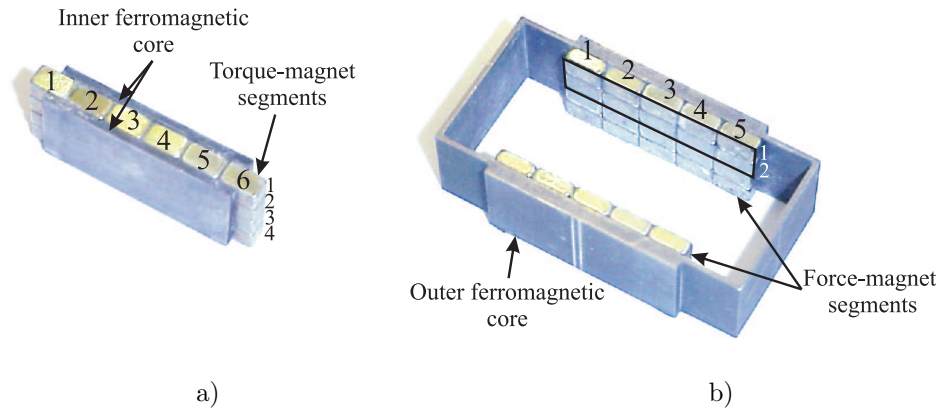
Figure 2.10: Field assembly of the 2-DoF actuator: a) torque-magnet segments, b) force-magnet segments.

the middle, built of six columns and four rows of magnet segments (see Fig. 2.10a), and four force magnets on the sides of the outer ferromagnetic core, each magnet being assembled with five columns and two rows of segments (see Fig. 2.10b).

The torque magnet creates a magnetic flux, as is depicted in Fig. 2.11a. The flux flows from one end of the magnet through the air gap to the outer ferromagnetic core, where it splits itself in two parts. Then, it flows on both sides of the magnet back through the second air gap to the other end of the magnet.

The flux path of the force magnets goes from one magnet through the air gap and the inner ferromagnetic core, and comes back through the other air gap and second magnet, as it can be seen from Fig. 2.11b. The flux lines close themselves through the outer ferromagnetic core, where the flux adds up with the flux of the torque magnet.

The topology of the actuator is chosen to satisfy the following objectives:

- low power dissipation,

- low moving mass,

- no cogging forces,

- high mechanical stiffness.

a)   b)

c)
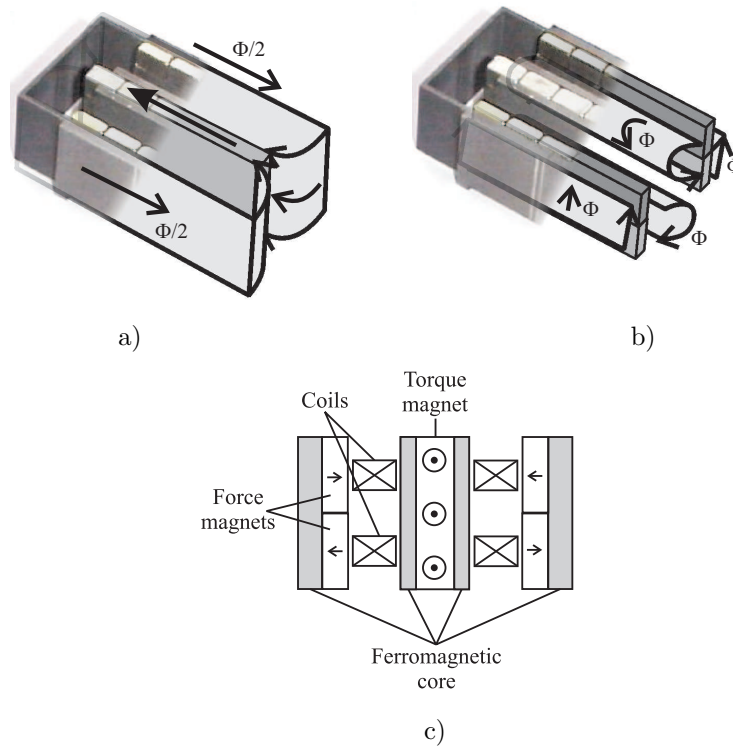
Figure 2.11: Magnetic fluxes in the 2-DoF actuator: a) flux of the torque magnet, b) flux of the force magnets, c) cross-section view.

Low power dissipation is ensured by choosing a configuration with short coils and long magnets. It also means that the mass of the coil assembly is much lower than the mass of the field assembly. For this reason, the coil assembly is used as moving part. To avoid cogging or reluctance forces the coil assembly does not contain any ferromagnetic material (air coil actuator). The magnet segments are long, covering the height of the coils and the length of the actuator stroke. This results in a thicker ferromagnetic core, and so its mechanical stiffness is improved.

Chapter 3

Static electromagnetic analysis

The first step in the development of a novel dedicated actuator is to decide on its topology, as it was done in the previous chapter. The next step is to establish a path that connects performance requirements with geometrical dimensions of the actuator. The connecting path represents a set of equations, also called sizing equations, that expresses mutual relations between requirements (continuous force, magnetic field density etc.) and dimensions (of magnets, ferromagnetic core etc.). Established sizing equations are then used as a design tool by which optimal dimensions and performance parameters of the actuator can be found.

There are many possible ways of describing the relationships between requirements and dimensions. For example, the magnetic field equations of permanent-magnet actuators may be derived from the method of magnetic charges [18, 19]. However, this approach is not suitable for the actuator described in this thesis, because the charge-mirroring principle would introduce a large error due to the boundaries of the ferromagnetic material [20]. Therefore, this method is out of the scope of the thesis. Another way is to use a magnetic equivalent circuit (MEC), which is in general used in rotary machines with relatively small air gap [21, 22]. The advantage of the MEC model is mainly the resulting simplicity of the circuit. For this reason, the MEC is chosen for analysis of the proposed topology of the actuator. On the other hand, the disadvantage of this method is that the circuit should be built with prior knowledge of the magnetic field distributions, which can be acquired by finite element simulation.

In this chapter, the electromagnetic sizing equations are derived from those of the magnetic field and force. Therefore, the fundamental theory of electromagnetism

is presented in section 3.1, with the intention of developing electromagnetic models that yield the magnetic field, forces and torques created by the permanent magnets and coils of the actuator. Two models are created: an analytical based on the method of magnetic equivalent circuits and a numerical based on the finite element method (FEM).

The concept of MECs, based on analogies between electric and magnetic circuits, is developed in section 3.2. FEM is described in section 3.3.

The two methods, MEC and FEM, are complementing each other in this design approach. The MEC model is analytical and relatively simple, which makes it suitable for optimization using the theory of nonlinear programming. But, as it will be shown, the MEC model is built of elements that are specified with difficulties if no prior investigation is done. Therefore, the FEM model is used to identify the elements of the MEC. The model is considered as more precise and no prior knowledge of magnetic field distribution is necessary to obtain correct results. After the optimization, which utilizes the MEC model, the FEM model is again used to verify the results of the optimization.

Force and torque equations are derived from known magnetic field equations. They are formulated by means of:

  - Lorentz's force,

  - Virtual work (energy method),

  - Maxwell stress tensor.

in section 3.4. Finally, simulation results of the MEC and FEM model are shown and compared in sections 3.5 and 3.6.

3.1 Electromagnetism

3.1.1 Maxwell's equations

Electromagnetic phenomena are analytically expressed by

$$\text{Gauss's law for electrostatic field} \qquad \nabla \cdot \vec{D} = \rho_\nu, \qquad (3.1)$$

$$\text{Gauss's law for magnetostatic field} \qquad \nabla \cdot \vec{B} = 0, \qquad (3.2)$$

$$\text{Faraday's law} \qquad \nabla \times \vec{E} = -\frac{\partial \vec{B}}{\partial t}, \qquad (3.3)$$

$$\text{Maxwell - Ampere law} \qquad \nabla \times \vec{H} = \vec{J} + \frac{\partial \vec{D}}{\partial t}, \qquad (3.4)$$

$$\text{equation of continuity} \qquad \nabla \cdot \vec{J} = -\frac{\partial \rho_\nu}{\partial t}. \qquad (3.5)$$

These equations are also called the Maxwell equations in the differential form where ∇ is the vector differential operator, $\vec{D}$ is the electric flux density, $\vec{B}$ is the magnetic flux density, $\vec{E}$ is the electric field intensity, $\vec{H}$ is the magnetic field intensity, ρ_ν is the volume charge density and $\vec{J}$ is the current density. If the time derivatives are zero and the current flow is constant, a static electromagnetic or magnetostatic field is produced. Then, the magnetostatic field is determined by (3.2), (3.4) and (3.5) as

$$\nabla \times \vec{H} = \vec{J}, \qquad (3.6)$$

$$\nabla \cdot \vec{J} = 0. \qquad (3.7)$$

3.1.2 Ampere's circuit law

Ampere's circuit law is applied in a design of magnetic circuits of electromagnetic devices. It is also one of the fundamental equations in the theory of magnetic equivalent circuits. By applying the curl theorem of Stoke to (3.6), Ampere's circuit law is obtained:

$$\oint \vec{H} \cdot d\vec{l} = I_{enc}, \qquad (3.8)$$

with $d\vec{l}$ being the differential length and I_{enc} being the net current enclosed by a closed path. The law states that the line integral of $\vec{H}$ around a closed path equals the net current enclosed by the path.

3.1.3 Magnetic vector and scalar potentials

Other important quantities in the magnetostatic analysis are the magnetic potentials $\vec{A}$ (vector) and V_m (scalar) of a vector field. The magnetic field is a vector field and thus it is uniquely characterized by its divergence and curl. The divergence (3.2) and curl (3.6) hold for the magnetostatic field. That means, the definition of the potentials should be in accordance with these two equations. Since

$$\nabla \cdot \vec{B} = 0,$$

it can be shown by vector calculus that the divergence of the curl of any field vector $\vec{X}$ equals zero, that is

$$\nabla \cdot \left(\nabla \times \vec{X} \right) = 0. \tag{3.9}$$

Then, the magnetic vector potential $\vec{A}$ is chosen as

$$\vec{B} = \nabla \times \vec{A}. \tag{3.10}$$

On the other hand, the magnetic scalar potential V_m is chosen by analogy with the electric potential and is related to $\vec{H}$. Taking Ampere's law

$$\nabla \times \vec{H} = \vec{J}$$

and again from the fact that the curl of the gradient of any field scalar V vanishes

$$\nabla \times (\nabla V) = 0, \tag{3.11}$$

the magnetic scalar potential is defined by:

$$\vec{H} = -\nabla V_m \quad \text{if } \vec{J} = 0, \tag{3.12}$$

but only in a region where the current density is zero, which is expressed by the condition attached to the definition.

3.1.4 Magnetic energy

The magnetic energy stored in a system of steady-state currents, which is made of current filaments, is defined as the energy needed to bring the filaments to a certain position from infinity [23]. However, the energy consists of two parts:

- The energy required to bring a filament with constant current from infinity overcoming the Lorentz force.

- The energy required to keep constant the current in this filament, and any existing filament.

Then, the magnetic energy W_m can by written as

$$W_m = \frac{1}{2} \int_{V_\infty} \left[\int_B \vec{H} \cdot \mathrm{d}\vec{B} \right] \mathrm{d}V, \tag{3.13}$$

where V_∞ denotes all of space.

3.2 Magnetic equivalent circuits

The basic terms and definitions used in the theory of magnetic equivalent circuits are introduced in this section. Then, the 2-DoF actuator is partitioned into passive and active elements of the circuit. An analytical equation is assigned to each element (reluctance or source). Finally, the MEC of the actuator is built and the analytical model, which will be used to find the optimal dimensions of the actuator, is derived.

3.2.1 Electric and magnetic circuit analogies

The magnetic equivalent circuit method [24, 25] is based on the analogies of the equations, which express relations of electrical and magnetic field quantities in materials, and other corresponding similarities, shown in Table 3.1:

$$\vec{B} = \mu \vec{H}, \tag{3.14}$$
$$\vec{D} = \epsilon \vec{E}, \tag{3.15}$$
$$\vec{J} = \sigma \vec{E}. \tag{3.16}$$

The method uses the reluctance $\mathcal{R}_m$ as the basic passive element. An active element of the magnetic circuit is a source. Two kinds of sources are defined by the analogy with the electrical sources:

- the magnetomotive force $\mathcal{F}$,

- the flux source Φ.

There is a difference between sources in magnetic and electrical circuits, since there is no quantity in a magnetic field that is analogous to an isolated charge in an electrostatic field [26].

Table 3.1: Analogies among different types of fields.

	Field		
	Magnetic	Electrostatic	Electric
Material property	μ	ϵ	σ
Flux or current density	$\vec{B}$	$\vec{D}$	$\vec{J}$
Reluctance, Capacitance, Resistance	$\mathcal{R}_m = \int_0^l \dfrac{\mathrm{d}x}{\mu(x)A(x)}$	$C = \int_0^l \dfrac{\mathrm{d}x}{\epsilon(x)A(x)}$	$R_{el} = \int_0^l \dfrac{\mathrm{d}x}{\sigma(x)A(x)}$
Potential difference	$\mathcal{F} = \int_0^l H\mathrm{d}x$	$V = \int_0^l E\mathrm{d}x$	$V = \int_0^l E\mathrm{d}x$
Flux, Charge, Current	$\Phi = \int_A B\mathrm{d}A = \dfrac{\mathcal{F}}{\mathcal{R}_m}$	$Q = \int_A D\mathrm{d}A = \dfrac{V}{C}$	$I = \int_A J\mathrm{d}A = \dfrac{V}{R_{el}}$

3.2.2   Categorization of reluctances

The reluctance is defined with the help of flux tubes. A flux tube, see Fig. 3.1, is a geometrical object with sides parallel and bases perpendicular to the flux lines enclosed by the tube. The flux tube can also be identified with the help of the magnetic field intensity vector, which is tangential to the flux lines. The reluctance can be written as

$$\mathcal{R}_m = \int_0^l \frac{\mathrm{d}x}{\mu(x)A(x)}, \tag{3.17}$$

with l being the length of the flux tube, $A(x)$ being the cross-section area and $\mu(x)$ being the flux tube magnetic permeability.

The general equation (3.17) shows that the reluctance can be categorized as:

- constant, with the flux tube geometry and permeability constant in time (e.g. smooth air gap),

- permanently (parametric) nonlinear, with the time-varying geometry of the flux tube, where the geometry of the flux tube changes with the movement of a machine (e.g. salient pole motor),
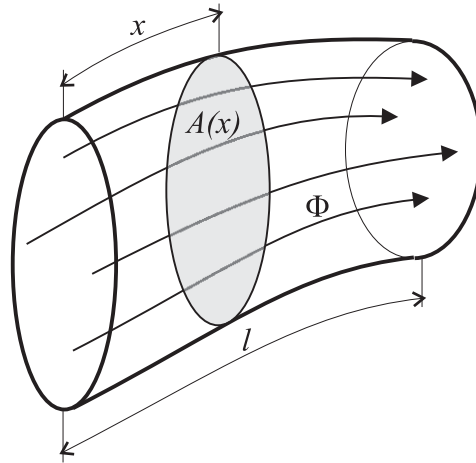
Figure 3.1: Flux tube in a field.

 - inherently nonlinear, with the time-varying permeability (e.g. transformer).

Before the parts of the 2-DoF actuator can be categorized into the above mentioned reluctances, the approximate shapes of the flux tubes have to be known. The shapes can be specified intuitively or more precisely by means of FEM analysis. The goal of the analysis is to find the distribution of $\breve{H}$ (see Fig. 3.2 and 3.5). Consequently, the shape of the flux lines can be drawn as it is shown in Fig. 3.3 and 3.6. Finally, the sides and the bases of a particular flux tube can be identified (see Fig. 3.4 and 3.7). Usually, it is difficult to find a suitable (integrable) mathematical expression of the flux tube shape. Therefore, it is convenient to use simple geometrical shapes (e.g cuboid, half cilinder, trapezoidal prism etc.)
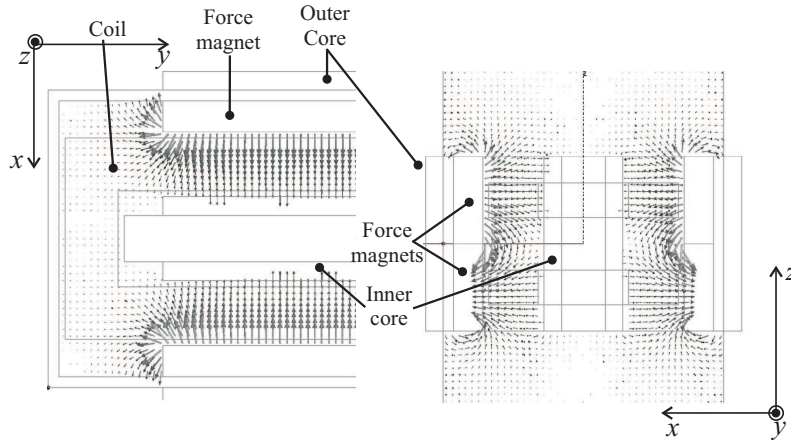
Figure 3.2: Vector plot of magnetic field intensity distribution of the force magnets.
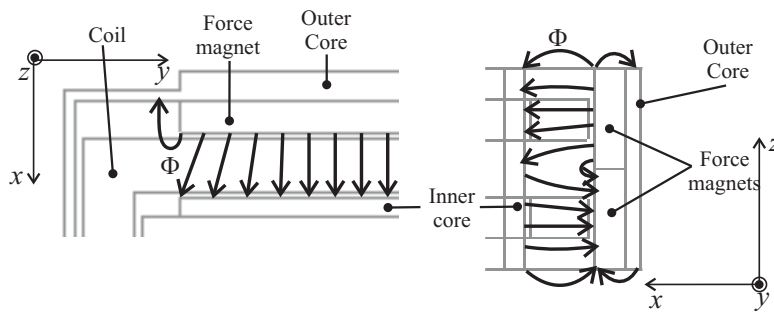
Figure 3.3: Flux lines of the force magnets.
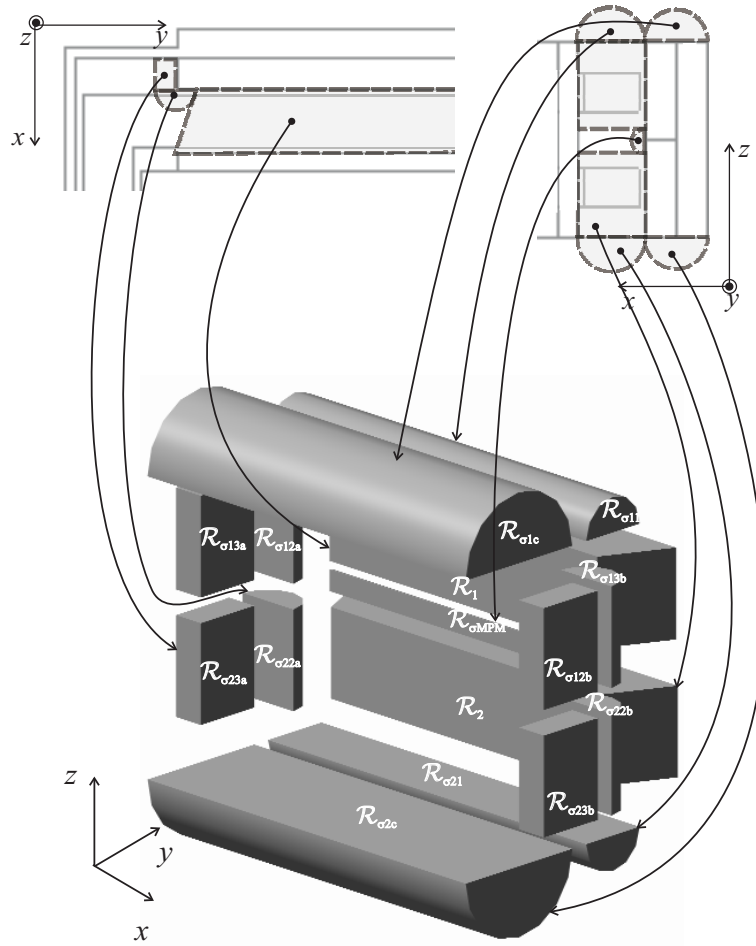
Figure 3.4: Flux tubes related to the force magnets.
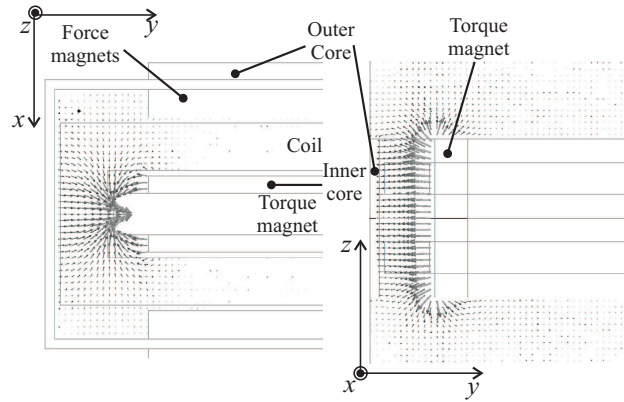
Figure 3.5: Vector plot of magnetic field intensity distribution of the torque magnet.
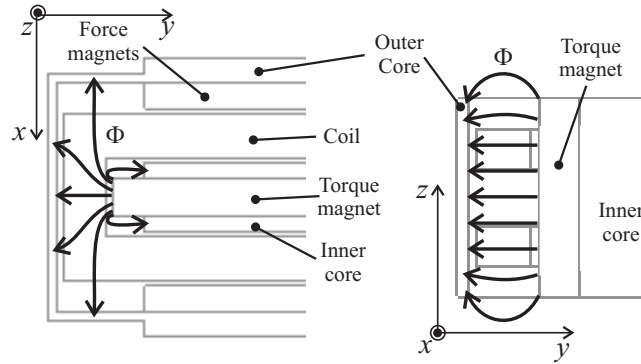
Figure 3.6: Flux lines of the torque magnet.
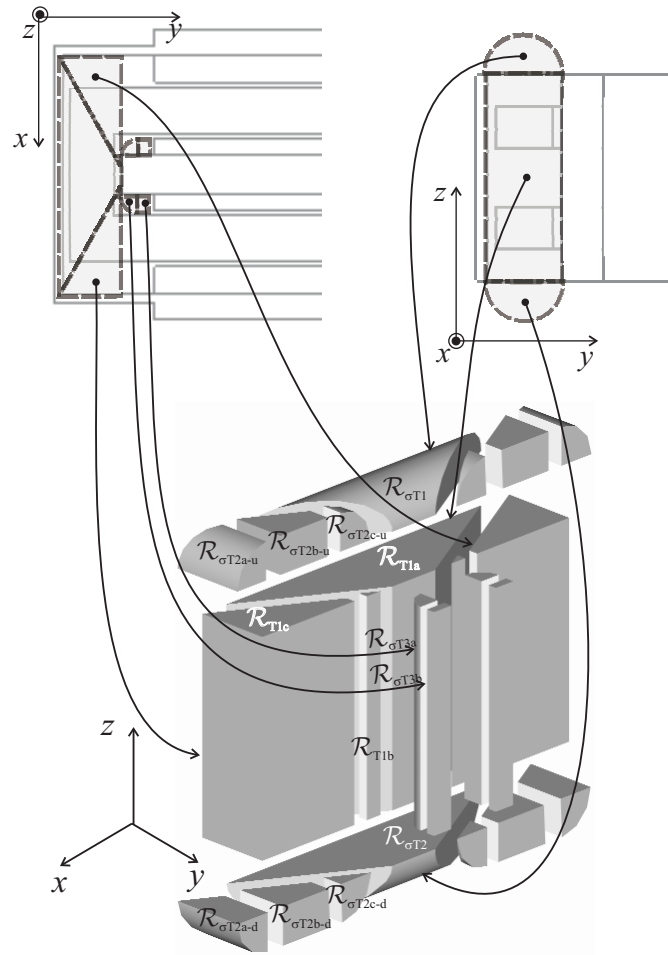
Figure 3.7: Flux tubes related to the torque magnet.

The flux tubes chosen for the air gap partitioning of the 2-DoF actuator are shown in Fig. 3.4. The reluctances of the tubes can now be calculated [27] by the following equations (see Appendix C for nomenclature):
quarter cylinder

$$\mathcal{R}_{mqc} = \frac{\pi}{4\mu \cdot W}, \tag{3.18}$$

half cylinder

$$\mathcal{R}_{mhc} = \frac{\pi}{2\mu \cdot W}, \tag{3.19}$$

tapered half cylinder

$$\mathcal{R}_{mthc} = \frac{\pi \ln(3)}{\mu \cdot W}, \tag{3.20}$$

rectangular prism

$$\mathcal{R}_{mrp} = \frac{L}{\mu \cdot W \cdot H}, \tag{3.21}$$

trapezoidal prism

$$\mathcal{R}_{mtp} = \frac{L \cdot (\ln[-H_1 \cdot L] - \ln[-H_2 \cdot L])}{\mu \cdot W \cdot (H_1 - H_2)}, \tag{3.22}$$

triangular prism

$$\mathcal{R}_{mtrianp} = \frac{1.333 \cdot L}{\mu \cdot W \cdot H}, \tag{3.23}$$

with L being the length, H the height and W the width of the flux tube.

The reluctances of the ferromagnetic core are neglected, because of its high permeability. That means the analytical model does not take into account the nonlinear character of the ferromagnetic material. The coil assembly does not contain any ferromagnetic material that would concentrate the magnetic field distribution leading to reluctance forces. The actuator has clearly another reluctance force component between the coils and the field assembly. It depends on the current level. However, this force can be neglected as it has been experimentally verified in [19].

3.2.3   Sources in a magnetic circuit

As mentioned earlier, there exist two kinds of sources, the magnetomotive force $\mathcal{F}$ and the flux source Φ. The magnetomotive force is mostly used in cases with current-carrying coils. The mmf of a coil with concentrated parameters can be conveniently determined by Ampere's law. The mmf of distributed coils can be expressed by the linear current density or current sheet J as
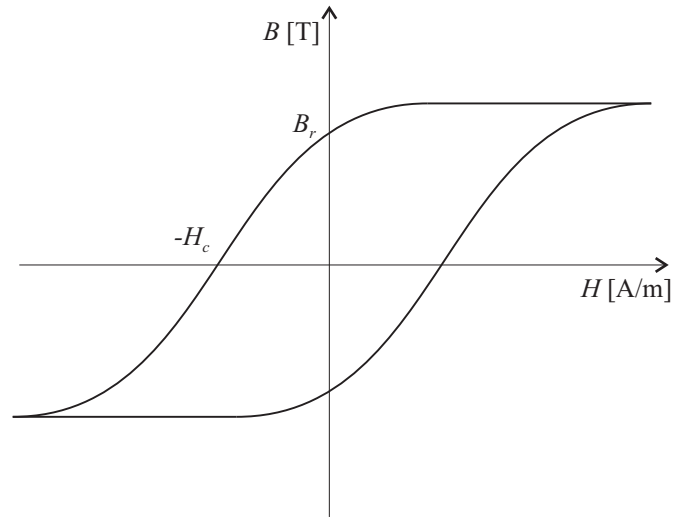
Figure 3.8: B-H characteristic of a permanent magnet.
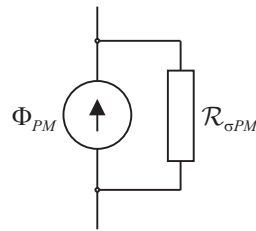
Figure 3.9: Equivalent circuit of a permanent magnet.

$$\mathcal{F} = \int J \mathrm{d}x + c, \tag{3.24}$$

with c as the integration constant.

Flux sources will be used in the following for the description of permanent magnets. The permanent magnet is modeled in a MEC by two components (see Fig. 3.9), the flux source [26]

$$\Phi_{PM} = B_r A, \tag{3.25}$$

and the leakage reluctance

$$\mathcal{R}_{\sigma PM} = \frac{H_c l}{B_r A}, \tag{3.26}$$

where B_r is the remanent magnetic flux density, H_c the coercitive force (see section 3.8), A the cross-section area of the permanent magnet, which is perpendicular to the direction of magnetization, and l the length of the magnet parallel to the direction of magnetization. This assumption holds when the BH curve in the second quadrant is linear, which is the case of the NdFeB magnets used in the actuator.

Five permanent magnets with cuboidal shape are used in the 2-DoF actuator (see Fig. 2.2.3). Therefore, the calculation of the flux sources and their leakage reluctances is straightforward by applying (3.25) and (3.26).
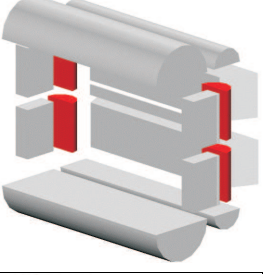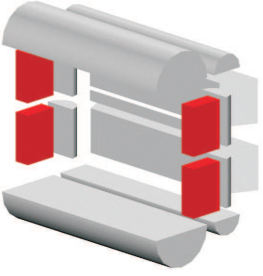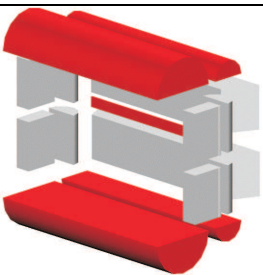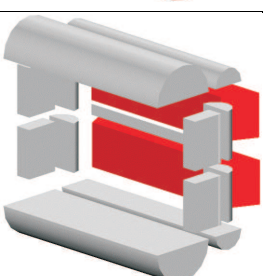
3.2.4   Magnetic equivalent circuit of the 2-DoF actuator

The MEC model of the 2-DoF actuator can be built by connecting the passive (reluctances) and active (sources) elements to a circuit. The connections between the reluctances and the sources are made in accordance with the magnetic flux flow in the actuator. It is assumed that the magnetic flux of the force magnets does not influence the magnetic flux of the torque magnet and vice-versa. As a result of this assumption, three decoupled circuits are identified, two force-magnet (FMC) and one torque-magnet circuit (TMC)(see Fig. 3.10). Therefore, the magnetic field of one circuit is not saturated by the other one. It is also assumed that the circuits are not saturated by the magnetic field of the coils.
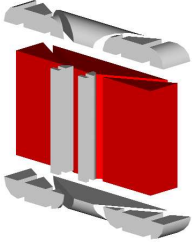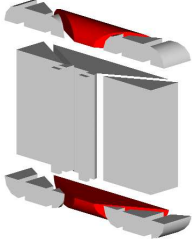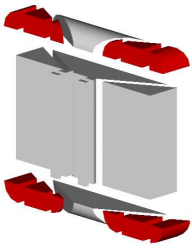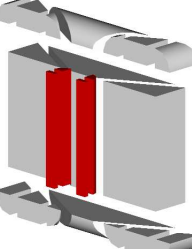
The circuit reluctances, which were identified by vector plots of $\vec{H}$ (Fig. 3.2 and 3.5) from the FEM analysis, are listed in Tabs. 3.2 and 3.3. Each reluctance in the tables is identified by its name and depicted shape of the flux tube. Thus, the appropriate equation, (C.1) - (C.6) or (3.26), can be applied to obtain the numerical value of the reluctances. Then, the values of the sources in the circuit are obtained by (3.25).

a)

b)

Figure 3.10: Magnetic equivalent circuit of a) the force magnets, b) a quarter of the torque magnet.

Table 3.2: Reluctances of flux tubes for the FMC.

Reluctance	Shape	Description
$\mathcal{R}_{\sigma PMF1,2}$	rectangular prism	equation (3.26)
$\mathcal{R}_{\sigma 12a,b}$, $\mathcal{R}_{\sigma 22a,b}$	half cylinder	
$\mathcal{R}_{\sigma 13a,b}$, $\mathcal{R}_{\sigma 23a,b}$	rectangular prism	
$\mathcal{R}_{\sigma 11,21}$, $\mathcal{R}_{\sigma 1,2c}$, $\mathcal{R}_{\sigma MPM}$	half cylinder	
$\mathcal{R}_{1,2}$	trapezoidal prism	

Table 3.3: Reluctances of flux tubes for the TMC.

Reluctance	Shape	Description
$\mathcal{R}_{\sigma PMT}$	rectangular prism	equation (3.26)
$\mathcal{R}_{T1a,b,c}$	trapezoidal prisms, triangular prism	
$\mathcal{R}_{\sigma T1,2}$	half tapered cylinder, half cylinder	
$\mathcal{R}_{\sigma T2a,b,c}$	quarter tapered cylinder, quarter cylinder, trapezoidal prism	
$\mathcal{R}_{\sigma T3a,b}$	rectangular prism, quarter cylinder	

3.2.5   Magnetic sizing equations of the FMC in the actuator

The sizing equations relate the mechanical dimensions of the actuator and the physical properties of the used materials to the magnetic field quantities in the actuator. They are derived from the corresponding MECs by applying equivalent Kirchhoff's current and voltage laws.

It is convenient to derive the equations of the magnetic fluxes Φ_{12}, Φ_{FMC} and Φ_{PMF} first. Subsequently, the magnetic flux densities in the reluctances $\mathcal{R}_1$ and $\mathcal{R}_2$, the ferromagnetic core and the permanent magnets can be found. These magnetic flux densities are needed for calculations of the Lorentz forces and designing of the ferromagnetic core.
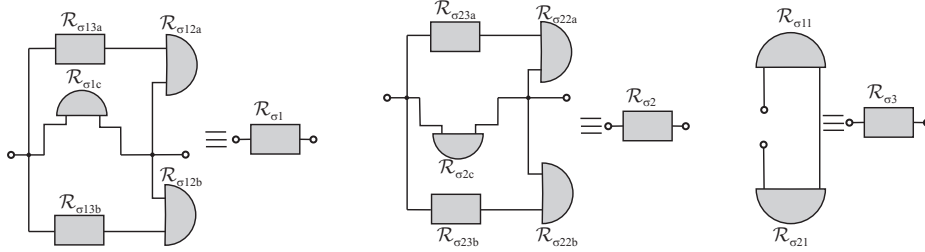
Figure 3.11: Simplifications of the leakage paths in the FMC.

It can be seen from Fig. 3.11 that the FMC can be simplified by writing the corresponding reluctances of the leakage paths as

$$\mathcal{R}_{\sigma 1} = \frac{(\mathcal{R}_{\sigma 12a} + \mathcal{R}_{\sigma 13a})(\mathcal{R}_{\sigma 12b} + \mathcal{R}_{\sigma 13b})\mathcal{R}_{\sigma 1c}}{(\mathcal{R}_{\sigma 12a} + \mathcal{R}_{\sigma 13a})(\mathcal{R}_{\sigma 12b} + \mathcal{R}_{\sigma 13b}) + (\mathcal{R}_{\sigma 12a} + \mathcal{R}_{\sigma 12b} + \mathcal{R}_{\sigma 13a} + \mathcal{R}_{\sigma 13b})\mathcal{R}_{\sigma 1c}}, \tag{3.27}$$

$$\mathcal{R}_{\sigma 2} = \frac{(\mathcal{R}_{\sigma 22a} + \mathcal{R}_{\sigma 23a})(\mathcal{R}_{\sigma 22b} + \mathcal{R}_{\sigma 23b})\mathcal{R}_{\sigma 2c}}{(\mathcal{R}_{\sigma 22a} + \mathcal{R}_{\sigma 23a})(\mathcal{R}_{\sigma 22b} + \mathcal{R}_{\sigma 23b}) + (\mathcal{R}_{\sigma 22a} + \mathcal{R}_{\sigma 22b} + \mathcal{R}_{\sigma 23a} + \mathcal{R}_{\sigma 23b})\mathcal{R}_{\sigma 2c}}, \tag{3.28}$$

$$\mathcal{R}_{\sigma 3} = \mathcal{R}_{\sigma 11} + \mathcal{R}_{\sigma 21}. \tag{3.29}$$

Further, two simplifications in accordance with Fig. 3.12 are made. The first related to the flux paths, which cross the coils

$$\mathcal{R}_{12} = \mathcal{R}_1 + \mathcal{R}_2, \tag{3.30}$$

and the second related to the parallel connection of $\mathcal{R}_{12}$, $\mathcal{R}_{\sigma 3}$ and $\mathcal{R}_{\sigma MPM}$

$$\mathcal{R}_{1\sigma 2} = \frac{\mathcal{R}_{12}\mathcal{R}_{\sigma 3}\mathcal{R}_{\sigma MPM}}{\mathcal{R}_{\sigma 3}\mathcal{R}_{\sigma MPM} + \mathcal{R}_{12}(\mathcal{R}_{\sigma 3} + \mathcal{R}_{\sigma MPM})}. \tag{3.31}$$

a)   b)
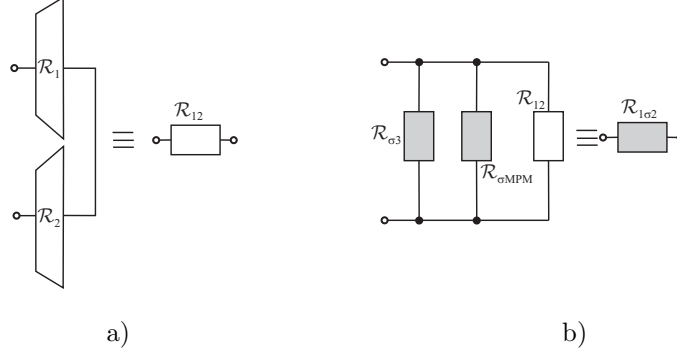
Figure 3.12: Simplifications in the FMC of a) the paths crossing the coils, b) the parallel connection of $\mathcal{R}_{12}$, $\mathcal{R}_{\sigma 3}$ and $\mathcal{R}_{\sigma MPM}$.

Based on the simplifications, the magnetic flux in the air gap can be written as

$$\Phi_{\mathcal{R}_{12}} = \frac{{}^{N}\Phi_{\mathcal{R}_{12}}}{{}^{D}\Phi_{\mathcal{R}_{12}}}, \tag{3.32}$$

where the numerator and denominator are

$${}^{N}\Phi_{\mathcal{R}_{12}} = \mathcal{R}_{\sigma 3}\mathcal{R}_{\sigma MPM}(\mathcal{R}_{\sigma 1}\mathcal{R}_{\sigma PMF1}(\mathcal{R}_{\sigma 2} + \mathcal{R}_{\sigma PMF2})\Phi_{PMF1} +$$
$$\mathcal{R}_{\sigma 2}(\mathcal{R}_{\sigma 1} + \mathcal{R}_{\sigma PMF1})\mathcal{R}_{\sigma PMF2}\Phi_{PMF2}), \tag{3.33}$$

$${}^{D}\Phi_{\mathcal{R}_{12}} = (\mathcal{R}_{\sigma 3}\mathcal{R}_{\sigma MPM} + \mathcal{R}_{12}(\mathcal{R}_{\sigma 3} + \mathcal{R}_{\sigma MPM}))$$
$$(\mathcal{R}_{\sigma 1}\mathcal{R}_{\sigma 2}\mathcal{R}_{\sigma PMF1} + \mathcal{R}_{\sigma 2}\mathcal{R}_{\sigma PMF2}\mathcal{R}_{\sigma PMF1} + \mathcal{R}_{\sigma 1}(\mathcal{R}_{\sigma 2} + \mathcal{R}_{\sigma PMF1})$$
$$\mathcal{R}_{\sigma PMF2} + \mathcal{R}_{1\sigma 2}(\mathcal{R}_{\sigma 1} + \mathcal{R}_{\sigma PMF1})(\mathcal{R}_{\sigma 2} + \mathcal{R}_{\sigma PMF2})). \tag{3.34}$$

This magnetic flux is required to obtain the average magnetic flux density $B_{\mathcal{R}_{12}}$ in the volume of the coils, which is then applied in the Lorentz equation. Thus, $B_{\mathcal{R}_{12}}$ is

$$B_{\mathcal{R}_{12}} = \frac{\Phi_{\mathcal{R}_{12}}}{A_{12}}, \tag{3.35}$$

where A_{12} is the cross-section area perpendicular to the flux tube related to $\mathcal{R}_1$ (see Fig. 3.13).
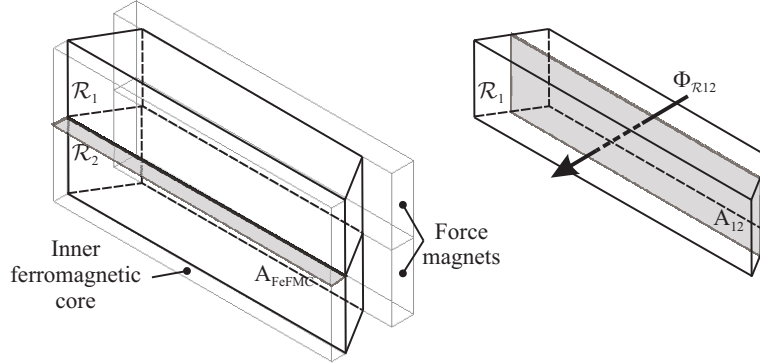
Figure 3.13: Illustrating the magnetic flux density calculation in flux tube $\mathcal{R}_1$ in the FMC.

The derivation above is only true if the magnetic permeability of the ferromagnetic parts is high, so that the related reluctances can be neglected. This assumption is ensured by sizing the ferromagnetic core in such a way that the core is not magnetically saturated ($B_{Fe} \leq B_{sat}$). Accordingly, the cross-section area of the core A_{FeFMC}, which is used by the total flux of the circuit Φ_{FMC}, as it is shown in Fig. 3.14, must satisfy

$$A_{FeFMC} \geq \frac{\Phi_{FMC}}{B_{sat}}, \tag{3.36}$$

where B_{sat} is the maximum allowable magnetic flux density and Φ_{FMC} is equal to

$$\Phi_{FMC} = \frac{^N\Phi_{FMC}}{^D\Phi_{FMC}}, \tag{3.37}$$

where

$$\begin{aligned}
^N\Phi_{FMC} = {} & \mathcal{R}_{\sigma 1}\mathcal{R}_{\sigma 2}(\mathcal{R}_{\sigma c} + \mathcal{R}_{\sigma PMF1})\mathcal{R}_{\sigma PMF2}\Phi_{PMF2} - \\
& \mathcal{R}_{\sigma PMF1}(\mathcal{R}_{1\sigma 2}\mathcal{R}_{\sigma 1}\mathcal{R}_{\sigma 2} - (\mathcal{R}_{1\sigma 2} + \mathcal{R}_{\sigma 1})\mathcal{R}_{\sigma c}\mathcal{R}_{\sigma 2} + (\mathcal{R}_{\sigma 1}(\mathcal{R}_{1\sigma 2} + \\
& \mathcal{R}_{\sigma 2}) - (\mathcal{R}_{1\sigma 2} + \mathcal{R}_{\sigma 1} + \mathcal{R}_{\sigma 2})\mathcal{R}_{\sigma c})\mathcal{R}_{\sigma PMF2})\Phi_{PMF1}, \tag{3.38}
\end{aligned}$$

$$^{D}\Phi_{FMC} = \mathcal{R}_{\sigma c}(\mathcal{R}_{\sigma 1}\mathcal{R}_{\sigma 2}\mathcal{R}_{\sigma PMF1} + \mathcal{R}_{\sigma 2}\mathcal{R}_{\sigma PMF1}\mathcal{R}_{\sigma PMF2} +$$
$$\mathcal{R}_{\sigma 1}(\mathcal{R}_{\sigma 2} + \mathcal{R}_{\sigma PMF1})\mathcal{R}_{\sigma PMF2} + \mathcal{R}_{1\sigma 2}(\mathcal{R}_{\sigma 1} +$$
$$\mathcal{R}_{\sigma PMF1})(\mathcal{R}_{\sigma 2} + \mathcal{R}_{\sigma PMF2})). \quad (3.39)$$
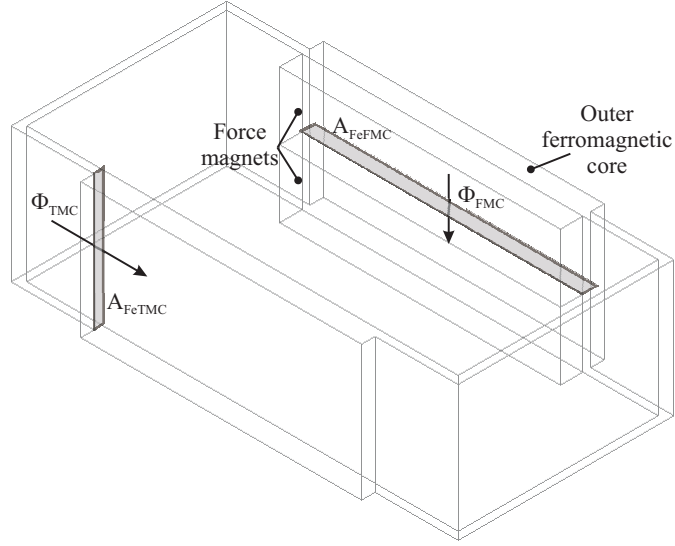
Figure 3.14: Illustrating the magnetic flux density calculation in the outer ferromagnetic core of the FMC.

So, to check the core for saturation, the maximum flux density in the core is

$$B_{FMC} = \frac{\Phi_{FMC}}{A_{FeFMC}} \leq B_{sat}. \quad (3.40)$$

It should be noted that the ferromagnetic core of the FMC has two parts, the inner core and a part of the outer core (see Fig. 2.10). Both parts are designed based on (3.36), thus, they have the same dimensions.

Finally, the magnetic flux produced by the magnets can be written as

$$\Phi_{PMF} = \frac{^{N}\Phi_{PMF}}{^{D}\Phi_{PMF}}, \quad (3.41)$$

where

$$^N\Phi_{PMF} = \mathcal{R}_{\sigma 1}\mathcal{R}_{\sigma 2}\mathcal{R}_{\sigma PMF1}\Phi_{PMF1} + (\mathcal{R}_{1\sigma 2} + \mathcal{R}_{\sigma 2})\mathcal{R}_{\sigma PMF1}\mathcal{R}_{\sigma PMF2}\Phi_{PMF2} +$$
$$\mathcal{R}_{\sigma 1}(\mathcal{R}_{1\sigma 2} + \mathcal{R}_{\sigma 2} + \mathcal{R}_{\sigma PMF1})\mathcal{R}_{\sigma PMF2}\Phi_{PMF2}, \tag{3.42}$$

$$^D\Phi_{PMF} = \mathcal{R}_{\sigma 1}\mathcal{R}_{\sigma 2}\mathcal{R}_{\sigma PMF1} + \mathcal{R}_{\sigma 2}\mathcal{R}_{\sigma PMF2}\mathcal{R}_{\sigma PMF1} + (\mathcal{R}_{\sigma 2} + \mathcal{R}_{\sigma PMF1}) \cdot$$
$$\cdot\mathcal{R}_{\sigma PMF2}\mathcal{R}_{\sigma 1} + \mathcal{R}_{1\sigma 2}(\mathcal{R}_{\sigma 1} + \mathcal{R}_{\sigma PMF1})(\mathcal{R}_{\sigma 2} + \mathcal{R}_{\sigma PMF2}). \tag{3.43}$$

3.2.6   Magnetic sizing equations of the TMC in the actuator

The sizing equations of the TMC are obtained by simplification as in the case of the FMC. First, the leakage reluctances of the circuit are simplified according to Fig. 3.15, where

$$\mathcal{R}_{\sigma 2} = \mathcal{R}_{\sigma T2a-u} + \mathcal{R}_{\sigma T2b-u} + \mathcal{R}_{\sigma T2c-u} = \mathcal{R}_{\sigma T2a-d} + \mathcal{R}_{\sigma T2b-d} + \mathcal{R}_{\sigma T2c-d}, \tag{3.44}$$

$$\mathcal{R}_{\sigma 3} = \mathcal{R}_{\sigma T3a} + \mathcal{R}_{\sigma T3b}, \tag{3.45}$$

$$\mathcal{R}_{\sigma} = \frac{\mathcal{R}_{\sigma 2}\mathcal{R}_{\sigma 3}}{\mathcal{R}_{\sigma 2} + 2\mathcal{R}_{\sigma 3}}, \tag{3.46}$$

$$\mathcal{R}_{\sigma T12} = \frac{\mathcal{R}_{\sigma T1}\mathcal{R}_{\sigma T2}}{\mathcal{R}_{\sigma T1} + \mathcal{R}_{\sigma T2}}. \tag{3.47}$$

The serial connection of the reluctances $\mathcal{R}_{T1b}$ and $\mathcal{R}_{T1c}$ in Fig. 3.16 yields

$$\mathcal{R}_{T1bc} = \mathcal{R}_{T1b} + \mathcal{R}_{T1c}. \tag{3.48}$$

The two parallel reluctances $\mathcal{R}_{T1a}$ and $\mathcal{R}_{T1bc}$ are crossing the coils. That means that two magnetic fluxes need to be expressed for the calculation of the actuator torque:

$$\Phi_{T1a} = \frac{^N\Phi_{T1a}}{^D\Phi_{T1a}}, \tag{3.49}$$

$$^N\Phi_{T1a} = \mathcal{R}_{T1bc}(\mathcal{R}_{\sigma}\mathcal{R}_{\sigma 2}\mathcal{R}_{\sigma 3} + \mathcal{R}_{T1a}(\mathcal{R}_{\sigma 2}\mathcal{R}_{\sigma 3} -$$
$$\mathcal{R}_{\sigma}(\mathcal{R}_{\sigma 2} + 2\mathcal{R}_{\sigma 3})))\mathcal{R}_{\sigma PMT}\mathcal{R}_{\sigma T1}\Phi_{PMT}, \tag{3.50}$$

$$^D\Phi_{T1a} = \mathcal{R}_{\sigma 2}\mathcal{R}_{\sigma 3}(\mathcal{R}_{T1a}\mathcal{R}_{T1bc}\mathcal{R}_{\sigma}\mathcal{R}_{\sigma PMT} + (2\mathcal{R}_{T1a}\mathcal{R}_{T1bc}\mathcal{R}_{\sigma} +$$
$$\mathcal{R}_{T1bc}\mathcal{R}_{\sigma PMT}\mathcal{R}_{\sigma} + \mathcal{R}_{T1a}(\mathcal{R}_{T1bc} + \mathcal{R}_{\sigma})\mathcal{R}_{\sigma PMT})\mathcal{R}_{\sigma T1}), \tag{3.51}$$
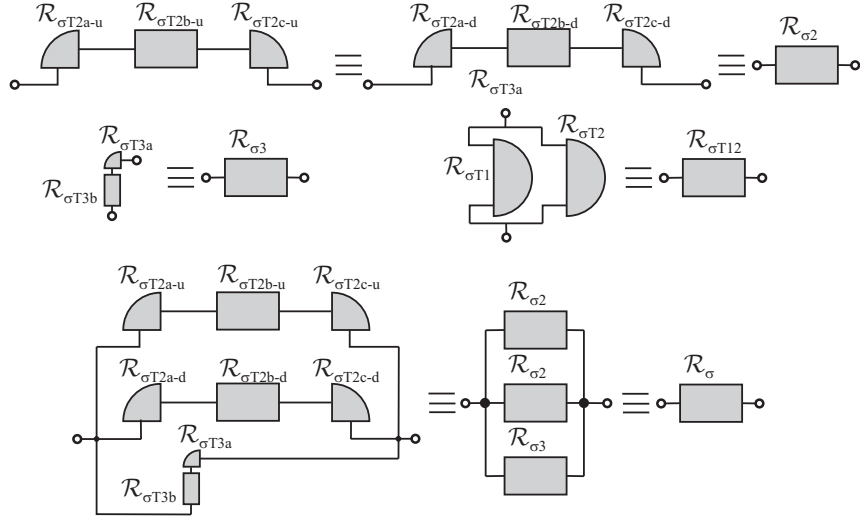
Figure 3.15: Simplifications of the leakage paths in the TMC.
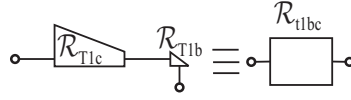
Figure 3.16: Simplifications of the path crossing the coils in the TMC.

$$\Phi_{T1bc} = \frac{{}^N\Phi_{T1bc}}{{}^D\Phi_{T1bc}}, \tag{3.52}$$

$${}^N\Phi_{T1bc} = \mathcal{R}_{T1a}\mathcal{R}_\sigma\mathcal{R}_{\sigma PMT}\mathcal{R}_{\sigma T1}\Phi_{PMT}, \tag{3.53}$$

$${}^D\Phi_{T1bc} = \mathcal{R}_{T1a}\mathcal{R}_{T1bc}\mathcal{R}_\sigma\mathcal{R}_{\sigma PMT} + (2\mathcal{R}_{T1a}\mathcal{R}_{T1bc}\mathcal{R}_\sigma + \mathcal{R}_{T1bc}\mathcal{R}_{\sigma PMT}\mathcal{R}_\sigma +$$
$$\mathcal{R}_{T1a}(\mathcal{R}_{T1bc} + \mathcal{R}_\sigma)\mathcal{R}_{\sigma PMT})\mathcal{R}_{\sigma T1}. \tag{3.54}$$

Then, the flux densities in the TMC in the coils are

$$B_{T1a} = \frac{\Phi_{T1a}}{A_{T1a}}, \tag{3.55}$$

$$B_{T1c} = \frac{\Phi_{T1bc}}{A_{T1c}}, \tag{3.56}$$

where A_{T1a} and A_{T1c} are the cross-section areas perpendicular to the flux in the $\mathcal{R}_{T1a}$ and $\mathcal{R}_{T1c}$ flux tubes in the middle of the coils, as depicted in Fig. 3.17.
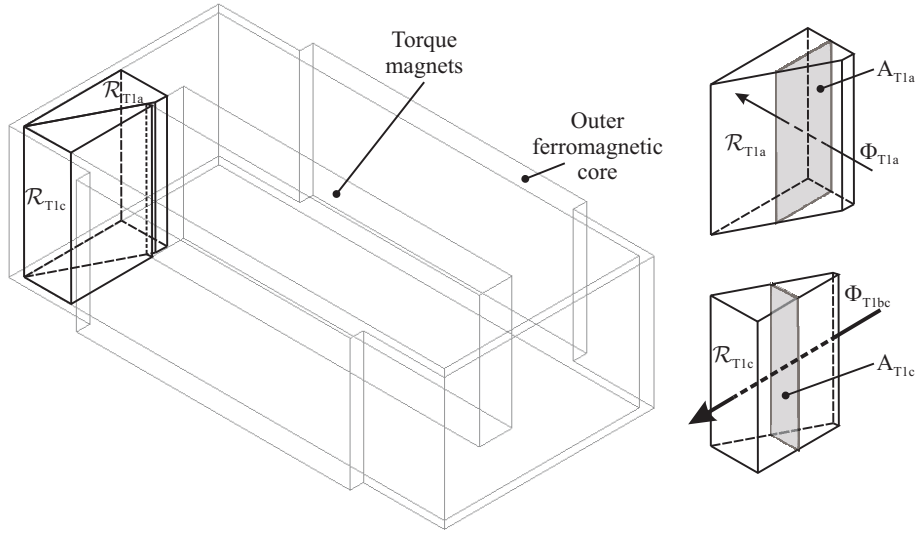
Figure 3.17: Illustrating the magnetic flux density calculation in the flux tubes $\mathcal{R}_{T1a}$ and $\mathcal{R}_{T1c}$ of the TMC.

If the reluctances of the ferromagnetic core are neglected, as in the case of the FMC, the cross-section of the TMC core should be

$$A_{FeTMC} \geq \frac{\Phi_{TMC}}{B_{sat}}. \tag{3.57}$$

with A_{FeTMC} representing the cross-section area of the TMC core shown in Fig. 3.14. In (3.57) the flux Φ_{TMC} is one half of the total flux Φ_{PMT} of the torque magnet,

because the flux is split in two parts and flows on both sides of the magnet. Thus, the flux equals

$$\Phi_{TMC} = \frac{^N\Phi_{TMC}}{^D\Phi_{TMC}}, \tag{3.58}$$

where the numerator is

$$^N\Phi_{TMC} = \mathcal{R}_{\sigma PMT}(\mathcal{R}_{T1bc}\mathcal{R}_\sigma\mathcal{R}_{\sigma 3}\mathcal{R}_{\sigma T1} + \mathcal{R}_{T1a}(\mathcal{R}_\sigma\mathcal{R}_{\sigma 3}\mathcal{R}_{\sigma T1} +$$
$$\mathcal{R}_{T1bc}(\mathcal{R}_\sigma\mathcal{R}_{\sigma 3} + \mathcal{R}_{\sigma T1}\mathcal{R}_{\sigma 3} - \mathcal{R}_\sigma\mathcal{R}_{\sigma T1})))\Phi_{PMT}, \tag{3.59}$$

and the denominator

$$^D\Phi_{TMC} = \mathcal{R}_{T1a}\mathcal{R}_{T1bc}\mathcal{R}_\sigma\mathcal{R}_{\sigma 3}\mathcal{R}_{\sigma PMT} + \mathcal{R}_{\sigma 3}(2\mathcal{R}_{T1a}\mathcal{R}_{T1bc}\mathcal{R}_\sigma +$$
$$\mathcal{R}_{T1bc}\mathcal{R}_{\sigma PMT}\mathcal{R}_\sigma + \mathcal{R}_{T1a}(\mathcal{R}_{T1bc} + \mathcal{R}_\sigma)\mathcal{R}_{\sigma PMT})\mathcal{R}_{\sigma T1}. \tag{3.60}$$

To check the saturation, the maximum magnetic flux density in the core of the TMC is

$$B_{FeTMC} = \frac{\Phi_{TMC}}{A_{FeTMC}}. \tag{3.61}$$

Finally, the magnetic flux produced by the torque magnet is

$$\Phi_T = \frac{^N\Phi_T}{^D\Phi_T}, \tag{3.62}$$

$$^N\Phi_T = \mathcal{R}_{\sigma PMT}(\mathcal{R}_{T1a}\mathcal{R}_{T1bc}\mathcal{R}_\sigma + \mathcal{R}_{T1bc}\mathcal{R}_{\sigma T1}\mathcal{R}_\sigma + \mathcal{R}_{T1a}(\mathcal{R}_{T1bc} + \mathcal{R}_\sigma)\mathcal{R}_{\sigma T1})\Phi_{PMT}, \tag{3.63}$$

$$^D\Phi_T = \mathcal{R}_{T1a}\mathcal{R}_{T1bc}\mathcal{R}_\sigma\mathcal{R}_{\sigma PMT} + (2\mathcal{R}_{T1a}\mathcal{R}_{T1bc}\mathcal{R}_\sigma + \mathcal{R}_{T1bc}\mathcal{R}_{\sigma PMT}\mathcal{R}_\sigma +$$
$$\mathcal{R}_{T1a}(\mathcal{R}_{T1bc} + \mathcal{R}_\sigma)\mathcal{R}_{\sigma PMT})\mathcal{R}_{\sigma T1}. \tag{3.64}$$

In section 3.2, the analytical model of the actuator is developed. It represents a set of equations by which relevant magnetic fluxes and magnetic flux densities can be calculated. In the following section, a numerical model of the same actuator is built to obtain the same magnetic field quantities, so the analytical and the numerical models can be compared with each other.

3.3 FEM magnetostatic analysis

For the purpose of high-accuracy simulations of the 2-DoF actuator, a finite element model of the actuator is built using the Maxwell software package. The FEM model is three dimensional. Although the part of the force magnets can be precisely simulated in two dimensions, the magnetic field of the torque magnet is essentially three dimensional.

It is a numerical approach for solving so-called boundary-value problems that are expressed by governing equations and boundary conditions. The general definition of a boundary-value problem can be found in [28, 29], being formulated by a variational method, the so-called Ritz method. They form the basis of the finite element method. Knowing this, the derivation of the FEM model can be done. The derivation can be divided in the following steps:

  - Discretization of the domain of interest,

  - Introduction of interpolation functions,

  - Formulation of the system of elemental equations and incorporation of the boundary conditions,

  - Solving the system of equations by direct or indirect methods.

3.4 Electric and magnetic forces

The MEC and FEM methods are applied in the design of the actuator's magnetic circuit. However, the forces and torques created by the actuator are not the direct outcome of these methods. Therefore, the forces and torques must be obtained by implementing one of the following three force-calculation methods, which are elaborated in the next subsections.

3.4.1 Lorentz's force

The Lorentz equation expresses the force on the electric charge Q in the electromagnetic field as

$$\vec{F} = \vec{F}_e + \vec{F}_m = Q\left(\vec{E} + \vec{v} \times \vec{B}\right), \tag{3.65}$$

where the first term is the electric force on the stationary or moving charge in the electric field $\vec{E}$ and the second term is the magnetic force that is produced only on the moving charge with the velocity $\vec{v}$ in the magnetic field $\vec{B}$. In the magnetostatic case, when $\vec{E} = 0$, (3.65) is simplified to

$$\vec{F} = Q\vec{v} \times \vec{B}. \tag{3.66}$$

For design purposes, it is more convenient to write the Lorentz equation as a function of the current density $\vec{J}$ by substituting

$$\vec{J}\mathrm{d}V = \frac{\mathrm{d}Q}{\mathrm{d}t\mathrm{d}\vec{S}}\mathrm{d}\vec{S}\mathrm{d}\vec{l} = \mathrm{d}Q\vec{v} \tag{3.67}$$

into (3.66), where $\mathrm{d}\vec{S}$ is the oriented element of the surface and $\mathrm{d}\vec{l}$ is the oriented element of the length perpendicular to $\mathrm{d}\vec{S}$ and parallel to $\mathrm{d}\vec{J}$. Then, the force $\vec{F}$ on the volume of the coil is equal to

$$\vec{F} = \int_{V_{coil}} \vec{J} \times \vec{B}\mathrm{d}V_{coil}. \tag{3.68}$$

The torque $\vec{T}$ can be written as the vector product of the force $\vec{F}$ and the moment arm $\vec{r}$:

$$\vec{T} = \int_{V_{coil}} \vec{r} \times \vec{J} \times \vec{B}\mathrm{d}V_{coil}. \tag{3.69}$$

These relationships are used for predicting forces and torques only on current-carrying non-ferromagnetic bodies.

3.4.2   Virtual-work method

The force calculation by the virtual-work method is based on the energy conservation and virtual displacement principle. It is equal to the ratio of stored-coenergy change ∂C to the displacement in direction q or rotation θ at constant coil current, as given by

$$F_q = \left.\frac{\partial C}{\partial q}\right|_{i=const}, \tag{3.70}$$

$$T_\theta = \left.\frac{\partial C}{\partial \theta}\right|_{i=const}. \tag{3.71}$$

If this approach is applied to the FEM, two finite element solutions of the field and the coenergy should be found, one for the original position and the second for the displacement ∂q or $\partial \theta$.

It is also possible to analytically derive the equations [30, 31, 29]

$$F_q = -\frac{1}{2\mu_0}\sum_e \left(V_e \frac{\partial B^2}{\partial q} + B^2 \frac{\partial V_e}{\partial q}\right), \tag{3.72}$$

$$T_\theta = -\frac{1}{2\mu_0} \sum_e \left(V_e \frac{\partial B^2}{\partial \theta} + B^2 \frac{\partial V_e}{\partial \theta} \right), \tag{3.73}$$

where the summation is done over the elements e that create a virtually distorted volume surrounding the body of interest. In this case, only one field solution needs to be found to compute the force and the torque.

3.4.3 Maxwell-stress method

This method defines the normal and tangential magnetic stresses f_n and f_t on a bounding surface S enclosing the body on which the force is calculated

$$f_n = \frac{1}{2\mu_0} \left(B_n^2 - B_t^2 \right), \tag{3.74}$$

$$f_t = \frac{1}{\mu_0} \left(B_n \cdot B_t \right), \tag{3.75}$$

with B_n and B_t being the magnetic flux density in the normal and tangential directions to the bounding surface. The bounding surface surrounding the body should not contain any sources (e.g. currents or magnetized material). The total force is obtained by the surface integral of the magnetic stresses over the closed surface S

$$\vec{F} = \oint_S f_n \mathrm{d}S\vec{n} + \oint_S f_t \mathrm{d}S\vec{t}, \tag{3.76}$$

where $\vec{n}$ and $\vec{t}$ are the unity vectors normal and tangential to the surface S.

3.5 Simulation results

Simulation results of the analytical MEC and the numerical FEM models of the actuator are compared in this section. The purpose of the comparison is to evaluate the accuracy of the MEC by means of the more precise FEM model. Afterwards, the saturation level of the ferromagnetic core and the working points of the magnets can be judged. The saturation level of the core is important for minimal mass of the actuator and the working points of the magnets determine whether the magnets will be demagnetized at the maximum operating temperature.

As it has been mentioned earlier, the two models yield magnetic field quantities, but not the force and torque of the actuator. Therefore, the Lorentz's force equation and the virtual-work method are used to obtain the resulting force and torque. These methods utilize the magnetic field density calculated by the MEC and FEM models.

Simulation results are given for the 2-DoF actuator with the dimensions and material properties listed in Appendix B.

The material of the magnets used in the actuator is NdFeB. It has been experimentally found that the material parameters of the permanent magnets provided in the manufacturer's data sheets slightly differ from those measured in the laboratory as it can be seen from Tab. B.1 of Appendix B. Therefore, simulation results are presented for the data-sheet and measured permanent magnets.

3.5.1 Magnetic field

Magnetic field quantities predicted by the MEC represent the average values in particular flux tubes, whereas the distribution of the magnetic field is found by the FEM. To compare these results, corresponding average magnetic field values, defined with the help of Figs. 3.18 and 3.19, are calculated from the FEM. Namely, the average magnetic flux entering a surface is calculated as

$$\Phi = \frac{\int_S |\vec{B}| \mathrm{d}S}{\int_S \mathrm{d}S}, \tag{3.77}$$

and the average magnetic flux density is calculated in two ways, as surface and volume average

$$B = \frac{\int_S |\vec{B}| \mathrm{d}S}{\int_S \mathrm{d}S}, \quad B = \frac{\int_V |\vec{B}| \mathrm{d}V}{\int_V \mathrm{d}V}. \tag{3.78}$$

The relevant magnetic flux values, magnetic flux densities and the relative errors defined as

$$E = \frac{|\text{FEM-MEC}|}{\text{FEM}}, \tag{3.79}$$

are presented in Tabs. 3.4 to 3.11. The magnetic flux density and magnetic field intensity distributions, obtained by FEM, are shown in Figs. 3.20 to 3.35. The magnetic field in these figures is created only by the force magnets and the torque magnet, respectively, while the current in the coils is set to zero.

The magnetic fluxes in the FMC are predicted with a maximum error of 21.82%. The high inaccuracy is related to the flux distribution in the flux tubes $\mathcal{R}_1$ and $\mathcal{R}_2$ in Fig 3.18. The difference is caused by the fact that the magnetic flux is assumed to be constant and parallel to the sides of the flux tubes in the MEC. However, $\Phi_{S_{F4}}$, $\Phi_{S_{F5}}$ and $\Phi_{S_{F6}}$ are not equal (see Tabs. 3.4 and 3.6). It can be noticed that $\Phi_{S_{F4}} > \Phi_{S_{F5}} > \Phi_{S_{F6}}$. This means that the magnetic flux is crossing partially the sides walls of the flux tubes, which leads to inaccuracies.
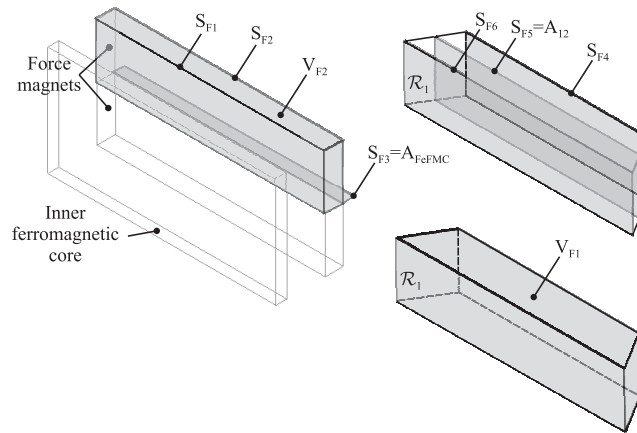
Figure 3.18: Illustrative cross sections and volumes of flux tubes for definitions of magnetic fluxes and magnetic flux densities in the FMC (see also Fig. 3.13).
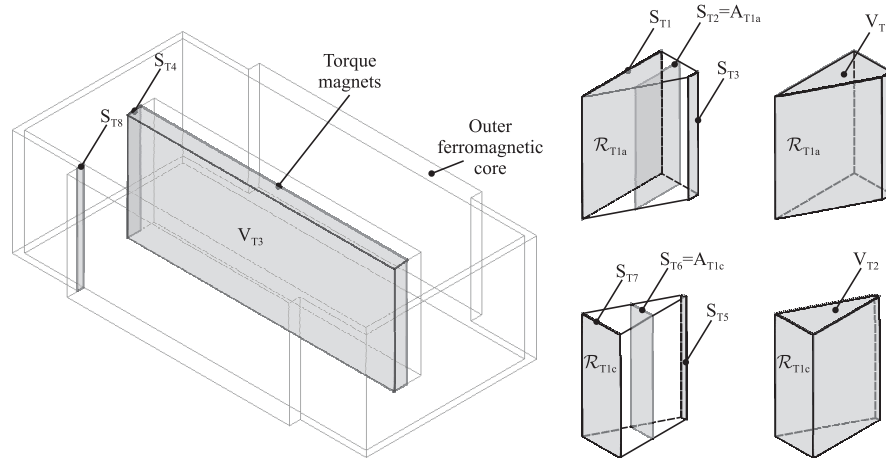
Figure 3.19: Illustrative cross sections and volumes of flux tubes for definitions of magnetic fluxes and magnetic flux densities in the TMC (see also Fig. 3.17).

On the other hand, Φ_{PMF} and Φ_{FMC} in the FMC are predicted with higher accuracy in Tabs. 3.4 and 3.6. It is because Φ_{PMF} of the magnet is well confined in a rectangular-shaped flux tube and Φ_{FMC} crosses perpendicularly the surface $S_{F3} = A_{FeFMC}$ of the core.

The magnetic flux densities in the FMC are predicted with a maximum error of 11.54%, if volume-average values are considered (see Tabs. 3.5 and 3.7). The highest error is again related to the flux tubes $\mathcal{R}_1$ and $\mathcal{R}_2$. It is only half of the error obtained with the predicted flux $\Phi_{\mathcal{R}_{12}}$, as given by (3.32). A volume average is closer to the definition of flux tubes and, therefore, it smooths local magnetic flux concentrations in space.

Table 3.4: Magnetic fluxes in the FMC with the data-sheet magnets.

	Φ [10^{-5} Wb]					
	$\Phi_{S_{F1}}$	$\Phi_{S_{F2}}$	$\Phi_{S_{F3}}$	$\Phi_{S_{F4}}$	$\Phi_{S_{F5}}$	$\Phi_{S_{F6}}$
	9.38	11.09	8.76	6.80	3.11	2.26
FEM	$\Phi_{PMF} \approx \dfrac{\sum_{i=1}^{n=2} \Phi_{S_{Fi}}}{2}$		$\Phi_{FMC} \approx \Phi_{S_{F3}}$	$\Phi_{\mathcal{R}_{12}} \approx \dfrac{\sum_{i=4}^{n=6} \Phi_{S_{Fi}}}{3}$		
	10.24		8.76	4.06		
MEC	9.68		8.08	3.18		
E	5.47%		7.76%	21.67%		

Table 3.5: Magnetic flux densities in the FMC with the data-sheet magnets.

	B [T]		
	$B_{PMF} = \dfrac{\Phi_{PMF}}{S_{F1}}$	$B_{FMC} = \dfrac{\Phi_{FMC}}{S_{F3}}$	$B_{\mathcal{R}_{12}} = \dfrac{\Phi_{\mathcal{R}_{12}}}{S_{F5}}$
	0.68	1.85	0.31
FEM	$B_{PMF} = \dfrac{\int_{V_{F2}} B \mathrm{d}V}{\int_{V_{F2}} \mathrm{d}V}$	$B_{FMC} = \dfrac{\int_{S_{F3}} B \mathrm{d}S}{\int_{S_{F3}} \mathrm{d}S}$	$B_{\mathcal{R}_{12}} = \dfrac{\int_{V_{F1}} B \mathrm{d}V}{\int_{V_{F1}} \mathrm{d}V}$
	0.71	1.85	0.27
MEC	0.65	1.70	0.24
E	8.45%	8.11%	11.11%
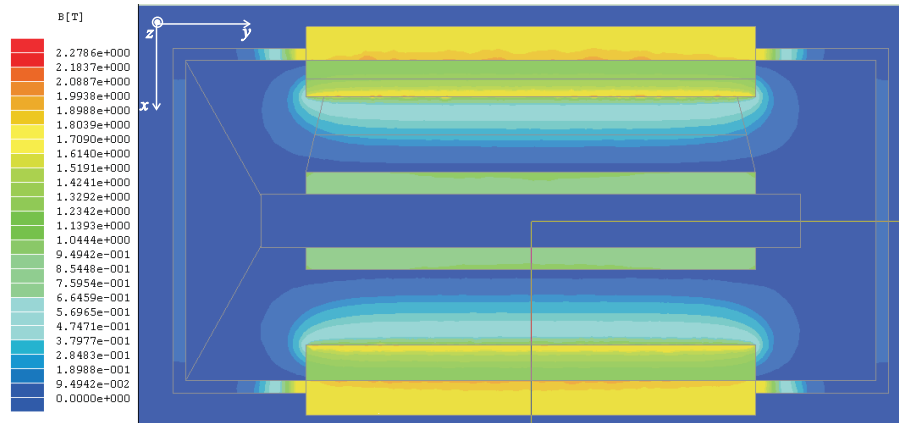
Figure 3.20: Modulus of the magnetic flux density produced by the force magnets in the xy-plane (FEM with the data-sheet magnets).
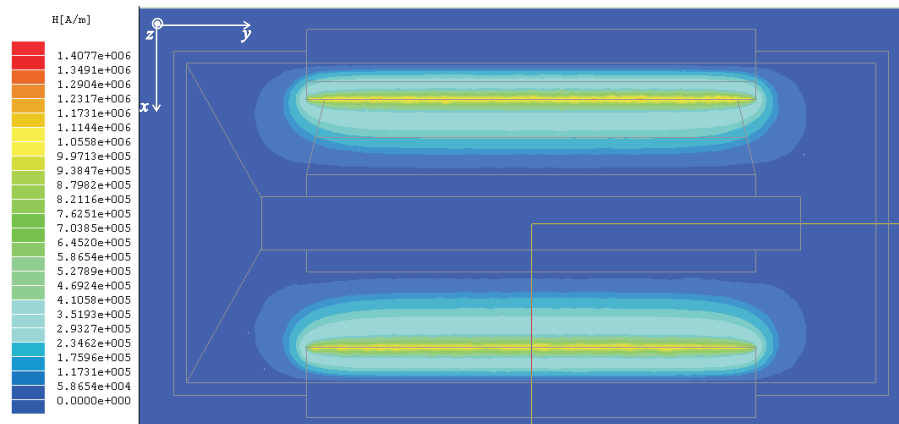
Figure 3.21: Modulus of the magnetic field intensity produced by the force magnets in the xy-plane (FEM with the data-sheet magnets).
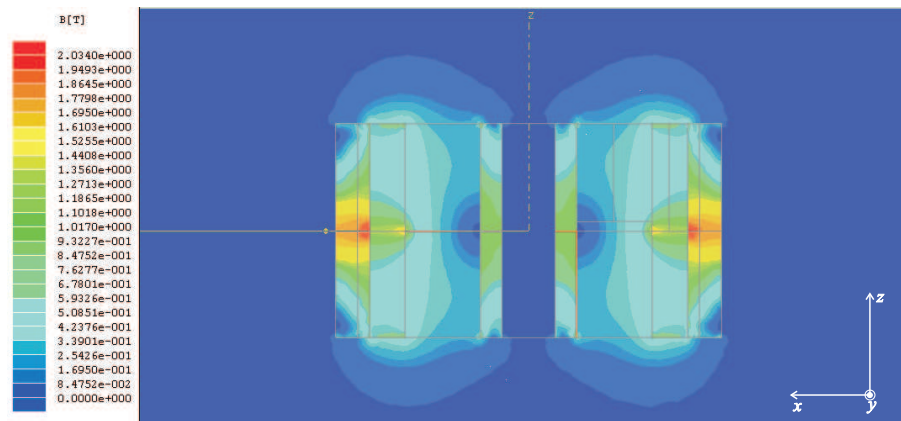
Figure 3.22: Modulus of the magnetic flux density produced by the force magnets in the xz-plane (FEM with the data-sheet magnets).
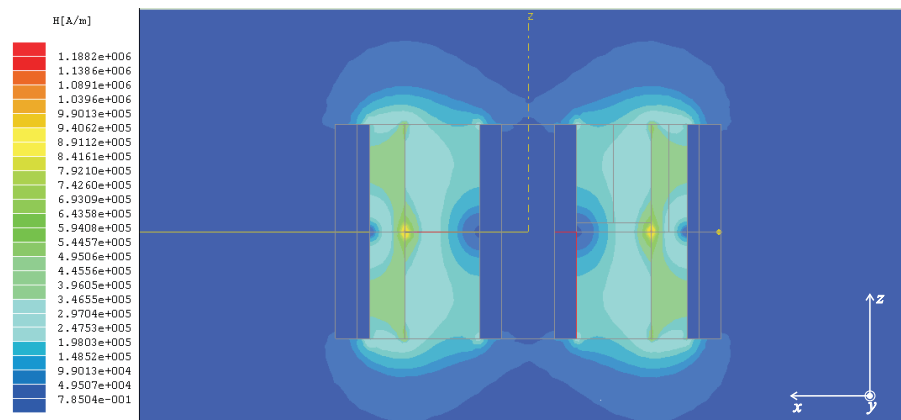
Figure 3.23: Modulus of the magnetic field intensity produced by the force magnets in the xz-plane (FEM with the data-sheet magnets).

Table 3.6: Magnetic fluxes in the FMC with the measured magnets.

	Φ [10^{-5} Wb]					
	$\Phi_{S_{F1}}$	$\Phi_{S_{F2}}$	$\Phi_{S_{F3}}$	$\Phi_{S_{F4}}$	$\Phi_{S_{F5}}$	$\Phi_{S_{F6}}$
	8.84	10.43	8.48	6.47	2.95	2.13
FEM	$\Phi_{PMF} \approx \dfrac{\sum_{i=1}^{n=2} \Phi_{S_{Fi}}}{2}$		$\Phi_{FMC} \approx \Phi_{S_{F3}}$	$\Phi_{\mathcal{R}_{12}} \approx \dfrac{\sum_{i=4}^{n=6} \Phi_{S_{Fi}}}{3}$		
	9.64		8.48	3.85		
MEC	9.17		7.65	3.01		
E	4.88%		9.79%	21.82%		

Table 3.7: Magnetic flux densities in the FMC with the measured magnets.

	B [T]		
	$B_{PMF} = \dfrac{\Phi_{PMF}}{S_{F1}}$	$B_{FMC} = \dfrac{\Phi_{FMC}}{S_{F3}}$	$B_{\mathcal{R}_{12}} = \dfrac{\Phi_{\mathcal{R}_{12}}}{S_{F5}}$
	0.64	1.79	0.29
FEM	$B_{PMF} = \dfrac{\int_{V_{F2}} BdV}{\int_{V_{F2}} dV}$	$B_{FMC} = \dfrac{\int_{S_{F3}} BdS}{\int_{S_{F3}} dS}$	$B_{\mathcal{R}_{12}} = \dfrac{\int_{V_{F1}} BdV}{\int_{V_{F1}} dV}$
	0.67	1.79	0.26
MEC	0.61	1.61	0.23
E	8.96%	10.06%	11.54%

Figure 3.24: Modulus of the magnetic flux density produced by the force magnets in the xy-plane (FEM with the measured magnets).
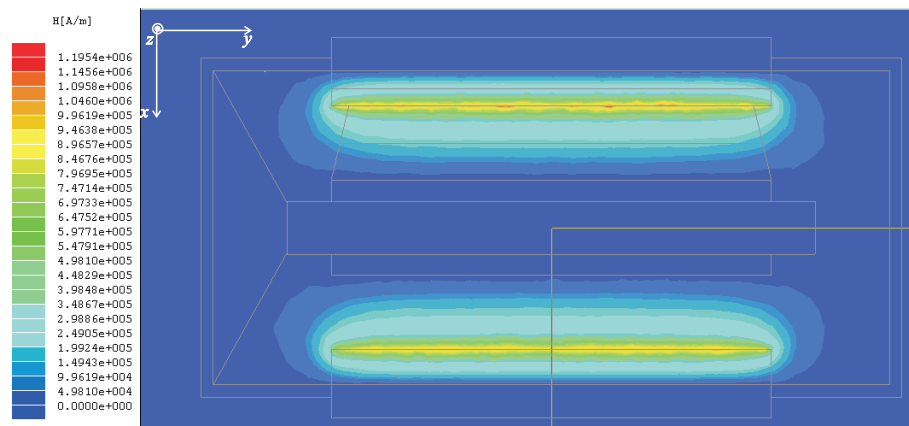
Figure 3.25: Modulus of the magnetic field intensity produced by the force magnets in the xy-plane (FEM with the measured magnets).
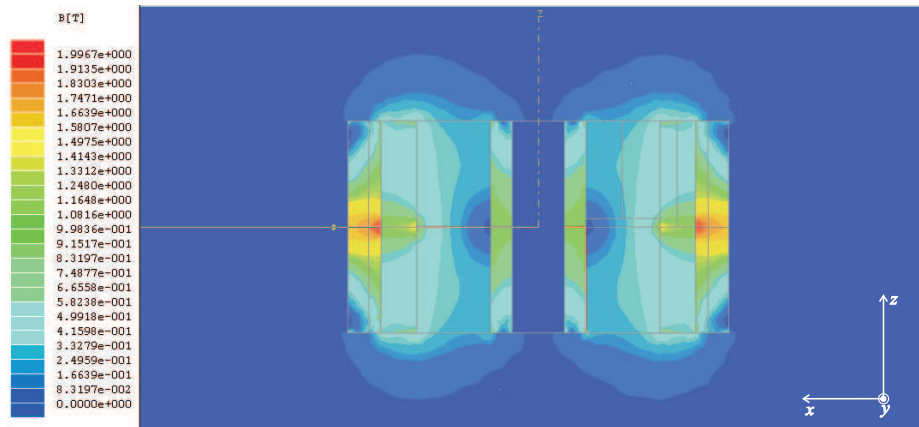
Figure 3.26: Modulus of the magnetic flux density produced by the force magnets in the xz-plane (FEM with the measured magnets).
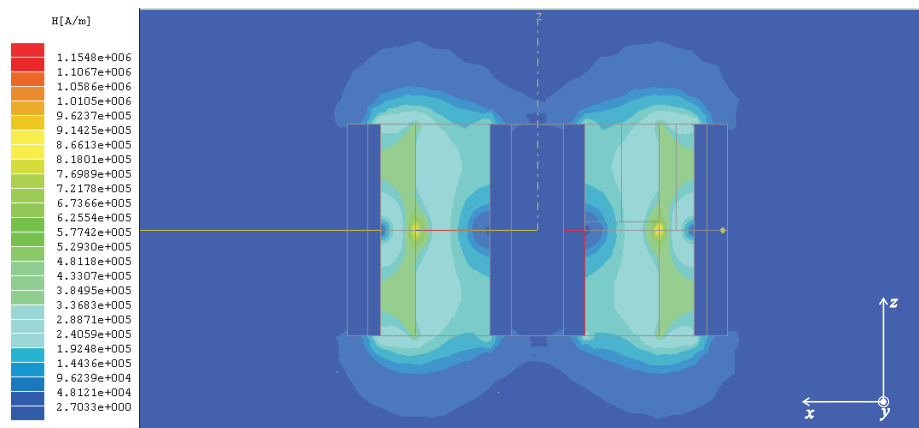
Figure 3.27: Modulus of the magnetic field intensity produced by the force magnets in the xz-plane (FEM with the measured magnets).

Table 3.8: Magnetic fluxes in the TMC with the data-sheet magnets.

Φ [10^{-5} Wb]								
	$\Phi_{S_{T1}}$	$\Phi_{S_{T2}}$	$\Phi_{S_{T3}}$	$\Phi_{S_{T4}}$	$\Phi_{S_{T5}}$	$\Phi_{S_{T6}}$	$\Phi_{S_{T7}}$	$\Phi_{S_{T8}}$
	0.66	0.76	0.91	1.32	0.032	0.101	0.064	1.64
FEM	$\Phi_{T1a} \approx \dfrac{\sum_{i=1}^{n=3} \Phi_{S_{Ti}}}{3}$			$\Phi_T \approx \Phi_{S_{T4}}$	$\Phi_{T1bc} \approx \dfrac{\sum_{i=5}^{n=7} \Phi_{S_{Ti}}}{3}$			$\Phi_{TMC} \approx \Phi_{T8}$
	0.78			1.32	0.066			1.64
MEC	1.05			2.04	0.101			1.54
E	34.61%			54.55%	53.03%			6.10%

Table 3.9: Magnetic flux densities in the TMC with the data-sheet magnets.

B [T]				
	$B_{T1a} = \dfrac{\Phi_{T1a}}{S_{T2}}$	$B_T = \dfrac{\Phi_T}{S_{T4}}$	$B_{T1c} = \dfrac{\Phi_{T1bc}}{S_{T6}}$	$B_{TMC} = \dfrac{\Phi_{FMC}}{S_{T8}}$
	0.13	0.73	0.026	1.96
FEM	$B_{T1a} = \dfrac{\int_{V_{T1}} B\mathrm{d}V}{\int_{V_{T1}} \mathrm{d}V}$	$B_T = \dfrac{\int_{V_{T3}} B\mathrm{d}V}{\int_{V_{T3}} \mathrm{d}V}$	$B_{T1c} = \dfrac{\int_{V_{T2}} B\mathrm{d}V}{\int_{V_{T2}} \mathrm{d}V}$	$B_{TMC} = \dfrac{\int_{S_{T8}} B\mathrm{d}S}{\int_{S_{T8}} \mathrm{d}S}$
	0.16	1.14	0.06	1.96
MEC	0.15	1.13	0.04	1.84
E	6.25%	0.90%	33.33%	6.12%

The magnetic fluxes in the TMC are predicted with a maximum error of 72.13% for Φ_T (Tab. 3.10) and 53.03% for Φ_{T1bc} (Tab. 3.8). The error of Φ_T is caused by the demagnetization of the torque magnet tip (see Fig. 3.32), which is the place where the flux is calculated. However, the demagnetization of the magnet is only local, as it is also confirmed by the volume average value of the magnetic flux density B_T that is obtained with the minimal error (the error is coincidentally zero in Tab. 3.11, which is a consequence of rounded numbers). The local flux

concentration is also the main cause of the error in Φ_{T1bc}.
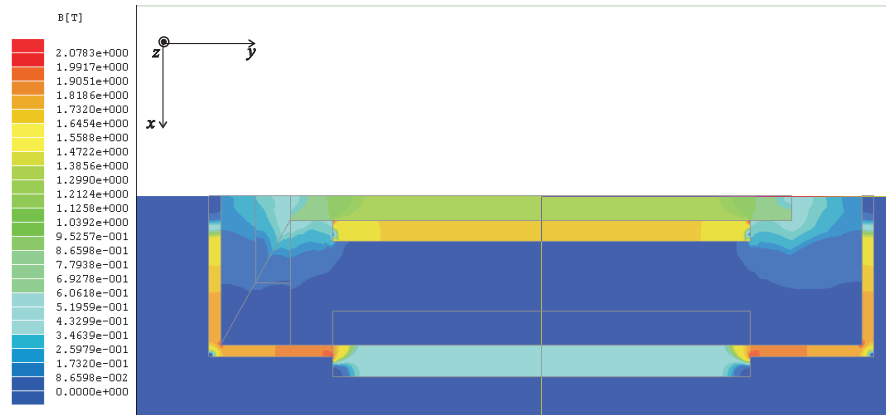
Figure 3.28: Modulus of the magnetic flux density produced by the torque magnet in the xy-plane (FEM with the data-sheet magnets).

Figure 3.29: Modulus of the magnetic field intensity produced by the torque magnet in the xy-plane (FEM with the data-sheet magnets).
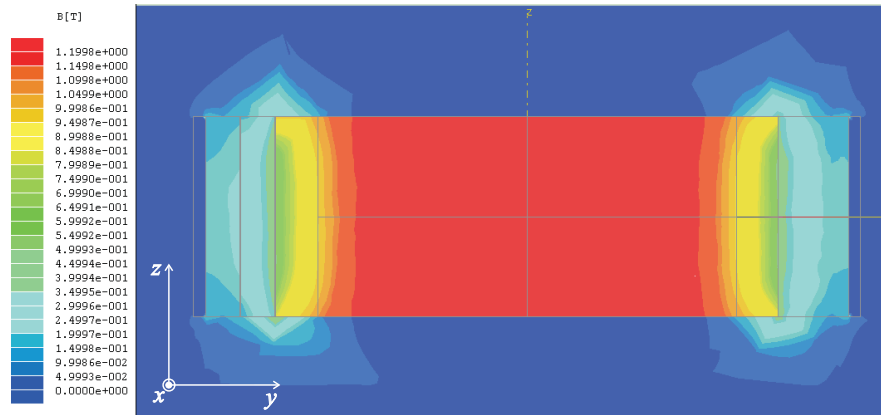
Figure 3.30: Modulus of the magnetic flux density produced by the torque magnet in the yz-plane (FEM with the data-sheet magnets).
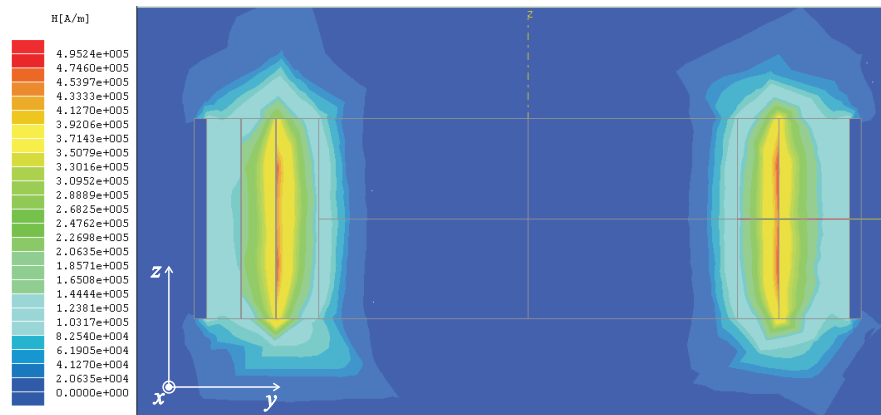
**Figure 3.31**: Modulus of the magnetic field intensity produced by the torque magnet in the yz-plane (FEM with the data-sheet magnets).

The magnetic flux densities in the TMC are obtained with an acceptable error except for the error of B_{T1c} in Tab. 3.11, which is 33.33%. The value of B_{T1c} is however small, compared to B_{T1a} (see the reluctance volumes in Fig. 3.19), and therefore it does not introduce a high inaccuracy in the torque calculation.

Table 3.10: Magnetic fluxes in the TMC with the measured magnets.

$[10^{-5}Wb]$	$\Phi_{S_{T1}}$	$\Phi_{S_{T2}}$	$\Phi_{S_{T3}}$	$\Phi_{S_{T4}}$	$\Phi_{S_{T5}}$	$\Phi_{S_{T6}}$	$\Phi_{S_{T7}}$	$\Phi_{S_{T8}}$
	0.68	0.762	0.99	1.22	0.047	0.11	0.066	1.65
FEM	$\Phi_{T1a} \approx \dfrac{\sum_{i=1}^{n=3} \Phi_{S_{Ti}}}{3}$			$\Phi_T \approx \Phi_{S_{T4}}$	$\Phi_{T1bc} \approx \dfrac{\sum_{i=5}^{n=7} \Phi_{S_{Ti}}}{3}$			$\Phi_{TMC} \approx \Phi_{S_{T8}}$
	0.81			1.22	0.075			1.65
MEC	1.08			2.10	0.104			1.59
E	33.33%			72.13%	38.67%			3.64%

Table 3.11: Magnetic flux densities in the TMC with the measured magnets.

	B [T]			
	$B_{T1a} = \dfrac{\Phi_{T1a}}{S_{T2}}$	$B_T = \dfrac{\Phi_T}{S_{T4}}$	$B_{T1c} = \dfrac{\Phi_{T1bc}}{S_{T6}}$	$B_{TMC} = \dfrac{\Phi_{FMC}}{S_{T8}}$
	0.13	0.68	0.029	1.77
FEM	$B_{T1a} = \dfrac{\int_{V_{T1}} BdV}{\int_{V_{T1}} dV}$	$B_T = \dfrac{\int_{V_{T3}} BdV}{\int_{V_{T3}} dV}$	$B_{T1c} = \dfrac{\int_{V_{T2}} BdV}{\int_{V_{T2}} dV}$	$B_{TMC} = \dfrac{\int_{S_{T8}} BdS}{\int_{S_{T8}} dS}$
	0.16	1.17	0.06	1.77
MEC	0.15	1.17	0.04	1.89
E	6.25%	0%	33.33%	6.78%
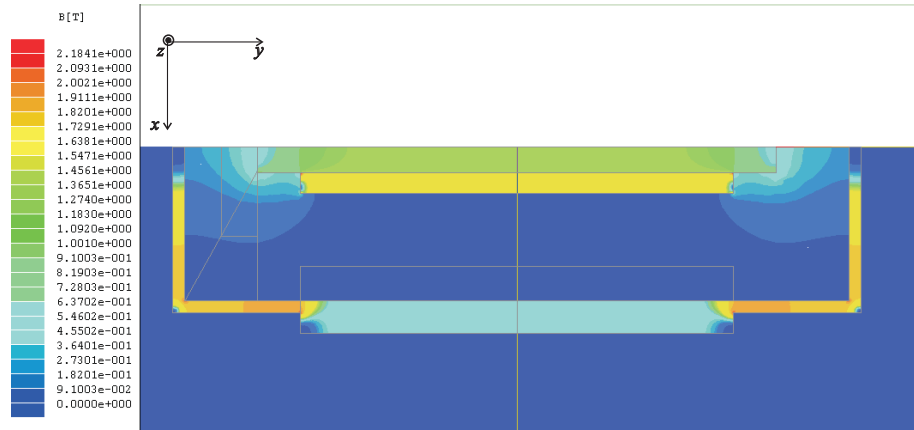
Figure 3.32: Modulus of the magnetic flux density produced by the torque magnet in the xy-plane (FEM with the measured magnets).
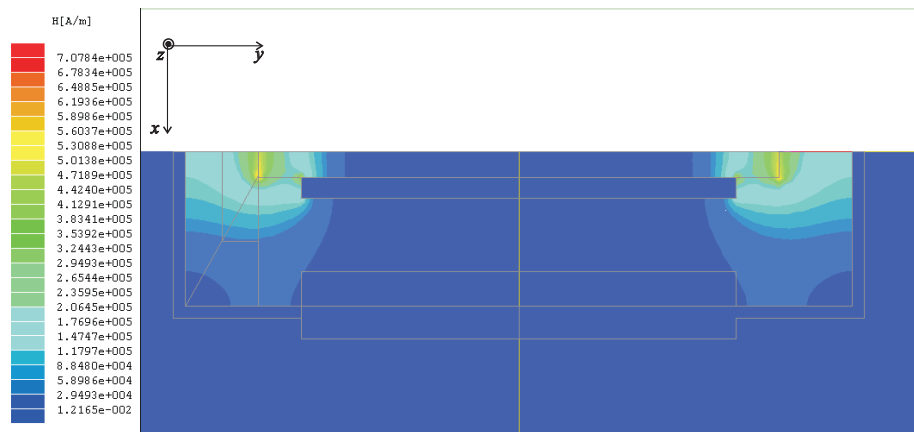
Figure 3.33: Modulus of the magnetic field intensity produced by the torque magnet in the xy-plane (FEM with the measured magnets).
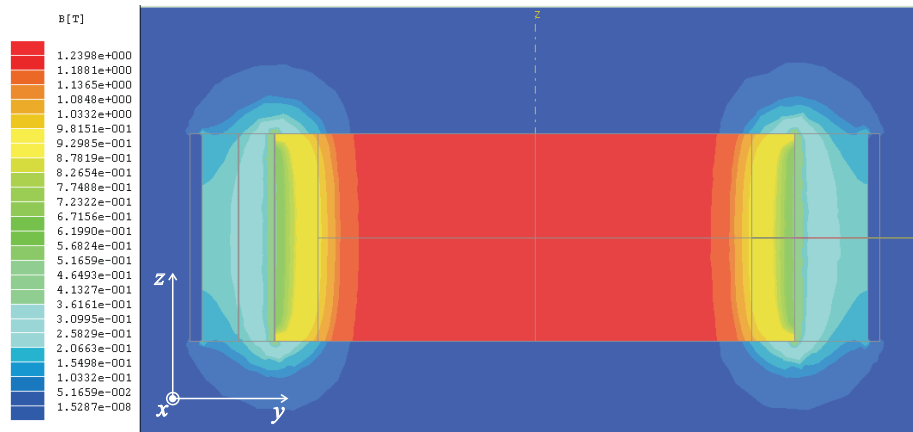
Figure 3.34: Modulus of the magnetic flux density produced by the torque magnet in the yz-plane (FEM with the measured magnets).
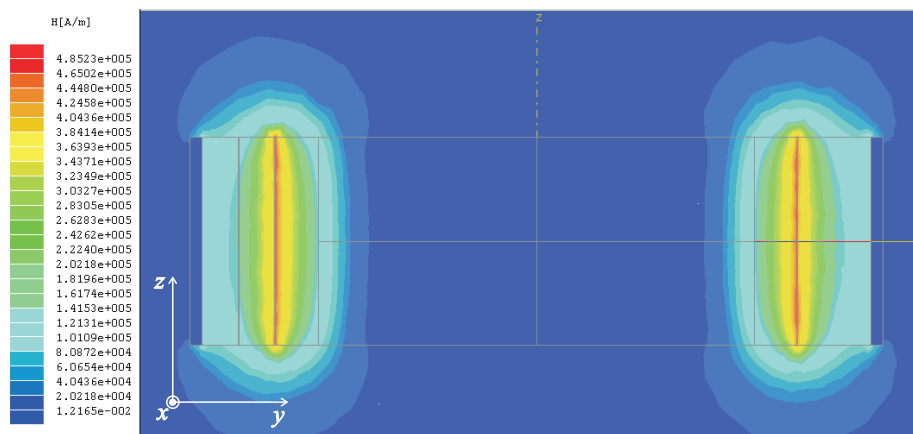
**Figure 3.35**: Modulus of the magnetic field intensity produced by the torque magnet in the yz-plane (FEM with the measured magnets).

With respect to saturation of the ferromagnetic core, the magnetic flux density should be below 2.1 T in the cobalt-iron core. The highest value of the magnetic flux density can be found in the outer ferromagnetic core in the xy-plane shown in Fig. 3.36, because the fluxes in the FMC and TMC are superimposed in these places. As it can be seen from Fig. 3.36, the maximum magnetic flux density in the outer ferromagnetic core is 2.08 T and 2.01 T for the data-sheet and measured magnets, respectively.

The level of demagnetization of the magnets is assessed by the magnetic field intensities in Tabs. 3.12 and 3.13, calculated by FEM.

Table 3.12: Magnetic field intensity in the force magnet.

H_{PM} [kA/m]	data-sheet magnets	measured magnets
H_{max}	1349.25	1617.57
H_{av}	411.94	392.72

Table 3.13: Magnetic field intensity in the torque magnet.

H_{PM} [kA/m]	data-sheet magnets	measured magnets
H_{max}	986.44	944.81
H_{av}	56.43	57.86

The maximum magnetic field intensity can be found on the edges of the force magnets. This value exceeds the demagnetization value of $700 kA/m$, which is a threshold for an irreversible loss of magnetization at $80°C$. It means that at $80°C$ the volume of the magnets with a magnetic field intensity higher than $700 kA/m$ will experience an irreversible loss of magnetization. However, only a very small volume is affected as can be seen from Fig. 3.23 and 3.27. According to the average values of $|\vec{H}|$, the force magnets do not undergo irreversible loss at $100°C$, which would affect the volume of the magnets with $|\vec{H}| > 530 kA/m$.

The maximum magnetic field intensity at the torque magnet appears in the tips and corners (see Figs. 3.31 and 3.35). The volume of the magnet with high magnetic field intensity is very small and thus this magnet does not experience a significant demagnetization at $80°C$. If the average magnetic field intensity is regarded, the irreversible loss does not appear even at $100°C$. The results in sec-

tions 4.7 and 6.2.1 of the thermal simulations and experiments confirm that the temperature of magnets does not exceed the maximum allowable temperature.
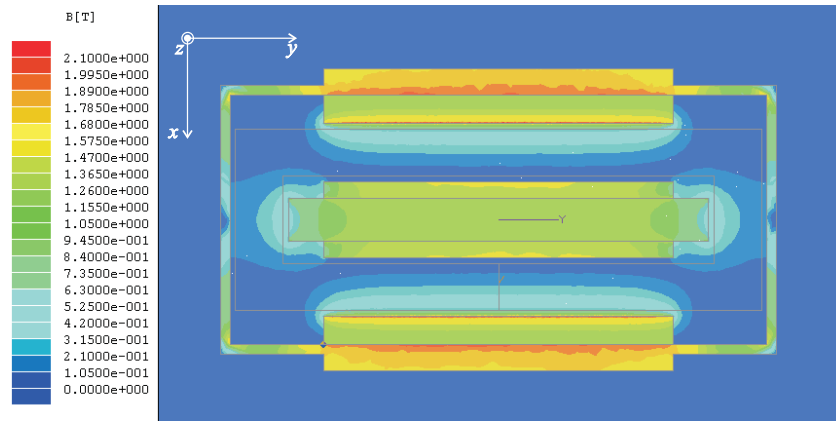
a)
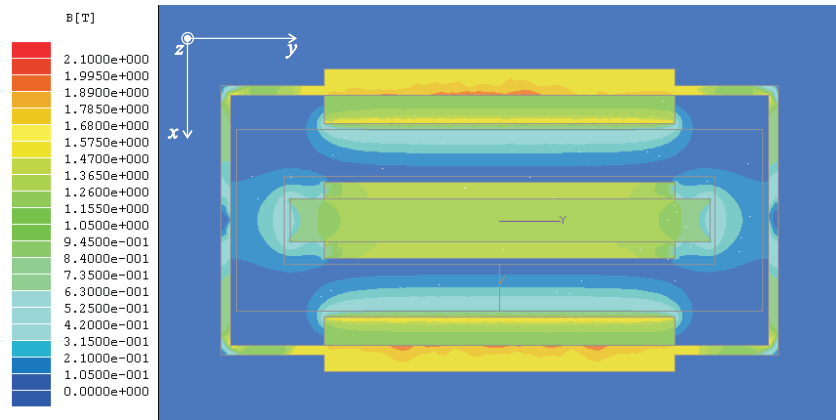
b)

Figure 3.36: Modulus of the magnetic flux density of the actuator produced by the force and torque magnets in the xy-plane with a) data-sheet magnets, b) measured magnets.

3.5.2 Force and torque

The force and torque of the actuator are obtained from the magnetic field as mentioned in section 3.4. They are calculated by three methods:

- FEM and Lorentz equation,

- FEM and virtual-work method,

- MEC and Lorentz equation.

In the first and second case, the magnetic field distribution is obtained by the FEM and then the Lorentz equation and the virtual-work method is applied. Three force components, F_x, F_y (parasitic forces) and F_z (main force), and three torque components, T_x (main torque), T_y and T_z (parasitic torques), are obtained as a function of the position. F_z, T_x and F_y as produced by the nominal current density are shown in Figs. 3.37 to 3.39. The other remaining force and torques are not shown because they are smaller than the numerical error caused by the discretization of the problem and the error of the force method calculation. Therefore, no clear pattern can be seen.

As a measure of the force and torque variation the following ratio of flatness is often used

$$\Delta_{F,T} = \frac{F,T_{max} - F,T_{min}}{F,T_{max}}. \tag{3.80}$$

The flatnesses of the force and torque characteristics related to each coil are displayed in Tab. 3.14. Usually, the flatness of voice coil actuators is between 10-20%. The low flatness of the 2-DoF actuator characteristics is a result of the optimization process (see Chapter 5) where no constraint or requirement for the flatness was set. However, by imposing only minimum mass constraint, the optimization problem allowing to find the design with lower mass is relaxed. If higher flatness is required then the ratio of the coil to magnet length should be used as the constraint to achieve a required flatness.

Table 3.14: Force and torque variations.

	Data-sheet PM	Measured PM
Δ_F	38.4%	37.9%
Δ_T	18.7%	16.7%
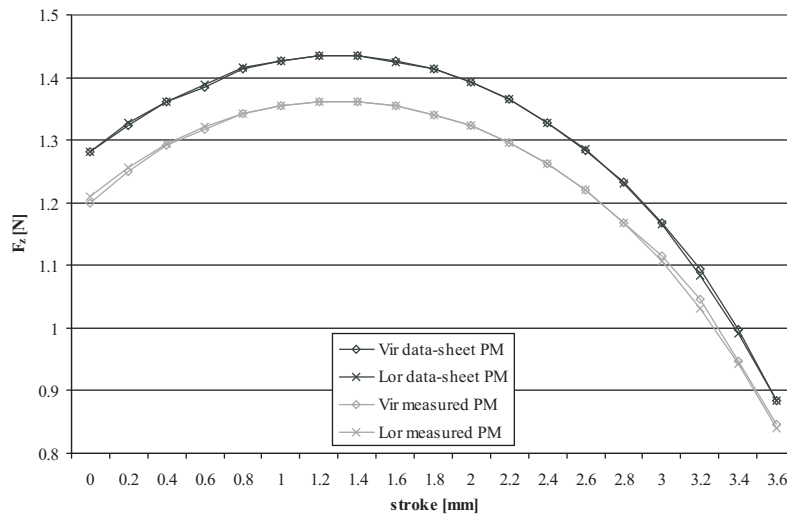
a)
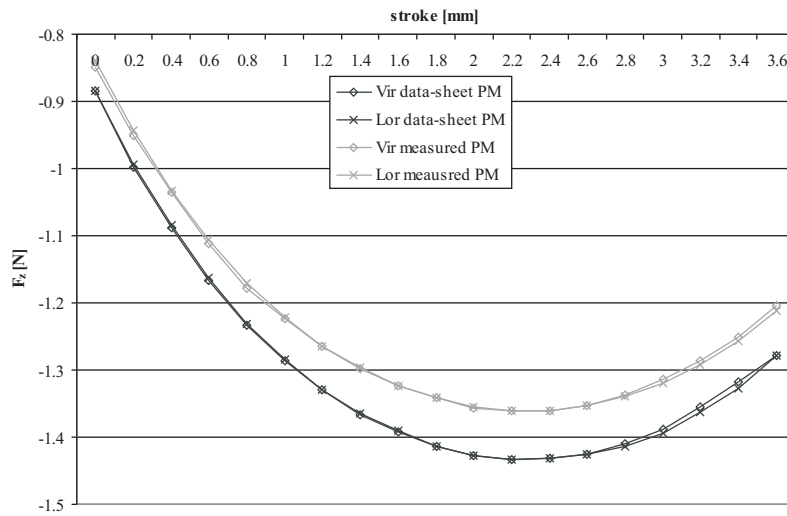
b)

Figure 3.37: Main forces on coils obtained from FEM by the Lorentz equation and virtual-work method a) the coil of the first stage, b) the coil of the second stage.
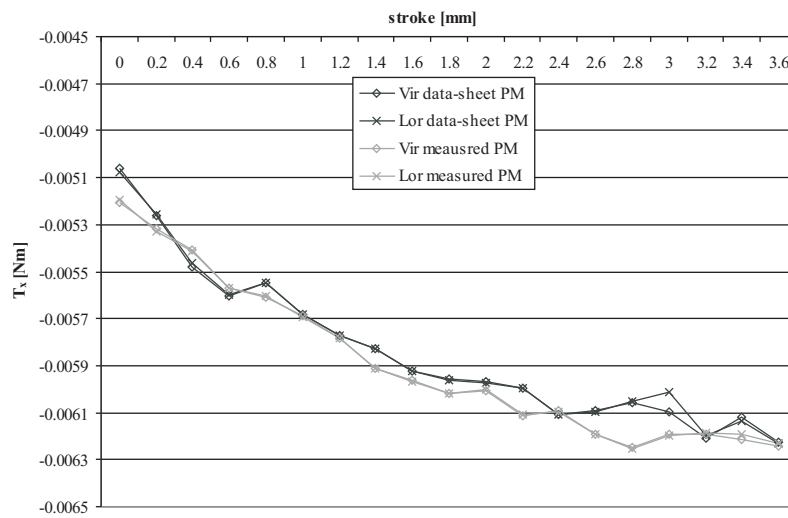
a)
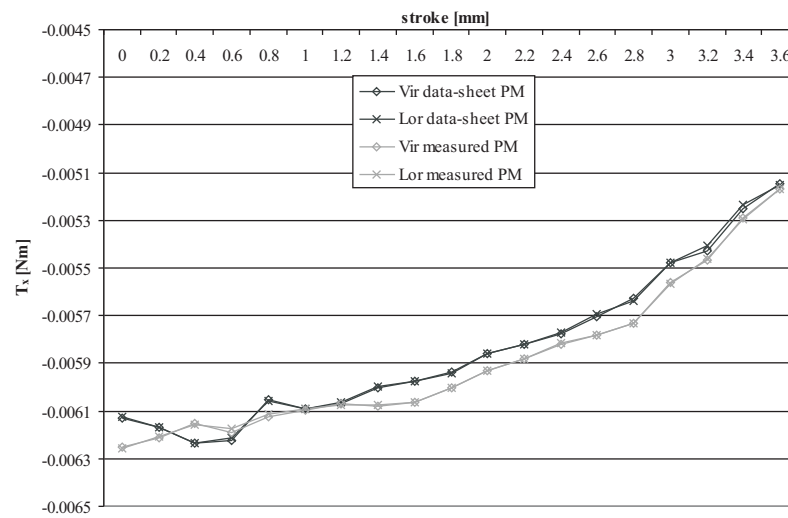
b)

Figure 3.38: Main torques on coils obtained from FEM by the Lorentz equation and virtual-work method a) the coil of the first stage, b) the coil of the second stage.
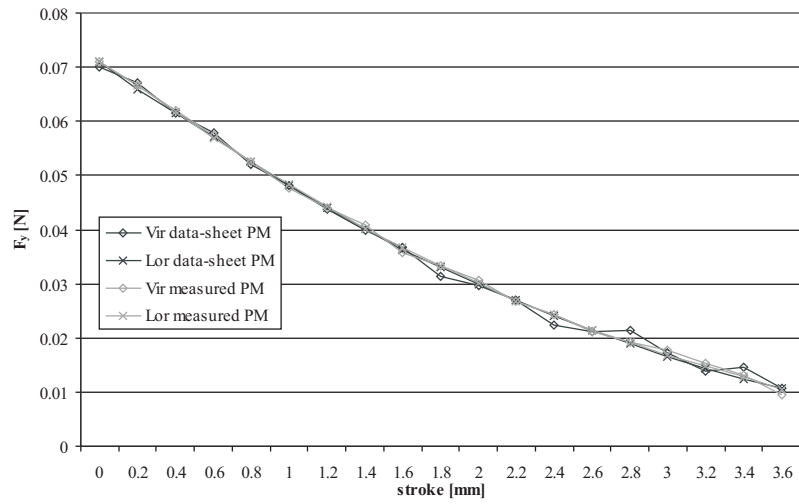
a)
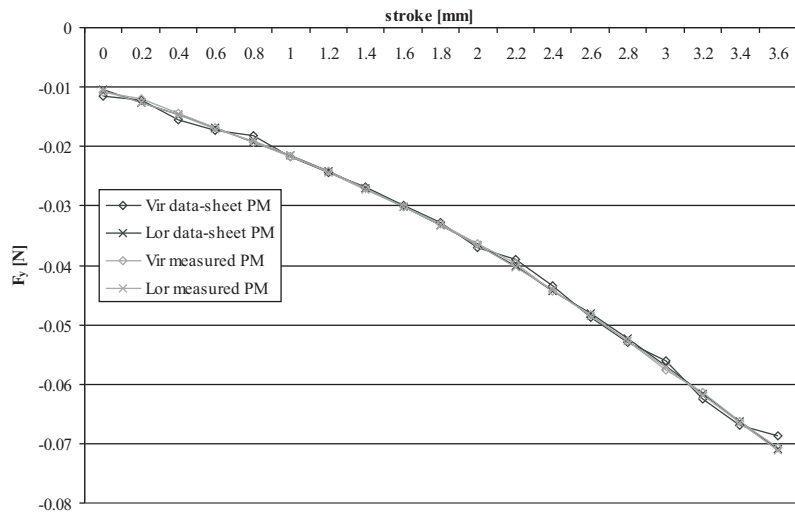
b)

Figure 3.39: Parasitic forces on coils in y-direction obtained from FEM by the Lorentz equation and virtual-work method a) the coil of the first stage, b) the coil of the second stage.

In the third case of force and torque calculation, the magnetic field is obtained by the MEC model, and then (3.68) and (3.69) are used to calculate the average force and torque. In (3.68) and (3.69), the integrals are replaced by the sums of the forces and torques produced in the intersections of particular flux tubes and corresponding volumes of coils:

$$F_z = \sum^i B_i \cdot J_i \cdot V_i, \tag{3.81}$$

$$T_x = \sum^i B_i \cdot J_i \cdot V_i \cdot r_i, \tag{3.82}$$

where F_z is the force of the actuator in z-direction, T_x the torque of the actuator around the x-axis, B_i the average magnetic flux density in the i-th tube, J_i the current density in the volume V_i of the coil intersecting the i-th flux tube and r_i the average distance from the volume V_i to a reference point. The reference point is fixed to the coil as shown in Fig. 3.40. It is assumed that the magnetic flux density
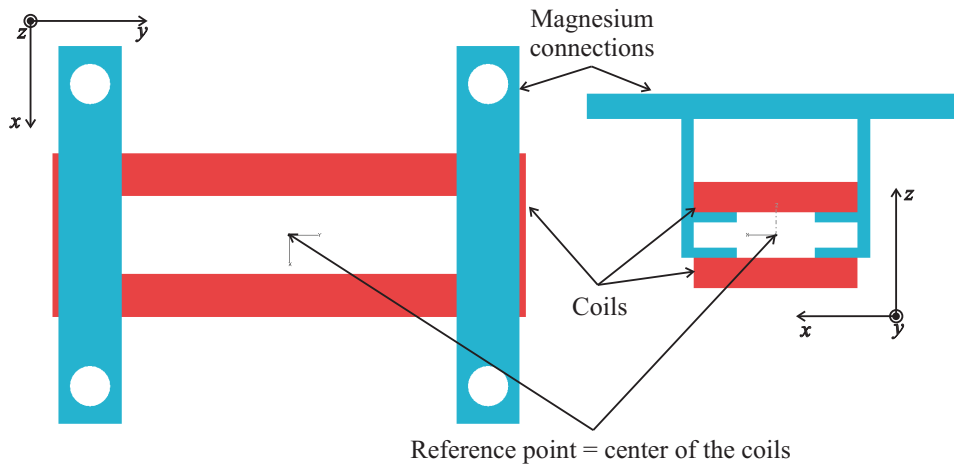
Figure 3.40: Reference point for calculation of the torque (coil assembly).

and the current density are perpendicular to each other in the intersection of the corresponding coil part and the flux tube. That means, the force and torque are not dependent on the position of the coils. The force and torque produced by the

nominal current density are listed in Tabs. 3.15 and 3.16, where the FEM values represent the average over the stroke of the actuator defined as

$$F_z = \frac{\sum_{i=1}^n F_i}{n}, \quad T_x = \frac{\sum_{i=1}^n T_i}{n}. \tag{3.83}$$

where F_i and T_i are the calculated samples (those in Figs. 3.37 and 3.38) for different positions and n is the number of samples.

The relative error is, again,

$$E = \frac{|\text{FEM-MEC}|}{\text{FEM}}. \tag{3.84}$$

Table 3.15: Force on one coil of the 2-DoF actuator.

$F_z\ [N]$	Data-sheet PM	Measured PM
FEM	1.30	1.23
MEC	1.30	1.24
E	0%	0.81%

Table 3.16: Torque on one coil of the 2-DoF actuator.

$T_x\ [10^{-3}N \cdot m]$	Data sheets PM	Measured PM
FEM	5.84	5.89
MEC	5.48	5.63
E	6.16%	4.41%

Comparing the MEC based approach with the FEM one, the force is predicted with 0.81% and the torque with 6.16% maximum error.

3.6   Conclusions

The purpose of the presented static electromagnetic analysis was to establish a set of equations, also called sizing equations, that express mutual relations between the requirements (continuous force, torque, magnetic field density etc.) and the

dimensions (of magnets, ferromagnetic core etc.) The performance requirements are expressed in this chapter as functions of the geometrical dimensions of the actuator in two ways:

- analytical (MEC model),

- numerical (FEM model).

It has been shown that, by using the proposed MEC model, the magnetic field, force and torque of the actuator can be predicted with sufficient accuracy for design purposes. This is evident by the low relative errors, which can be found if the resulting values of the analytical model are compared with the corresponding average values obtained by the numerical model.

As the investigation shows, the proposed MEC model is more complex than the models known from examples of machines with a relatively small air gap, for which it is possible to make simplifications due to geometrical symmetries. The consequence of a relatively large air gap is that the model has to describe the magnetic field by means of average values linked to the volume of the respective flux tubes. On the other hand, the FEM model offers magnetic field distributions and it can reveal local field concentrations or core saturation.

The predicted magnetic field in the actuator proves that the ferromagnetic core is optimally utilized. In other words, the core is not magnetically saturated. The force and torque magnets can operate at temperatures up to $80°C$ without permanent demagnetization.

It can be concluded that the analytical description can be used for design and optimization purposes. Although it is found to be a less accurate model offering less precise results, it can be conveniently supplemented by the FEM model to obtain a high-precision solution. This approach will be used in Chapter 5 for optimization purposes.

Chapter 4

Thermal analysis

The temperature distribution in electrical actuators is one of the most important design aspects. It influences the operation conditions as continuous load, overload, allowable ambient temperature etc.

Each part of an actuator has a corresponding maximum temperature. That is to say, if a part reaches its maximum temperature it cannot perform its specified function within required tolerances. Otherwise stated, the maximum temperature is determined by the function and the material of a component. For example, the function of coils is to conduct current and to transfer created forces. So, a coil must have a certain mechanical strength and high conductivity, which can be reached by an insulated copper wire compressed by glue in case of self-contained coils. However, if the coil is heated by its ohmic losses the glue may loose its strength and the coil may disintegrate or the electrical insulation can be damaged. Therefore, in self-contained coil actuators, the maximum allowable temperature of the coils mostly limits the overal performance.

On the other hand, the function of magnets is to create a magnetic field that is, in turn, dependent on temperature. The higher the temperature of the magnets used, the weaker the magnetic field and consequently the lower the generated force. In order to avoid magnetic field variation or even demagnetization the temperature of magnets should not exceed a certain maximum value.

So, in order to design an actuator that satisfies performance specifications, the temperature distribution should be predicted with sufficient accuracy. For this purpose a so-called lumped parameter model, which can describe steady-state as well as transient heat transfer in the actuator, is proposed. It has the form of an

equivalent thermal circuit containing lumped thermal resistances and capacitances.

In the following sections, the heat transfer is described by heat flux equations in three modes. Then, the principle of energy conversation is introduced and a heat diffusion equation is derived. Based on the diffusion equation the corresponding thermal resistances and capacitances are obtained. Further, the actuator is analyzed in order to determine the direction of heat flux is determined and to find planes of symmetry. According to the heat transfer modes the parts of the actuators are replaced by equivalent resistances and capacitances creating the lumped parameter thermal model. Then, the model is verified by thermal measurements, which are show in Chapter 6.

4.1   Heat transfer

Heat transfer is defined as thermal energy transfer that appears in a medium or between media with temperature difference. The heat transfer has three different modes [32, 33]:

- conduction,

- convection,

- radiation.

The conduction heat transfer takes place through a medium with a temperature difference. The convection heat transfer refers to thermal energy transfer between a surface and moving fluid or gas. The radiation of energy from a surface in form of electromagnetic waves in absence of media appears between two surfaces.

All heat transfer modes can be found in electrical applications. Most common are conduction and convection. In many cases heat is transferred from the heat source (winding, high conducting sheets with induced currents etc.) by conduction through several layers of solid media e.g. permanent magnet - glue - iron core of an actuator to a surface where the energy is further transferred by convection to a moving fluid (usually air or water). In special applications, where an actuator operates in vacuum, radiation could become most significant.

4.2   Heat flux equations

The heat flux equations in this section express the amount of energy transferred per unit time. That is to say, for now the equations of the three different modes describe the heat transfer related to space geometry and materials, but not to time variations.

4.2.1   Conduction

The heat transfer by conduction can be attributed to a random translation of molecules of a gas or liquid with zero net flow, or to iteration of particles (atoms) in a lattice and movement of free electrons in solids. The conduction can be quantified by the conduction heat flux $\vec{q}''_{cond}$, a vector quantity. It is the heat transferred through a unit area perpendicular to the direction of transfer and can be written as

$$\vec{q}''_{cond} = -k\nabla T, \tag{4.1}$$

where k is the thermal conductivity of the material, ∇ is the three dimensional Nabla operator and T is the scalar temperature field. This equation, known as Fourier's law, implies that the heat flux has the direction of decreasing temperature perpendicular to isotherms.

4.2.2   Convection

Convection heat transfer occurs between a surface and a fluid or gas in motion, which are at different temperatures. It comprises random molecular motion of particles and net flow of a gas or liquid.

Convection is a complex physical mechanism. It can be described by so-called hydrodynamic and thermal boundary layers. The hydrodynamic layer is the velocity distribution of the fluid, which varies from zero at the surface to a finite velocity of the flow. The temperature layer is the distribution of the temperature from the boundary surface in the direction perpendicular to the surface.

The convection can be further classified according to the nature of the flow.

Natural convection caused by buoyancy force, which originates from mass density difference caused by temperature variations.

Forced convection caused by external means as a fan or a compressor.

In spite of the complexity of the phenomena the convective heat flux per unit area, q''_{conv}, has the following simple form:

$$q''_{conv} = h\left(T_s - T_\infty\right) \tag{4.2}$$

where h is the convection heat transfer coefficient (comprising all the complexity), T_s is the surface temperature and T_∞ is the fluid temperature.

4.2.3 Radiation

Radiation is predicated to the changes of electron configuration. The radiation can be emitted from or incident on a surface. The emission and absorption of the radiation power can be characterized by the rates of the emissive E_λ and absorbed $G_{\lambda abs}$ irradiative power from or on a real surface as

$$E_\lambda = \epsilon_\lambda \sigma_{SB} T_s^4, \tag{4.3}$$

$$G_{\lambda abs} = \alpha_\lambda G_\lambda, \tag{4.4}$$

where λ designates the wavelength of the radiation, ϵ_λ is the spectral emissivity of the surface, σ_{SB} is the Stefan-Boltzmann constant, T_s is the absolute temperature of the surface, α_λ is the spectral absorptivity and G_λ is the spectral irradiation.

In practice, a radiation energy exchange between two surfaces, where one isothermal surface at temperature T_{sur} completely surrounds the second smaller one at temperature T_s ($T_{sur} \neq T_s$), often occurs. In this case, the net heat flux per unit area can be conveniently expressed as the difference between the thermal energy released by the radiation emission and the energy absorbed by the radiation absorption yielding

$$q''_{rad} = \int_\lambda \epsilon_\lambda \sigma_{SB} T_s^4 - \int_\lambda \alpha_\lambda \sigma_{SB} T_{sur}^4, \tag{4.5}$$

which simplifies to

$$q''_{rad} = \epsilon_\lambda \sigma_{SB} \left(T_s^4 - T_{sur}^4 \right), \tag{4.6}$$

assuming $\epsilon_\lambda = \alpha_\lambda$.

4.3 Energy conservation

The time change of the temperature of media, i. e. the transient thermal energy transfer, is not captured by the heat flux equations. It is described by the law of energy conversation, also known as energy balance.

The energy balance is defined in a control volume (volume of interest) that is bounded by a control surface through which energy enters of leaves the control volume. The law of energy conservation states that the rate at which the thermal and mechanical energy enters a control volume, plus the rate at which the thermal energy is generated within the control volume, minus the rate at which the thermal and mechanical energy leaves the control volume must equal the rate of increase of energy stored within the control volume. Otherwise stated [32, 33],

$$\dot{E}_{in} + \dot{E}_g - \dot{E}_{out} = \dot{E}_{st}, \tag{4.7}$$

where the energy rate entering $\dot{E}_{in}$ or leaving $\dot{E}_{out}$ the volume is the energy transferred by one or combination of the conduction, convection or radiation through part of the whole control surface. The generated energy rate $\dot{E}_g$ may have different origins. It is the energy converted from another form as electrical, electromagnetic etc. to thermal energy. The stored energy rate $\dot{E}_{st}$ in the case of actuators is considered to be only the thermal energy.

4.4 Thermal modeling of the 2-DoF actuator

The heat produced by the 2-DoF actuator is transferred to the surroundings in two ways. The first way is the transfer from the outer surfaces of the actuator to the surrounding air. This transfer is a natural convection. The second way is the transfer through the magnesium connections to the beam, which is considered to be at ambient temperature. No forced cooling is applied to the actuator.

The heat inside the actuator is transferred by internal conduction. Radiation energy transfer in the actuator is negligible (less than 2%, based on a coil temperature of $116.4°C$), thus, this transfer is not taken into account in the following analysis.

Because of the nature of the heat transfer, e.g. multidimensional heat transfer, it is often not possible to find the exact analytical solution of equation (4.7). Exceptions are certain geometries, where shape and temperature distribution symmetry can be utilized to simplify the equation of energy conservation. For this reason, the heat transfer in the actuator should be first qualitatively analyzed in order to evaluate the possibility of modeling simplification.

Complexity reduction of the 2-DoF actuator

It is always convenient to try to develop reduced models of complex thermal systems. The most common way of reducing the complexity is to find planes of geometrical symmetry. These planes are mostly parallel to the heat flow. In other words, there is no heat flow perpendicular to the symmetry plane, which is then called adiabatic plane. If adiabatic planes can be found, then the modeled volume may be reduced and so the complexity of the model.

Two adiabatic planes and the heat flow in the xy-plane of the 2-DoF actuator are shown in Fig. 4.1. The heat flow in the xz-plane that crosses the magnesium connection of the coils is illustrated in Fig. 4.2a. The direction of the flow is restricted by the shape of the connection and there is about 200 times lower heat flow between the connection and the outer ferromagnetic core with respect to the flow in the connection (see Fig. 4.2b). Assuming that the heat flow between the connection
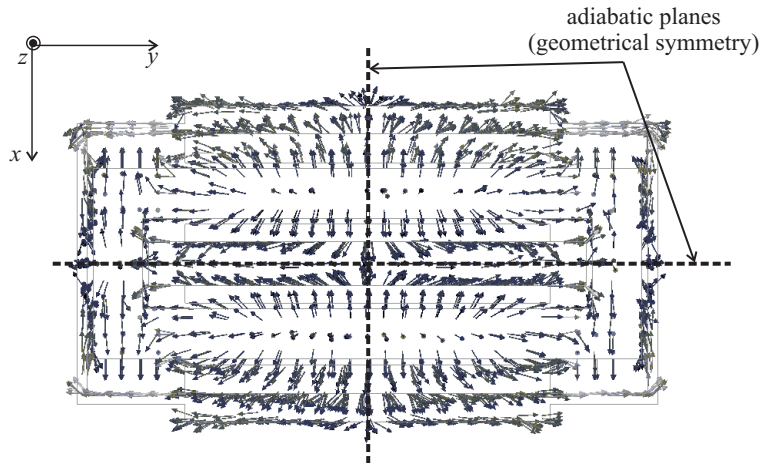
Figure 4.1: Heat flow of the 2-DoF actuator in the xy-plane.

and outer ferromagnetic core is negligible, another adiabatic plane, which is not a plane of geometrical symmetry, can be drawn (see Fig. 4.3).

The three adiabatic planes divide the actuator into eight parts. As a result, the heat flow can be modeled by considering only one eighth of the actuator.

From Figs. 4.1 to 4.3, it can be noticed that the heat flow in the actuator is three dimensional. As it is mentioned at the beginning of this section it is not possible to find the exact analytical solution of the multidimensional heat transfer. Thus, if an analytical thermal model is desired, the heat flow description in the actuator should be further simplified.

4.5   Model elements and their equivalent circuit representations

As it is known from [32, 33], an analytical description of one-dimensional heat flow problems can be derived. Further, analogy between one-dimensional heat diffusion and electrical charge can be found. The analogy leads to the important concept of an equivalent thermal circuit. Thermal modeling is therefore often restricted to one dimension or to a combination of one-dimensional heat flows as it can be found
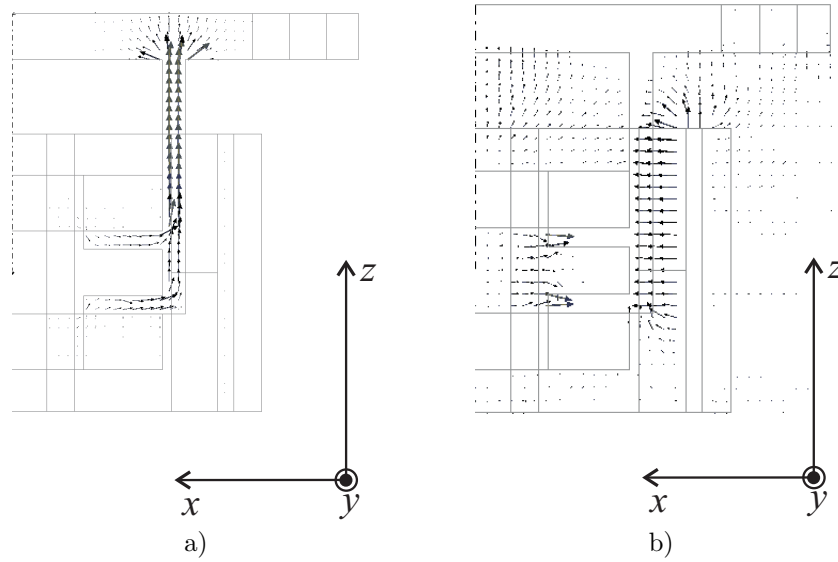
Figure 4.2: Heat flow a) in the magnesium connection, b) between the magnesium connection and the surrounding air.
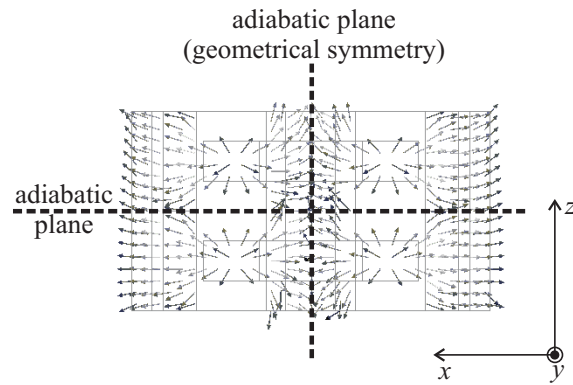
Figure 4.3: Heat flow of the 2-DoF actuator in the xz-plane.

in [34, 35, 36]. It is assumed that these one-dimensional heat flows in different directions are uncorrelated.

The 2-DoF actuator will be modeled by a reduced equivalent thermal circuit. However, the model should not be over-simplified and too coarse so that it still corresponds with the reality. The resulting analytical representation should describe the problem in sufficient details. In order to make appropriate simplifications, local heat flows of various actuator parts will be determined and the equivalent thermal circuit of each part is derived in the following subsections.

4.5.1 Magnesium connection

The heat in the magnesium connection is transferred by conduction. The conduction can be described by applying the energy conservation principle in a differential control volume (see Fig. 4.4).
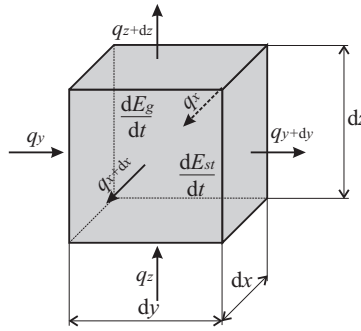
Figure 4.4: Differential control volume.

By substituting

$$\dot{E}_{in} = q_x + q_y + q_z, \tag{4.8}$$

$$\dot{E}_{out} = q_{x+dx} + q_{y+dy} + q_{z+dz}, \tag{4.9}$$

$$\dot{E}_g = p\,dx\,dy\,dz \tag{4.10}$$

and

$$\dot{E}_{st} = \rho c_p \frac{\partial T}{\partial t} dx\,dy\,dz, \tag{4.11}$$

into (4.7), the general form of the heat diffusion equation, which relates the heat flow to time and space, is found to be

$$\frac{\partial^2 T}{\partial x^2} + \frac{\partial^2 T}{\partial y^2} + \frac{\partial^2 T}{\partial z^2} + \frac{1}{k}p = \frac{\rho c_p}{k}\frac{\partial T}{\partial t}, \tag{4.12}$$

where p is the heat generation rate per unit volume, ρ is the mass density and c_p is the specific heat of the material.

Under the assumption made in subsection 4.4, the heat flow in the magnesium connection, denoted by "c" in Fig. 4.5, can be represented by an one-dimensional heat flow in planes without heat generation and constant heat flux.
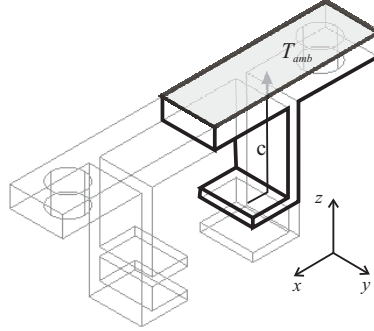
Figure 4.5: Heat flow in the half of the magnesium connection.

It is assumed in Fig 4.5 that there is no temperature change in the y-direction, therefore

$$\frac{\partial^2 T}{\partial y^2} = 0. \tag{4.13}$$

Moreover, the thermal flow in the x- and z-directions can be considered separately. For steady-state conduction in the x-direction only and without heat generation in the material, (4.12) simplifies to

$$\frac{\partial^2 T}{\partial x^2} = 0. \tag{4.14}$$

If the conductivity of the magnesium is considered constant, (4.14) can be integrated twice yielding

$$T(x) = C_1 x + C_2. \tag{4.15}$$

By applying the boundary conditions

$$T(0) = T_{s,1}, \tag{4.16}$$

$$T(L) = T_{s,2}, \tag{4.17}$$

where L is the average length of the heat flux path, the temperature distribution in the magnesium connection equals

$$T(x) = (T_{s,2} - T_{s,1})\frac{x}{L} + T_{s,1}. \tag{4.18}$$

Then, by using (4.1), the total heat flux rate in the x-direction is

$$q_x = q_x'' A = \frac{kA}{L}(T_{s,1} - T_{s,2}). \tag{4.19}$$

The last equation shows an analogy between the heat transfer rate and Ohm's law for the electrical conduction like

$$I = \frac{\Delta V}{R_e}. \tag{4.20}$$

Thus, the thermal resistance for the thermal conduction can be defined as

$$R_{t,cond} \equiv \frac{T_{s,1} - T_{s,2}}{q_x} = \frac{L}{kA}. \tag{4.21}$$

The thermal resistance is used to model the magnesium connection in the steady state. The same reasoning can be applied to the heat conduction in the z-direction in Fig. 4.5, and both resistances may be added together.

To include the transient behavior the following assumptions are made:

- The thermal capacity is uniformly distributed.

- The average temperature of an element determines the stored energy.

- The average temperature determines the direction of the heat flow.

Then, the total stored energy is found to be

$$E_{st} = \rho V c_p T_{av}, \tag{4.22}$$

where ρ, V and c_p are the specific density, volume and specific heat of the material. The energy storage term can be represented by a capacitor with a value equal to

$$C_t = \rho V c_p. \tag{4.23}$$

If it is assumed that the temperature distribution in the element during transient states is linear, as in (4.18), the average temperature will be in the middle of the element. In terms of the equivalent circuit, the average temperature corresponds with the point of connection between two thermal resistances, where each resistance is equal to half of the total resistance defined by (4.21). Therefore, the capacitor should be connected between the two resistances as it can be seen from the thermal equivalent circuit of the magnesium connection in Fig. 4.6.
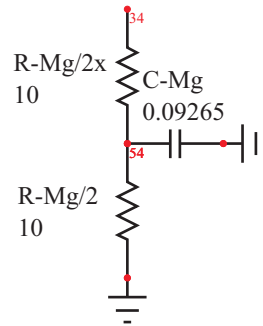
Figure 4.6: Thermal equivalent circuit of the magnesium connection.

In the equivalent circuit of the magnesium connection, node 34 represents the temperature of the surface that is glued to the coil. The grounding of the resistance R-Mg/2 is the surface attached to the flexible beam. The beam as a whole is considered to be at the ambient temperature; therefore, no thermal resistance is associated to it.

4.5.2   Torque magnet

The heat flow in the torque magnet is a combination of three independent one-dimensional heat transfers a,b and c in Fig. 4.7. In all cases the heat is transferred by conduction, so, they are represented by thermal resistances as defined by (4.21).

Because the heat flow is symmetric with respect to the adiabatic planes, the thermal resistances as given by (4.21) should be calculated to represent only one-eight of the total resistances in the corresponding directions (see Fig. 4.7, where only one-eight of the magnet is taken in consideration). Finally, Fig. 4.8 shows the resulting thermal resistances, which represent the heat transfer for each direction. Since the heat flow does not cross the adiabatic planes, it is sufficient to use only

the half of the T-equivalent circuit (as in Fig. 4.6) for each one-dimensional heat conduction.
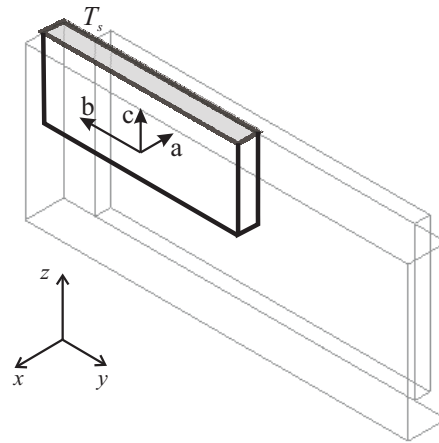
Figure 4.7: Heat flow in one-eight of the torque magnet.
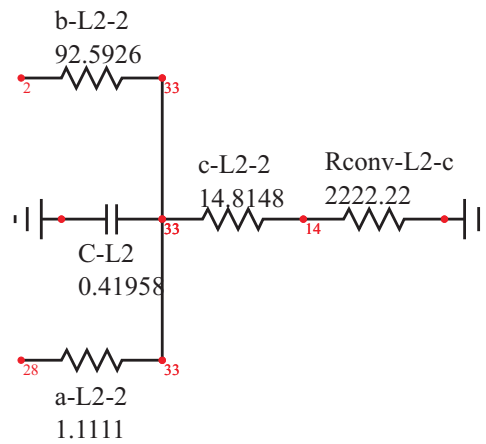
Figure 4.8: Thermal equivalent circuit of one-eight of the torque magnet.

Node 14 in Fig. 4.8 represents the temperature T_s of the top surface of the torque magnet. The heat in the c-direction flows to the surrounding air and, therefore, a convection thermal resistance is connected to the conduction resistance in the c-direction at node 14. The convection resistance is defined by analogy between Ohm's law and Newton's law of cooling (4.2), as

$$q = hA(T_s - T_{amb}), \tag{4.24}$$

thus,

$$R_{t,conv} = \frac{1}{hA}. \tag{4.25}$$

The lumped thermal capacitance is obtained by (4.23). It is connected between node 33, representing the average temperature of the magnet, and the ambient temperature. Further, node 2 of the equivalent circuit is the surface neighboring the air gap between the coil and the magnet. Node 28 is in contact with the inner ferromagnetic core.

4.5.3   Inner ferromagnetic core

The heat flow in the ferromagnetic core is most significant in two directions, a and c in Fig. 4.9.
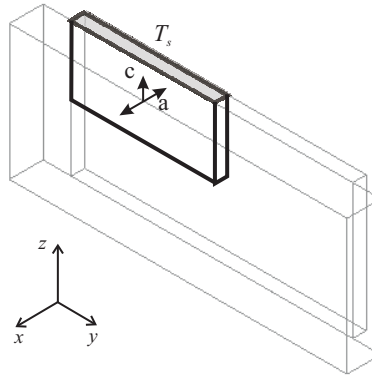
Figure 4.9: Heat flow in one-fourth of the inner ferromagnetic core.
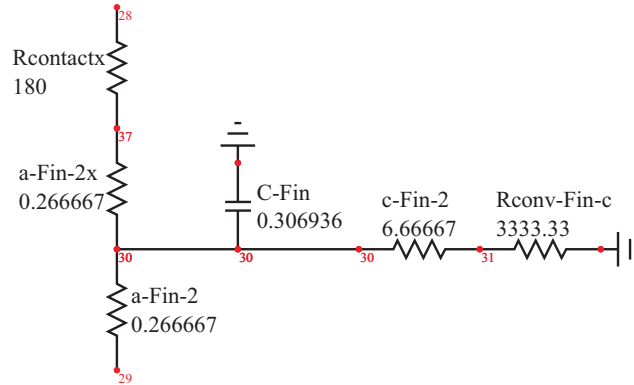
Figure 4.10: Thermal equivalent circuit of one-fourth of the inner ferromagnetic core.

The heat path in the c-direction is a combination of conduction and convection. Similarly to the case of the torque magnet, a convection resistance is connected to the top surface of the inner ferromagnetic core (node 31 in Fig. 4.10). In the a-direction a contact resistance between the torque magnet and the inner ferromagnetic core is added to the contact surfaces in node 37 (core) and 28 (torque magnet). This resistance takes into account the surface roughness and represents the temperature drop across a thin layer. This temperature drop is usually modeled by one resistance without capacitance. For a more precise model, two parallel resistances can be used, the first one representing direct contacts between the two surfaces and the second representing small cavities usually filled with air.

4.5.4 Coil

The heat produced by the coil is transferred to the surrounding air by conduction through the magnesium connection and by conduction and convection in the air gap. It is assumed that the resistance of heat transfer through the magnesium connection is lower than the resistance to the surrounding air gap. As a consequence, the temperature of the coil volume close to the magnesium connection is lower than that of the volume surrounded by air. Therefore, it is appropriate to split the coil into two parts as it is shown in Fig. 4.11. Part I of the coil is glued to the magnesium connection and part II is facing the air gap and the adiabatic plane between the coils.

The heat flow in both parts is three dimensional with internally uniform heat generation. According to [37, 38, 39], a steady-state solution of one-dimensional conduction heat transfer with uniform heat generation can be found by solving (4.12) in the following simplified form

$$\frac{\partial^2 T}{\partial x^2} = -\frac{p}{k}. \tag{4.26}$$

Then, the temperature distribution is found to be

$$T(x) = T_{s,1} + \frac{T_{s,2} - T_{s,1}}{L}x + p\left(\frac{Lx}{2k} - \frac{x^2}{2k}\right) \tag{4.27}$$

where $T_{s,1}$ and $T_{s,2}$ are the surface temperatures at $x = 0$ and $x = L$, respectively.

The average temperature can be found from the temperature distribution in (4.27) as

$$T_{av} = \frac{L^2 p}{12k} + \frac{T_{s,1} + T_{s,2}}{2}. \tag{4.28}$$

Based on this equation an equivalent circuit of the one-dimensional conduction heat flow with uniformly distributed heat generation in Fig. 4.11 can be proposed as in Fig. 4.12. The equivalent thermal resistance is defined as

$$R_0 = \frac{L}{kA}. \tag{4.29}$$

It is straightforward to deduce for the situation in Fig. 4.12 that

$$T_{s,1} - T_{s,2} = R_0\left(q_1 + \frac{1}{2}q\right), \tag{4.30}$$

where q_1 is the total heat entering the coil in a given direction and q is the total heat generated internally. Therefore, it is necessary to introduce a resistance with negative value, as shown in Fig. 4.12, in order to obtain the value of T_{av} given by (4.28) at the point of insertion of q.
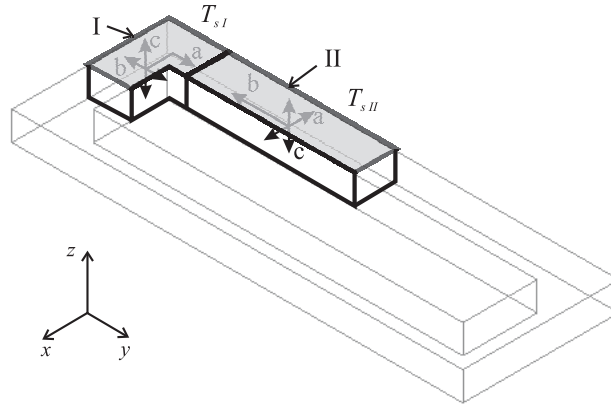
Figure 4.11: Heat flow in one fourth of the coil.
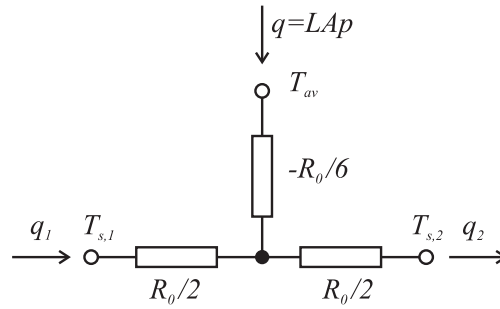
Figure 4.12: Thermal equivalent circuit of one-dimensional heat conduction with internally uniform heat generation.

Although the equivalent circuit is derived from the steady-state equation, it has been successfully applied in transient analysis [40, 41]. In these examples of transient analysis, a thermal capacitance is connected to the point with the average temperature. In the same way, the equivalent circuits of the two parts of the coil

are created by combination of the proposed equivalent circuit in Fig 4.12 with a thermal capacitance.

In part I (Fig. 4.13), node 3 is the node with the average temperature where the thermal capacitance and heat source are connected. In the c-direction of the heat flow, two resistances are added. R-glue represents the glue layer joining the magnesium connection in node 34 with the coil in node 32. The capacitance of the glue layer is neglected. Resistance Rconvxx represents the convection from the top of the coil in node 27. The heat flow in the a-direction is restricted by the adiabatic plane and, therefore, only one branch of the T-equivalent circuit is used.
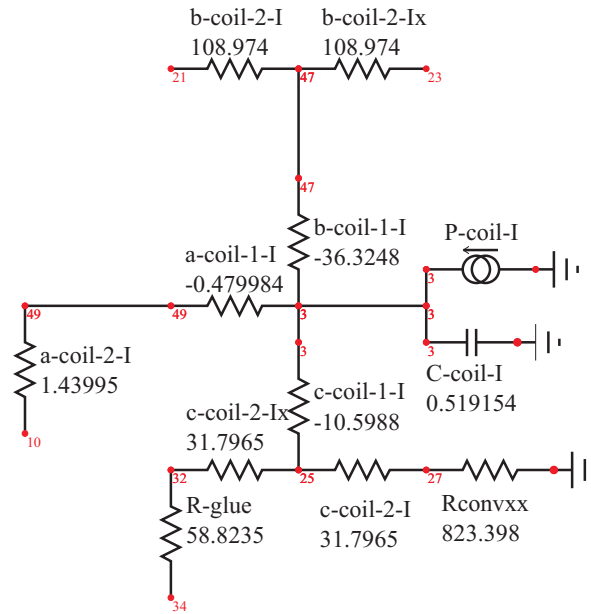
Figure 4.13: Thermal equivalent circuit of part I of the coil.

In part II (Fig. 4.14), the average temperature can be found in node 16. The heat flow in the b-direction is symmetric with respect to the adiabatic plane; so, only two resistances in series are in the flux path related to this direction. The heat flow in the b-direction of part II and in the a-direction of part I is the axial flow in the coil wires. Thus, the equivalent resistances in both directions are connected in series in node 10. Resistance Rconv-coil-c represents the convection in the c-direction from
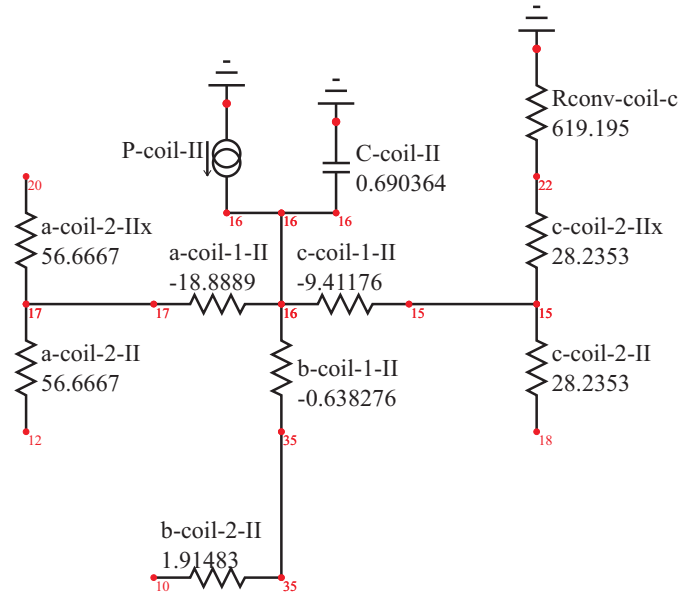
Figure 4.14: Thermal equivalent circuit of part II of the coil.

the top surface of the coil in node 22.

4.5.5   Force magnet

The heat flow in the force magnet in Fig. 4.15 has the same form as the flow in the inner ferromagnetic core (Fig. 4.10). Thus, the thermal equivalent circuit of the magnet has the same form, but with values of resistances and capacitances corresponding to the magnet material and dimensions.

Now, the average temperature of the magnet is in node 8 of the equivalent circuit in Fig. 4.16. The circuit has a contact resistance between the two touching surfaces of the magnet in node 6 and the outer ferromagnetic core in node 11. The convection from the top surface of the magnet in node 39 is in series with the heat conduction resistance in the c-direction, c-L1-2.
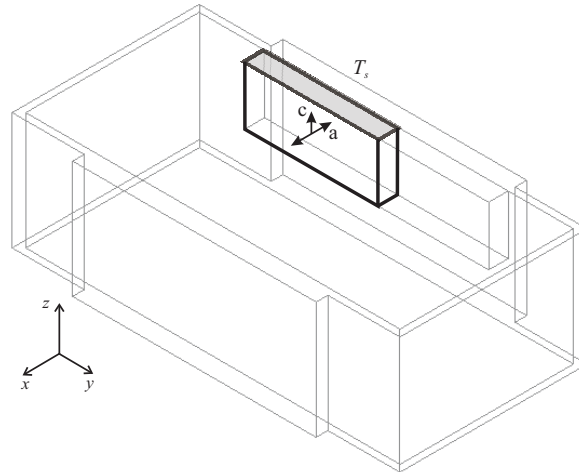
Figure 4.15: Heat flow in one half of the force magnet.
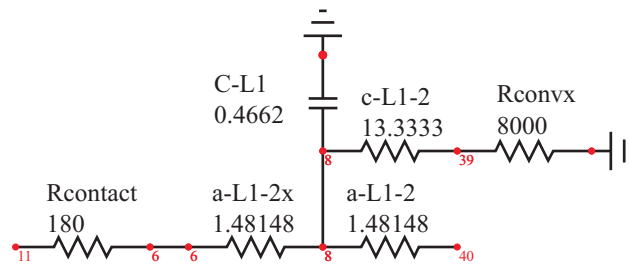
Figure 4.16: Thermal equivalent circuit of one half of the force magnet.

4.5.6   Outer ferromagnetic core

The heat flow in the vicinity of the magnesium connection creates a temperature difference in the coil, which is explained in section 4.5.4. Similarly, the influence of the magnesium connection results in a temperature difference in the outer ferromagnetic core. For this reason, the outer ferromagnetic core is split into parts I and II (Fig. 4.17).
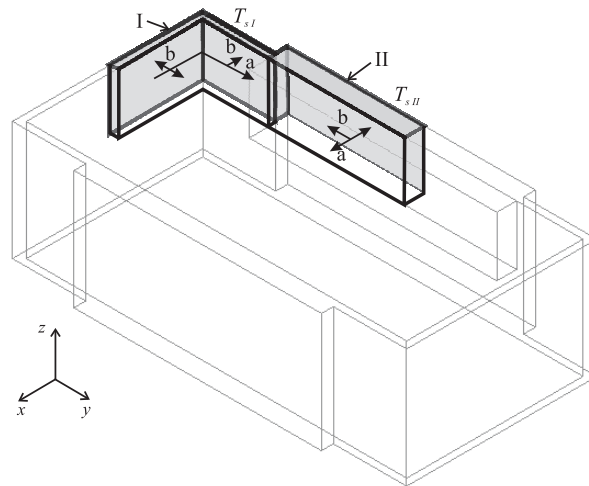
Figure 4.17: Heat flow in one-fourth of the outer ferromagnetic core (case 1).

The majority of the heat flow from part I of the coil in the vicinity of part I of the outer core is channelled through the magnesium connection, whereas the heat flow of part II of the coil is transferred through the force magnet to part II of the outer core. Therefore, the average temperature is expected to be lower in part I than in part II of the outer core.

The heat flow in the parts is considered to be two-dimensional. The heat in the a-direction of part I flows only within the core, whereas the heat flowing in the b-direction is in each place perpendicular to the a-direction heat flow. It can be seen from Fig. 4.18a that the convection resistance Rconv is in series with the b-direction resistances. It means that the convection resistance represents all outer surfaces of part I.

Similarly, the heat flow in the b-direction of part II is internal. The convection resistance in series with the a-direction resistances takes all outer surfaces of part II into account (Fig. 4.18b).

The outer ferromagnetic core can also be divided as in Fig. 4.19. Then, the values of the equivalent thermal resistances and capacitances are changed accordingly, as it is shown in Fig. 4.20.
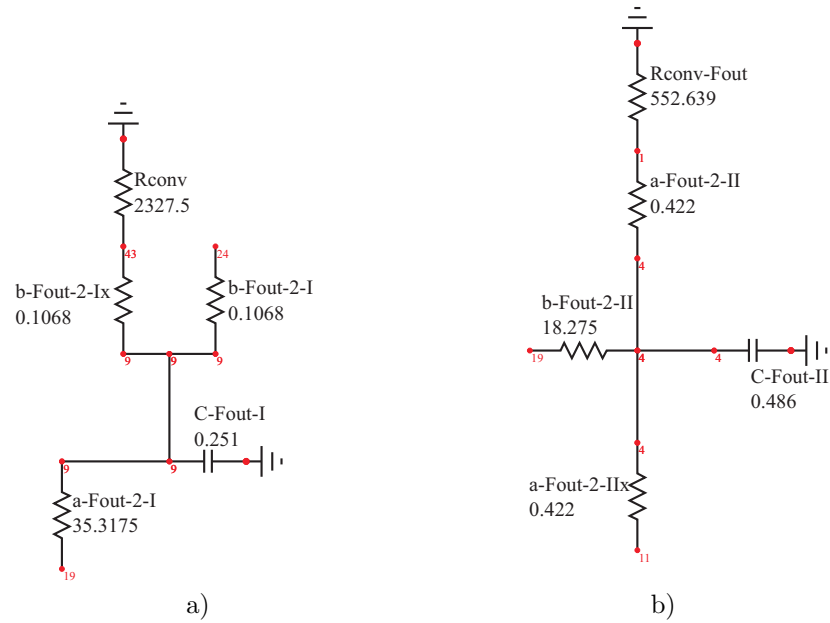
Figure 4.18: First thermal equivalent circuits of the outer ferromagnetic core a) part I, b) part II.
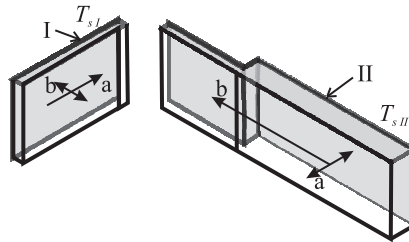
Figure 4.19: Heat flow in one fourth of the outer ferromagnetic core with different division (case 2).
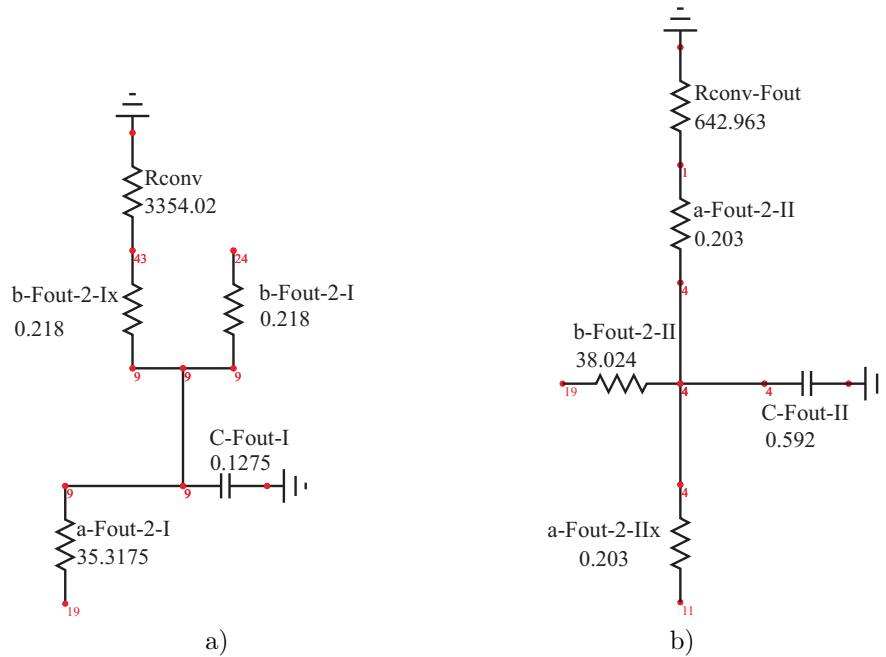
Figure 4.20: Second thermal equivalent circuits of the outer ferromagnetic core with different division a) part I, b) part II.

4.5.7   Air gap

Because the coil and the outer ferromagnetic core are divided into two parts the air gap of the actuator is also divided accordingly. Several heat flux paths through the air gap are specified. They are attached to the coil parts I and II.

The air gap heat flux paths from part I of the coil are shown in Fig. 4.21. It can be seen that the heat transfer from the top and bottom surfaces consists of convection to the surrounding air and conduction to the magnesium connection through the glue layer, respectively. These two transfers have been already included in the thermal equivalent circuit of part I of the coil (Fig. 4.13).

The other two air gap heat paths, I and II in Fig. 4.21, are included in the model. As it can be seen from Fig. 4.21 and 4.23, path I comprises the air between the coil surface (node 21) and the surface of part I of the outer ferromagnetic core
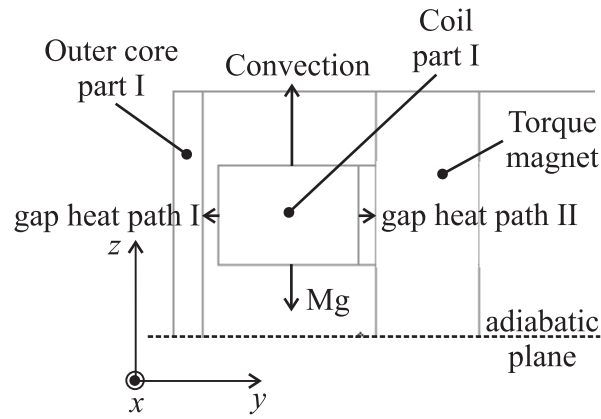
Figure 4.21: Heat flow from the coil part I in the air gap.
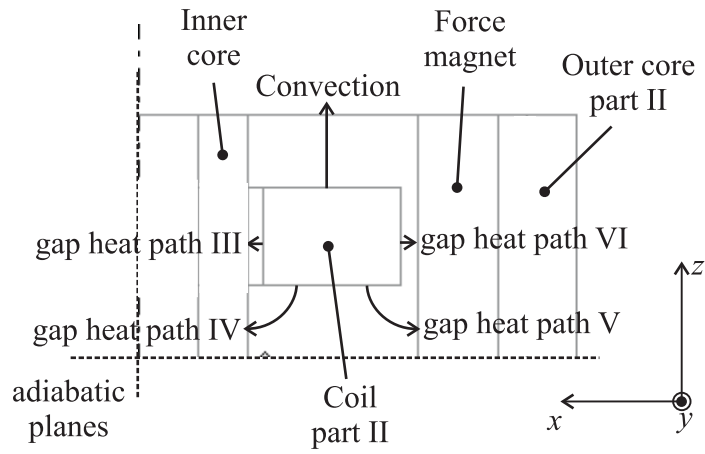
Figure 4.22: Heat flow from the coil part II in the air gap.

(node 24). Path II is the air between the coil part I surface (node 23) and the torque magnet surface (node 2). These two paths are modeled as one-dimensional conduction heat transfers through the air without internal heat generation. The rest of the air in the vicinity of the coil part I is not taken into consideration.

The heat flow from part II of the coil is more complicated than that from part I. It is caused by the fact that part II of the coil is surrounded only by air and so the heat flow is distributed more evenly in space. Consequently, five heat flux paths are identified as shown in Fig. 4.22. Aside from the convection path, the other four paths are represented in the complete thermal circuit of the actuator in Fig. 4.23 as one-dimensional conduction paths through the air without internal heat generation.

The heat flux path III comprises the air between the surface of the coil (node 12) and the surface of the force magnet (node 40). The heat flux paths IV and V begin at the bottom surface of the coil (node 18). Then, path IV ends on the surface of the inner ferromagnetic core (node 40) and path V ends at the surface of the force magnet (node 29). The last path VI represents the air between the surface of the coil (node 20) and the surface of the force magnet (node 29).

4.6   Thermal equivalent circuit of the 2-DoF actuator

A global thermal equivalent circuit of the 2-DoF actuator is shown in Fig. 4.23. As it was mentioned in section 4.4, the circuit represents one eight of the entire actuator. This is because the heat flow was considered to be symmetric about three adiabatic planes. If the symmetry is disturbed, then a number of similar circuits should be connected with each other accordingly.

In the model, two sources of heat, which represent the copper losses in part I and II of the coil, are considered. They are equal to

$$P_{cu} = \rho \cdot V_{cu} \cdot J^2, \tag{4.31}$$

where ρ is the resistivity, V_{cu} is the volume of the coil part and J is the current density.

Because a transient electromagnetic analysis is not elaborated in this thesis, eddy currents and hysteresis losses are not included in the thermal analysis. However, the losses caused by transient states could be incorporated in the thermal equivalent circuit by replacing the affected parts with equivalent circuits of one-dimensional heat conduction and uniform heat generation.
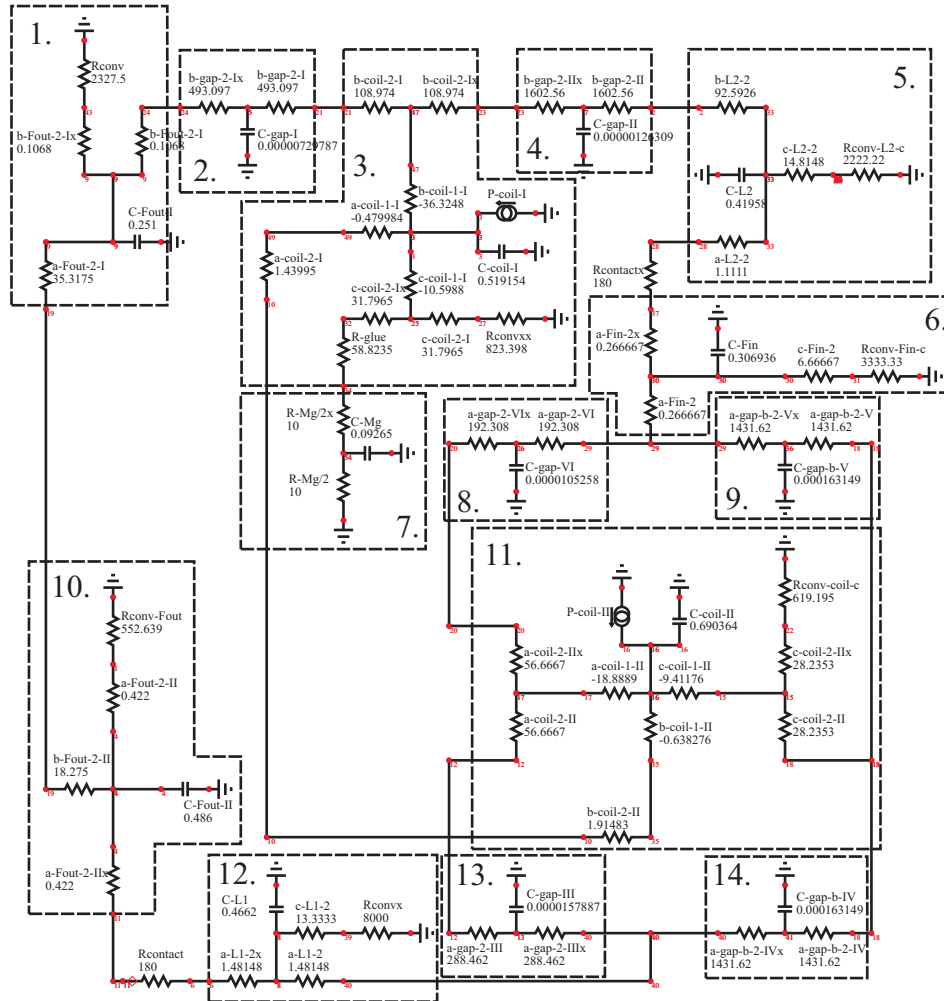
Figure 4.23: Thermal equivalent circuit of one eight of the 2-DoF actuator 1) outer ferromagnetic core part I, 2) air gap I, 3) coil part I, 4) air gap II, 5) torque magnet, 6) inner ferromagnetic core, 7) magnesium connection, 8)air gap VI, 9) air gap V, 10) outer ferromagnetic core part II, 11) coil part II, 12) force magnet, 13) air gap III, 14) air gap IV.

4.7   Simulation results

The thermal equivalent circuit in Fig. 4.23 was used to simulate the warming of the actuator starting from ambient temperature until steady-state temperatures were reached. Two different outer ferromagnetic core divisions, case 1 in Fig. 4.17 and case 2 in 4.19, were considered. The warming simulation is done at constant copper losses of $7W$ and $10W$ in the whole actuator, corresponding to a current in both coils of $1.6A$ and $2.1A$, respectively.

The average surface temperature increases of the chosen solids are illustrated in Figs. 4.24 to 4.30. The temperatures correspond to the shaded surfaces in the figures of each part shown in previous subsections. The steady-state average surface temperature rises ΔT_{av} of the actuator parts are given in Tab. 4.1.

Table 4.1: Steady-state average surface temperature rise of the actuator parts.

Power loss	$7W$		$10W$	
Part	$\Delta T_{av}\ [K]$ (case 1)	$\Delta T_{av}\ [K]$ (case 2)	$\Delta T_{av}\ [K]$ (case 1)	$\Delta T_{av}\ [K]$ (case 2)
Torque magnet	46.2	46.4	65.2	65.5
Inner ferromagnetic core	49.4	49.7	69.7	70.1
Coil part I	64.3	64.8	90.8	91.4
Coil part II	58.6	59.1	82.8	83.4
Force magnet	37.6	39.8	53.1	56.2
Outer ferromagnetic core I	31	34.2	42.6	46.7
Outer ferromagnetic core II	30.2	33.1	43.8	48.2

The highest surface temperature is found on the coil. Contrary to the initial assumption in section 4.5.4, the surface temperature of coil part I is higher than the surface temperature of coil part II. It can be explained by inaccuracies introduced by simplifications and neglecting the heat flow from the magnesium connection through the air gap into the outer ferromagnetic core.

It can also be noticed that the second highest temperatures are the ones of the inner ferromagnetic core and the torque magnet. This was expected because the inner core and torque magnet are enclosed by the coils. They have only small surfaces that are in contact with the cooling air at ambient temperature.

The simulations considering the two cases of outer core division give almost the same results except for the temperatures of the force magnet and outer ferromagnetic core. The highest difference in steady-state temperature is nearly 10% for

the outer ferromagnetic core I. The two cases will be compared with measurements in Chapter 6 and it will be shown that case 1 is closer to the reality.
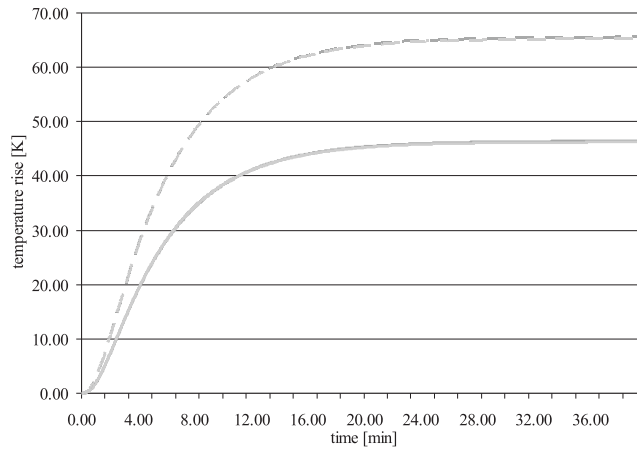
Figure 4.24: Simulated temperature rise of torque magnet (light gray - case 1, dark gray - case 2; solid - 7W, dashed - 10W).
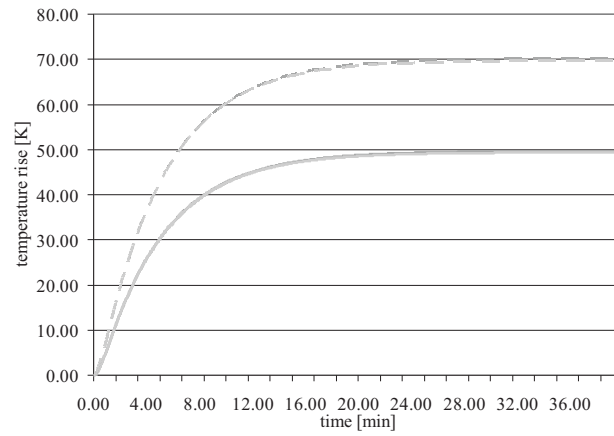
Figure 4.25: Simulated temperature rise of inner ferromagnetic core (light gray - case 1, dark gray - case 2; solid - 7W, dashed - 10W).
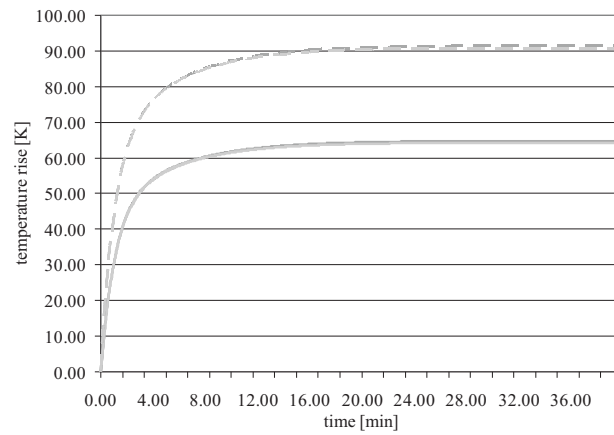
Figure 4.26: Simulated temperature rise of coil part I (light gray - case 1, dark gray - case 2; solid - 7W, dashed - 10W).
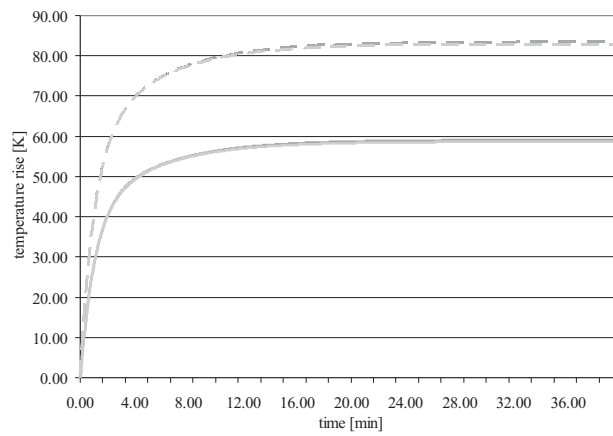
Figure 4.27: Simulated temperature rise of coil part II (light gray - case 1, dark gray - case 2; solid - 7W, dashed - 10W).
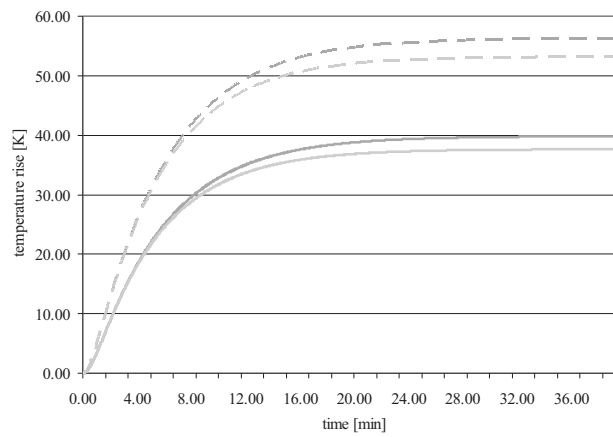
Figure 4.28: Simulated temperature rise of force magnet (light gray - case 1, dark gray - case 2; solid - 7W, dashed - 10W).
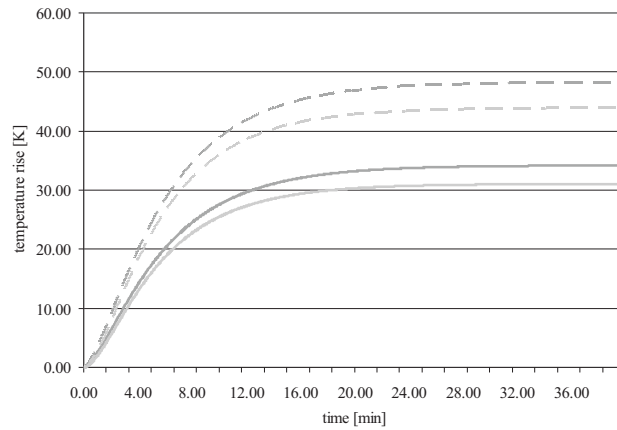
Figure 4.29: Simulated temperature rise of outer ferromagnetic core I (light gray - case 1, dark gray - case 2; solid - 7W, dashed - 10W).
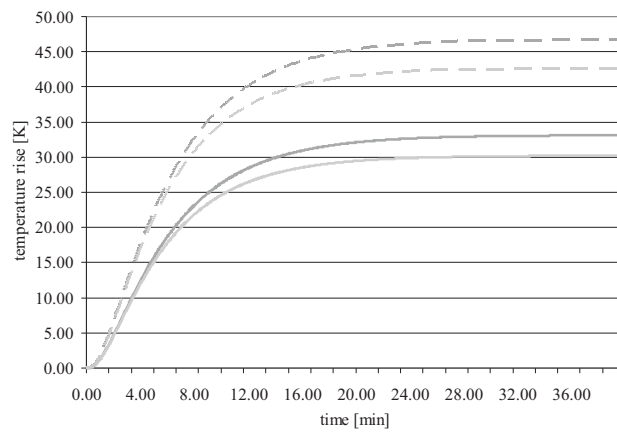
Figure 4.30: Simulated temperature rise of outer ferromagnetic core II (light gray - case 1, dark gray - case 2; solid - 7W, dashed - 10W).

The maximum temperatures reached at the operation condition of $10W$ continuous power loss and $25°C$ ambient temperature are listed in Tab. 4.2. The maximum allowed temperatures of the actuator parts are determined by the materials used. According to the demagnetization characteristic (Fig. B.1) of the magnets for $100°C$ and the average magnetic field intensity of $414kA/m$ in the magnet, the magnets do not experience the irreversible loss of magnetization. The ferromagnetic core has a Curie temperature of $950°C$, but the maximum allowed temperature of the glue, which fixes the magnets to the core, is only $185°C$. Therefore, the temperature of the glue is the limiting factor. The maximum allowed temperature of the coils is limited by the class of their insulation and that is $155°C$.

Table 4.2: Maximum reached and allowed temperatures in the actuator at $25°C$ ambient, $10W$ continuous power loss.

Part	$T_{max-reached}$ $[°C]$	$T_{max-allowed}$ $[°C]$
Torque magnet	90.5	100
Inner ferromagnetic core	95.1	185
Coil part I	116.4	155
Coil part II	108.4	155
Force magnet	81.2	100
Outer ferromagnetic core I	71.7	185
Outer ferromagnetic core II	73.2	185

It can be seen from Tab. 4.2 that the maximum reached temperatures of the actuator parts at $10W$ continuous power loss do not exceed the maximum allowed temperatures.

4.8   Conclusions

The main purpose of the thermal analysis was to find a suitable model that can describe the thermal behavior of the innovative actuator with sufficient details and accuracy. Therefore, a thermal equivalent circuit, which can describe steady states as well as transients of the 2-DoF actuator, has been presented. It consists of equivalent sub-circuits of the various constitutive elements. The sub-circuits are derived based on the expected heat flows and the shapes of these elements.

The resulting equivalent circuit is rather complex, the complexity being caused by three characteristics of the actuator:

- The relatively large air gap, where the heat transfer is not as simple as, for example, in rotary machines with an air gap of tenths of millimeters.

- The complicated shape of the actuator with only three planes of symmetry, which are used to reduce the number of elements in the circuit.

- The essentially multidimensional heat transfer in almost every part of the actuator, which cannot be simplified.

Other objectives were to evaluate the thermal operation conditions of the actuator as, for example, to determine the temperatures of the actuator parts at continuous load. The simulation results showed that under continuous operation conditions the temperature of any part of the actuator does not exceed the allowed limit.

It can be concluded that the proposed circuit describes the thermal behavior of each important part of the actuator. Thus, all key parameters for the prediction of the operation conditions can be obtained. Validation through experimental results will be given in Chapter 6.

The proposed model describes only one eight of the actuator under the assumption of symmetrical boundary conditions, but, if necessary, it can be adapted also for modeling of the actuator under asymmetrical boundary conditions. In addition, the circuit is suitable for simulations of the actuator with forced or liquid cooling where the topology of the circuit is preserved and just the affected thermal resistances should be changed.

Chapter 5

Design optimization

5.1 Introduction

Traditional machines are often designed relying on previous experience, on the basis of relations among main dimensions (e.g. diameter of rotor, active length of windings etc.) and performance requirements (e.g. angular speed, power, torque etc.). Based on the main dimensions and performance requirements, a detailed machine design is elaborated with the help of fundamental equations [42, 43, 44]. However, if a machine with a new topology has to be conceived, the first set of dimensions is normally specified from a machine with similar characteristics or even from a completely different machine or equipment. Then, according to the estimated performance, obtained by analytical models, the next set of design parameters and dimensions is chosen. This is repeated until the required performance parameters are reached. The machine obtained by this way often suffers from so-called child diseases (high mass, bad utilization of materials etc.) caused by an immature design. Drawbacks of immature designs are in general eliminated by subsequently obtained experience. The elimination of the drawbacks may even take several years.

In the case of the 2-DoF actuator, the innovative actuator topology and the combination of a number of severe requirements would make the design process, as described in the previous paragraph, time consuming and difficult. Unfortunately there is no prior knowledge that would help to determine the first or the optimal set of dimensions and design parameters. Furthermore, the actuator can be used in different applications. Consequently, the actuator will need to be designed for different specifications as various forces, torques, strokes or operation conditions.

For these reasons, it is important to propose a suitable and quicker procedure in order to find the optimal solution according to various requirements and to reduce the time of the design.

The purpose of this chapter is to establish an optimization approach to find optimal dimensions at minimal mass of the 2-DoF actuator. Thus, in the next sections, an optimization problem is stated in the form of the basic definitions of a nonlinear programming problem by introducing equations for the mass (the objective function), force and torque (the equality constraints) of the actuator. Then, with the aim to reach the objective of the optimization, input parameters and design variables are chosen. In order to meet practical manufacturability, the last step in the optimization problem formulation is the restriction of feasible regions. Arriving at the mathematically formulated optimization problem, a constrained optimization process is described. The process is based on the augmented Lagrangian penalty function in combination with the Newton method of finding minima. Finally, the solution of the process, i. e. the optimal set of the design variables, is presented and discussed.

5.2   Problem formulation

In general, an optimization problem can be stated as [45, 46]:

$$
\begin{aligned}
\text{minimize} \quad & f(\vec{x}), \\
\text{subject to} \quad & g_i(\vec{x}) \le 0, \quad \text{for } i = 1, ..., m, \\
& h_j(\vec{x}) = 0, \quad \text{for } j = 1, ..., l, \\
& \vec{x} \in X,
\end{aligned}
\tag{5.1}
$$

where $f(\vec{x})$ is the objective function, $g_i(\vec{x})$ for $i = 1, ..., m$ are called inequality constraints and $h_j(\vec{x})$ for $j = 1, ..., l$ are the equality constraints. The functions $f(\vec{x})$, $g_i(\vec{x})$ and $h_j(\vec{x})$ are defined on a nonempty feasible variable space E_n, $\vec{x}$ is a vector of n components and X is a subset of E_n.

If any of the functions in the optimization problem is nonlinear the problem defined by (5.1) is called nonlinear programming problem.

The first step in the optimization process is to identify $f(\vec{x})$, $g_i(\vec{x})$ and $h_j(\vec{x})$ as functions of design variables. As it was already mentioned, the objective of the optimization is to find dimensions of the actuator for a given force and torque at a minimum total mass of the actuator. Thus, the problem can be restated in terms

of (5.1) as

$$\text{minimize the total mass of the actuator} \quad M_{act}(\vec{x}),$$
$$\text{subject to equality constraints} \quad F_{act}(\vec{x}) - F_{req} = 0,$$
$$T_{act}(\vec{x}) - T_{req} = 0, \qquad (5.2)$$

where $M_{act}(\vec{x})$ is the total mass of the actuator as a function of design variables, $F_{act}(\vec{x})$ and $T_{act}(\vec{x})$ are the force and torque produced by the actuator as a function of design variables, F_{req} and T_{req} are the required force and torque of the actuator.

The inequality constraints are missing in (5.2), because they are not explicitly expressed in the design problem. However, they are added to the problem formulation in subsection 5.2.6.

5.2.1   Objective function

The problem (5.2) is a direct translation of the design assignment. It can be seen from (5.1) and (5.2) that the objective function is

$$f(\vec{x}) = M_{act}(\vec{x}) = M_{cu}(\vec{x}) + M_{PM}(\vec{x}) + M_{Fe}(\vec{x}), \qquad (5.3)$$

where $M_{cu}(\vec{x})$ is the mass of coils, $M_{PM}(\vec{x})$ is the mass of all magnets, $M_{Fe}(\vec{x})$ is the mass of the ferromagnetic core. The functions $M_{cu}(\vec{x})$, $M_{PM}(\vec{x})$ and $M_{Fe}(\vec{x})$ are basically products of the volume of the particular material and its mass density. It should be noted that the mass of the magnesium connections as well as the mass of the glue used to assemble the actuator are not considered in the objective function, due to their very small contribution to the total mass.

5.2.2   Equality constraints

The equality constraints in the optimization problem consist of the following functions:

$$h_1(\vec{x}) = F_{act}(\vec{x}) - F_{req}, \qquad (5.4)$$
$$h_2(\vec{x}) = T_{act}(\vec{x}) - T_{req}. \qquad (5.5)$$

The force $F_{act}(\vec{x})$ is derived from (3.35) and (3.68), thus, it can be written as

$$F_{act}(\vec{x}) = J(\vec{x}) \cdot B_{\mathcal{R}_{12}}(\vec{x}) \cdot V_{\mathcal{R}_{12}}(\vec{x}), \qquad (5.6)$$

where the scalar J is the coil current density, $B_{\mathcal{R}_{12}}$ is the magnetic field density in the flux tubes related to the reluctances $\mathcal{R}_1$ and $\mathcal{R}_2$ (see Fig. 3.18), and $V_{\mathcal{R}_{12}}$ is the volume of the coils crossing the flux tubes related to the reluctances $\mathcal{R}_1$ and $\mathcal{R}_2$.

The torque $T_{act}(\vec{x})$ is obtained from (3.55), (3.56) and (3.69):

$$T_{act}(\vec{x}) = r(\vec{x}) \cdot J(\vec{x}) \cdot (B_{T1a}(\vec{x}) \cdot V_{T1a}(\vec{x}) + B_{T1c}(\vec{x}) \cdot V_{T1c}(\vec{x})), \qquad (5.7)$$

where $r(\vec{x})$ is the average length of the torque arm, $B_{T1a}(\vec{x})$ and $B_{T1c}(\vec{x})$ are the magnetic flux densities in the flux tubes related to the reluctances $\mathcal{R}_{T1a}$ and $\mathcal{R}_{T1c}$ (see Fig. 3.19), respectively, and finally, $V_{T1a}(\vec{x})$ and $V_{T1c}(\vec{x})$ are the volumes of the coils crossing the flux tubes related to the reluctances $\mathcal{R}_{T1a}$ and $\mathcal{R}_{T1c}$, respectively.

5.2.3   Design variables

At this place, it is important to explain the meaning of optimization variables and parameters. An optimization variable is a symbol or name that represents a value. During an optimization process the value of the variable is changing.

An optimization parameter is also a symbol that defines a value, but once chosen, the value of the parameter is kept constant during an optimization process.

The vector $\vec{x}$ represents a set of design variables. In the broader sense, variables can be

- materials and their physical properties,

- material distribution,

- geometrical dimensions.

Materials are usually chosen according to the requirements of a particular design, e.g. low price, low mass etc. When the materials are selected, their physical properties are constant during an optimization procedure. They are usually considered as input parameters, which can be changed based on possible trade-offs, as for example, low quality material-low price. Consequently, the physical properties can be varied in discrete steps.

If the material distribution is a design variable the respective optimization problem is called topology optimization [47]. The topology optimization tries to find an optimal distribution of materials. This kind of optimization allows for change of a topology, which would evolve during an optimization process as in a somewhat simplified example shown in Fig. 5.1.

Because the topology of the 2-DoF actuator is chosen, the optimization described in this chapter is related to shape optimization [48, 49, 50]. Therefore, the design variables are geometrical dimensions.

The subject of the input parameters and the design variables and their choice is treated in the following two subsections.
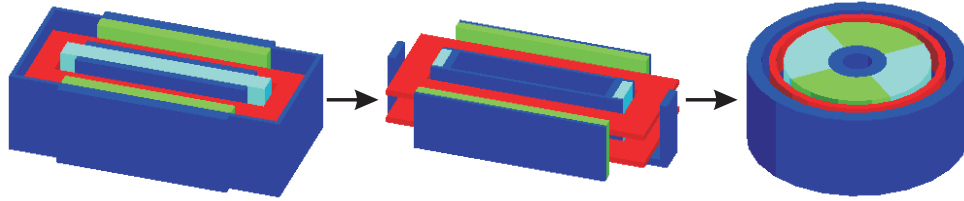
Figure 5.1: Possible evolution of topology optimization of the 2-DoF actuator.

5.2.4 Input parameters

Optimization input parameters can be divided into three groups related to

- performance,

- geometry,

- materials.

Performance parameters

Performance parameters or requirements of voice coil actuators can be defined as basic and application related. The basic requirements arise from the functions of the actuator:

- force, torque,

- longitudinal stroke, angular stroke,

where the force and torque are important for the required dynamics of a mechanical structure driven by the actuator, which must be reached over a certain longitudinal or angular stroke.

The application related requirements can be very different, but for precision technology applications, they can be reduced to more specific ones:

- position dependency of force/torque characteristics,

- power dissipation,

- parasitic forces,

- moving and static mass,

- mechanical damping.

The position dependency of force/torque characteristics influences the complexity of the actuator control algorithm and the dissipative power production in the coils. If the characteristics are almost constant, then the model of the actuator can be considered as linear and therefore does not require high effort to implement a control algorithm. Consequently, the control algorithm needs low computational power and the control accuracy is relatively high.

There is also a relation between the position dependency of the force/torque characteristics and the power dissipation in the coils of an actuator. As it can be seen from typical force characteristics of a voice coil actuator in Fig. 5.2, it is necessary to apply different currents ($I_1 < I_2$) to produce the same force at two different positions p_1 and p_2 of the actuator coil with respect to its field assembly. Because the power dissipation in the coils is proportional to the square of the coil current the dissipation in p_2 is higher than in p_1. It also means that an actuator
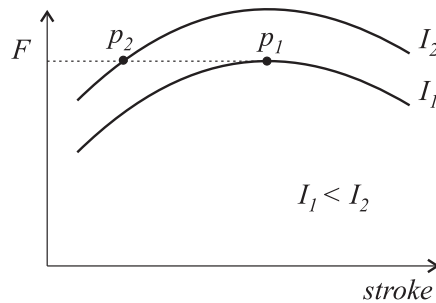
Figure 5.2: Typical force characteristics of voice-coil actuator at different coil currents.

with a force-stroke characteristic as flat as possible produces less dissipation than an actuator of which the force-stroke characteristic is highly dependent on the stroke.

The parasitic forces can be of different nature, for example, reluctance or Lorentz forces, but they have the same attributes. They are hard to compensate for and they can induce unwanted deformations and vibrations in mechanical components.

Although the problem of the mass of actuators was already several times addressed in this thesis, it can be added that the total mass of the actuator is not always strongly interconnected with the dynamics of the mechanical system. This

is the case when the concept of the drive system is one-stroke, where only a moving mass influences the dynamics. However, precision positioning systems are often based on a two-stroke concept (a coarse precision drive with a fine precision drive on top of it). That means that the total mass of the fine precision drive affects the design of the coarse drive and therefore, the total mass of the fine precision drive should be kept minimal.

Mechanical damping in an actuator means the interaction between the moving and electrically conductive part and the stationary magnetic field, or vice-versa. The interaction causes power dissipation as a consequence of eddy currents. This effect is very similar to a mechanical damping.

Table 5.1: Performance requirements of the 2-DoF actuator.

Continuous force	1.5	N/per coil
Continuous torque	0.005	Nm/per coil
Longitudinal stroke	4	mm
Angular stroke	$1 - 10$	°
Maximum temperature of coils	150	$°C$
Total mass of the actuator	to be minimized	

All performance parameters imposed on the 2-DoF actuator are shown in Tab. 5.1. The rest of the previously discussed requirements, which is not mentioned in this table, are not explicitly included in the optimization problem.

Geometry parameters

The maximum dimensions of the actuator can be considered as the geometry parameters. They are determined according to the available space of a machine wherein the actuator is placed. The maximum dimensions of the 2-DoF actuator were not specified, but the vector of design variables (see section 5.2.5) is confined to certain intervals. The minimum values of the intervals are defined by the minimum dimensions of commercially available permanent magnets and diameters of copper wires. For instance, the standard diameter of the copper wire determines the filling factor of the coil. Therefore, the minimum dimension of the coil cross-section is chosen according to the selected diameter of the coil wire, and the corresponding filling coefficient is calculated. Together, they are used as geometry parameters.

The maximum values are set empirically in order to avoid investigation of a large feasibility region, which would cost more time. The intervals assigned to the

design variables are incorporated into the mathematical formulation of the optimization problem as inequality constraints (see section 5.2.6).

There are also dimensions that are limited by tolerances of the actuator parts. These tolerances are given by the production technology of the separate parts. The most important tolerance is the clearance between the coil and the field assembly. The coils of the actuator were produced with a tolerance of the inner and outer dimensions of 0.02 mm and 0.1 mm, respectively. The clearance between the coils and field assembly should also contain the space needed for the required angular stroke. The selected geometry parameters are listed in Tab. 5.2.

Table 5.2: Geometry parameters of the 2-DoF actuator (for the dimensions see also Fig. 5.3).

Min/Max coil dimensions		
d_{cu}	0.3/3.5	mm/mm
h_{cu}	0.3/20	mm/mm
Min/Max permanent magnets dimensions		
L_1	1.6/50	mm/mm
w_1	1/10	mm/mm
L_2	1/50	mm/mm
Minimal clearance of coils	0.4	mm

Material parameters

As mentioned in subsection 5.2.3, the input parameters related to materials are connected to the design requirements and certain design trade-offs. The choice of materials for

- magnets,

- ferromagnetic cores,

- coils,

- coils holders (magnesium connections),

- binding material,

complies with the low mass requirement of the 2-DoF actuator, which is considered as the most important one.

The trade-off in case of the magnets is among mass density - operation temperature - irreversible demagnetization level - level of remanent magnetism. The mass density of different permanent-magnet materials is in the range from $3700 kg/m^3$ for plastic-bonded hard ferrite to $8300 kg/m^3$ for samarium-cobalt. The lightest plastic-bonded hard ferrite has a very low remanence, around $0.26T$, that would result in large magnets. The heavy samarium-cobalt has a remanence of $1.05T$ and can operate in temperatures up to $300°C$. Because such high temperatures do not appear in precision technology drives, NdFeB magnets with a lower operation temperature range $(80 - 160°C)$ and higher B_r (1.08-1.47 T) have been selected (see Tab. B.1).

The ferromagnetic cores can be made of a wide range of steels with small differences in the mass density $(7870 - 8130 kg/m^3)$. Therefore, the most significant property of the ferromagnetic steels is the magnetic-saturation level. The steel with the highest saturation level $(2.1 - 2.35T)$ at low coercivity $(800 - 2400 A/m)$ is cobalt-iron (49Co-Fe-1.9V).

The coils are the moving part of the actuator. They are moving in air and they should produce as less power dissipation as possible to avoid thermal deformations and irreversible thermal demagnetization of the magnets. Thus, the material of the actuator coils is chosen by evaluating mass density - electrical conductivity - thermal conductivity. Copper, which is used for the 2-DoF actuator, is the mostly used coil material. Although copper is three times heavier than aluminium, it has about two times higher thermal and 1.6 times better electrical conductivity.

The coil holders material is applied on the moving part, so, it needs to have a low mass, which will result in a small inertia. Because the coils are surrounded by air, which is a good thermal isolator, the coil holders should have a high thermal conductivity. If so, the holders can significantly improve the heat transfer from the coil to the cooling system and, consequently, they can increase the continuous force and torque of the actuator. Last but not least, the holders are closest to the coils and, therefore, they are exposed to a changing magnetic field, which causes eddy currents. A suitable (but not the only) material of the coil holders is magnesium. Magnesium is an electrical conductor but its conductivity is lower than that of aluminium. Despite this fact, it is very light and it has a high thermal conductivity of $156 W/m \cdot K$. For this reason, but also due to its non-ferromagnetic property, magnesium is selected for the coil assembly.

The last material in the actuator is glue, which is the bonding material. The mass of the glue is only a fraction of the total actuator mass, so, it is neglected in the optimization. However, it should be strong enough and should sustain high

temperature. For this purpose, a glue with a strength of $22N/mm^2$ and a maximum temperature of $180°C$ is used.

The material parameters are listed in Appendix B.

5.2.5   Geometrical variables

The choice of the geometrical dimensions of the actuator as the design variables is dependent on the optimization problem formulation. From (5.2), the total mass, force and torque of the actuator should be expressed as functions of the geometrical dimensions. This can be done by several different linearly independent dimensions. In other words, there exists a set of linearly independent dimensions and the rest of the dimensions can be expressed as linear functions of the linearly independent dimensions.

The central equation for the selection of the design-variables $\vec{x}$, in this case geometrical dimensions, is the Lorentz equation:

$$\vec{F} = \int_V \vec{J} \times \vec{B}\mathrm{d}V. \tag{5.8}$$

The terms $\vec{J}$ and $\mathrm{d}V$ of the equation are related to the current source and the dimensions of the source, respectively. $\vec{B}$ is related to the magnetic field created by the permanent magnets of the 2-DoF actuator. For this reason, the design variables are the dimensions of the coils and of the permanent magnets of the actuator.

Starting with the permanent magnets, the force magnet is defined by the length L_1, width w_1 and height h_1. If the smallest mass of the force magnets and related ferromagnetic core needs to be reached and L_1 and w_1 are chosen as independent variables, then h_1 is determined as:

$$h_1 = st_{act} + h_{cu}, \tag{5.9}$$

where st_{act} is the stroke of the actuator and h_{cu} is the height of the coil (see Fig. 5.3). In this way, the height h_1 is the smallest needed to reach the required longitudinal stroke. Consequently, the mass of the force magnets and related ferromagnetic core will always be the smallest.

Similarly, the torque magnet is defined by L_2, w_2 and h_2, i.e. the length, width and height, respectively. Again, if the mass of the torque magnet and its ferromagnetic core should be the smallest possible and considering L_2 as independent variable, then the width of the magnet is determined as

$$w_2 = L_1 + 2d_{cu}, \tag{5.10}$$

where d_{cu} is the width of the coil. The height of the torque magnet is obtained by analogy with (5.9) remembering that the magnet accommodates two coils, thus,

$$h_2 = 2 \cdot (st_{act} + h_{cu}). \tag{5.11}$$
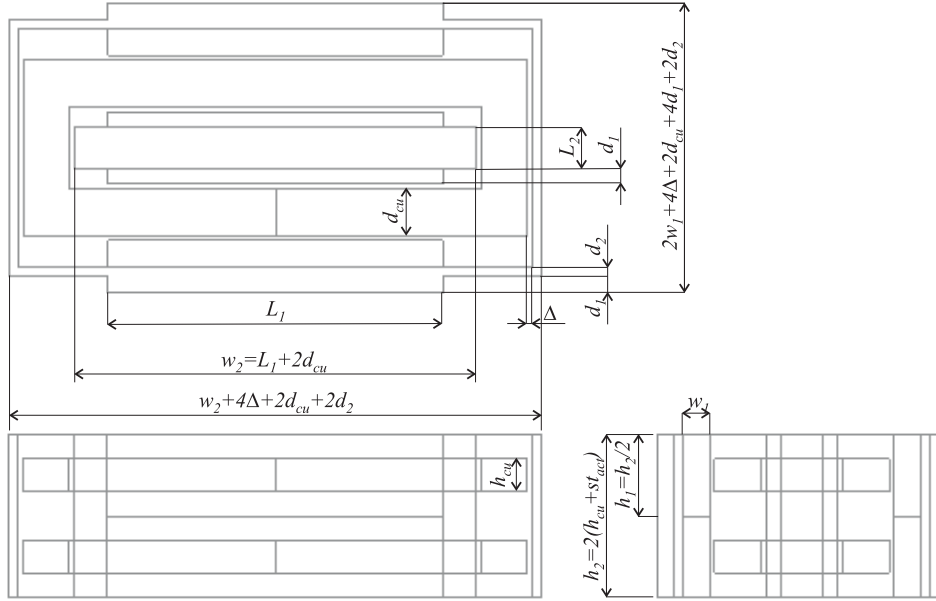
Figure 5.3: Dimensions of the 2-DoF actuator (see also Figs. 3.2 and 3.5).

The equations (5.9) and (5.11) express the topology of the actuator with long magnets and short coils. In other words, the magnets cover the height of the coils and the stroke. This configuration ensures less power dissipation in the coils than the inverted configuration with long coils and short magnets. Here, the priority was given to the requirement of minimal heat production and low mass of the moving coil assembly rather than to the requirement of low total mass, because, in general, the field assembly is heavier than the coil assembly. This choice is also supported by the fact that at the required force and torque of the actuator with short magnets and long coils the ferromagnetic core would have even smaller thickness than in the configuration with long magnets and short coils. This would make the mechanical

structure of the ferromagnetic core more flexible and apt to vibrations, and thus, making the actuator a source of disturbances.

Based on the previous discussions, the vector of the independent design variables is

$$\vec{x} = [L_1, L_2, w_1, d_{cu}, h_{cu}] \tag{5.12}$$

and all remaining dimensions can be obtained as a linear combination of $\vec{x}$. The relations among the independent design variables and the remaining dimensions are quite straightforward, and are shown in Fig. 5.3.

5.2.6   Inequality constraints

The inequality constraints do not arise directly from the definition of the optimization problem, but there are also reasons to restrict the feasible variable space related to the optimization problem.

A reason to restrict the feasible variable space is that the function $M_{act}(\vec{x})$ does not have a physical representation for its negative objective value. That means that each design variable should be at least equal to zero or a positive real number. This implies that the feasible variable space is constrained by imposing single-sided inequality constraints to each component of the design variable vector.

The form of the inequality constraints is influenced by the considerations as discussed in subsection 5.2.4. The optimal dimensions (e.g. of permanent magnets and coil wires available on the market) do have a positive minimal value. Therefore, the minimum of the design variables is not assigned zero but the minimum dimension available on the market.

Because the optimized actuator will have finite dimensions, it is not necessary to investigate the whole variable space of positive real numbers. Consequently, an upper boundary of the design variable is also determined.

The restriction of the feasible variable space by minimal and maximal values of the design variable vector results in several double-sided inequalities. Since the vector of design variables is

$$\vec{x} = [L_1, L_2, w_1, d_{cu}, h_{cu}],$$

five double-sided inequalities are incorporated in the optimization as ten single-sided

inequalities:

$$L_{1min} \leq L_1 \leq L_{1max} \Rightarrow \begin{cases} g_1(L_1) = L_{1min} - L_1, \\ g_2(L_1) = L_1 - L_{1max}, \end{cases} \tag{5.13}$$

$$L_{2min} \leq L_2 \leq L_{2max} \Rightarrow \begin{cases} g_3(L_2) = L_{2min} - L_2, \\ g_4(L_2) = L_2 - L_{2max}, \end{cases} \tag{5.14}$$

$$w_{1min} \leq w_1 \leq w_{1max} \Rightarrow \begin{cases} g_5(w_1) = w_{1min} - w_1, \\ g_6(w_1) = w_1 - w_{1max}, \end{cases} \tag{5.15}$$

$$d_{cumin} \leq d_{cu} \leq d_{cumax} \Rightarrow \begin{cases} g_7(d_{cu}) = d_{cumin} - d_{cu}, \\ g_8(d_{cu}) = d_{cu} - d_{cumax}, \end{cases} \tag{5.16}$$

$$h_{cumin} \leq h_{cu} \leq h_{cumax} \Rightarrow \begin{cases} g_9(h_{cu}) = h_{cumin} - h_{cu}, \\ g_{10}(h_{cu}) = h_{cu} - h_{cumax}. \end{cases}$$

By specifying the inequality constraints, the mathematical formulation of the optimization problem is completed. In the following section, subjects related to the minimization of the optimization problem are treated.

5.3 Optimization approach

The optimization of the 2-DoF actuator is formulated as a nonlinear constrained optimization problem in section 5.2. The solution to this problem can be found by various approaches. The approach chosen to optimize the actuator in the constrained variable space is based on the optimization of a sequence of unconstrained problems. This sequence is defined as a sequence of penalized unconstrained problems. Each unconstrained problem contains penalty functions, specified by the use of the equality and inequality constraints, and penalty parameters also called Lagrange multipliers.

Because an unconstrained problem is the core of the approach, optimality conditions of the unconstrained optimization are discussed in the following two subsections.

5.3.1 Optimality conditions of unconstrained problems

In the first place, the term minimum should be defined. In general, local and global minima of an unconstrained problem are known. The vector $\vec{x}^*$ is an unconstrained local minimum of the function $f(\vec{x})$ if

$$f(\vec{x}^*) \leq f(\vec{x}), \quad \forall \vec{x} \text{ with } \|\vec{x} - \vec{x}^*\| < \epsilon, \tag{5.17}$$

where $\epsilon > 0$.

The vector $\vec{x}^*$ is an unconstrained global minimum of the function $f(\vec{x})$ if

$$f(\vec{x}^*) \leq f(\vec{x}), \quad \forall \vec{x} \in E_n. \tag{5.18}$$

If $\vec{x} \neq \vec{x}^*$ and the two inequalities are valid, then $\vec{x}^*$ is said to be a strict local or global minimum, respectively (see Fig. 5.4).
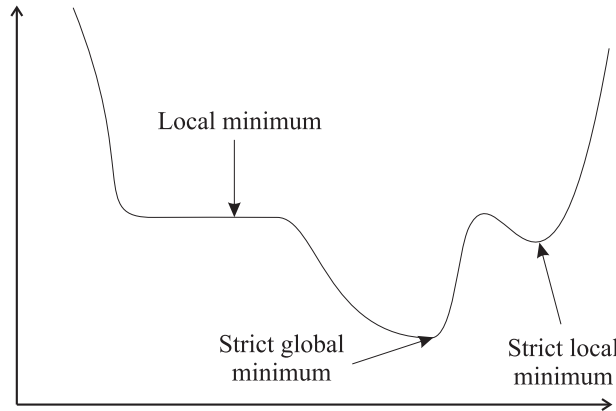
Figure 5.4: Minima of a function.

In contrast to the unconstrained minimum, a constrained local or global minimum is related to a constrained problem, as in (5.2). They are similarly defined as in (5.17) and (5.18), but the function $f(\vec{x})$ is defined over $X \subset E_n$. Thus, $\vec{x}^* \in X$.

Two important properties are associated with the unconstrained minimum of an objective function. First, if the objective function $f(\vec{x})$ is continuously differentiable in an open set containing $\vec{x}^*$, then $f(\vec{x}^*)$ in a minimum satisfies the condition:

$$\nabla f(\vec{x}^*) = 0. \tag{5.19}$$

Because the condition above uses the first partial derivatives, it is called a first-order optimality condition. However, this condition is necessary but not sufficient for the optimality, because it holds for minimum, maximum and inflection points as well.

Secondly, if the function $f(\vec{x})$ is twice continuously differentiable, then for $f(\vec{x}^*)$ also holds that

$$\nabla^2 f(\vec{x}^*) \geq 0, \tag{5.20}$$

in other words, the second partial derivative of the function is a positive semidefinite matrix. This condition is called a second-order optimality condition and it is also the only necessary condition for optimality.

In the case of a convex function $f(\vec{x})$, conditions (5.19) and (5.20) become first- and second-order sufficient conditions of the optimality, respectively. The reason is that every local minimum of a convex function is also a global minimum. It can also be mentioned that if the second partial derivative of the function is a positive definite matrix

$$\nabla^2 f(\vec{x}^*) > 0, \tag{5.21}$$

then the vector $\vec{x}^*$ is a strict global minimum.

The optimality conditions (5.19) and (5.20) are fundamental for finding optimal solutions of optimization problems. The most basic way to use the conditions is to find all points that satisfy the first-order necessary conditions. If the investigated function is not convex, the second-order necessary condition is used to test all points, which satisfy the first-order necessary condition. The points that satisfy the first and second conditions are local minima. Finally, the local minima can be evaluated by condition (5.21) to find out whether they are strict local minima.

5.3.2   Existence of optimal solutions

A very important issue in optimization is the existence of the optimal solution. In many cases a function $f(\vec{x})$ does not have to have an extreme value. Thus, it is also important to find out whether the function of the total mass of the 2-DoF actuator has a minimum.

It can be done by Weierstrass' theorem [46] that states that if a function $f(\vec{x})$ is continuous on a closed set X, then $f(\vec{x})$ has both a maximum and a minimum on X. If $f(\vec{x})$ has an extreme value on an open set X, then the extreme value occurs at a critical point. In other words, an extreme point (i.e. maximum or minimum) of the continuous function $f(\vec{x})$ on X always exists if the feasible space X is nonempty, closed and bounded.

Thus, by using Weierstrass' theorem, the existence of the minimum solution can be claimed just on the basis of inequality constraints and continuity of $M_{act}(\vec{x})$. Therefore, the minimum of the total mass of the 2-DoF actuator exists because the feasible space X of the problem defined by the inequality constraints mentioned in section 5.2.6, is nonempty, closed and bounded.

5.3.3   Optimality conditions of constrained problems

The optimality conditions of a constrained problem can also be classified, as discussed in subsection 5.3.1, according to first- and second-order partial derivatives. Further, the conditions can be necessary or sufficient according to the convexity assumptions that are made. Thus, the first-order necessary condition, also called Karush-Khun-Tucker (KKT) necessary condition, states that if a feasible solution $\vec{x}^*$ solves the problem [45, 46]

$$\begin{aligned}
&\text{minimize } f(\vec{x}), \\
&\text{subject to } g_i(\vec{x}) \leq 0, \text{ for } i = 1, \ldots, m, \\
&\qquad\qquad h_j(\vec{x}) = 0 \text{ for } j = 1, \ldots, l, \\
&\qquad\qquad \vec{x} \in X,
\end{aligned} \qquad (5.22)$$

locally, then unique scalars u_i for $i \in I$ and v_j for $j = 1, \ldots, l$, called Lagrange multipliers, exist such that

$$\nabla f(\vec{x}^*) + \sum_{i \in I} u_i \nabla g_i(\vec{x}^*) + \sum_{j=1}^{l} v_j \nabla h_j(\vec{x}^*) = 0$$

$$u_i \geq 0, \text{ for } i \in I. \qquad (5.23)$$

This holds under the following conditions:

   X is a nonempty open set in E_n

   $f(\vec{x}) : E_n \rightarrow E_1$, $g_i(\vec{x}) : E_n \rightarrow E_1$ for $i = 1, \ldots, m$, $h_j(\vec{x}) : E_n \rightarrow E_1$ for $j = 1, \ldots, l$,

   $I = \{i : g_i(\vec{x}^*) = 0\}$, $f(\vec{x}^*)$ and $g_i(\vec{x}^*)$ for $i \in I$ are differentiable,

   each $g_i(\vec{x}^*)$ for $i \notin I$ is continuous, each $h_j(\vec{x}^*)$ for $j = 1, \ldots, l$ is continuously differentiable

   $\nabla g_i(\vec{x}^*)$ for $i \in I$ and $\nabla h_j(\vec{x}^*)$ are linearly independent.

   The KKT condition can also be written in the following form

$$\nabla f(\vec{x}^*) + \sum_{i=1}^{m} u_i \nabla g_i(\vec{x}^*) + \sum_{j=1}^{l} v_j \nabla h_j(\vec{x}^*) = 0$$

$$u_i g_i(\vec{x}^*) = 0, \text{ for } i = 1, \ldots, m$$

$$u_i \geq 0, \text{ for } i = 1, \ldots, m, \qquad (5.24)$$

if the condition,

$g_i(\vec{x}^*)$ for $i \notin I$ is differentiable,

is valid in addition to the previous assumptions.

The KKT sufficient condition shows that there exist scalars $u_i^* \geq 0$ for $i \in I$ and v_j^* for $j = 1, \ldots, l$ such that

$$\nabla f(\vec{x}^*) + \sum_{i \in I} u_i^* \nabla g_i(\vec{x}^*) + \sum_{j=1}^{l} v_j^* \nabla h_j(\vec{x}^*) = 0 \tag{5.25}$$

Then, $\vec{x}^*$ is a global optimal solution to problem (5.22) and the KKT necessary conditions (5.23) with the related assumptions hold. Further, $J = \{j : v_j^* > 0\}$ and $K = \{j : v_j^* < 0\}$, $f(\vec{x}^*)$ is pseudoconvex, $g_i(\vec{x}^*)$ is quasiconvex for $i \in I$, $h_j(\vec{x}^*)$ is quasiconvex for $j \in J$ and $h_j(\vec{x}^*)$ is quasiconcave $j \in K$.

The general convexity assumptions on the objective and constraint functions hold very rarely. But, if they hold in a small vicinity of $\vec{x}^*$, then $\vec{x}^*$ is a local minimum of the problem (5.22).

Similar to the evaluation of the unconstrained problem optimality, where the convexity of functions is hard to proof, the constrained problem optimality can be evaluated against the first-order necessary condition for constrained problems in order to find extreme points. Then, the points identified by the first-order condition are checked against the second-order condition. As a result, the points are classified as local minimum, local maximum or saddle point.

The KKT second-order necessary condition considers the optimization problem defined by (5.22), where the objective and constraint functions are twice-differentiable, X is a nonempty open set in E_n. Define $I = \{i : g_i(\vec{x}^*) = 0\}$, a restricted Lagrangian function

$$L(\vec{x}) = f(\vec{x}) + \sum_{i \in I} u_i^* g_i(\vec{x}) + \sum_{i=1}^{l} v_j^* h_j(\vec{x}) \tag{5.26}$$

and its Hessian at $\vec{x}^*$

$$\nabla^2 L(\vec{x}^*) = \nabla^2 f(\vec{x}^*) + \sum_{i \in I} u_i^* \nabla^2 g_i(\vec{x}^*) + \sum_{i=1}^{l} v_j^* \nabla^2 h_j(\vec{x}^*), \tag{5.27}$$

where $\nabla^2 f(\vec{x}^*)$, $\nabla^2 g_i(\vec{x}^*)$ and $\nabla^2 h_j(\vec{x}^*)$ are Hessians of $f(\vec{x}^*)$, $g_i(\vec{x}^*)$ for $i \in I$ and $h_j(\vec{x}^*)$ for $j = 1, \ldots, l$, respectively, and $g_i(\vec{x}^*)$ for $i \in I$ and $h_j(\vec{x}^*)$ for $j = 1, \ldots, l$ are linearly independent. If $\vec{x}^*$ is a KKT point (i.e. a point that complies with the first-order necessary KKT condition), then [45, 46]

$$\vec{d}^t \nabla^2 L(\vec{x}^*) \vec{d} \geq 0, \tag{5.28}$$

where $\vec{d}$ is the descent direction (and $\vec{d}^t$ denotes the transposed vector), for $\vec{d} \in C'$ with

$$C' = \{\vec{d} \neq 0 : \nabla g_i(\vec{x}^*)^t \vec{d} \leq 0 \text{ for all } i \in I,$$
$$\nabla h_j(\vec{x}^*)^t \vec{d} = 0 \text{ for all } j = 1, \ldots, l\}. \tag{5.29}$$

In order to verify the KKT second-order sufficient conditions, consider the problem defined by (5.22), where the objective and constraint functions are twice-differentiable, X is a nonempty open set in E_n. Further, $\vec{x}^*$ is a KKT point, $I = \{i : g_i(\vec{x}^*)\} = 0$, $I^+ = \{i \in I : g_i(u_i^*)\} > 0$, and $I^0 = \{i \in I : g_i(u_i^*)\} = 0$. The restricted Lagrangian function $L(\vec{x}^*)$ and its Hessian are defined by (5.26) and (5.27), respectively. Then, if

$$\vec{d}^t \nabla^2 L(\vec{x}^*) \vec{d} > 0, \text{ for all } \vec{d} \in C, \tag{5.30}$$

$\vec{x}^*$ is a strict local minimum, where

$$C = \{\vec{d} \neq 0 : \nabla g_i(\vec{x}^*)^t \vec{d} = 0, \text{ for } i \in I^+, \nabla g_i(\vec{x}^*)^t \vec{d} \leq 0, \text{ for } i \in I^0,$$
$$\nabla h_j(\vec{x}^*)^t \vec{d} = 0, \text{ for } j = 1, \ldots, l\}. \tag{5.31}$$

Many optimization algorithms for constrained problems utilize some characteristics of the KKT optimality conditions. The algorithms can be divided into two classes:

- Finding the optimal solution by solving the necessary optimality conditions.

- Finding the optimal solution by transformation of a constrained problem into a convergent sequence of unconstrained problems.

In the first case, the optimal solution is found by solving the necessary conditions as a system of equations, where the optimal vector of variables and associated Lagrange multipliers need to be calculated. In the second case, the solution is obtained in an iterative way, where each iteration contains the minimization of an unconstrained problem and an update of so-called penalty terms. Then, the updated penalty terms specify the next unconstrained problem in a convergent sequence.

The augmented Lagrangian method, which belongs to the second class of the constrained optimization algorithms, is used to find the optimal design of the 2-DoF actuator. It is described in the next subsection.

5.3.4 Augmented Lagrangian method

Augmented Lagrangian penalty function

As the word "Lagrangian" in the name of the method already implies, the method uses a Lagrangian function $L(\vec{x})$ as the core to transform a constrained optimization problem into an unconstrained one. The main idea of the transformation is to augment penalty terms to $L(\vec{x})$, which provide a high cost to infeasible points. Before the augmented $L(\vec{x})$ is formulated, the inequality constraints of the problem are converted into equality constraints. Thus, the original problem with equality and inequality constraints

$$
\begin{aligned}
\text{minimize} \quad & f(\vec{x}), \\
\text{subject to} \quad & g_i(\vec{x}) \leq 0, \quad \text{for } i = 1, ..., m, \\
& h_j(\vec{x}) = 0, \quad \text{for } j = 1, ..., l, \\
& \vec{x} \in X,
\end{aligned}
\tag{5.32}
$$

can be transformed into a problem with only equality constraints as follows

$$
\begin{aligned}
\text{minimize} \quad & f(\vec{x}), \\
\text{subject to} \quad & g_i(\vec{x}) + s_i^2 = 0, \quad \text{for } i = 1, ..., m, \\
& h_j(\vec{x}) = 0, \quad \text{for } j = 1, ..., l, \\
& \vec{x} \in X,
\end{aligned}
\tag{5.33}
$$

where s_i is an additional variable. Then, $L(\vec{x})$ related to (5.33) is

$$
L(\vec{x}) = f(\vec{x}) + \sum_{i=1}^{m} u_i \left[g_i(\vec{x}) + s_i^2 \right] + \sum_{i=1}^{l} v_j h_j(\vec{x}).
\tag{5.34}
$$

Now, penalty terms need to be added to (5.34). Because all equality constraints have the minimum in zero, the simplest way is to use a quadratic form of the constraints. The quadratic functions,

$$
a_i \left[g_i(\vec{x}) + s_i^2 \right]
\tag{5.35}
$$

$$
b_j h_j^2(\vec{x})
\tag{5.36}
$$

where a_i and b_j are the penalty parameters associated with $g_i(\vec{x}) + s_i^2$ and $h_j(\vec{x})$, respectively, create penalty functions that enforce the minimum in zero and penalize

all infeasible points. Consequently, the optimization of (5.32) is represented by the minimization of the augmented Lagrangian function:

$$\min_{\vec{x}, \vec{s}} L(\vec{x}, \vec{s}, \vec{u}, \vec{v}) = f(\vec{x}) + \sum_{i=1}^{m} u_i \left[g_i(\vec{x}) + s_i^2 \right] + \sum_{i=1}^{m} a_i \left[g_i(\vec{x}) + s_i^2 \right]^2$$
$$+ \sum_{i=1}^{l} v_j h_j(\vec{x}) + \sum_{i=1}^{l} b_j h_j^2(\vec{x}) \tag{5.37}$$

Update formulas of Lagrange multipliers and penalty coefficients

In section 5.3.3, it is mentioned that the augmented Lagrangian method belongs to the group of iterative algorithms, which minimizes a constrained problem by a sequence of unconstrained problems. In practice, it means that the solution of the constrained problem (5.32) is found by means of the unconstrained problem described by (5.37). The solution of (5.32) is close to the solution of (5.37) if

$$\vec{u} \to \vec{u}^*,$$
$$\vec{v} \to \vec{v}^*, \tag{5.38}$$

or

$$\vec{a} \to \infty,$$
$$\vec{b} \to \infty, \tag{5.39}$$

In this case, the Lagrangian multipliers or penalty parameters are updated in an iterative process. The idea behind the iterative process of optimization is to update the parameters in each iteration k. As a result, the $k + 1^{st}$ unconstrained problem (5.37) with $k + 1^{st}$ parameters is created. Iterations are repeated until the solution of (5.37) converges.

   To reach a high convergence rate and avoid ill-conditioning, attention should be paid to the way of updating the parameters. Based on condition (5.38), the Lagrangian parameters $\vec{u}$ and $\vec{v}$ should be updated to converge to $\vec{u}^*$ and $\vec{v}^*$ associated with $\vec{x}^*$. It can be proven, that if a sequence of $[\vec{x}]_k$ converges to a local minimum $\vec{x}^*$ (KKT point), then the sequences:

$$[u_i]_k + [a_i]_k \cdot g_i([\vec{x}]_k) \to u_i^*$$
$$\max \left[0, [v_j]_k + [b_j]_k \cdot h_j([\vec{x}]_k) \right] \to v_j^* \tag{5.40}$$

converge to the corresponding Lagrange multipliers u_i^* and v_i^*, respectively. Thus, the update formulas are:

$$[u_i]_{k+1} = [u_i]_k + [a_i]_k \cdot g_i([\vec{x}]_k)$$
$$[v_j]_{k+1} = \max\left[0, [v_j]_k + [b_j]_k \cdot h_j([\vec{x}]_k)\right] \qquad (5.41)$$

Based on condition (5.39), the penalty parameters should approach to infinity in order to obtain a solution close to the optimal one. However, if the increase of the penalty parameters is to high the problem can become ill-conditioned. On the other hand, the problem starts to converge after the penalty parameters become larger than a certain threshold. For these reasons, it is advisable that the increase of $\vec{a}$ and $\vec{b}$ is done only by a reasonable rate and not necessarily in each iteration. As it can be seen from (5.37), different penalty coefficients are assigned to each constraint. Thus, each penalty coefficient is increased only if the related constrained violation is decreased by the factor γ in

$$[a_i]_{k+1} = \begin{cases} \beta \cdot [a_i]_k & \text{if } \|g_i([\vec{x}]_k) + [s_i]_k^2\| > \gamma \cdot \|g_i([\vec{x}]_{k-1}) + [s_i]_{k-1}^2\| \\ [a_i]_k & \text{if } \|g_i([\vec{x}]_k) + [s_i]_k^2\| \le \gamma \cdot \|g_i([\vec{x}]_{k-1}) + [s_i]_{k-1}^2\|, \end{cases} \qquad (5.42)$$

$$[b_j]_{k+1} = \begin{cases} \beta \cdot [b_j]_k & \text{if } \|h_j([\vec{x}]_k)\| > \gamma \cdot \|h_j([\vec{x}]_{k-1})\| \\ [b_j]_k & \text{if } \|h_j([\vec{x}]_k)\| \le \gamma \cdot \|h_j([\vec{x}]_{k-1})\|, \end{cases} \qquad (5.43)$$

where $\beta > 1$ is the increase rate, which is assigned empirically.

Stop criterion

In practice, it would be time consuming and difficult to fulfill the conditions (5.38) and (5.39) by the iteration process. It is also not necessary to find exactly the optimal point that meets the first-order optimality condition:

$$\|\nabla_{\vec{x}} L(\vec{x}_k, \vec{u}_k, \vec{v}_k)\| = 0. \qquad (5.44)$$

Consequently, in the majority of the cases, it is sufficient if

$$\|\nabla_{\vec{x}} L(\vec{x}_k, \vec{u}_k, \vec{v}_k)\| \le \epsilon. \qquad (5.45)$$

Alternatively, the stop criterion can be based on the constraint violation defined as:

$$Viol(\vec{x}) = \max\left(\|g_i(\vec{x}) + s_i^2\|, \|h_j(\vec{x})\|\right). \qquad (5.46)$$

Thus, if the constraint violation in the kth iteration is less than a tolerance $\epsilon > 0$,

$$Viol\left([\vec{x}]_k\right) < \epsilon, \qquad (5.47)$$

then the calculation is terminated with $[\vec{x}]_k$ as a KKT point.

Algorithm

The iterative algorithm is shown in Fig. 5.5. It starts with the initialization of
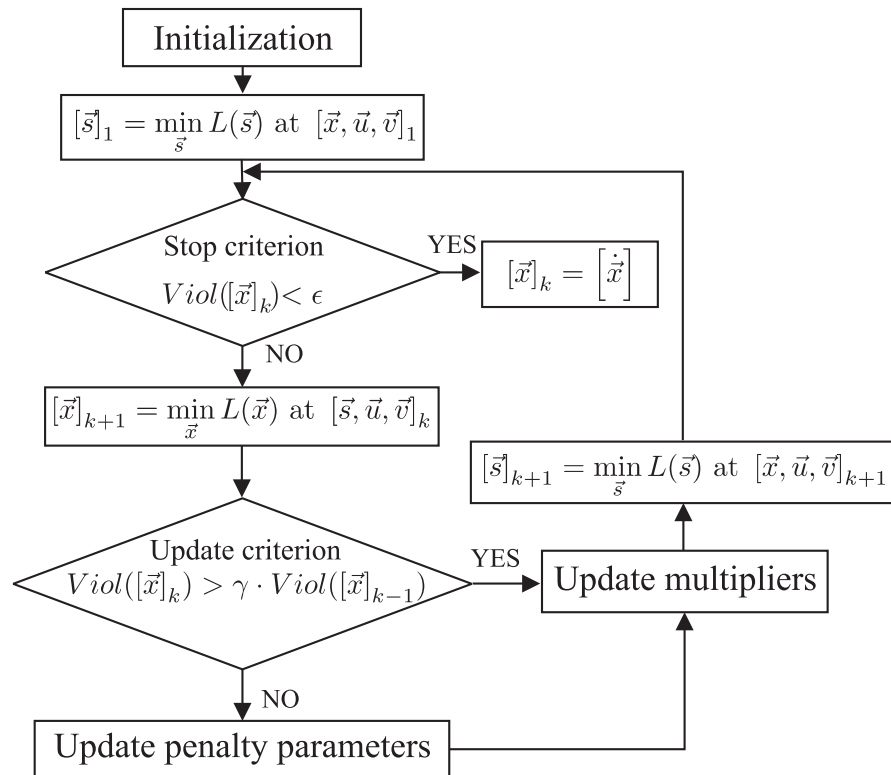
Figure 5.5: Augmented Lagrangian algorithm for the actuator optimization.

variables and constants, and the minimization of $L(\vec{x}, \vec{s}, \vec{u}, \vec{v})$ with respect to the additional variables $\vec{s}$. Then, the stop criterion (5.47) is evaluated. If the condition is true, the optimal design variable vector is $[\vec{x}]_k$. If the condition is false, $L(\vec{x}, \vec{s}, \vec{u}, \vec{v})$ is two times minimized. The first time it is minimized with respect to $\vec{x}$ with $[\vec{s}]_k$ being obtained from the previous minimization. The second minimization of $L(\vec{x}, \vec{s}, \vec{u}, \vec{v})$ with respect to the additional variables $\vec{s}$ is done after evaluation of

the update criterion and eventual penalty-coefficients and Lagrangian-multipliers update at the newly obtained point $[\vec{x}]_{k+1}$.

Newton method of finding minima

The algorithm in Fig. 5.5 contains two minimizations of the augmented Lagrangian function $L(\vec{x}, \vec{s}, \vec{u}, \vec{v})$, the minimization with respect to the auxiliary variable $\vec{s}$ and that with respect to the vector of the design variables $\vec{x}$. Both minimizations are done by the Newton method (also known as the Newton-Raphson method).

The Newton-Raphson method is considered as one of the fastest gradient methods. The method, which was for the first time published in 1690 by Raphson [51], is built on the quadratic approximation of a function around a given point $[\vec{x}]_k$, under the assumption of a two times continuously differentiable function $f\left([\vec{x}]_k\right)$:

$$f\left([\vec{x}]_k\right) + \nabla f\left([\vec{x}]_k^t\right)\left(\vec{x} - [\vec{x}]_k\right) + \frac{1}{2}\left(\vec{x} - [\vec{x}]_k\right)^t H([\vec{x}]_k)\left(\vec{x} - [\vec{x}]_k\right), \qquad (5.48)$$

where $\nabla f\left([\vec{x}]_k^t\right)$ and $H([\vec{x}]_k)$ are the Jacobian and the Hessian of the function $f\left([\vec{x}]_k\right)$ at the point $[\vec{x}]_k$, respectively.

The application of a necessary optimality condition to (5.48) yields

$$\nabla f\left([\vec{x}]_k^t\right) + H([\vec{x}]_k)\left(\vec{x} - [\vec{x}]_k\right) = 0, \qquad (5.49)$$

and, consequently, if an inverse of the Hessian matrix $H([\vec{x}]_k)$ exists, the next point in a sequence, which converges to a minimum, is

$$[\vec{x}]_{k+1} = [\vec{x}]_k - H([\vec{x}]_k)^{-1}\nabla f\left([\vec{x}]_k^t\right). \qquad (5.50)$$

The Newton-Raphson method always converges except for $H([\vec{x}]_k)$ singular or if the so-called Newton direction

$$\vec{d}_k = -H([\vec{x}]_k)^{-1}\nabla f\left([\vec{x}]_k^t\right) \qquad (5.51)$$

is not a descent direction, i.e. that the Hessian is not positive definite. The important point to note is that, if a starting point $\vec{x}_1$ is close to $\vec{x}^*$, then the method is well defined and converges to this local minimum.

As it can be seen from the previous text, the convexity of the optimization problem functions plays an important role in two aspects:

- convergence of the algorithm,

- global optimality.

If the convexity of the functions can be proved, then the convergence and the global optimal solution are easily reached. However, in most practical cases, it is difficult to prove the convexity of the functions. For this reason, the prove of the convexity can by replaced in practice by several optimizations with different starting points. Consequently, some of the starting points may be close enough to a local minimum and the optimization may converge. The goal of optimizations from different starting points is not only to ensure convergence of the algorithm but also to find all local minima. Then, by comparing the local minima, the global minimum can be obtained. This very effective approach is used in the optimization of the 2-DoF actuator.

5.4   Solution of the optimization problem

The augmented Lagrangian method was applied to the optimization problem (5.2). The augmented Lagrangian function (5.37) was minimized and the optimal vector of the design variables was found by using the Mathematica software package.

The performance parameters of the optimized and the prototype actuator (analyzed in chapter 3) are listed for comparison in Tab. 5.3 (the objectives are given in Tab. 5.1). The total mass is obtained from (5.3). The force and torque in Tab. 5.1 are average values. They are calculated from the characteristics obtained by FEM for the optimized actuator at the nominal current density, which are shown in Fig. 5.6. The results for the prototype actuator were already shown in section 3.5. The dimensions of the two actuators are shown in Figs. 5.7 to 5.9.

The key difference between the actuators in Figs. 5.7 to 5.9 is the height of the coils, which is larger in the optimized actuator. From (5.9) and (5.11) can be seen that higher coils result in a larger magnet height and, consequently, a larger ferromagnetic core height.

Table 5.3: Comparison of the optimized and prototype actuators.

		Optimized	Prototype
Total mass	$[g]$	53.5	46.5
Mass of coils	$[g]$	10.5	13.3
Mass of magnets	$[g]$	14.5	15.3
Mass of core	$[g]$	28.5	17.9
F_z	$[N]$	2.17	1.23
T_x	$[10^{-3}Nm]$	5.04	5.89
Δ_F (flatness)	$[\%]$	12.8	37.9
Δ_T (flatness)	$[\%]$	13	16.7
J	$[10^7 A/m^2]$	1.97	1.39

The total mass of the optimized actuator is $7g$ larger than that of the prototype. The most significant increase of the mass is related to the ferromagnetic core and equals $10.6g$. Since the mass of actuators is proportional to the force or torque they have to produce, the rise of the total mass can be attributed to the rise of the force of the actuator. The force of the optimized actuator is higher than the force of the prototype, whereas the torques of both actuators are comparable. The masses of the coils and the magnets are lower than those of the prototype.
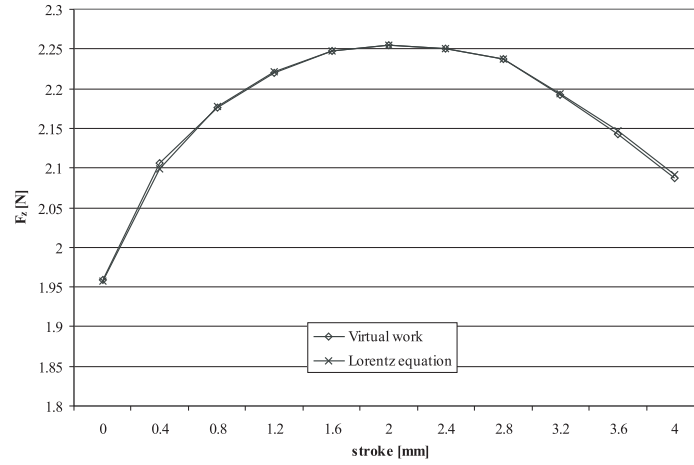
a)
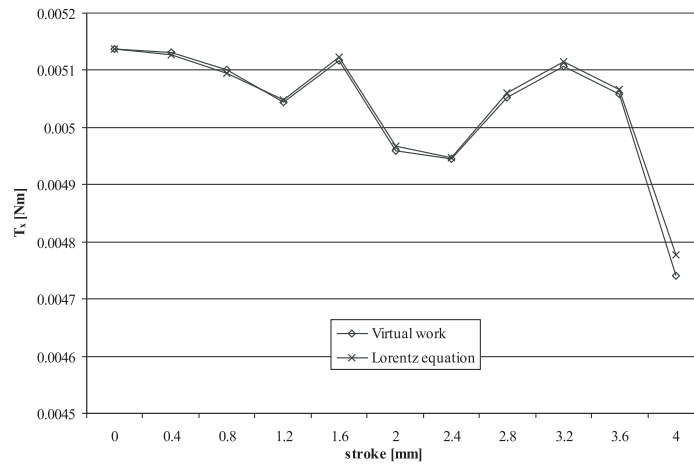
b)

Figure 5.6: Predicted force (a) and torque (b) characteristic of the optimized the 2-DoF actuator (FEM results).

It can also be noticed that the predicted force of the optimized actuator is higher than F_{req}. This difference is caused by the specified leakage factor of the force magnet circuit, which was kept constant during the optimization. The dimensions in the FMC have changed compared to those in the prototype. Therefore, a variation in the leakage factor can be expected. To reach a closer agreement between optimization and realty a new leakage factor, which corresponds to the optimal design, should be used. In the case of the TMC, the dimensions of the TMC of both actuators are not significantly different. Thus, the difference between the TMC leakage factors is very small and, therefore, the torques of both actuators are close to each other and to T_{req}.

The flatness of the characteristics is also improved. The improvement is connected to the ratio of the heights of coils and magnets. The closer the ratio to one the flater the characteristics. The ratio is 0.58 for the optimized actuator and 0.4
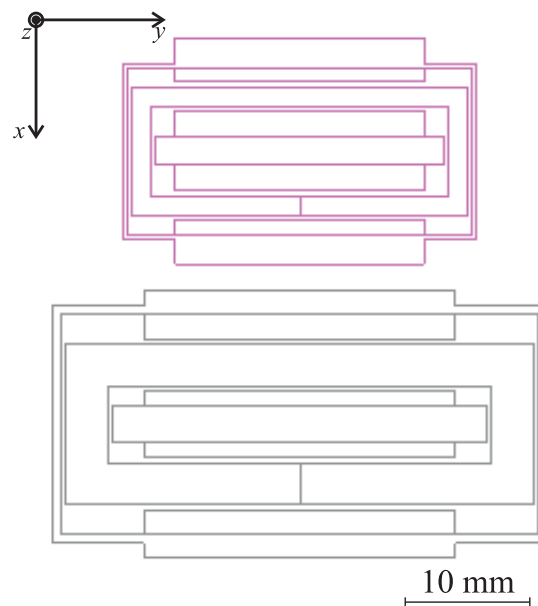
Figure 5.7: Comparison of the 2-DoF actuator dimensions in the xy-plane (top - optimal, bottom - prototype).
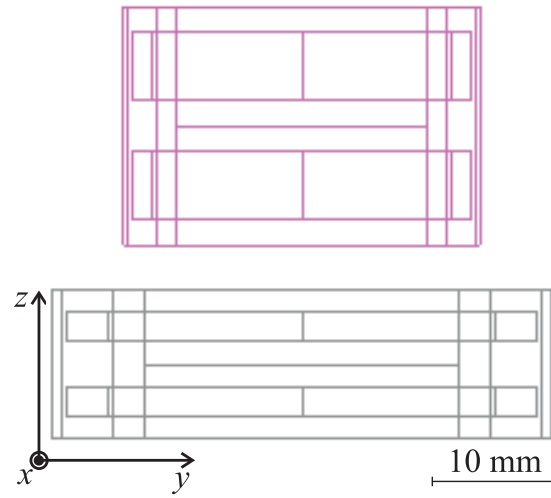
Figure 5.8: Comparison of the 2-DoF actuator dimensions in the yz-plane (top - optimal, bottom - prototype).
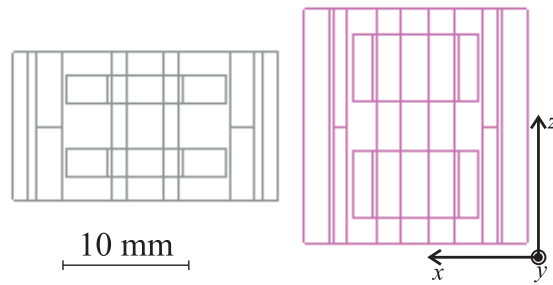
Figure 5.9: Comparison of the 2-DoF actuator dimensions in the xz-plane (right - optimal, left - prototype).

for the prototype.

5.5   Conclusions

The objective of this investigation was to overcome drawbacks of immature design, which usually appear in case of innovative topologies, and to create a computational tool for designing the 2-DoF actuator. This was reached by establishing an optimization approach, which is based on the augmented Lagrangian method.

The proposed approach uses the analytical MEC model of the actuator to find a required force and torque at minimal mass. By using this method the optimal actuator dimensions can be found.

From the results obtained by the proposed optimization approach can be seen that the height of the coils is a very important variable. It influences the total mass and the flatness of the force and torque characteristics of the actuator and, consequently, the power dissipation in the coils.

The values of the force and torque obtained by the optimization method based on the implemented MEC model show that the leakage factors are dependent on the dimensions of the geometry. The leakage factors influence the optimal solution and, therefore, they have to be updated. This can be done during the optimization rounds [52] or after finding an optimum that has significantly different dimensions than those used as the starting point for optimization. In this way a good consistency between the values of the force and the torque obtained by the resulting optimized MEC model and the FEM model can be achieved.

Chapter 6

Experimental results

In the previous chapters, the static-electromagnetic (Chapter 3) and thermal (Chapter 4) behaviors of the innovative 2-DoF actuator were described by analytical and numerical models. The proposed modeling approaches are based on adaptation of well-known theories commonly applied to the design of electrical machines. The goal of this chapter is to present experimental results to demonstrate the validity of the proposed models.

This chapter is arranged as follows. Section 6.1 outlines the comparison of simulation and measurement results of magnetic flux densities, forces and torques related to the MEC and FEM models. In section 6.2, the verification of the thermal model is discussed. Finally, in section 6.3 two lightweight positioning test setups are presented and compared.

6.1 Experimental verification of the static-electromagnetic models

6.1.1 Magnetic flux density measurements

In order to compare the established MEC and FEM models with the reality, the magnetic flux densities in the air gap of the force and torque magnets of the 2-DoF actuator were measured at several positions.

The measurements of the magnetic flux density in the FMC and TMC air gaps of the actuator prototype were done by means of a fluxmeter and a field coil (EF-5 and FS 100 /2, respectively, from MAGNET – PHYSIK Dr. Steingroever GmbH)
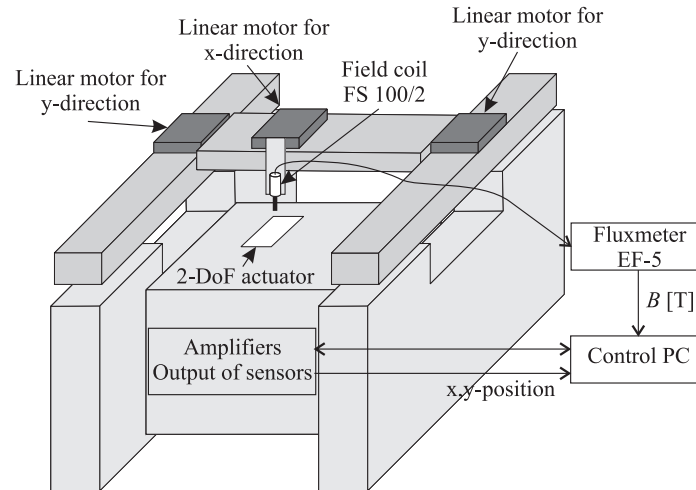
Figure 6.1: Magnetic field measurement setup.

that was attached to an H-drive, as shown in Fig. 6.1. The fluxmeter contains an electronic circuit that integrates the induced voltage in the field coil, which is proportional to the magnetic flux. The fluxmeter calculates the resulting magnetic flux density based on the known total area and resistance of the field coil. To be able to obtain a graph of the magnetic flux density as a function of position, the coil was moved with small velocity in the air gaps. The precise coordinates of the coil and the related measured values of the magnetic flux density were stored in a data file in the control PC, as suggested in Fig. 6.1.

The experimentally obtained magnetic flux densities of the force magnet and torque magnet along the middle lines of the air gap (see also Fig. B.8) are compared in Figs. 6.2 and 6.3, respectively, with the values obtained form the FEM solution of the actuator with corresponding parameters of the measured permanent magnets. A high correlation between the curves obtained by measurement and FEM results is apparent.

It would be quite impractical to compare measured magnetic flux densities with those calculated by the MEC model. Therefore, the FEM results, which can be easily post-processed, have been used instead of measured results. This is justified due to the high correlation between of the FEM results and measurements as
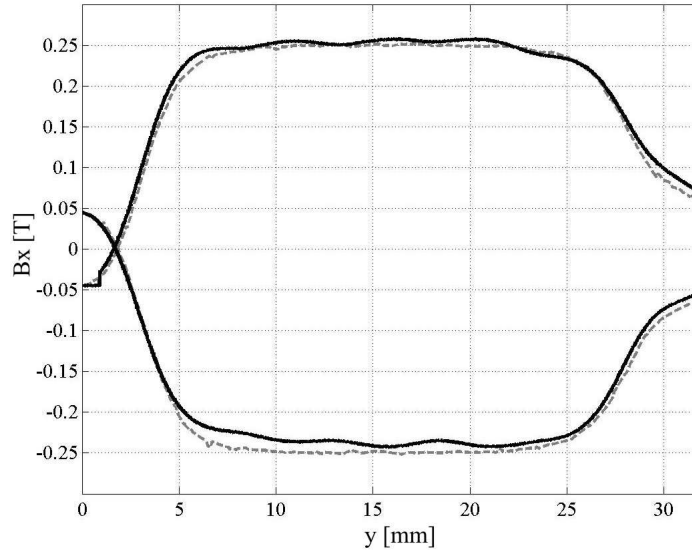
Figure 6.2: Magnetic flux density B_x in the air gap of the force magnets (dashed - FEM results, solid - measurement).

Table 6.1: Magnetic flux densities in the FMC.

	B_{PMF} [T]	B_{FMC} [T]	$B_{\mathcal{R}_{12}}$ [T]
FEM	0.67	1.79	0.26
MEC	0.61	1.61	0.23
E	8.96%	10.06%	11.54%

confirmed by Figs. 6.2 and 6.3.

In Tabs. 6.1 and 6.2, some average magnetic flux densities in the actuator obtained by the MEC model are compared with the average magnetic flux densities in the volume of the corresponding flux tubes calculated from the FEM magnetic field distribution (by using the Maxwell 3D software package). The obtained values show that the magnetic flux density in the air gap of the FMC is sufficiently accu-
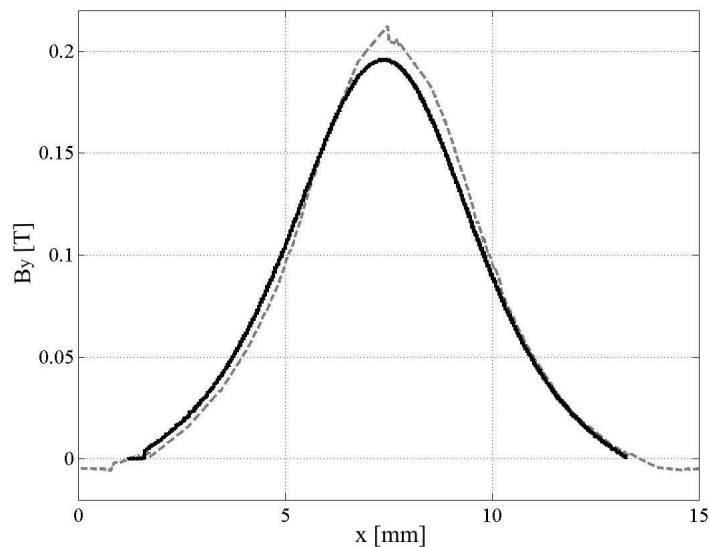
Figure 6.3: Magnetic flux density B_y in the air gap of the torque magnet (dashed - FEM results, solid - measurement).

Table 6.2: Magnetic flux densities in the TMC.

	B_{PMT} [T]	B_{TMC} [T]	B_{T1a} [T]	B_{T1c} [T]
FEM	1.17	1.77	0.16	0.06
MEC	1.17	1.89	0.15	0.04
E	0%	6.78%	6.25%	33.33%

rately predicted, with a maximum relative error E of 11.54% (where E is defined by (3.79)). The most relevant magnetic flux densities in the TMC are also in good agreement, with acceptable errors as shown in Tab. 6.2.

The error of B_{T1c} in Tab. 6.2, which is 33.33%, may be attributed to the inaccurate description of the corresponding flux tubes in the region close to the torque magnet edges. In the model, the dimensions and shapes of these flux tubes have

been determined on the basis of the physical geometry of the actuator rather than on the shape of simulated magnetic flux lines. The high error could be considered at first sight as unacceptable. However, the flux density B_{T1c} has low impact on the accuracy of the torque estimation, because the value of B_{T1a} is dominant in the calculations, being in practice always much larger than B_{T1c}. Therefore, in order to allow fast calculations during optimization iterations, it is convenient to accept this modeling error and to keep the analytical calculations of B_{T1c} based only on the physical geometry of the actuator.

6.1.2   Force and torque measurements

Experimental results were obtained by measuring the force and torque of the actuator with a 6-axis force/torque sensor (F/T Mini40 Si-20-1, silicon strain gauges principle, from SCHUNK GmbH & Co. KG), capable of measuring simultaneously three perpendicular forces and three torques. The actuator with the sensor was attached to a mechanical setup with one translational DoF movement and with a resolution of $0.01mm$ realized by a micro-positioning head, as shown in Fig. 6.4.

The outputs of the force/torqe sensor were amplified and transmitted to a system controller. The signals were converted to the three force components F_x, F_y, F_z and the three torque components T_x, T_y, T_z via the calibration matrix. The F_z and T_x signals represent the force and torque of the actuator, respectively. To increase the accuracy of the measurement, a higher force and torque than the nominal ones need to be produced. Thus, the coil of the setup was supplied by a current with an amplitude of $6A$. Because this current is almost three times the nominal one $(= 2.11A)$, the signal was a square waveform with a $10Hz$ period and a 20% duty-cycle to prevent thermal damage of the coil and permanent magnets. The analogue output of the force/torque sensor system controller was displayed and measured by means of an oscilloscope.

The force F_z and torque T_x of the actuator were computed from the magnetic field solution of the FEM model using the virtual work method, also at a coil current of $6A$. The characteristics of the force and torque, as function of the coil z-position with respect to the magnets at the zero x-rotation angle (see Fig. 6.5), are shown together with the measured ones in Figs. 6.6 to 6.7. It can be seen that, up to the used current excitation level, the shapes of the measured force/torque curves are in good agreement with the FEM simulation results.

During the measurements, the other force components, F_x and F_y, and torque components, T_y and T_z, were also sensed by the force/torque sensor. However, they were so small that it was not feasible to obtain reliable data-readings due to measurement noise generated by the available measurement equipment.
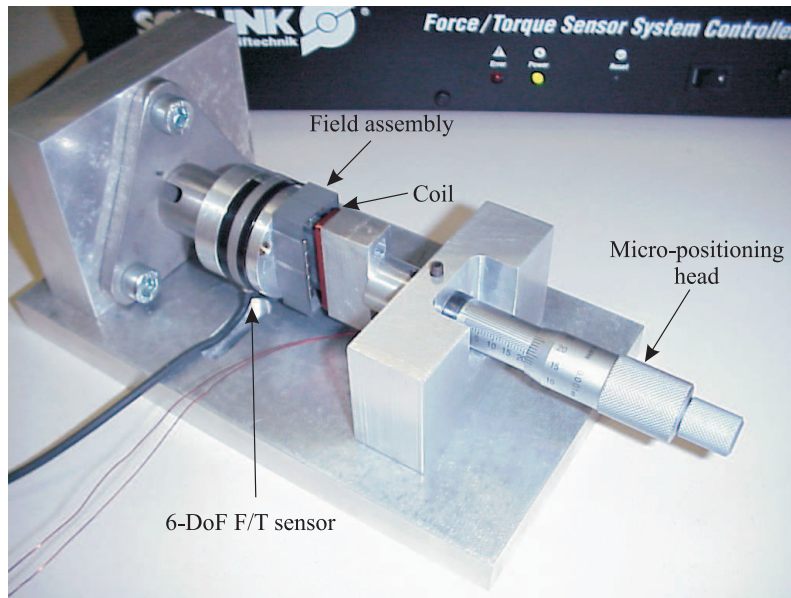
Figure 6.4: Force and torque measurement setup.
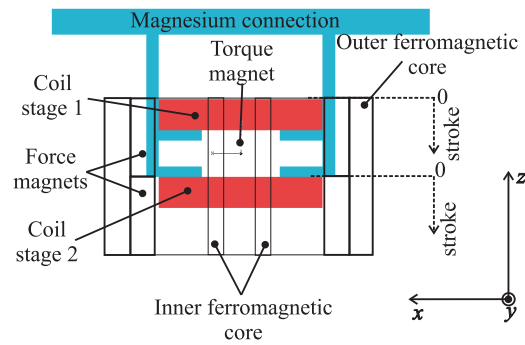
Figure 6.5: Definition of stroke for Figs. 6.6 and 6.7.
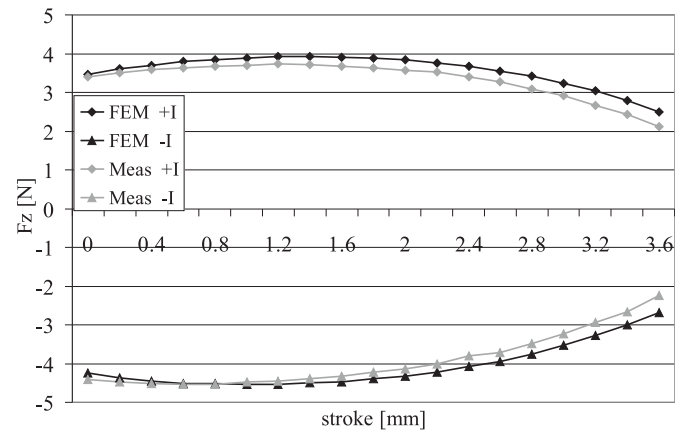
a)
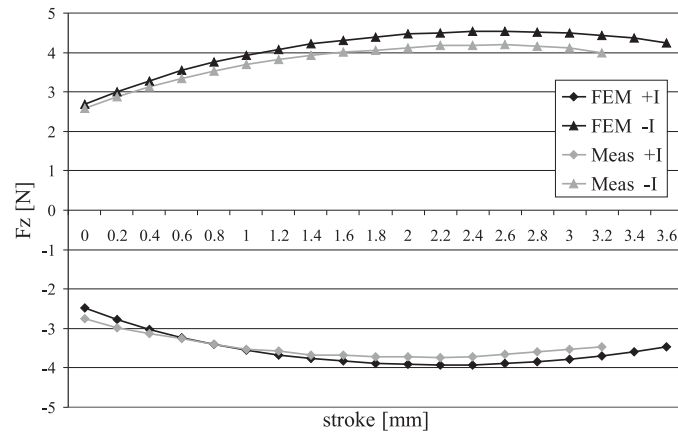
b)

Figure 6.6: Force characteristics of a) stage 1, b) stage 2.
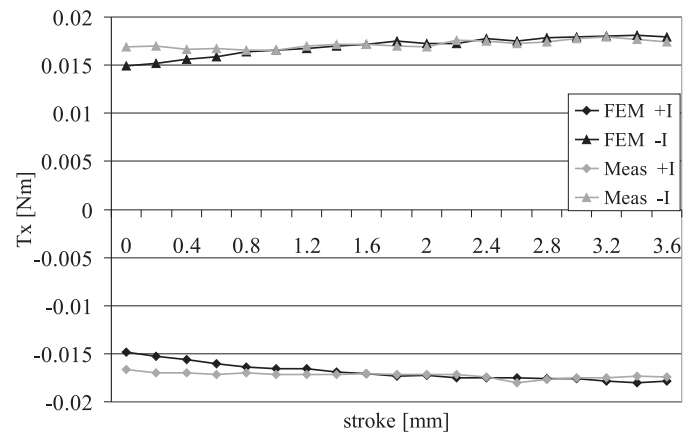
a)
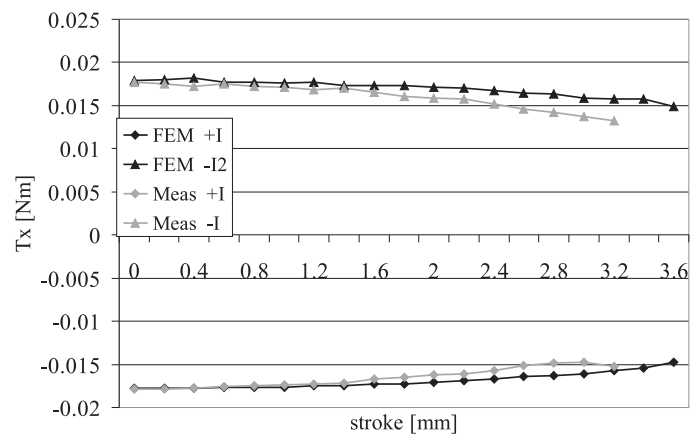
b)

Figure 6.7: Torque characteristics of a) stage 1, b) stage 2.

Table 6.3: Average values of force and torque of one coil of the 2-DoF actuator.

	F_z [N]	T_x [10^{-3} Nm]
MEC	3.71	16.00
FEM	3.82	16.95
Measurement	3.62	16.56

Table 6.4: Relative errors of force and torque of one coil of the 2-DoF actuator.

	E_F [%]	E_T [%]
MEC vs FEM	2.70	5.56
MEC vs Meas	2.47	4.68
FEM vs Meas	5.10	1.14

The results of the MEC model are average values of magnetic flux densities. Consequently, only average values of force and torque can be estimated by the Lorentz equation. In order to compare the results of the MEC model and Lorentz equation with the FEM and the measured force/torque characteristics, average values over the stroke have been calculated (see Tab. 6.3). The force/torque errors are listed in Tab. 6.4. It can be seen that the average values of the force and torque can be estimated by the MEC model with maximal errors of 2.70% and 5.56%, respectively.

6.1.3   Conclusions

Based on the comparison of the results in Tabs. 6.3 and 6.4, it can be concluded that the magnetic field, force and torque of the actuator can be predicted with sufficient accuracy by the analytical MEC model and Lorentz equation up to the specified coil current level. This implies that even if the shapes of the assumed flux tubes do not exactly follow the magnetic flux lines, the MEC model still yields acceptable results. However, it is important that the geometric space, where the major part of the magnetic flux is flowing, should be decomposed into sufficiently small flux tubes to be included in the MEC.

6.2   Experimental verification of the thermal model

Thermal measurements of electrical machines are usually done by means of temperature sensors, which can measure the temperature on the basis of various principles, as for example, resistive thermometers or thermocouples. These sensors are often placed inside of windings, teeth, iron or stator frame, which is convenient if the machines have a closed structure. They can also be used for surface temperature measurements.

Due to the dimensions of the available temperature sensors and the 2-DoF actuator, which are in some cases almost the same, it would be unfeasible to place or attach these sensors in or on the actuator. Therefore, thermography was used to measure the actuator temperatures.

In general, thermography uses infrared imaging to measure the thermal energy emitted from a surface in the form of light. The emitted light has wavelengths inside the infrared spectrum and, therefore, it is not visible to the human eye. However, the invisible heat radiation can be transformed into an image, which contains information about the temperatures of surfaces, by an infrared thermography camera. Thus, the infrared camera is a means of precise non-contact measurement, suitable to measure surface temperatures of open structures as the 2-DoF actuator. The schematic of the temperature measurement setup is shown in Fig. 6.8.

The coil assembly of the actuator is fixed by attachment bolts (see Fig. 6.9) to an aluminium cooling fin. This is done to create an homogeneous boundary condition on the top surface of the magnesium connection. In the thermal equivalent circuit (Fig. 4.6), the top of the magnesium connection is attached to the point with ambient temperature. For this reason, the cooling fin is kept at ambient temperature by the air flow forced by a fan on the other side of the cooling fin, so that the natural air cooling on the side of the actuator is not disturbed.

The field assembly of the actuator is attached to the aluminium cooling fin by a thermal isolator plate, as it can be seen from Fig. 6.9. Consequently, the heat of the field assembly is transferred to the surrounding air only by natural convection from the outer surface.

The infrared camera is focused on the surface of the actuator, where the surface temperatures of the torque magnet, inner ferromagnetic core, coil, force magnets and outer ferromagnetic core can be measured. The camera is connected to a computer with a dedicated software, which allows further processing of the thermal images.
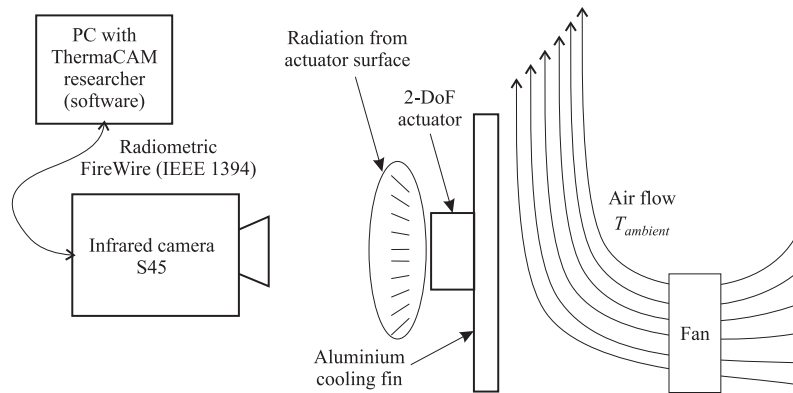
Figure 6.8: Thermal measurement setup.
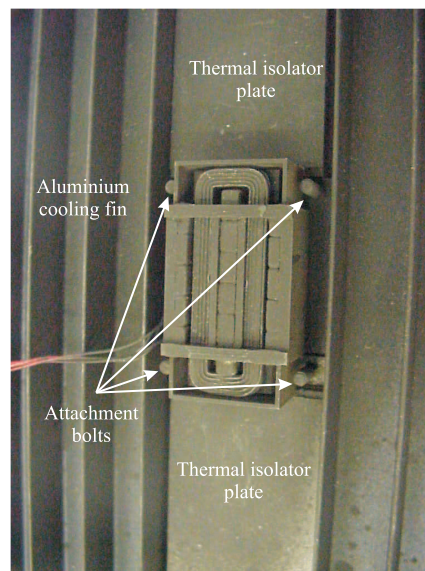
Figure 6.9: Interconnection of the actuator with the aluminium cooling fin.

6.2.1   Steady-state thermal measurements

By using the available software in the infrared scanning apparatus (Fig. 6.8), average surface temperatures can be obtained. In Fig. 6.10, an image of the infrared camera is shown. White lines represent borders of areas where average temperatures are calculated from. The volume divisions are related to the two thermal equivalent circuits that model the outer ferromagnetic core in two different ways, as it has been demonstrated in Figs. 4.17 and 4.19, respectively.

The steady-state temperature distribution in Fig. 6.10, obtained at constant nominal power of $10W$ dissipated in the coils and $25°C$ ambient temperature, shows that if the ferromagnetic core is divided as in case 1, then the part I of the outer ferromagnetic core has approximately the same temperature over the whole surface. This confirms that case 1 is closer to the reality and can describe the thermal behavior better than case 2, as discussed in section 4.7.

The measured and calculated average temperature rises of the actuator surfaces (section 4.7) in steady state for $10W$ dissipation in the coils are listed in Tab.
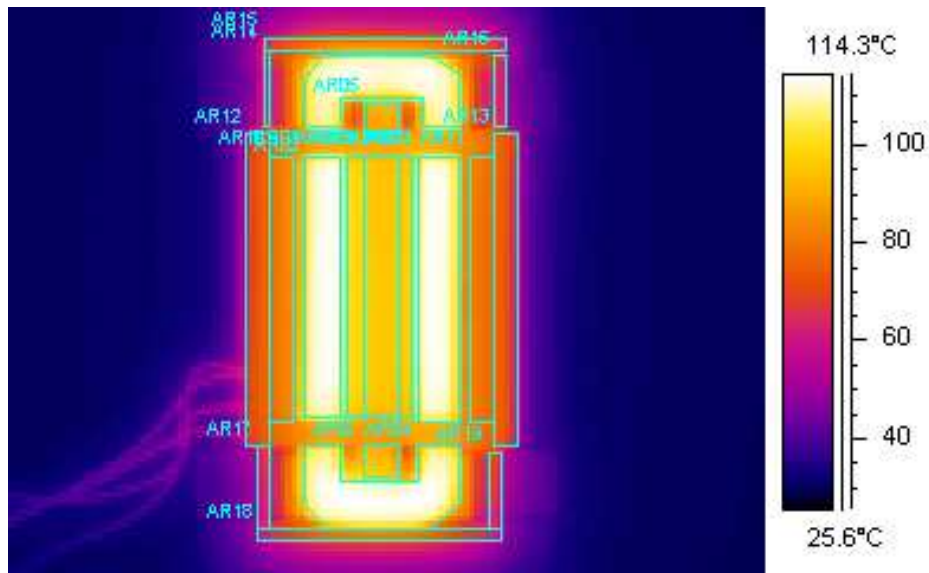
Figure 6.10: Thermal image of the 2-DoF actuator with a dissipated power in the coils of 10W.

6.5. As it can be seen, the predicted and measured values of the temperature rise are close to each other.

The relative errors, defined as

$$E = \frac{|T_{measured} - T_{simulation}|}{T_{measured}}, \tag{6.1}$$

are shown in Tab. 6.6.

Table 6.5: Average temperature rise of the actuator surfaces (10W, steady state).

Part	T_{av} (case 1)$[K]$	T_{av} (case 2)$[K]$	measured $[K]$
Torque magnet	65.2	65.5	66.8
Inner ferromagnetic core	69.7	70.1	72.5
Coil part I	90.8	91.4	82.7
Coil part II	82.8	83.4	84.5
Force magnet	53.1	56.2	54.8
Outer ferromagnetic core			
part I	42.6	46.7	45.4
part II	43.8	48.2	44.7

Table 6.6: Relative errors (10W, steady state).

Part	case 1 $[\%]$	case 2 $[\%]$
Torque magnet	2.4	1.9
Inner ferromagnetic core	3.9	3.3
Coil part I	9.8	10.5
Coil part II	2.0	1.3
Force magnet	3.1	2.6
Outer ferromagnetic core part I	6.2	2.9
Outer ferromagnetic core part II	2.0	7.8

The largest relative error of 10.5% is found for coil part I. If necessary this modeling error may be reduced by refining the value of the thermal resistance of

the glue layer that attaches the coil to the magnesium connection. The thermal resistance of the layer varies based on the conditions at the gluing process. Because the measured temperature of the coil part I is lower than the predicted, the real resistance of the glue layer is lower than the assumed one in the thermal model.

Further, the two models with different divisions of the outer ferromagnetic core, give acceptable results in steady state.

6.2.2   Transient-states thermal measurements

If the average surface temperatures are extracted from the images that have been recorded with a frequency of $2Hz$, then transient states can be obtained. During the transient both coils were connected in series to a current source through a multimeter, which allows measuring the electrical power. During the first 20 minutes of measurements, the power was kept constant at the level of $10W$ by means of manual adjustment of the current level. When the thermal steady state was reached the current was $2.1A$, which is the nominal current. After that no power was applied during the next 20 minutes, so the actuator cools down to the ambient temperature of $25°C$.

The results of the thermal transient measurements and predicted surface temperatures of the actuator are shown in Figs. 6.11 to 6.17. The average measured surface temperatures were calculated according to the case 1 division of the outer ferromagnetic core unless stated otherwise in the figures. In Figs. 6.11 to 6.14, the simulation results for both cases are almost identical.
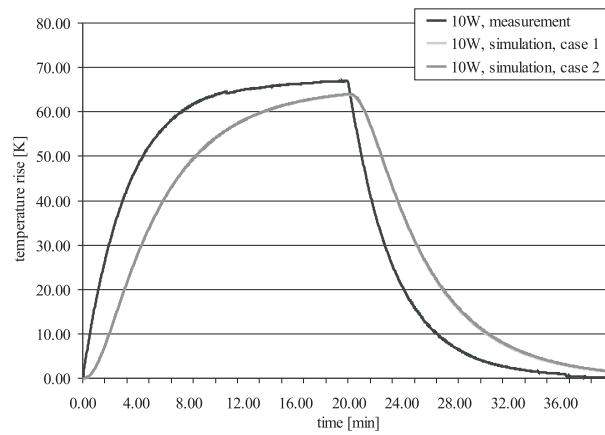
Figure 6.11: Temperature rise of torque magnet.
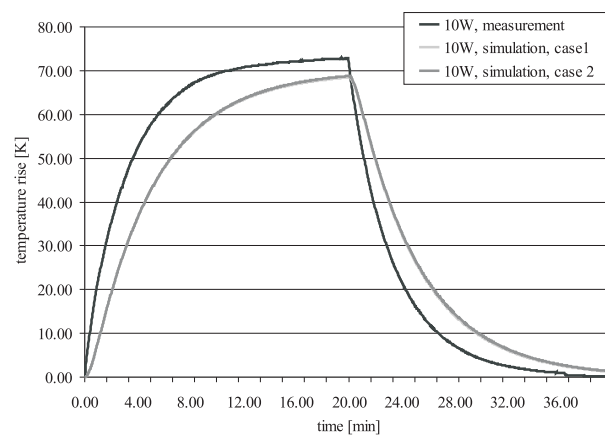
Figure 6.12: Temperature rise of inner ferromagnetic core.
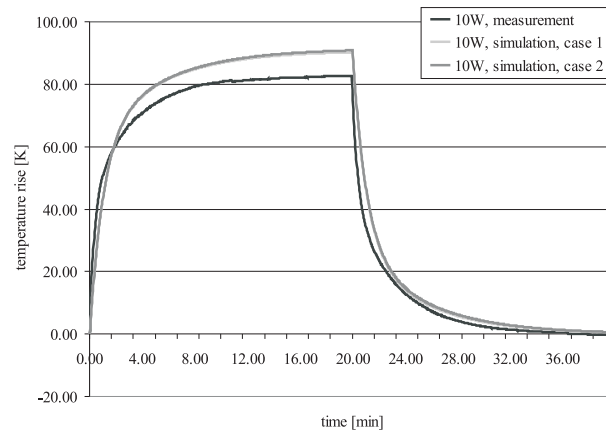
Figure 6.13: Temperature rise of coil part I.
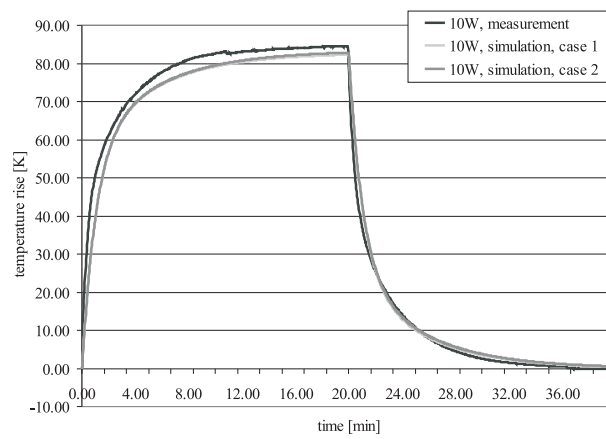
Figure 6.14: Temperature rise of coil part II.
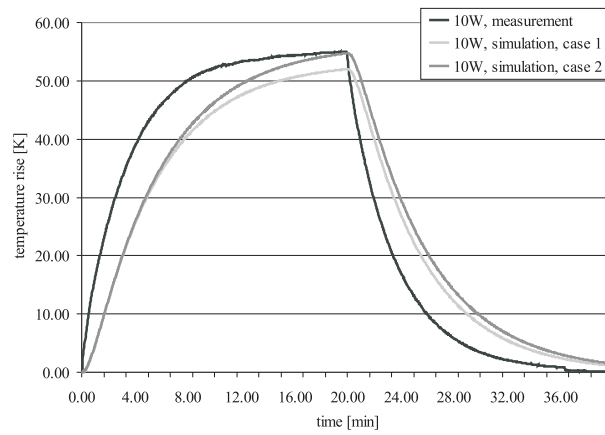
Figure 6.15: Temperature rise of force magnet.
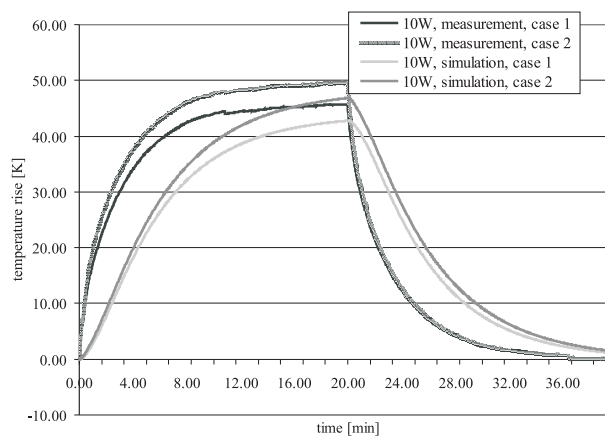
Figure 6.16: Temperature rise of outer ferromagnetic core part I.
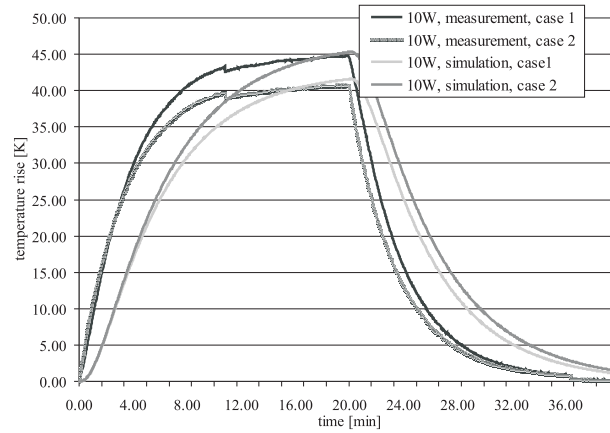
Figure 6.17: Temperature rise of outer ferromagnetic core part II.

From all graphs it is visible that the predicted average temperatures during transients are lagging the measured ones. In published literature, a comparable case of analyzing thermal transients of a similarly complex electromechanical device (essentially 3D structure with 3D heat flow) as the innovative 2-DoF actuator can hardly be found. But, comparable lagging results were also obtained by similar modeling approaches [40, 53] of much simpler and axially symmetric rotary machines (with a model reduced to 2D with 2D heat flow).

It can be said that the thermal transients of complex electromechanical structures are problematical to be modeled with high precision. Fortunately, for the design of the 2-DoF actuator, steady-state temperatures are more relevant than the thermal transients. Since no temperature oscillations occur during the transients (first order systems), and the orders of magnitude of time constants to reach the steady states are well described by the presented model, the transient errors are acceptable.

The absolute errors between the measured and predicted temperatures (case 1 division) are shown in Fig. 6.18. The errors are increasing from zero to a maximum value and then they decrease to their steady-state values.
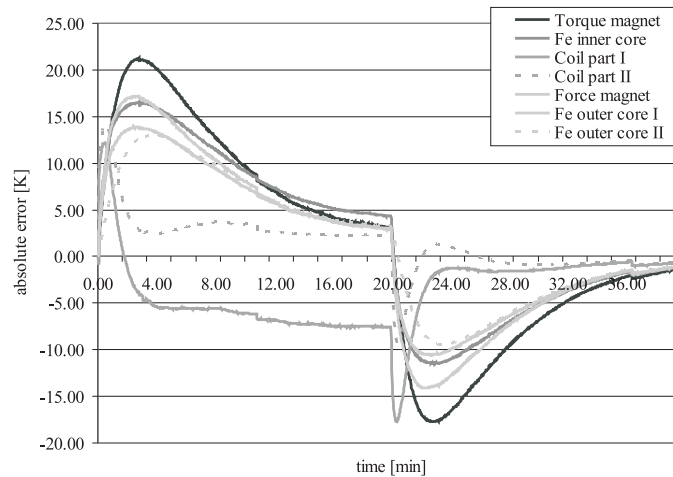
Figure 6.18: Absolute errors.

The absolute errors might be accounted to three factors:

- the lumped parameters of the thermal equivalent circuit are derived from steady-state equations and the transient effects are implemented by adding thermal capacitances of a particular part to the point with an assumed average temperature,

- the derivation is based on a linear distribution of temperatures in the actuator parts, see section 4.5.1 (except for the coils, section 4.5.4),

- deviations of thermal material properties of the actuator parts, e. g. glue layers, permanent magnets etc.

A better representation of the transients could be achieved by subdividing the elements of the proposed model into smaller ones. This would allow a better approximation of the different temperature distributions by linear modeling.

As it was already discussed, the material properties can vary depending on manufacturing and assembly processes. However, these deviations may be minimized by, for example, thermal equivalent circuit parameter fitting techniques [34], which are based on the knowledge of detailed experimental results.

6.2.3 Conclusions

In this section, the two thermal equivalent circuits with different outer ferromagnetic core divisions (section 4.5.6), were experimentally verified.

Considering the steady-state results, it is reasonable to conclude that both circuits give results with an error less than 10.5%. Consequently, the proposed circuits take all relevant features of the heat transfer into account and thus they can model the real actuator in sufficient details.

With respect to the thermal transient states, initially, the absolute deviation increases, but it is reduced to its steady-state value. The error is due to the assumed linear distribution of the temperatures in the actuator parts and due to deviations of thermal material properties.

6.3 Experimental setup of the lightweight positioning system

On the system level, the study was focused on the mass reduction of actuators, together with the mechanical structure driven by the actuators, and the improvement of the frequency characteristics of the system by means of control strategies. Two lightweight positioning system prototypes with a flexible beam, one based on 1-DoF voice coil actuators and the other based on 2-DoF innovative actuators, as shown in Fig. 6.19, were built.

In both cases, beams with a reduced mass to 38.6% of that of the stiff beam were used. Further, comparing the two lightweight systems, both have almost the same total mass of actuators. While in the first setup each actuator creates only a force as a control variable, in the second setup each actuator produces two control variables, a force and a torque. To compare the two lightweight positioning setups a new figure of merit is introduced: the mass-variable factor MV, which is the ratio of the mass of an actuator M_{act} per number of independent control variables n_{var}:

$$MV = \frac{M_{act}}{n_{var}}, \quad [g]. \tag{6.2}$$

Consequently, MV equals $34.4g$ for the 1-DoF actuator and for the optimized 2-DoF actuator it is $26.75g$. Although the total mass of the 1-DoF actuators in the first setup is 3.8 g lower than the total mass of the 2-DoF actuators in the second setup, it can be concluded that the MV factor in the second setup is lower by 22.2%.

There is still one aspect of the system design that had not been foreseen at the beginning of the project, because it originated from the concept of the innovative actuator. This aspect can be seen from Fig. 6.19.
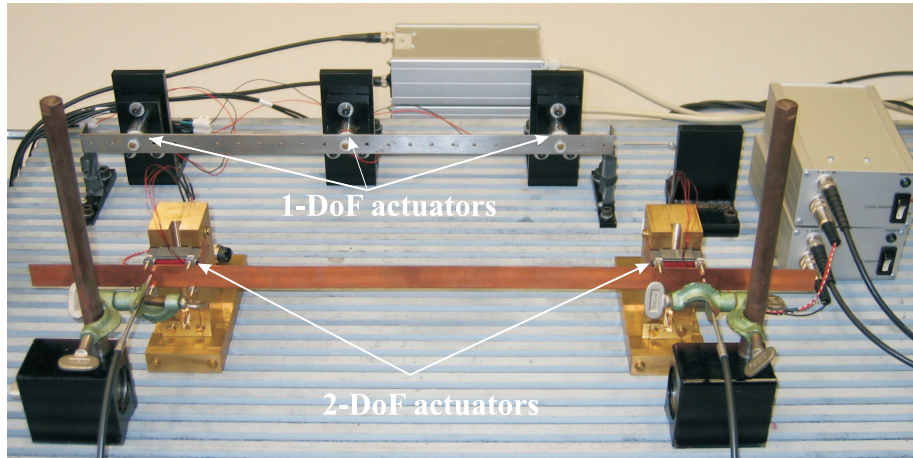
Figure 6.19: Lightweight positioning systems with 1-DoF and 2-DoF actuators.

The difference between the two setups is that in the first case the 1-DoF voice coil actuator in the middle needs a mechanical support, whereas in the second setup the middle support may be left out. This is because the torque, which is equivalent to the one produced between the middle and side actuators in the first setup, is created in the second setup by just one actuator.

In both setups the supports are static parts. However, if such a system is intended to be placed as a high-accuracy positioning module on top of a coarse positioning module, the mass reduction reached by the setup with 2-DoF actuators will be even more significant than in the case of the setup with conventional 1-DoF actuators.

This quite important fact shows that the lightweight positioning principle, combining over-actuation and 2-DoF actuators, can result in an even higher mass reduction and more possibilities for control of the structural vibrations (due to the higher number of control variables) than just the lightweight positioning with over-actuation.

Chapter 7

Conclusions and recommendations for future research

In this chapter, conclusions are drawn form the work described in this thesis and recommendations are made for future research. The conclusions are related to the following objectives:

- to find the most suitable structure for use in lightweight positioning systems,

- to design a 2-DoF electromechanical actuator for this system,

- to derive comprehensive analytical models (electromagnetic and thermal) of the new actuator,

- to optimize the actuator geometry for the selected system dimensions.

7.1 System structure

The lightweight design philosophy focuses on mass reduction of the moving parts in a motion system. Figs. 1.7 and 1.9 illustrate two novel actuation concepts, where light and flexible beams have low frequencies of the dominant vibration modes. In order to control the dominant vibration modes with frequencies lower than the required control bandwidth the placement of actuators is governed by two rules, which are combined in the design of the actuators:

- a vibration mode is not excited if the points of actuation (positions of the actuators) are exactly in the nodes of the mode,

- a vibration mode is controllable if the points of actuation are out of the nodes.

A comparison of the resulting prototypes with flexible beams shows a significant improvement of the system mass-variable factor.

7.2   Innovative 2-DoF actuator

The resulting high mass in current positioning systems is a consequence of a conventional design. Such design puts high demands on power, forces and mass of actuators and power amplifiers, creating the need for new solutions that would soften the requirements. Therefore, the lightweight methodology for precise positioning is investigated. The approach is based on flexible structures actuated by a higher number of actuator-sensor pairs than the number of degrees of freedom of the positioning system. In addition, this over-actuation principle makes use of innovative actuators specially designed for positioning and damping of mechanical vibrations, as described in this thesis. The aim, which has been successfully reached, was to reduce the mass of the stiff beam system. Consequently, the power, forces and mass of the actuators were reduced, while keeping the same control bandwidth as an equivalent high-stiffness positioning system.

The working principle of the lightweight positioning system, presented in this thesis, called for an innovative 2-DoF electromechanical actuator with air coils and permanent magnets. Among several design possibilities, a concept with four force magnets and one torque magnet was chosen for analysis, optimization and prototyping. The innovative nature of the air coil actuator is extensively discussed in this thesis. The basic concept can be used to derive different topologies and modifications of the actuator, and so, to create a customized actuator for various applications.

7.3   Modeling and design

Several models were needed to analyze and design the novel electromechanical actuator. The correctness of the derived models has been verified experimentally. The following conclusions may be drawn regarding these models.

7.3.1   Static electromagnetic analysis

The analysis presented in this thesis starts from an analytical magnetostatic model, based on the theory of magnetic equivalent circuit. The magnetic equivalent circuit was created by decomposing the air gap of the actuator into flux tubes, where the results from FEM modeling were used for the specification of the flux tube shapes and for the verification of the analytical MEC model. It is also important to divide

the air gap of the actuator into a sufficient number of flux tubes in order to capture all important flux paths in the analytical model.

Force and torque were calculated utilizing magnetic flux densities in the air gap found by MEC and FEM models. Two methods of force and torque calculation were implemented, the Lorentz force equation and the method of virtual work, respectively.

The selected concept of the actuator was also built and tested. The measurements of the magnetic flux densities in the air gap of the 2-DoF actuator showed that the estimated magnetic flux densities of both MEC and FEM models highly coincide with the measured ones.

The static force and torque characteristics were also measured. Experimental results proved that the simulation method gives sufficiently precise results in the cases where reluctance forces can be neglected.

Finally, it may be concluded that the resulting MEC model may be used for the magnetostatic design and analysis of the proposed actuator. Moreover, due to the fact that the magnetic flux tubes are coupled to the actuator dimensions, it is also suitable for design optimization where a high number of alternatives with different dimensions is calculated.

7.3.2   Thermal analysis

A 3D thermal model was proposed based on lumped parameters. The modeling method is principally similar to the magnetic equivalent circuit. However, the thermal flux tubes are chosen differently in comparison with the magnetic ones, because heat transfer has a different nature of sources, physical parameters and also different boundary conditions.

The actuator was simulated in 3D FEM to analyze the shapes of the heat fluxes. These simulations confirmed essentially a three-dimensional heat flow. Therefore, the 3D heat flux was composed of three independent one-dimensional heat flows, which increased the number of lumped parameters needed to model the actuator in sufficient details. To reduce the complexity of the model three adiabatic planes were identified. Under symmetric boundary conditions, these planes divided the actuator in eight parts with a symmetric heat flow, which considerably simplified the model.

In the model, thermal convection, conduction and heat generation were considered. For each type of heat transfer, basic one-dimensional equivalent circuits of heat flows were derived based on steady-state equations. In the case of conduction with internal heat generation the equivalent circuit was derived under the assumption of a quadratic temperature distribution, whereas in the case of conduction

without internal heat generation a linear temperature distribution was assumed. The heat capacity of separate parts of the actuator was implemented in the model by means of a capacitor connected between the point with the average temperature of a given part and the point with ambient temperature. In this way, transient states could also be simulated.

Most of the lumped parameters could be determined based on literature information except for the convection coefficient of the coil that had to be determined experimentally.

The behavior of the reduced thermal model was verified by means of an infrared thermography camera allowing to obtain precise temperature measurements on several outer surfaces of the actuator. Comparing these results with the predicted ones it can be concluded that the model reaches sufficient accuracy for steady states as well as transients. However, larger errors can be seen during transients than in steady states. This is due to two assumptions. First, one-dimensional equivalent circuits were derived from a stationary operating condition. Secondly, only quadratic and linear temperature distributions in conducting elements were considered. Nevertheless, the obtained results of the models and measurements showed that the temperature of the actuator can be predicted with reasonable accuracy in all important parts of the actuator.

7.4   Optimization

An essential part of the study elaborated in this thesis is related to optimization. The need for optimization was a central issue to achieve total mass reduction, which was reached by lightweight positioning with respect to conventional positioning. The objective was to find an optimal solution to the problem of total actuator mass minimization at required force and torque. For this purpose a deterministic approach was selected.

The optimization problem was especially defined with careful consideration of different topologies of the 2-DoF actuator so that the number of independent design variables was minimal. The independent variables were coupled to other dimensions of the actuator in a way to ensure always the minimum mass of the actuator in any optimization step. The feasible space was constrained to avoid an extensive investigation of the number of local minima and the search for the global minimum. This has resulted in a nonlinear constrained optimization problem.

To solve the optimization problem a nonlinear optimization technique was proposed. This approach applies the transformation of a constrained optimization into an unconstrained optimization by means of a Lagrangian multiplier function

with penalty terms. This function provides a high penalty for solutions outside the feasible space.

The optimal solution was found in an iterative process, by creating a sequence of unconstrained optimization problems. The sequence converged to local optimal solutions. Because the convexity of the problem was not investigated, optimization from different starting points was used to find as much local minima as possible. The local minima were evaluated and the global minimum was found.

The suggested optimization technique utilized a model of mass, force and torque in an analytical form. Thus, a time consuming FEM-based optimization was not necessary.

The results of the optimization showed that the obtained solution may deviate from the given requirements. This was caused by the geometry dependence of the leakage factors in the MEC model. Therefore, after a few optimization iterations, it is advisable to correct the leakage coefficients of the analytical MEC model by means of FEM, when the dimensions in the magnetic equivalent circuit change significantly from those at the starting point.

7.5   Recommendations

For future developments or improvements of the innovative actuator it is recommended

- to focus on the development of new coil connections, which would not introduce stresses by thermal expansion in the coils and beam structure,

- to investigate topologies that would experience less reluctance force between the coil and field assemblies in case of water cooled coils with high current densities,

- to propose a magnetostatic model that would take reluctance forces into account in the cases where reluctance forces can not be neglected,

- to analyse transient electromagnetic states and eddy current losses in the field assembly and in the magnesium connections,

- to implement parameter identification in the thermal transient modeling based on transient measurements,

- to extend the optimization method with space mapping techniques to reduce the influence of leakage coefficients dependence on the actuator dimensions.

Appendix A

List of symbols

Symbol		Unit
A	cross-section area	m^2
$\vec{A}$	magnetic vector potential	Tm
$\vec{B}$	vector of magnetic flux density	T
B_r	remanent flux density	T
c_p	heat capacity	$J/(kg \cdot K)$
C	magnetic co-energy	J
C_t	thermal capacitance	J/K
$\vec{D}$	vector of electric flux density	C/m^2
$\mathrm{d}\vec{l}$	differential length	m
$\vec{E}$	vector of electric field intensity	V/m
$\dot{E}_g$	rate of energy generaton	W
$\dot{E}_{in}$	rate of energy transfer into a control volume	W
$\dot{E}_{out}$	rate of energy transfer out of a control volume	W
$\dot{E}_{st}$	rate of increase of energy stored within a control volume	W
E_λ	surface emissive power	W/m^2
E_n	feasible variable space	$-$

Symbol		Unit
F	force	N
$\mathcal{F}$	magneto motive force	A
$G_{\lambda abs}$	surface absorbed power	W/m^2
h	convection heat transfer coefficient	$W/(m^2 \cdot K)$
$\vec{H}$	vector of magnetic field intensity	A/m
H_c	coercitive field intensity	A/m
I_{enc}	current enclosed by closed integration path	A
$\vec{J}$	vector of current density	A/m^2
k	thermal conductivity of material	$W/(m \cdot K)$
R_t	thermal resistance	K/W
P_{cu}	copper losses in a coil	W
p	rate of energy generation per unit volume	W/m^3
$\vec{q}''_{cond}$	vector of conduction heat flux	W/m^2
q''_{conv}	convection heat flux	W/m^2
q''_{rad}	net radiation heat flux	W/m^2
Q	electric charge	C
$\vec{r}$	moment arm	m
$\mathcal{R}_m$	magnetic reluctance	A/Wb or $1/H$
t	time	s
T	torque	Nm
T	temperature	$^\circ C$
$\vec{v}$	velocity	m/s
V	volume	m^3
V_{cu}	volume of a coil	m^3
V_m	scalar magnetic potential	A
W_m	magnetic energy	J
$\vec{x}$	vector of design parameters	−
$\vec{x}^*$	optimal vector of design parameters	−
X	subset of E_n	−

Symbol		Unit
α_λ	spectral absorptivity of surface	$-$
∇	Nabla (vector differential) operator	$-$
ϵ	permittivity	F/m
ϵ_λ	spectral emissivity of surface	$-$
λ	wave length of radiation	μm
μ	magnetic permeability	H/m
μ_0	magnetic permeability of free space	H/m
μ_r	relative magnetic permeability	$-$
ρ	mass density	kg/m^3
ρ_ν	volume charge density	C/m^3
σ	electric conductivity	S/m
σ_{SB}	Stefan-Boltzmann constant	$W/m^2 \cdot K^4$
Φ	flux	Wb

Dimensions and material properties of the 2-DoF actuator

Table B.1: Physical properties of magnets.

Material	NdFeB	
Mass density	7350 $kg \cdot m^{-3}$	
Specific heat	440 $J/(kg \cdot K)$	
Thermal conductivity	9 $W/(m \cdot K)$	
Convection heat transfer coefficient	10 $W/(m^2 \cdot K)$	
	Data sheets PM	Measured PM
Force magnet		
Relative magnetic permeability μ_r	1.1	1.044
Remanence B_r	1.2 T	1.11 T
Torque magnet		
Relative magnetic permeability μ_r	1.1	1.184
Remanence B_r	1.2 T	1.24 T
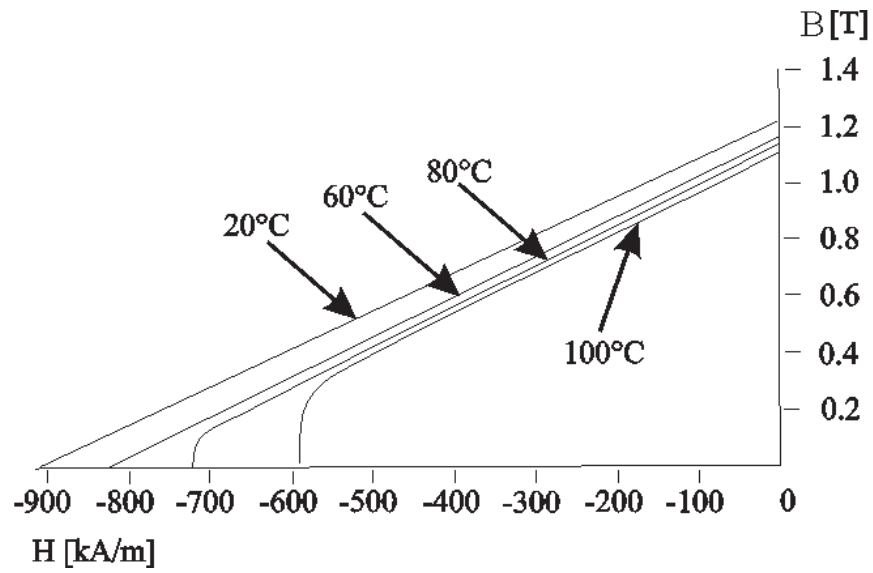
Figure B.1: Demagnetization characteristics of permanent-magnet material (BM 35, NdFeB - Bakker Magnetics).

Table B.2: Physical properties of coils.

Material	Copper
Mass density	$8933\ kg \cdot m^{-3}$
Specific heat	$385\ J/(kg \cdot K)$
Electrical resistivityρ	$167\ \mu\Omega \cdot m$
Nominal current density	$13.8753\ MA \cdot m^{-2}$
Thermal conductivity of the coil	
in direction perpendicular to the coil current flow	$1\ W/(m \cdot K)$
in direction parallel to the coil current flow	$280\ W/(m \cdot K)$
Convection heat transfer coefficient	$38\ W/(m^2 \cdot K)$

Table B.3: Physical properties of the ferromagnetic core.

Material	Cobalt iron (Co-48, V-2)
Mass density	$8120\ kg \cdot m^{-3}$
Specific heat	$440\ J/(kg \cdot K)$
Electrical resistivity ρ	$440\ \mu\Omega \cdot m$
Thermal conductivity	$45\ W/(m \cdot K)$
Convection heat transfer coefficient	$10\ W/(m^2 \cdot K)$
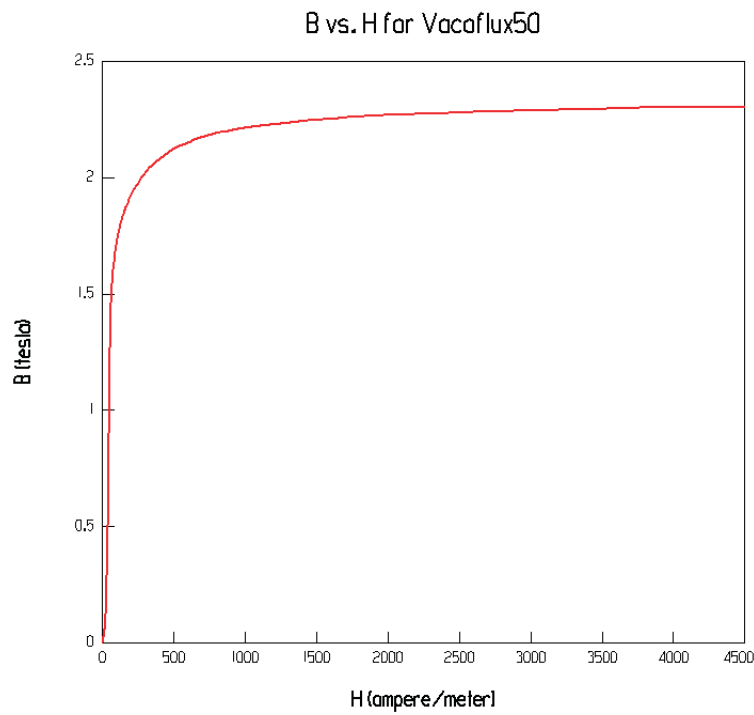
Figure B.2: Magnetization curve of the ferromagnetic material Vacoflux 50.

Table B.4: Physical properties of magnesium.

Mass density	$1770\ kg \cdot m^{-3}$
Specific heat	$1024\ J/(kg \cdot K)$
Thermal conductivity	$156\ W/(m \cdot K)$

Table B.5: Physical properties of the glue.

Material	MESA Industrielijm dik SUPER+
Thermal conductivity	$0.1\ W/(m \cdot K)$

Table B.6: Physical properties of air.

Mass density	$1.1614\ kg \cdot m^{-3}$
Specific heat	$1007\ J/(kg \cdot K)$
Thermal conductivity	$0.026\ W/(m \cdot K)$
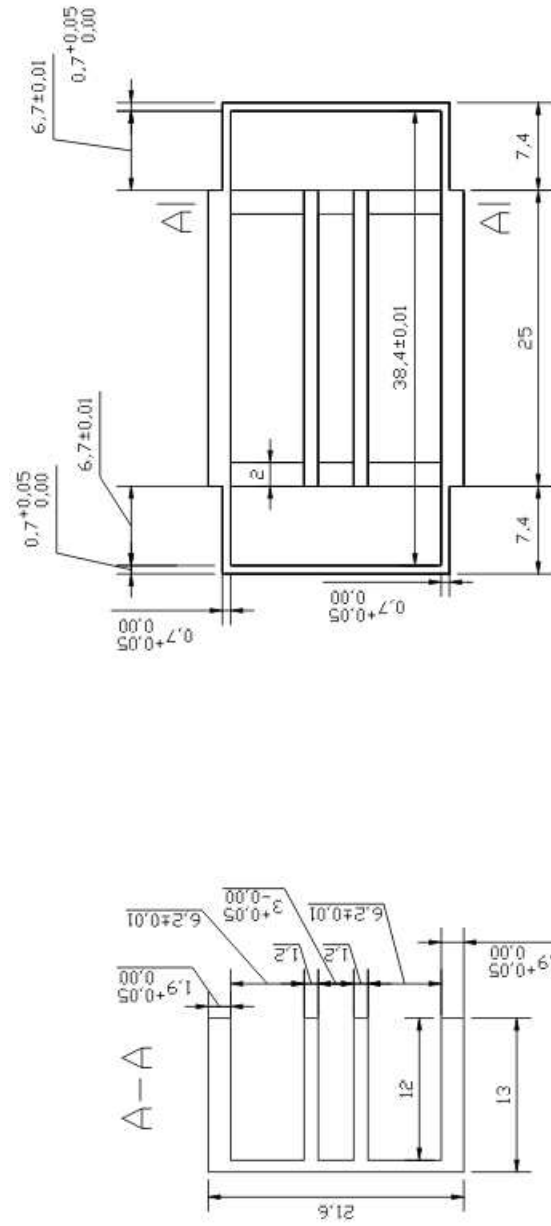
Figure B.3: Ferromagnetic core of the 2-DoF actuator.
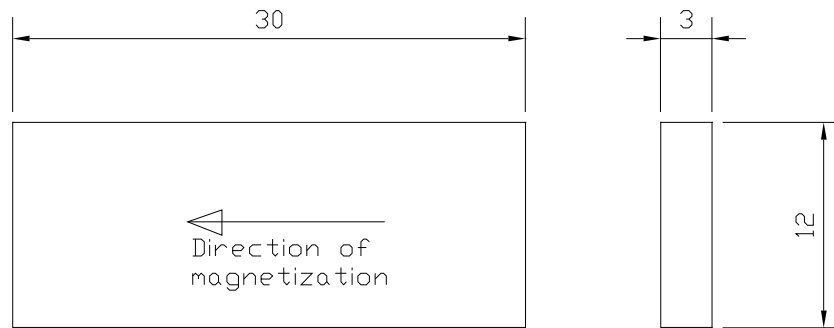
Figure B.4: Torque magnet of the 2-DoF actuator.
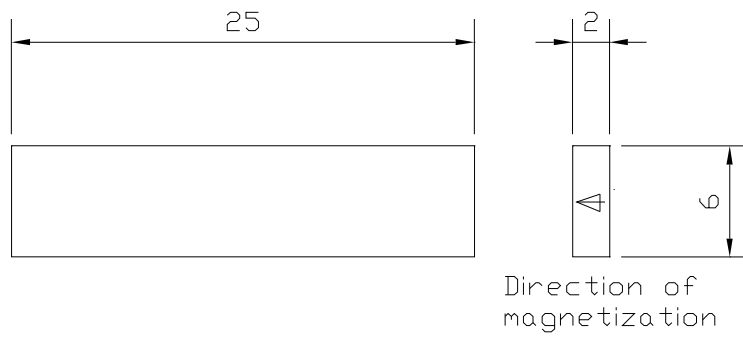
Figure B.5: Force magnet of the 2-DoF actuator.
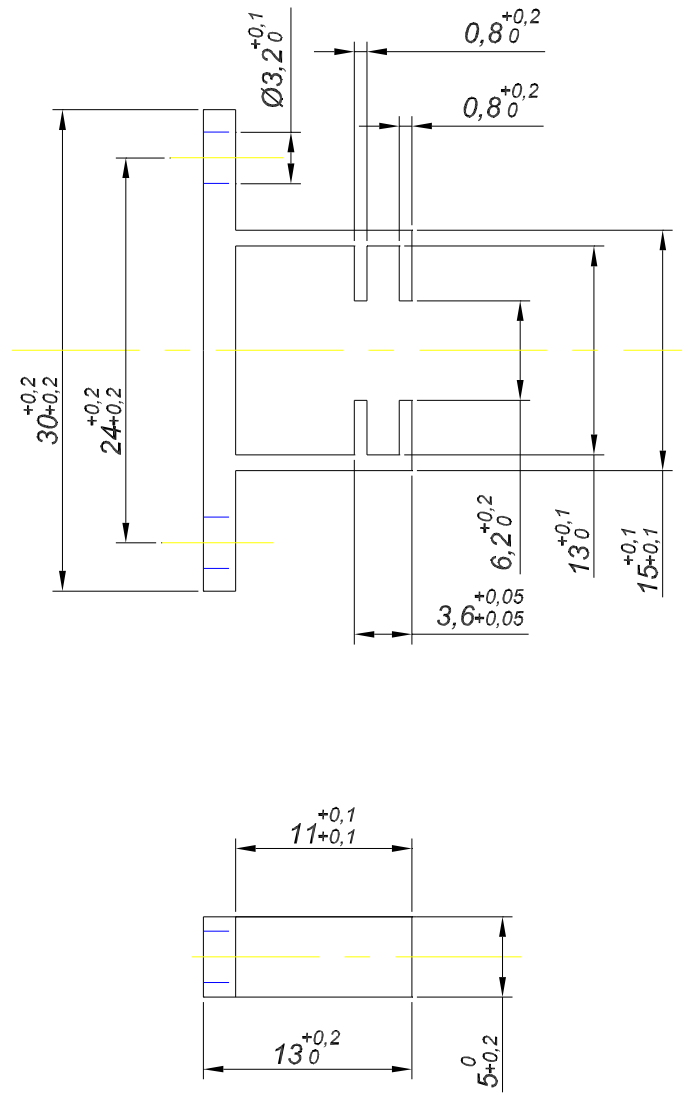
Figure B.6: Magnesium connection of the 2-DoF actuator.
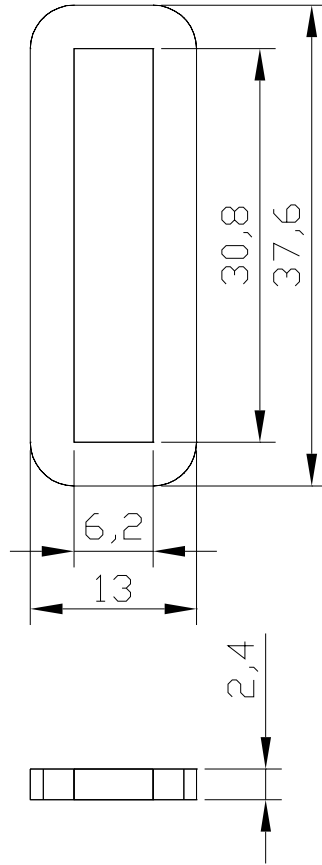
Figure B.7: Coil of the 2-DoF actuator.
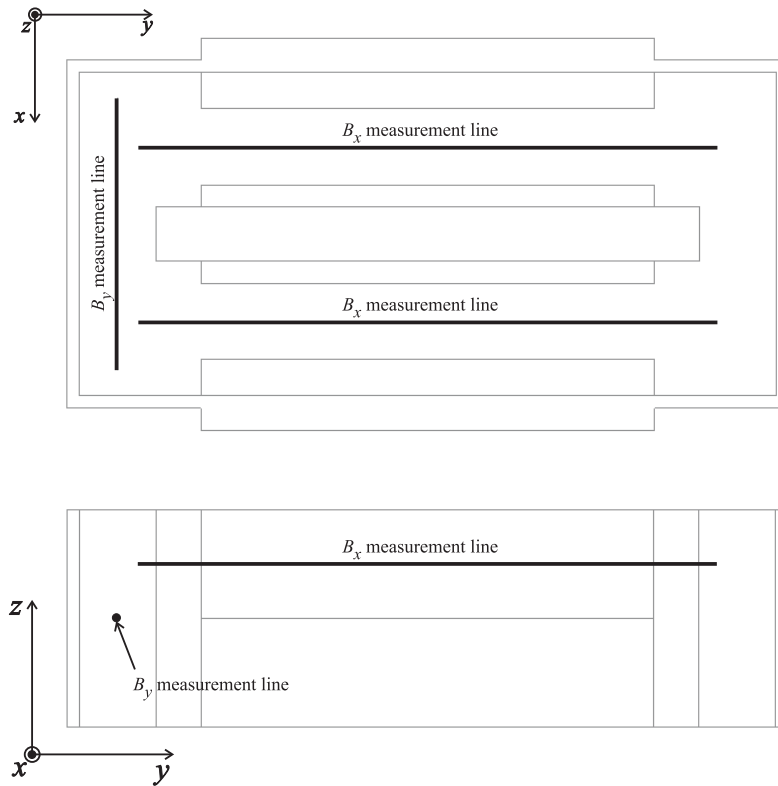
Figure B.8: Lines where B_y of the force magnets and B_x of the torque magnets were measured.

Appendix C

Reluctance calculation of simple solids

Quarter cylinder
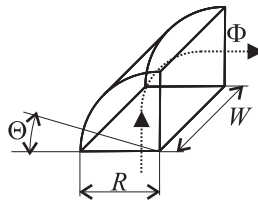
Figure C.1: Quarter cylinder.

$$\mathcal{R}_{mqc} = \frac{1}{\mu} \int_0^{\pi/2} \frac{(R/2)\,\mathrm{d}\Theta}{R \cdot W} = \frac{\pi/4}{\mu \cdot W} \qquad (\mathrm{C.1})$$

183
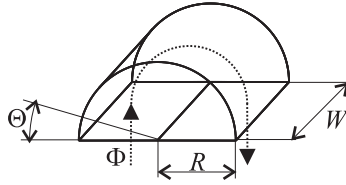
Half cylinder

Figure C.2: Half cylinder.

$$\mathcal{R}_{mhc} = \frac{1}{\mu} \int_0^\pi \frac{(R/2) \, \mathrm{d}\Theta}{R \cdot W} = \frac{\pi/2}{\mu \cdot W} \tag{C.2}$$

Tapered-half cylinder
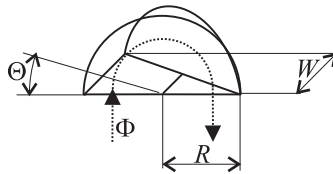
Figure C.3: Tapered-half cylinder.

$$\mathcal{R}_{mthc} = \frac{1}{\mu} \int_0^\pi \frac{(R/2) \, \mathrm{d}\Theta}{\dfrac{W \cdot R}{4} + \left[\dfrac{W \cdot R}{2} \cdot \dfrac{\Theta}{\pi} \right]} = \frac{\pi \ln(3)}{\mu \cdot W} \tag{C.3}$$

Rectangular prism
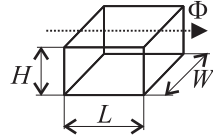
Figure C.4: Rectangular prism.

$$\mathcal{R}_{mrp} = \frac{1}{\mu} \int_0^L \frac{d\ell}{H \cdot W} = \frac{L}{\mu \cdot W \cdot H} \tag{C.4}$$

Trapezoidal prism
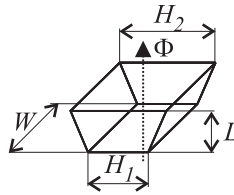
Figure C.5: Trapezoidal prism.

$$\mathcal{R}_{mtp} = \frac{1}{\mu} \int_0^L \frac{d\ell}{W \cdot \left[H_1 + (H_2 - H_1) \frac{\ell}{L} \right]} = \frac{L \cdot (\ln[-H_1 \cdot L] - \ln[-H_2 \cdot L])}{\mu \cdot W \cdot (H_1 - H_2)} \tag{C.5}$$

Triangular prism
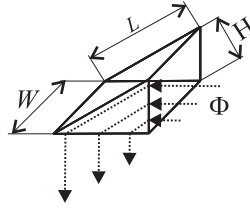
Figure C.6: Triangular prism.

$$\mathcal{R}_{mtrianp} = \frac{1}{\mu} \frac{\frac{2}{3}L}{\frac{W \cdot H}{2}} = \frac{1.333 \cdot L}{\mu \cdot W \cdot H} \tag{C.6}$$

Appendix D

Optimization source code

Optimal design of linear actuator

Minimization of mass of linear actuator for given force and torque (short coil)

Given parameters

```
Br=SetAccuracy[1.2,40];   (*remanence*)

Bsat=SetAccuracy[2.1,40];   (*saturation of steel*)

\[Mu]rpm=SetAccuracy[1.01,40];   (*relative permeability of magnet*)

\[CapitalDelta]=
  SetAccuracy[0.0004,40];   (*tolerance on both sides of winding*)

\[Lambda]c=SetAccuracy[40,40];   (*heat convection constant of coil*)

\[CapitalDelta]T=SetAccuracy[130,40];   (*temperature rise of the coil*)

fill=SetAccuracy[0.7166,40];  (*filling factor of the coil*)

\[Rho]=SetAccuracy[2.73*10^-8,40];   (*resistivity of copper at 155,
  1.67*10^-8 at 20*)

\[Rho]cu=SetAccuracy[8933,40];  (*mass density of copper*)
```

```
\[Rho]fe=SetAccuracy[7870,40]; (*mass density of Fe*)

\[Rho]pm=SetAccuracy[7500,40];    (*mass density of permanent magnet*)

stroke=SetAccuracy[0.004,40];    (*stroke of the actuator*)

F1req=SetAccuracy[1.5,40];    (*required force*)

Treq=SetAccuracy[0.005,40];    (*required torque*)

Massmax=0.050;    (*maximum mass of the actuator*)

(*leakage coefficients*)
L\[Sigma]1=0.08; (*percento z dlzky L1, cez ktore prechadza rozptyl*)

L\[Sigma]mpm=0.08; (*percento leakage medzi magnetmi*)

L\[Sigma]2=0.07;(*percento z dlzky L2, cez ktore prechadza rozptyl*)


(*Data sheet force permanent magnet*)
Brpm1=1.2;   (*remanence,1.22*)

Brpm2=1.2;   (*remanence*)

\[Mu]r1=1.1;   (*relative permeability of magnet, 1.1*)

\[Mu]r2=1.1;   (*relative permeability of magnet*)

(*(*Prototype force permanent magnet*)
  Brpm1=1.11;   (*remanence,1.22*)

  Brpm2=1.11;   (*remanence*)

  \[Mu]r1=1.0436;   (*relative permeability of magnet, 1.01*)

  \[Mu]r2=1.0436;   (*relative permeability of magnet*)*)

(*Data sheet torque permanent magnet*)
BrpmT=1.2;   (*remanence,1.22*)

\[Mu]rT=1.1;   (*relative permeability of magnet, 1.01*)

(*(*Real torque permanent magnet*)
  BrpmT=1.24;   (*remanence,1.22*)

  \[Mu]rT=1.1837;   (*relative permeability of magnet, 1.01*)*)
```

Objective function

```
\!\(\(\(\(\(hmag = hcu + stroke;\)\(\[IndentingNewLine]\)
  \)\[IndentingNewLine]
  \(wT = L1 +
      dcu;\)\  (*\(+2\)*\[CapitalDelta]*) \[IndentingNewLine]\
\[IndentingNewLine]
  \(C1 = wT +
      2*\[CapitalDelta];\)\  (*inner\ length\ of\ coil\ at\ the\ force\ \
magnet*) \[IndentingNewLine]\[IndentingNewLine]
  C2 = L2 + 2*din1 +
      2*\[CapitalDelta]; \  (*innner\ length\ of\ coil\ at\ the\ torque\ \
magnet*) \[IndentingNewLine]\[IndentingNewLine]\[IndentingNewLine]din1 = \
\(\(\((hcu + stroke)\)\^2\ w1\ \(\(\(1\/\(hcu +
                    stroke\)\) \(\(\((L1\ L\[Sigma]1\ \[Pi] +
                  4\ w1)\)\ \(\(2\ Brpm1\ w1\ \(\((L\[Sigma]1\ \[Pi]\ \((4\
\ hcu + L1 + 4\ stroke)\) + 4\ w1)\) +
                  Brpm2\ \(\((L1\ L\[Sigma]1\ \[Pi] +
                      4\ w1)\)\ \(\((2\ w1 + \[Pi]\ \((hcu +
                            stroke)\)\ \[Mu]r1)\) +
                  Brpm1\ \[Pi]\ \((hcu +
                      stroke)\)\ \((L1\ L\[Sigma]1\ \[Pi] +
                      4\ w1)\)\ \[Mu]r2)\))\) + \((8\ Brpm1\ \
L\[Sigma]1\ \[Pi]\ \((dcu +
                      2\ \[CapitalDelta])\)\ \((2\ w1\ \((L\[Sigma]1\ \[Pi]\
\ \((2\ hcu + L1 + 2\ stroke)\) + 4\ w1)\) + \[Pi]\ \((hcu +
                      stroke)\)\ \((L1\ L\[Sigma]1\ \[Pi] +
                      4\ w1)\)\ \[Mu]r2)\)\ \(\(\(-Log[\(-L1\)\ \((dcu \
+ 2\ \[CapitalDelta])\)]\) +
                  Log[L1\ \(\(\(-1\) + L\[Sigma]1)\)\ \((dcu +
                        2\ \[CapitalDelta])\)])\)\)\)\)/\((L\[Sigma]1\ \
\(\(\(-1\) + L\[Sigma]mpm)\)\ \[Pi]\ \((hcu + stroke)\) +
                  2\ \(\(\(-3\) + 2\ L\[Sigma]1)\)\ \((dcu +
                        2\ \[CapitalDelta])\)\ \((Log[\(-L1\)\ \((dcu +
                            2\ \[CapitalDelta])\)] -
                      Log[L1\ \(\(\(-1\) + L\[Sigma]1)\)\ \((dcu +
                            2\ \[CapitalDelta])\)])\)\)\)\)\)\)/\((Bsat\ \
\((w1\ \((L1\ L\[Sigma]1\ \[Pi] +
                      4\ w1)\)\ \((L1\ L\[Sigma]1\ \[Pi]\ \((4\ w1 + \[Pi]\ \
stroke\ \((\[Mu]r1 + \[Mu]r2)\))\) +
                      4\ w1\ \((4\ w1 + \[Pi]\ stroke\ \((2\ L\[Sigma]1 + \
\[Mu]r1 + \[Mu]r2)\))\))\) +
                  hcu\ \[Pi]\ \((4\ w1\ \((\[Mu]r1 + \[Mu]r2)\) +
                      L\[Sigma]1\ \((8\ w1 +
                            L1\ \[Pi]\ \((\[Mu]r1 + \[Mu]r2)\))\))\))\))\) + \
\((2\ \((dcu +
                        2\ \[CapitalDelta])\)\ \((2\ w1\ \((L\[Sigma]1\ \[Pi]\
\ \((2\ hcu + L1 + 2\ stroke)\) + 4\ w1)\) + \[Pi]\ \((hcu +
```

```
                                     stroke)\)\ \((L1\ L\[Sigma]1\ \[Pi] +
                                  4\ w1)\)\ \[Mu]r1)\)\ \((2\ w1\ \((L\[Sigma]1\ \
\[Pi]\ \((2\ hcu + L1 + 2\ stroke)\) + 4\ w1)\) + \[Pi]\ \((hcu +
                                  stroke)\)\ \((L1\ L\[Sigma]1\ \[Pi] +
                                  4\ w1)\)\ \[Mu]r2)\)\ \((\(-Log[\(-L1\)\ \((dcu \
+ 2\ \[CapitalDelta])\)]\) +
                              Log[L1\ \((\(\(-1\) + L\[Sigma]1)\)\ \((dcu +
                                     2\ \[CapitalDelta])\)]\)\)\)\)/\((L\[Sigma]1\ \
\((\(\(-1\) + L\[Sigma]mpm)\)\ \[Pi]\ \((hcu + stroke)\) +
                          2\ \((\(\(-3\) + 2\ L\[Sigma]1)\)\ \((dcu +
                                2\ \[CapitalDelta])\)\ \((Log[\(-L1\)\ \((dcu +
                                      2\ \[CapitalDelta])\)] -
                              Log[L1\ \((\(\(-1\) + L\[Sigma]1)\)\ \((dcu +
                                    2\ \[CapitalDelta])\)])\)\)\)\)\)\);\
\[IndentingNewLine]\[IndentingNewLine]\[IndentingNewLine]
  \(din2 = \((BrpmT\ L2\ \((hcu +
                stroke)\)\ wT\ \((\(1\/\@\((dcu + 2\ \[CapitalDelta])\)\^2\) \
\((0.6665`\ \[Sqrt]\((8\ dcu\^2 + \((2\ din1 + L2\ L\[Sigma]2 + 2\ w1)\)\^2 +
                          8\ \((2\ din1 + L2\ L\[Sigma]2 +
                                2\ w1)\)\ \[CapitalDelta] +
                          32\ \[CapitalDelta]\^2 +
                          4\ dcu\ \((2\ din1 + L2\ L\[Sigma]2 + 2\ w1 +
                                8\ \[CapitalDelta])\))\)\)\ \[Sqrt]\((\(\((8\ \
dcu\^2 + \((2\ din1 + L2\ L\[Sigma]2 + 2\ w1)\)\^2 +
                          8\ \((2\ din1 + L2\ L\[Sigma]2 +
                                2\ w1)\)\ \[CapitalDelta] +
                          32\ \[CapitalDelta]\^2 +
                          4\ dcu\ \((2\ din1 + L2\ L\[Sigma]2 + 2\ w1 +
                                8\ \[CapitalDelta])\))\)\)/\((2\ dcu + 2\ \
din1 + L2\ L\[Sigma]2 + 2\ w1 + 4\ \[CapitalDelta])\)\^2)\)\)\) - \((2\ \((dcu \
+ 2\ \[CapitalDelta])\)\ \((Log[
                                L2\ \((\(\(-1\) + L\[Sigma]2)\)\ \((dcu +
                                      2\ \[CapitalDelta])\)] -
                              Log[\(-\((dcu +
                                      2\ \[CapitalDelta])\)\)\ \((2\ dcu +
                                    2\ din1 + L2 + 2\ w1 +
                                    4\ \[CapitalDelta])\)])\)\)\)/\((2\ dcu +
                        2\ din1 + L2\ L\[Sigma]2 + 2\ w1 +
                        4\ \[CapitalDelta])\) + \((\(\((dcu + din1 + w1 +
                          2\ \[CapitalDelta])\)\ \((\(-Log[\(-\((dcu +
                                      2\ \[CapitalDelta])\)\)\ \((dcu +
                                    din1 + w1 + 2\ \[CapitalDelta])\)]\) +
                              Log[\(-\((L2\ L\[Sigma]2\ \@\((dcu + 2\ \
\[CapitalDelta])\)\^2\ \((dcu + din1 + w1 +
                                          2\ \[CapitalDelta])\)\)\)/\(2\ dcu +
                                    2\ din1 + L2\ L\[Sigma]2 + 2\ w1 +

                                    4\ \[CapitalDelta])\)\)\)])\)\)\)/\((\(\(-dcu\
\) - 2\ \[CapitalDelta] + \(L2\ L\[Sigma]2\ \@\((dcu + 2\ \
```

```
\[CapitalDelta]))\)\^2\)\/\(2\ dcu + 2\ din1 + L2\ L\[Sigma]2 + 2\ w1 + 4\ \
\[CapitalDelta]\))\)))\)\)\)/\((4\ Bsat\ hmag\ \(((\(-\(\((\((2\ L2\ \((dcu +
                    2\ \[CapitalDelta])\)\)\ \[Mu]rT\ \((Log[
                        L2\ \((\(\(-1\) + L\[Sigma]2)\)\ \((dcu +
                            2\ \[CapitalDelta])\)] -
                      Log[\(-\((dcu +
                            2\ \[CapitalDelta])\)\)\)\ \((2\ dcu +
                          2\ din1 + L2 + 2\ w1 +
                          4\ \[CapitalDelta])\)])\)\)\ \(((\((0.6665`\ \
\[Sqrt]\((8\ dcu\^2 + \((2\ din1 + L2\ L\[Sigma]2 + 2\ w1)\)\^2 +
                          8\ \((2\ din1 + L2\ L\[Sigma]2 +
                            2\ w1)\)\ \[CapitalDelta] +
                          32\ \[CapitalDelta]\^2 +
                          4\ dcu\ \((2\ din1 + L2\ L\[Sigma]2 +
                            2\ w1 +
                            8\ \[CapitalDelta])\)\))\)\ \
\[Sqrt]\((\(\((8\ dcu\^2 + \((2\ din1 + L2\ L\[Sigma]2 + 2\ w1)\)\^2 +
                          8\ \((2\ din1 + L2\ L\[Sigma]2 +
                            2\ w1)\)\ \[CapitalDelta] +
                          32\ \[CapitalDelta]\^2 +
                          4\ dcu\ \((2\ din1 + L2\ L\[Sigma]2 +
                            2\ w1 +
                            8\ \[CapitalDelta])\)\))\)\)/\((2\ dcu + \
2\ din1 + L2\ L\[Sigma]2 + 2\ w1 + 4\ \[CapitalDelta])\)\)\^2)\)\))\)/\((\@\((dcu \
+ 2\ \[CapitalDelta])\)\^2)\) + \(((\((dcu + din1 + w1 +
                          2\ \[CapitalDelta])\)\ \
\((\(-Log[\(-\((dcu + 2\ \[CapitalDelta])\)\)\)\ \((dcu + din1 + w1 +
                            2\ \[CapitalDelta])\)]\) +
                      Log[\(-\(\((L2\ L\[Sigma]2\ \@\((dcu + \
2\ \[CapitalDelta])\)\^2\ \((dcu + din1 + w1 +
                            2\ \[CapitalDelta])\)\)\)/\((2\ dcu +
                            2\ din1 + L2\ L\[Sigma]2 + 2\ w1 +
                            4\ \[CapitalDelta])\)\)\)\)])\)\))\)/\((\(\(\
-dcu\) - 2\ \[CapitalDelta] + \(L2\ L\[Sigma]2\ \@\((dcu + 2\ \
\[CapitalDelta])\)\^2\)\/\(2\ dcu + 2\ din1 + L2\ L\[Sigma]2 + 2\ w1 + 4\ \
\[CapitalDelta]\))\)\)\)\)\)/\((2\ dcu + 2\ din1 + L2\ L\[Sigma]2 + 2\ w1 +
                4\ \[CapitalDelta])\)\)\) +
              wT\ \((\(\((0.6665`\ \[Sqrt]\((8\ dcu\^2 + \((2\ din1 + L2\ L\ \
\[Sigma]2 + 2\ w1)\)\^2 + 8\ \((2\ din1 + L2\ L\[Sigma]2 +
                          2\ w1)\)\ \[CapitalDelta] +
                      32\ \[CapitalDelta]\^2 +
                      4\ dcu\ \((2\ din1 + L2\ L\[Sigma]2 +
                          2\ w1 +
                          8\ \[CapitalDelta])\)\))\)\ \
\[Sqrt]\((\(\((8\ dcu\^2 + \((2\ din1 + L2\ L\[Sigma]2 + 2\ w1)\)\^2 +
                      8\ \((2\ din1 + L2\ L\[Sigma]2 +
                          2\ w1)\)\ \[CapitalDelta] +
                      32\ \[CapitalDelta]\^2 +
                      4\ dcu\ \((2\ din1 + L2\ L\[Sigma]2 +
```

```
                                              2\ w1 +
                                              8\ \[CapitalDelta])\)))\)/\((2\ dcu + \
2\ din1 + L2\ L\[Sigma]2 + 2\ w1 + 4\ \[CapitalDelta])\))\^2\)))\)/\((\@\((dcu \
+ 2\ \[CapitalDelta])\)\^2)\) - \((2\ \((dcu +
                                        2\ \[CapitalDelta])\)\ \((Log[
                                          L2\ \((\(\(-1\) + L\[Sigma]2)\)\ \((dcu +
                                              2\ \[CapitalDelta])\)] -
                                        Log[\(-\((dcu +
                                              2\ \[CapitalDelta])\)\)\ \((2\ dcu +
                                              2\ din1 + L2 + 2\ w1 +
                                              4\ \[CapitalDelta])\)])\))\)\)/\((2\ \
dcu + 2\ din1 + L2\ L\[Sigma]2 + 2\ w1 +
                                      4\ \[CapitalDelta])\) + \((\(\((dcu + din1 + w1 +
                                          2\ \[CapitalDelta])\)\ \((\((-Log[\(-\((dcu +
                                              2\ \[CapitalDelta])\)\)]\ \((dcu +
                                              din1 + w1 +
                                              2\ \[CapitalDelta])\)]\) +
                                        Log[\(-\(\((L2\ L\[Sigma]2\ \@((dcu + 2\ \
\[CapitalDelta])\)\)\^2\ \((dcu + din1 + w1 +
                                              2\ \[CapitalDelta])\)\))\)/\((2\ dcu +
                                              2\ din1 + L2\ L\[Sigma]2 + 2\ w1 +
                                              4\ \[CapitalDelta])\)\)\)])\)))\)\)/\((\(\(\
-dcu\) - 2\ \[CapitalDelta] + \(L2\ L\[Sigma]2\ \@((dcu + 2\ \
\[CapitalDelta])\)\)\^2\)\)/\(2\ dcu + 2\ din1 + L2\ L\[Sigma]2 + 2\ w1 + 4\ \
\[CapitalDelta]\)\)\))\))\)\)\);\)\[IndentingNewLine]\[IndentingNewLine]\
\[IndentingNewLine]
  \(Mcu =
      2*\((2*\((C1 + 2*dcu)\)*hcu*dcu +
            2*C2*hcu*
              dcu)\)*\[Rho]cu;\)\ \ \  (*mass\ of\ the\ coil\
*) \[IndentingNewLine]\[IndentingNewLine]
  \(Mmag = \((4*L1*w1*hmag +
            2*L2*wT*hmag)\)*\[Rho]pm;\)\ \ \  (*mass\ of\ permanent\ magnets\
*) \[IndentingNewLine]\[IndentingNewLine]
  \(Mfe = \((4*L1*din1*2*hmag +
            2*\((wT + 4*\[CapitalDelta] + 2*dcu + 2*din2)\)*din2*2*hmag +
            2*\((L2 + 2*din1 + 4*\[CapitalDelta] + 2*dcu + 2*w1)\)*din2*2*
              hmag)\)*\[Rho]fe;\)\ \ \ \  (*mass\ of\ the\ inner\ and\ outter\
\ yoke*) \[IndentingNewLine]\[IndentingNewLine]
  \(Mass[L1_, L2_, w1_, dcu_, hcu_] =
      Mcu + Mmag + Mfe;\)\)\( (*Simplify[\((Mcu + Mmag + Mfe)\),
      TimeConstraint \[Rule] 3]*) \)\)\)
```

Inequality constraints

g1[L1_]=-L1+0.0016;(*+0.002;*)

g2[L1_]=L1-0.05;

```
g3[L2_]=-L2+0.001;(*+0.002;*)

g4[L2_]=L2-0.05;

g5[w1_]=-w1+0.001;(**)

g6[w1_]=w1-0.01;

g9[dcu_]=-dcu+0.0003;

g10[dcu_]=dcu-0.0035;

g11[hcu_]=-hcu+0.0003;

g12[hcu_]=hcu-0.02;

g13[L1_,L2_,w1_,dcu_,hcu_]=Mass[L1,L2,w1,dcu,hcu]-Massmax;
```

Equality constraints

```
\!\(\(\(\(\(F1[L1_, w1_,
        hcu_] = \(-\((2\ \@dcu\ \@fill\ \@hcu\ \@\(dcu + 2\ hcu\)\ L1\ \
\((\(\(-1\) + L\[Sigma]1)\)\ L\[Sigma]1\ \((\(\(-1\) +
                  L\[Sigma]mpm)\)\ \[Pi]\ \((hcu +
                  stroke)\)\ w1\ \((L1\ L\[Sigma]1\ \[Pi] +
                  4\ w1)\)\)\ \@\[CapitalDelta]T\ \@\[Lambda]c\ \((2\ Brpm1\ w1\
\ \((L\[Sigma]1\ \[Pi]\ \((2\ hcu + L1 + 2\ stroke)\) + 4\ w1)\) +
                  2\ Brpm2\ w1\ \((L\[Sigma]1\ \[Pi]\ \((2\ hcu + L1 +
                        2\ stroke)\) + 4\ w1)\) +
                  Brpm2\ \[Pi]\ \((hcu +
                      stroke)\)\ \((L1\ L\[Sigma]1\ \[Pi] +
                      4\ w1)\)\ \[Mu]r1 +
                  Brpm1\ \[Pi]\ \((hcu +
                      stroke)\)\ \((L1\ L\[Sigma]1\ \[Pi] +
                      4\ w1)\)\ \[Mu]r2)\)\)\)\)/\(\(\((1 -
              L\[Sigma]1)\)\ \((1 -
              L\[Sigma]mpm)\)\ \@\[Rho]\ \((L\[Sigma]1\ \((\(\(-1\) +
                  L\[Sigma]mpm)\)\ \[Pi]\ \((hcu + stroke)\) +
                2\ \((\(\(-3\) + 2\ L\[Sigma]1)\)\ \((dcu +
                    2\ \[CapitalDelta])\)\ \((Log[\(-L1\)\ \((dcu +
                          2\ \[CapitalDelta])\)] -
                    Log[L1\ \((\(\(-1\) + L\[Sigma]1)\)\ \((dcu +
                        2\ \[CapitalDelta])\)])\)])\)\)\)\ \((w1\ \((L1\ L\
\[Sigma]1\ \[Pi] +
                  4\ w1)\)\ \((L1\ L\[Sigma]1\ \[Pi]\ \((4\ w1 + \[Pi]\ \
stroke\ \((\[Mu]r1 + \[Mu]r2)\))\) +
                  4\ w1\ \((4\ w1 + \[Pi]\ stroke\ \((2\ L\[Sigma]1 + \
\[Mu]r1 + \[Mu]r2)\))\)\) +
                  hcu\ \[Pi]\ \((4\ w1\ \((\(\[Mu]r1 + \[Mu]r2)\) +
```

```
                        L\[Sigma]1\ \((8\ w1 +
                            L1\ \[Pi]\ \((\(\[Mu]r1 + \[Mu]r2\)\)\)\)\)\)\) \
+ \((2\ \((dcu +
                        2\ \[CapitalDelta])\)\) \((2\ w1\ \((L\[Sigma]1\ \
\[Pi]\ \((2\ hcu + L1 + 2\ stroke)\) + 4\ w1)\) + \[Pi]\ \((hcu +
                            stroke)\)\ \((L1\ L\[Sigma]1\ \[Pi] +
                            4\ w1)\)\ \[Mu]r1)\)\ \((2\ w1\ \((L\[Sigma]1\
\ \[Pi]\ \((2\ hcu + L1 + 2\ stroke)\) + 4\ w1)\) + \[Pi]\ \((hcu +
                            stroke)\)\ \((L1\ L\[Sigma]1\ \[Pi] +
                            4\ w1)\)\ \[Mu]r2)\)\ \((\(\(-Log[\(-L1\)\ \
\((dcu + 2\ \[CapitalDelta])\)]\) +
                        Log[L1\ \((\(\(-1\) + L\[Sigma]1)\)\ \((dcu +
                            2\ \[CapitalDelta])\)]\)\)\)\)/\((L\[Sigma]1\ \
\((\(\(-1\) + L\[Sigma]mpm)\)\ \[Pi]\ \((hcu + stroke)\) +
                    2\ \((\(\(-3\) + 2\ L\[Sigma]1)\)\ \((dcu +
                        2\ \[CapitalDelta])\)\)\ \((Log[\(-L1\)\ \((dcu +
                            2\ \[CapitalDelta])\)] -
                        Log[
                          L1\ \((\(\(-1\) + L\[Sigma]1)\)\ \((dcu +
                            2\ \[CapitalDelta])\)])\)\)\)\)\)\)\);\)\
\[IndentingNewLine]\[IndentingNewLine]\[IndentingNewLine]\[IndentingNewLine]
  \(\(T[L1_, L2_, w1_, dcu_,
        hcu_] = \((BrpmT\ \@dcu\ \@hcu\ \@\(dcu + 2\ hcu)\ L2\ wT\ \((dcu +
                wT + 2\ \[CapitalDelta])\)\ \@\[CapitalDelta]T\ \@\[Lambda]c\ \
\(((\(-\(\(\((\((dcu + 2\ \[CapitalDelta])\)\^2\ \((2\ dcu + 2\ din1 + 3\ L2 -
                    2\ L2\ L\[Sigma]2 + 2\ w1 +
                    4\ \[CapitalDelta])\)\)\ \((Log[
                  L2\ \((\(\(-1\) + L\[Sigma]2)\)\ \((dcu +
                    2\ \[CapitalDelta])\)] -
                Log[\(-\((dcu +
                        2\ \[CapitalDelta])\)\)\)\ \((2\ dcu +
                    2\ din1 + L2 + 2\ w1 +
                    4\ \[CapitalDelta])\)])\)\)\)/\((2\ dcu +
                    2\ din1 + L2\ L\[Sigma]2 + 2\ w1 +
                    4\ \[CapitalDelta])\)\)\)\) + \((dcu\/2 + \
\[CapitalDelta])\)\ \((2\ dcu + 2\ din1 + 2\ L2 - L2\ L\[Sigma]2 +
                    4\ \[CapitalDelta])\)\)\ \((\(\(((0.6665`\ \[Sqrt]\((1 + \(4\
\ dcu\^2\)\)/\((2\ dcu + 2\ din1 + L2\ L\[Sigma]2 + 2\ w1 + 4\ \
\[CapitalDelta])\)\)\^2 + \(16\ dcu\ \[CapitalDelta]\)\)/\((2\ dcu + 2\ din1 + \
L2\ L\[Sigma]2 + 2\ w1 + 4\ \[CapitalDelta])\)\)\^2)\)\ \[Sqrt]\((8\ dcu\^2 + 4\ din1\^2 +
                        L2\^2\ L\[Sigma]2\^2 +
                        4\ L2\ L\[Sigma]2\ w1 + 4\ w1\^2 +
                        8\ L2\ L\[Sigma]2\ \[CapitalDelta] +
                        16\ w1\ \[CapitalDelta] +
                        32\ \[CapitalDelta]\^2 +
                        4\ din1\ \((L2\ L\[Sigma]2 + 2\ w1 +
                            4\ \[CapitalDelta])\) +
```

```
                                                4\ dcu\ \((2\ din1 + L2\ L\[Sigma]2 +
                                                    2\ w1 +
                                                    8\ \[CapitalDelta])\)\)\)\)\)/\((\@\(((\
dcu + 2\ \[CapitalDelta])\)\)\^2)\) + \(((\((dcu + din1 + w1 +
                                                2\ \[CapitalDelta])\)\ \(((\(-Log[\(-\((dcu +
                                                    2\ \[CapitalDelta])\)\)\)\ \((dcu +
                                                    din1 + w1 +
                                                    2\ \[CapitalDelta])\)]\) +
                                                Log[\(-\(\((L2\ L\[Sigma]2\ \@\((dcu + 2\ \
\[CapitalDelta])\)\)\^2\ \((dcu + din1 + w1 +
                                                2\ \[CapitalDelta])\)\)\)/\((2\ dcu +
                                                    2\ din1 + L2\ L\[Sigma]2 + 2\ w1 +
                                                    4\ \[CapitalDelta])\)\)\)\)])\)\)\)\)/\(((\
-dcu\) - 2\ \[CapitalDelta] + \(L2\ L\[Sigma]2\ \@\((dcu + 2\ \
\[CapitalDelta])\)\)\^2\)/\(2\ dcu + 2\ din1 + L2\ L\[Sigma]2 + 2\ w1 + 4\ \
\[CapitalDelta]\))\)\)\)\)\)\)\)/\((\@fill\ \((dcu +
                                                2\ \[CapitalDelta])\)\ \((dcu + din1 + \(3\ L2\)\)/2 -
                                                L2\ L\[Sigma]2 + w1 +
                                                2\ \[CapitalDelta])\)\ \@\[Rho]\ \(((\(-\(\((2\ L2\ \((dcu +
                                                    2\ \[CapitalDelta])\)\ \[Mu]rT\ \((Log[
                                                        L2\ \((\(-1\) + L\[Sigma]2)\)\ \((dcu +
                                                        2\ \[CapitalDelta])\)] -
                                                Log[\(-\((dcu +
                                                    2\ \[CapitalDelta])\)\)\ \((2\ dcu +
                                                    2\ din1 + L2 + 2\ w1 +
                                                    4\ \[CapitalDelta])\)]\)\)\)\ \(((\((0.6665`\ \
\[Sqrt]\((1 + \(4\ dcu\^2\)\)/\((2\ dcu + 2\ din1 + L2\ L\[Sigma]2 + 2\ w1 + 4\
\ \[CapitalDelta])\)\^2 + \(16\ dcu\ \[CapitalDelta]\)/\((2\ dcu + 2\ din1 + \
L2\ L\[Sigma]2 + 2\ w1 + 4\ \[CapitalDelta])\)\^2 + \(16\ \
\[CapitalDelta]\^2\)/\((2\ dcu + 2\ din1 + L2\ L\[Sigma]2 + 2\ w1 + 4\ \
\[CapitalDelta])\)\^2)\)\ \[Sqrt]\((8\ dcu\^2 + 4\ din1\^2 +
                                                L2\^2\ L\[Sigma]2\^2 +
                                                4\ L2\ L\[Sigma]2\ w1 + 4\ w1\^2 +
                                                8\ L2\ L\[Sigma]2\ \[CapitalDelta] +
                                                16\ w1\ \[CapitalDelta] +
                                                32\ \[CapitalDelta]\^2 +
                                                4\ din1\ \((L2\ L\[Sigma]2 + 2\ w1 +
                                                4\ \[CapitalDelta])\) +
                                                4\ dcu\ \((2\ din1 + L2\ L\[Sigma]2 +
                                                2\ w1 +
                                                8\ \[CapitalDelta])\)\)\)\)\)/\((\@\(((\
dcu + 2\ \[CapitalDelta])\)\)\^2)\) + \(((\((dcu + din1 + w1 +
                                                2\ \[CapitalDelta])\)\ \
\(((\(-Log[\(-\((dcu + 2\ \[CapitalDelta])\)\)\)\ \((dcu + din1 + w1 +
                                                2\ \[CapitalDelta])\)]\) +
                                                Log[\(-\(\((L2\ L\[Sigma]2\ \@\((dcu + \
2\ \[CapitalDelta])\)\)\^2\ \((dcu + din1 + w1 +
                                                2\ \[CapitalDelta])\)\)\)/\((2\ dcu +
                                                2\ din1 + L2\ L\[Sigma]2 + 2\ w1 +
```

```
                                                    4\ \[CapitalDelta])\)\)\)])\)\)\)/\((\(\
-dcu\) - 2\ \[CapitalDelta] + \(L2\ L\[Sigma]2\ \@\((dcu + 2\ \
\[CapitalDelta])\))\^2\)\)/\((2\ dcu + 2\ din1 + L2\ L\[Sigma]2 + 2\ w1 + 4\ \
\[CapitalDelta]\))\)\)\)\)\)/\((2\ dcu + 2\ din1 + L2\ L\[Sigma]2 + 2\ w1 +
                            4\ \[CapitalDelta])\)\)\)\) +
                wT\ \((\(\((0.6665`\ \[Sqrt]\((1 + \(4\ dcu\^2\)\)/\((2\ dcu + 2\
\ din1 + L2\ L\[Sigma]2 + 2\ w1 + 4\ \[CapitalDelta])\))\^2 + \(16\ dcu\ \
\[CapitalDelta]\)\)/\((2\ dcu + 2\ din1 + L2\ L\[Sigma]2 + 2\ w1 + 4\ \
\[CapitalDelta])\))\^2 + \(16\ \[CapitalDelta]\^2\)\)/\((2\ dcu + 2\ din1 + L2\ \
L\[Sigma]2 + 2\ w1 + 4\ \[CapitalDelta])\))\^2)\)\ \[Sqrt]\((8\ dcu\^2 +
                                    4\ din1\^2 + L2\^2\ L\[Sigma]2\^2 +
                                    4\ L2\ L\[Sigma]2\ w1 + 4\ w1\^2 +
                                    8\ L2\ L\[Sigma]2\ \[CapitalDelta] +
                                    16\ w1\ \[CapitalDelta] +
                                    32\ \[CapitalDelta]\^2 +
                                    4\ din1\ \((L2\ L\[Sigma]2 + 2\ w1 +
                                        4\ \[CapitalDelta])\) +
                                    4\ dcu\ \((2\ din1 + L2\ L\[Sigma]2 +
                                        2\ w1 +
                                        8\ \[CapitalDelta])\)\)\)\)/\((\(\@\((\
dcu + 2\ \[CapitalDelta])\))\^2)\) - \((2\ \((dcu +
                                        2\ \[CapitalDelta])\)\ \((Log[
                                        L2\ \((\(-1\) + L\[Sigma]2)\)\ \((dcu +
                                        2\ \[CapitalDelta])\)] -
                                    Log[\(-\((dcu +
                                        2\ \[CapitalDelta])\)\)\ \((2\ dcu +
                                        2\ din1 + L2 + 2\ w1 +
                                        4\ \[CapitalDelta])\)])\)\)\)/\((2\ \
dcu + 2\ din1 + L2\ L\[Sigma]2 + 2\ w1 +
                                    4\ \[CapitalDelta])\) + \((\(\((dcu + din1 + w1 +
                                        2\ \[CapitalDelta])\)\ \((\(-Log[\(-\((dcu +
                                        2\ \[CapitalDelta])\)\)\ \((dcu +
                                        din1 + w1 +
                                        2\ \[CapitalDelta])\)]\) +
                                    Log[\(-\(\((L2\ L\[Sigma]2\ \@\((dcu + 2\ \
\[CapitalDelta])\))\^2\ \((dcu + din1 + w1 +
                                        2\ \[CapitalDelta])\)\)\)/\((2\ dcu +
                                        2\ din1 + L2\ L\[Sigma]2 + 2\ w1 +
                                        4\ \[CapitalDelta])\)\)\)]\)\)\)\)/\((\(\
-dcu\) - 2\ \[CapitalDelta] + \(L2\ L\[Sigma]2\ \@\((dcu + 2\ \
\[CapitalDelta])\))\^2\)\)/\((2\ dcu + 2\ din1 + L2\ L\[Sigma]2 + 2\ w1 + 4\ \
\[CapitalDelta]\))\)\)\)\)\)\)\);\)\(\(\[IndentingNewLine]\)
  \)\[IndentingNewLine]
  \(h1[L1_, w1_, dcu_,
        hcu_] = \((F1[L1, w1, dcu, hcu] - F1req)\)\^2;\)\ \  (*required\ \
force*) \[IndentingNewLine]\[IndentingNewLine]
  \(h2[L1_, L2_, w1_, dcu_,
      hcu_] = \((T[L1, L2, w1, dcu, hcu] - Treq)\)\^2;\)\)\(\ \ \ \)\( (*\
    required\ torque*) \)\(\[IndentingNewLine]\)
```

```
  \)\)

Augmented Lagrangian algorithm

Optimization of torque

hess={{0,0,0,0,0},{0,0,0,0,0},{0,0,0,0,0},{0,0,0,0,0},{0,0,0,0,
      0}}; (*initialisation of hessian matrix*)

x0={0.027,0.005,0.001,0.002,0.003};          (*starting point*)

\[Mu]={0.001,0.001,0.001,0.001,0.001,0.001,0,0,0.001,0.001,0.001,0.001,
     0.001};          (*lagrangian multipliers associated with inequalities*)
\


\[Lambda]={1,
     1};                                              \
(*lagrangian multipliers associated with equalities*)

c={1000,1,1000,1,1000,1,0,0,1000,1,1000,1,1000,1000,
     1000};    (*penalty parameter*)

\[Beta]=1.2;                                             \
 (*coefficient for increasing c*)

\[Beta]1=1.10;

\[Gamma]=0.99999;                                        \
 (*coefficient for measure of constrains violation*)

ivioleklow=Infinity;

iviolekup=Infinity;

eviolek=Infinity;

iviolemaxlow=Max[ivioleklow];

iviolemaxup=Max[iviolekup];

eviolemax=Max[eviolek];

eps=10^-12;

deb=0;

ideb1low=0;
```

```
ideb2low=0;

ideb3low=0;

ideb1up=0;

ideb2up=0;

ideb3up=0;

edeb1=0;

edeb2=0;

edeb3=0;

\[Beta]=5;
\[Gamma]=3;

$Line=69;
\[Beta]=5;
\[Gamma]=3;
$HistoryLength=127;

While[(ivioleklow>eps||iviolekup>eps||eviolek>eps),

    Share[];
    sim1[z_,x_]=\[Mu][[1]]*(g1[x]+z^2)+c[[1]]/2*(g1[x]+z^2)^2;
    sim2[z_,x_]=\[Mu][[2]]*(g2[x]+z^2)+c[[2]]/2*(g2[x]+z^2)^2;
    sim3[z_,x_]=\[Mu][[3]]*(g3[x]+z^2)+c[[3]]/2*(g3[x]+z^2)^2;
    sim4[z_,x_]=\[Mu][[4]]*(g4[x]+z^2)+c[[4]]/2*(g4[x]+z^2)^2;
    sim5[z_,x_]=\[Mu][[5]]*(g5[x]+z^2)+c[[5]]/2*(g5[x]+z^2)^2;
    sim6[z_,x_]=\[Mu][[6]]*(g6[x]+z^2)+c[[6]]/2*(g6[x]+z^2)^2;
    sim9[z_,x_]=\[Mu][[9]]*(g9[x]+z^2)+c[[9]]/2*(g9[x]+z^2)^2;
    sim10[z_,x_]=\[Mu][[10]]*(g10[x]+z^2)+c[[10]]/2*(g10[x]+z^2)^2;
    sim11[z_,x_]=\[Mu][[11]]*(g11[x]+z^2)+c[[11]]/2*(g11[x]+z^2)^2;
    sim12[z_,x_]=\[Mu][[12]]*(g12[x]+z^2)+c[[12]]/2*(g12[x]+z^2)^2;
    sim13[z_,L1_,L2_,w1_,dcu_,hcu_]=\[Mu][[13]]*(g13[L1,L2,w1,dcu,hcu]+z^2)+
        c[[15]]/2*(g13[L1,L2,w1,dcu,hcu]+z^2)^2;

    Share[];
    as1=FindMinimum[sim1[z,x0[[1]]],{z,1},MaxIterations\[Rule]500,
        Method\[Rule]Newton];
    as2=FindMinimum[sim2[z,x0[[1]]],{z,1},MaxIterations\[Rule]500,
        Method\[Rule]Newton];
    as3=FindMinimum[sim3[z,x0[[2]]],{z,1},MaxIterations\[Rule]500,
        Method\[Rule]Newton];
    as4=FindMinimum[sim4[z,x0[[2]]],{z,1},MaxIterations\[Rule]500,
        Method\[Rule]Newton];
```

```
as5=FindMinimum[sim5[z,x0[[3]]],{z,1},MaxIterations\[Rule]500,
    Method\[Rule]Newton];
as6=FindMinimum[sim6[z,x0[[3]]],{z,1},MaxIterations\[Rule]500,
    Method\[Rule]Newton];
as9=FindMinimum[sim9[z,x0[[4]]],{z,1},MaxIterations\[Rule]500,
    Method\[Rule]Newton];
as10=FindMinimum[sim10[z,x0[[4]]],{z,1},MaxIterations\[Rule]500,
    Method\[Rule]Newton];
as11=FindMinimum[sim11[z,x0[[5]]],{z,1},MaxIterations\[Rule]500,
    Method\[Rule]Newton];
as12=FindMinimum[sim12[z,x0[[5]]],{z,1},MaxIterations\[Rule]500,
    Method\[Rule]Newton];
as13=FindMinimum[sim13[z,x0[[1]],x0[[2]],x0[[3]],x0[[4]],x0[[5]]],{z,1},
    MaxIterations\[Rule]500,Method\[Rule]Newton];

z1=as1[[2,1,2]];
z2=as2[[2,1,2]];
z3=as3[[2,1,2]];
z4=as4[[2,1,2]];
z5=as5[[2,1,2]];
z6=as6[[2,1,2]];
z9=as9[[2,1,2]];
z10=as10[[2,1,2]];
z11=as11[[2,1,2]];
z12=as12[[2,1,2]];
z13=as13[[2,1,2]];

Share[];
Fe[L1_,w1_,dcu_,hcu_]=\[Lambda][[1]]*h1[L1,w1,dcu,hcu]+
    c[[13]]/2*h1[L1,w1,dcu,hcu]^2;
Te[L1_,L2_,w1,dcu_,hcu_]=\[Lambda][[2]]*h2[L1,L2,w1,dcu,hcu]+
    c[[14]]/2*h2[L1,L2,w1,dcu,hcu]^2;

constrains[L1_,L2_,w1_,dcu_,hcu_,z1_,z2_,z3_,z4_,z5_,z6_,z9_,z10_,z11_,
    z12_,z13_]=
  sim1[z1,L1]+sim2[z2,L1]+sim3[z3,L2]+sim4[z4,L2]+sim5[z5,w1]+sim6[z6,w1]+
    sim9[z9,dcu]+sim10[z10,dcu]+sim11[z11,hcu]+sim12[z12,hcu]+
    sim13[z13,L1,L2,w1,dcu,hcu]+Fe[L1,w1,dcu,hcu]+Te[L1,L2,w1,dcu,hcu];

eq[L1_,L2_,w1_,dcu_,hcu_]=
  Mass[L1,L2,w1,dcu,
      hcu]+(constrains[L1,L2,w1,dcu,hcu,z1,z2,z3,z4,z5,z6,z9,z10,z11,z12,
        z13]);


Share[];
df1[L1_,L2_,w1_,dcu_,hcu_]=
  N[Derivative[1,0,0,0,0][eq][L1,L2,w1,dcu,hcu]];
Share[];
```

```
df2[L1_,L2_,w1_,dcu_,hcu_]=
  N[Derivative[0,1,0,0,0][eq][L1,L2,w1,dcu,hcu]];
Share[];
df3[L1_,L2_,w1_,dcu_,hcu_]=
  N[Derivative[0,0,1,0,0][eq][L1,L2,w1,dcu,hcu]];
Share[];
df4[L1_,L2_,w1_,dcu_,hcu_]=
  N[Derivative[0,0,0,1,0][eq][L1,L2,w1,dcu,hcu]];
Share[];
df5[L1_,L2_,w1_,dcu_,hcu_]=
  N[Derivative[0,0,0,0,1][eq][L1,L2,w1,dcu,hcu]];


(*hess[L1_,L2_,w1_,dcu_,
      hcu_]={{Derivative[2,0,0,0,0][eq][L1,L2,w1,dcu,hcu],
        Derivative[1,1,0,0,0][eq][L1,L2,w1,dcu,hcu],
        Derivative[1,0,1,0,0][eq][L1,L2,w1,dcu,hcu],
        Derivative[1,0,0,1,0][eq][L1,L2,w1,dcu,hcu],
        Derivative[1,0,0,0,1][eq][L1,L2,w1,dcu,
          hcu]},{Derivative[1,1,0,0,0][eq][L1,L2,w1,dcu,hcu],
        Derivative[0,2,0,0,0][eq][L1,L2,w1,dcu,hcu],
        Derivative[0,1,1,0,0][eq][L1,L2,w1,dcu,hcu],
        Derivative[0,1,0,1,0][eq][L1,L2,w1,dcu,hcu],
        Derivative[0,1,0,0,1][eq][L1,L2,w1,dcu,
          hcu]},{Derivative[1,0,1,0,0][eq][L1,L2,w1,dcu,hcu],
        Derivative[0,1,1,0,0][eq][L1,L2,w1,dcu,hcu],
        Derivative[0,0,2,0,0][eq][L1,L2,w1,dcu,hcu],
        Derivative[0,0,1,1,0][eq][L1,L2,w1,dcu,hcu],
        Derivative[0,0,1,0,1][eq][L1,L2,w1,dcu,
          hcu]},{Derivative[1,0,0,1,0][eq][L1,L2,w1,dcu,hcu],
        Derivative[0,1,0,1,0][eq][L1,L2,w1,dcu,hcu],
        Derivative[0,0,1,1,0][eq][L1,L2,w1,dcu,hcu],
        Derivative[0,0,0,2,0][eq][L1,L2,w1,dcu,hcu],
        Derivative[0,0,0,1,1][eq][L1,L2,w1,dcu,
          hcu]},{Derivative[1,0,0,0,1][eq][L1,L2,w1,dcu,hcu],
        Derivative[0,1,0,0,1][eq][L1,L2,w1,dcu,hcu],
        Derivative[0,0,1,0,1][eq][L1,L2,w1,dcu,hcu],
        Derivative[0,0,0,1,1][eq][L1,L2,w1,dcu,hcu],
        Derivative[0,0,0,0,2][eq][L1,L2,w1,dcu,hcu]}};
  xk1=
    x0-(Inverse[hess[x0[[1]],x0[[2]],x0[[3]],x0[[4]],x0[[5]]]].df[x0[[1]],
          x0[[2]],x0[[3]],x0[[4]],x0[[5]]]);
  xaux=x0;*)

ClearCache[];

Share[];
hess[[1,1]]=
  N[Derivative[1,0,0,0,0][df1][x0[[1]],x0[[2]],x0[[3]],x0[[4]],x0[[5]]]];
```

```
Share[];
hess[[1,2]]=
  N[Derivative[0,1,0,0,0][df1][x0[[1]],x0[[2]],x0[[3]],x0[[4]],x0[[5]]]];
Share[];
hess[[1,3]]=
  N[Derivative[0,0,1,0,0][df1][x0[[1]],x0[[2]],x0[[3]],x0[[4]],x0[[5]]]];
Share[];
hess[[1,4]]=
  N[Derivative[0,0,0,1,0][df1][x0[[1]],x0[[2]],x0[[3]],x0[[4]],x0[[5]]]];
Share[];
hess[[1,5]]=
  N[Derivative[0,0,0,0,1][df1][x0[[1]],x0[[2]],x0[[3]],x0[[4]],x0[[5]]]];

ClearCache[];

Share[];
hess[[2,1]]=
  N[Derivative[1,0,0,0,0][df2][x0[[1]],x0[[2]],x0[[3]],x0[[4]],x0[[5]]]];
Share[];
hess[[2,2]]=
  N[Derivative[0,1,0,0,0][df2][x0[[1]],x0[[2]],x0[[3]],x0[[4]],x0[[5]]]];
Share[];
hess[[2,3]]=
  N[Derivative[0,0,1,0,0][df2][x0[[1]],x0[[2]],x0[[3]],x0[[4]],x0[[5]]]];
Share[];
hess[[2,4]]=
  N[Derivative[0,0,0,1,0][df2][x0[[1]],x0[[2]],x0[[3]],x0[[4]],x0[[5]]]];
Share[];
hess[[2,5]]=
  N[Derivative[0,0,0,0,1][df2][x0[[1]],x0[[2]],x0[[3]],x0[[4]],x0[[5]]]];

ClearCache[];

Share[];
hess[[3,1]]=
  N[Derivative[1,0,0,0,0][df3][x0[[1]],x0[[2]],x0[[3]],x0[[4]],x0[[5]]]];
Share[];
hess[[3,2]]=
  N[Derivative[0,1,0,0,0][df3][x0[[1]],x0[[2]],x0[[3]],x0[[4]],x0[[5]]]];
Share[];
hess[[3,3]]=
  N[Derivative[0,0,1,0,0][df3][x0[[1]],x0[[2]],x0[[3]],x0[[4]],x0[[5]]]];
Share[];
hess[[3,4]]=
  N[Derivative[0,0,0,1,0][df3][x0[[1]],x0[[2]],x0[[3]],x0[[4]],x0[[5]]]];
Share[];
hess[[3,5]]=
  N[Derivative[0,0,0,0,1][df3][x0[[1]],x0[[2]],x0[[3]],x0[[4]],x0[[5]]]];
```

```
ClearCache[];

Share[];
hess[[4,1]]=
  N[Derivative[1,0,0,0,0][df4][x0[[1]],x0[[2]],x0[[3]],x0[[4]],x0[[5]]]];
Share[];
hess[[4,2]]=
  N[Derivative[0,1,0,0,0][df4][x0[[1]],x0[[2]],x0[[3]],x0[[4]],x0[[5]]]];
Share[];
hess[[4,3]]=
  N[Derivative[0,0,1,0,0][df4][x0[[1]],x0[[2]],x0[[3]],x0[[4]],x0[[5]]]];
Share[];
hess[[4,4]]=
  N[Derivative[0,0,0,1,0][df4][x0[[1]],x0[[2]],x0[[3]],x0[[4]],x0[[5]]]];
Share[];
hess[[4,5]]=
  N[Derivative[0,0,0,0,1][df4][x0[[1]],x0[[2]],x0[[3]],x0[[4]],x0[[5]]]];

ClearCache[];

Share[];
hess[[5,1]]=
  N[Derivative[1,0,0,0,0][df5][x0[[1]],x0[[2]],x0[[3]],x0[[4]],x0[[5]]]];
Share[];
hess[[5,2]]=
  N[Derivative[0,1,0,0,0][df5][x0[[1]],x0[[2]],x0[[3]],x0[[4]],x0[[5]]]];
Share[];
hess[[5,3]]=
  N[Derivative[0,0,1,0,0][df5][x0[[1]],x0[[2]],x0[[3]],x0[[4]],x0[[5]]]];
Share[];
hess[[5,4]]=
  N[Derivative[0,0,0,1,0][df5][x0[[1]],x0[[2]],x0[[3]],x0[[4]],x0[[5]]]];
Share[];
hess[[5,5]]=
  N[Derivative[0,0,0,0,1][df5][x0[[1]],x0[[2]],x0[[3]],x0[[4]],x0[[5]]]];

ClearCache[];

xk1=Re[
    x0-(Inverse[
          Re[hess]].Re[{df1[x0[[1]],x0[[2]],x0[[3]],x0[[4]],x0[[5]]],
            df2[x0[[1]],x0[[2]],x0[[3]],x0[[4]],x0[[5]]],
            df3[x0[[1]],x0[[2]],x0[[3]],x0[[4]],x0[[5]]],
            df4[x0[[1]],x0[[2]],x0[[3]],x0[[4]],x0[[5]]],
            df5[x0[[1]],x0[[2]],x0[[3]],x0[[4]],x0[[5]]]}])];
xaux=x0;

If[xk1[[1]]\[GreaterEqual]0,x0[[1]]=xk1[[1]],x0[[1]]=0.00001];
If[xk1[[2]]\[GreaterEqual]0,x0[[2]]=xk1[[2]],x0[[2]]=0.00001];
```

```
If[xk1[[3]]\[GreaterEqual]0,x0[[3]]=xk1[[3]],x0[[3]]=0.00001];
If[xk1[[4]]\[GreaterEqual]0,x0[[4]]=xk1[[4]],x0[[4]]=0.00001];
If[xk1[[5]]\[GreaterEqual]0,x0[[5]]=xk1[[5]],x0[[5]]=0.00001];


(*If[xk1[[1]]\[GreaterEqual]0,x0[[1]]=xk1[[1]],x0[[1]]=xaux[[1]];
    c[[1]]=\[Beta]1*c[[1]]];
  If[xk1[[2]]\[GreaterEqual]0,x0[[2]]=xk1[[2]],x0[[2]]=xaux[[2]];
    c[[3]]=\[Beta]1*c[[3]]];
  If[xk1[[3]]\[GreaterEqual]0,x0[[3]]=xk1[[3]],x0[[3]]=xaux[[3]];
    c[[5]]=\[Beta]1*c[[5]]];
  If[xk1[[4]]\[GreaterEqual]0,x0[[4]]=xk1[[4]],x0[[4]]=xaux[[4]];
    c[[9]]=\[Beta]1*c[[9]]];
  If[xk1[[5]]\[GreaterEqual]0,x0[[5]]=xk1[[5]],x0[[5]]=xaux[[5]];
    c[[11]]=\[Beta]1*c[[11]]];*)


iviolemaxlow=
  Max[Abs[{g1[x0[[1]]]+z1^2,g3[x0[[2]]]+z3^2,g5[x0[[3]]]+z5^2,
        g9[x0[[4]]]+z9^2,g11[x0[[5]]]+z11^2}]];
iviolemaxup=
  Max[Abs[{g2[x0[[1]]]+z2^2,g4[x0[[2]]]+z4^2,g6[x0[[3]]]+z6^2,
        g10[x0[[4]]]+z10^2,g12[x0[[5]]]+z12^2,
        g13[x0[[1]],x0[[2]],x0[[3]],x0[[4]],x0[[5]]]+z13^2}]];

eviolemax=
  Max[{Abs[h1[x0[[1]],x0[[3]],x0[[4]],x0[[5]]]],
      Abs[h2[x0[[1]],x0[[2]],x0[[3]],x0[[4]],x0[[5]]]]}];

If[iviolemaxlow<eps,
  ideb1low=ideb1low+1;
  ,

  If[iviolemaxlow\[LessEqual]ivioleklow*\[Gamma],
    ideb2low=1+ideb2low;
    \[Mu][[1]]=\[Mu][[1]]+c[[1]]*Max[g1[x0[[1]]],-\[Mu][[1]]/c[[1]]];
    \[Mu][[3]]=\[Mu][[3]]+c[[3]]*Max[g3[x0[[2]]],-\[Mu][[3]]/c[[3]]];
    \[Mu][[5]]=\[Mu][[5]]+c[[5]]*Max[g5[x0[[3]]],-\[Mu][[5]]/c[[5]]];
    \[Mu][[9]]=\[Mu][[9]]+c[[9]]*Max[g9[x0[[4]]],-\[Mu][[9]]/c[[9]]];
    \[Mu][[11]]=\[Mu][[11]]+
        c[[11]]*Max[g11[x0[[5]]],-\[Mu][[11]]/c[[11]]];
    ,

    ideb3low=1+ideb3low;
    If[Abs[g1[x0[[1]]]+z1^2]>ivioleklow*\[Gamma],c[[1]]=\[Beta]*c[[1]]];
    If[Abs[g3[x0[[2]]]+z3^2]>ivioleklow*\[Gamma],c[[3]]=\[Beta]*c[[3]]];
    If[Abs[g5[x0[[3]]]+z5^2]>ivioleklow*\[Gamma],c[[5]]=\[Beta]*c[[5]]];
    If[Abs[g9[x0[[4]]]+z9^2]>ivioleklow*\[Gamma],c[[9]]=\[Beta]*c[[9]]];
    If[Abs[g11[x0[[5]]]+z11^2]>ivioleklow*\[Gamma],
```

```
        c[[11]]=\[Beta]*c[[11]]];

    \[Mu][[1]]=\[Mu][[1]]+c[[1]]*Max[g1[x0[[1]]],-\[Mu][[1]]/c[[1]]];
    \[Mu][[3]]=\[Mu][[3]]+c[[3]]*Max[g3[x0[[2]]],-\[Mu][[3]]/c[[3]]];
    \[Mu][[5]]=\[Mu][[5]]+c[[5]]*Max[g5[x0[[3]]],-\[Mu][[5]]/c[[5]]];
    \[Mu][[9]]=\[Mu][[9]]+c[[9]]*Max[g9[x0[[4]]],-\[Mu][[9]]/c[[9]]];
    \[Mu][[11]]=\[Mu][[11]]+
        c[[11]]*Max[g11[x0[[5]]],-\[Mu][[11]]/c[[11]]];

    ]];

If[iviolemaxup<eps,
  ideb1up=ideb1up+1;
  ,

  If[iviolemaxup\[LessEqual]iviolekup*\[Gamma],
    ideb2up=1+ideb2up;
    \[Mu][[2]]=\[Mu][[2]]+c[[2]]*Max[g2[x0[[1]]],-\[Mu][[2]]/c[[2]]];
    \[Mu][[4]]=\[Mu][[4]]+c[[4]]*Max[g4[x0[[2]]],-\[Mu][[4]]/c[[4]]];
    \[Mu][[6]]=\[Mu][[6]]+c[[6]]*Max[g6[x0[[3]]],-\[Mu][[6]]/c[[6]]];
    \[Mu][[10]]=\[Mu][[10]]+
        c[[10]]*Max[g10[x0[[4]]],-\[Mu][[10]]/c[[10]]];
    \[Mu][[12]]=\[Mu][[12]]+
        c[[12]]*Max[g12[x0[[5]]],-\[Mu][[12]]/c[[12]]];
    \[Mu][[13]]=\[Mu][[13]]+
        c[[15]]*Max[
            Re[g13[x0[[1]],x0[[2]],x0[[3]],x0[[4]],x0[[5]]]],-\[Mu][[13]]/
              c[[15]]];
    ,

    ideb3up=1+ideb3up;
    If[Abs[g2[x0[[1]]]+z2^2]>iviolekup*\[Gamma],c[[2]]=\[Beta]*c[[2]]];
    If[Abs[g4[x0[[2]]]+z4^2]>iviolekup*\[Gamma],c[[4]]=\[Beta]*c[[4]]];
    If[Abs[g6[x0[[3]]]+z6^2]>iviolekup*\[Gamma],c[[6]]=\[Beta]*c[[6]]];
    If[Abs[g10[x0[[4]]]+z10^2]>iviolekup*\[Gamma],
      c[[10]]=\[Beta]*c[[10]]];
    If[Abs[g12[x0[[5]]]+z12^2]>iviolekup*\[Gamma],
      c[[12]]=\[Beta]*c[[12]]];
    If[
      Abs[g13[x0[[1]],x0[[2]],x0[[3]],x0[[4]],x0[[5]]]+z13^2]>
        iviolekup*\[Gamma],c[[15]]=\[Beta]*c[[15]]];

    \[Mu][[2]]=\[Mu][[2]]+c[[2]]*Max[g2[x0[[1]]],-\[Mu][[2]]/c[[2]]];
    \[Mu][[4]]=\[Mu][[4]]+c[[4]]*Max[g4[x0[[2]]],-\[Mu][[4]]/c[[4]]];
    \[Mu][[6]]=\[Mu][[6]]+c[[6]]*Max[g6[x0[[3]]],-\[Mu][[6]]/c[[6]]];
    \[Mu][[10]]=\[Mu][[10]]+
        c[[10]]*Max[g10[x0[[4]]],-\[Mu][[10]]/c[[10]]];
    \[Mu][[12]]=\[Mu][[12]]+
        c[[12]]*Max[g12[x0[[5]]],-\[Mu][[12]]/c[[12]]];
```

```
        \[Mu][[13]]=\[Mu][[13]]+
            c[[15]]*Max[
                Re[g13[x0[[1]],x0[[2]],x0[[3]],x0[[4]],x0[[5]]]],-\[Mu][[13]]/
                  c[[15]]]];

        ]];

    If[eviolemax<eps,
      edeb1=edeb1+1;
      ,

      If[eviolemax\[LessEqual]eviolek*\[Gamma],
        edeb2=1+edeb2;
        \[Lambda]={\[Lambda][[1]]+
              c[[13]]*h1[x0[[1]],x0[[3]],x0[[4]],x0[[5]]],
            \[Lambda][[2]]+
              c[[14]]*h2[x0[[1]],x0[[2]],x0[[3]],x0[[4]],x0[[5]]]};

        ,


        edeb3=1+edeb3;
        If[Abs[h1[x0[[1]],x0[[3]],x0[[4]],x0[[5]]]]>eviolek*\[Gamma],
          c[[13]]=\[Beta]*c[[13]]];
        If[Abs[h2[x0[[1]],x0[[2]],x0[[3]],x0[[4]],x0[[5]]]]>eviolek*\[Gamma],
          c[[14]]=\[Beta]*c[[14]]];

        \[Lambda]={\[Lambda][[1]]+
              c[[13]]*h1[x0[[1]],x0[[3]],x0[[4]],x0[[3]]],
            \[Lambda][[2]]+
              c[[14]]*h2[x0[[1]],x0[[2]],x0[[3]],x0[[4]],x0[[3]]]};


        ]];

    ivioleklow=iviolemaxlow;
    iviolekup=iviolemaxup;
    eviolek=eviolemax;
    Print[{ivioleklow,iviolekup,eviolek, "     ",
        F1[x0[[1]],x0[[3]],x0[[4]],x0[[5]]],"     ",
        T[x0[[1]],x0[[2]],x0[[3]],x0[[4]],x0[[5]]],"     ",
        Mass[x0[[1]],x0[[2]],x0[[3]],x0[[4]],x0[[5]]]}];
    ClearCache[];
    ];
$HistoryLength=\[Infinity];

Print[{ivioleklow,iviolekup,eviolek, "     ",
      F1[x0[[1]],x0[[3]],x0[[4]],x0[[5]]],"     ",
      T[x0[[1]],x0[[2]],x0[[3]],x0[[4]],x0[[5]]],"     ",
      Mass[x0[[1]],x0[[2]],x0[[3]],x0[[4]],x0[[5]]]}];
```

```
\[Mu]
\[Lambda]
c
{ideb1low,ideb2low,ideb3low}
{ideb1up,ideb2up,ideb3up}
{edeb1,edeb2,edeb3}
```

Bibliography

[1] J. Makarovic, M. G. E. Schneiders, A. M. van der Wielen, E. Lomonova, M. J. G. van de Molengraft, R. M. van Druten, J. C. Compter, M. Steinbuch, and P. H. J. Schellekens, "Integrated design of a lightweight positioning system," in *Proc. 7th International Conference on Motion and Vibration Control*, St. Louis, USA, Aug. 2004, pp. 1–10.

[2] M. G. E. Schneiders, J. Makarovic, M. J. G. van de Molengraft, and M. Steinbuch, "Design considerations for electromechanical actuation in precision motion systems," in *16th IFAC World Congress*, Prague, Czech Republic, July 2005, pp. 1–6.

[3] M. G. E. Schneiders, M. J. G. van de Molengraft, and M. Steinbuch, "Modal framework for closed-loop analysis of over-actuated motion systems," in *Proceedings of the 2004 ASME International Mechanical Engineering Congres*, Anaheim, California, USA, Nov. 2004, pp. 1–6.

[4] ——, "Benefits of over-actuation in motion systems," in *Proceeding of the 2004 American Control Conference*, Boston, Massachusetts, USA, June 2004, pp. 505–510.

[5] M. G. E. Schneiders, "Over-actuated motion control - a modal approach," Ph.D. dissertation, Eindhoven University of Technology, 2006, in preparation.

[6] A. M. van der Wielen, "Mechanical design of lightweight positioning system," Ph.D. dissertation, Eindhoven University of Technology, 2006, in preparation.

[7] H. M. J. R. Soemers, "Design of high performance manipulators," in *International Conference on Advance Intelligent Mechatronics Proceedings*, Como, Italy, July 2001, pp. 26–31.

[8] D. Mead, *Passive Vibration Control*.   London, England: John Wiley & Sons Ltd., 1998.

[9] C. R. Fuller, S. J. Elliott, and P. A. Nelson, *Active Control of Vibration*.   London, England: Academic Press, 1996.

[10] J. Holterman, "Vibration control of high-precision machines with active structural elements," Ph.D. dissertation, University of Twente, 2002.

[11] F. M. Carter and D. Stenabaugh, "System for reducing the effect of reactive forces on a stage using a balance mass," U.S. Patent US2 004 160 203, 2004.

[12] E. Saffert, C. Schäffel, and E. Kallenbach, "Planar multi-coordinate drives," in *Proceedings of Power Conversion and Intelligent Motion*, Nurnberg, Germany, May 1998, pp. 1–8.

[13] W. J. Kim, "High-precision planar magnetic levitator," Ph.D. dissertation, Massachusetts Institute of Technology, 1997.

[14] J. C. Compter, P. C. M. Frissen, A. J. A. Peijnenburg, and E. R. Loopstra, "Displacement device," European Patent WO 01/18 944 A1, 2001.

[15] J. C. Compter, "Electro-dynamic planar motor," *Elsevier - Precision Engineering*, vol. 28, no. 2, pp. 171–180, Apr. 2004.

[16] L. Molenaar, "A novel planar magnetic bearing and motor configuration applied in a positioning stage," Ph.D. dissertation, Technische Universiteit Delft, 2000.

[17] A. V. Lebedev, E. A. Lomonova, P. G. V. Leuven, J. Steinberg, and D. A. H. Laro, "Analysis and initial synthesis of a novel linear actuator with active magnetic suspension," in *Conference Record of the 39th Annual Meeting of Industry Applications Society*, Seattle, USA, Oct. 2004, pp. 2111–2118.

[18] J. P. Yonnet and G. Akoun, "3D analytical calculation of the forces exerted between two cuboidal magnets," *IEEE Trans. Magn.*, vol. 20, no. 5, pp. 1962–1964, 1984.

[19] J. C. Compter, E. A. Lomonova, and J. Makarovic, "Direct 3D analytical method for performance prediction of linear moving coil actuator with various topologies," *IEE Proceedings - Science, Measurement and Technology*, vol. 150, no. 4, pp. 183–191, July 2003.

[20] B. Hague, *The principles of electromagnetism, applied to electrical machines.* New York, USA: Dover publications, 1962.

[21] Y. Kano, T. Kosaka, and N. Matsui, "Simple non-linear magnetic analysis for permanent magnets motors," in *Electric Machines and Drives IEEE International Conference*, June 2003, pp. 1201–1207.

[22] N. Matsui, M. Nakamura, and T. Kosaka, "Instantaneous torque analysis of hybrid stepping motor," *IEEE Transactions on Industry Applications*, vol. 32, no. 5, pp. 1176 – 1182, Sept. 1996.

[23] E. J. Rothwell and M. J. Cloud, *Electromagnetics.* Boca Raton, USA: CRC Press, 2001.

[24] E. R. Laithwaite, "Magnetic equivalent circuits for electric machines," *Proc. IEE*, vol. 114, no. 11, pp. 1805–1809, Nov. 1967.

[25] C. J. Carpenter, "Magnetic equivalent circuits," *Proc. IEE*, vol. 115, no. 10, pp. 1503–1511, Oct. 1968.

[26] V. Ostović, *Dynamics of saturated electric machines.* Berlin Heidelberg, Germany: Springer-Verlag New York Inc., 1989.

[27] H. C. Roters, *Electromagnetic devices.* New York, USA: John Wiley & Sons, Inc., 1955.

[28] J. Jin, *The finite element method in electromagnetics.* New York, USA: John Wiley & Sons, Inc., 2002.

[29] A. B. J. Reece and T. W. Preston, *Finite element method in electrical power engineering.* Oxford, UK: Oxford University press, 2000.

[30] J. L. Coulomb, "A methodology for the determination of global electromechanical quantities from a finite element analysis and its application to the evaluation of magnetic forces, torques and stifness," *IEEE Trans. Magn.*, vol. Mag-19, no. 6, pp. 2514–2519, Nov. 1983.

[31] J. L. Coulomb and G. Meunier, "Finite element implementation of the virtual work principle for magnetic or electric force and torque computation," *IEEE Trans. Magn.*, vol. Mag-20, no. 5, pp. 1503–1511, Sept. 1984.

[32] F. P. Incropera and D. P. DeWitt, *Fundamentals of heat and mass transfer*. New York, USA: John Wiley & Sons, Inc., 2002.

[33] F. Kreith and M. S. Bohn, *Principles of heat transfer*. New York, USA: Thomson-Engineering, 2000.

[34] G. Henneberger, K. B. Yahia, and M. Schmitz, "Calculation and identification of a thermal equivalent circuit of a water cooled induction motor for electric vehicle applications," in *Proceedings of Electric Machines and Drives conference*, Durham, UK, Sept. 1995, pp. 6–10.

[35] G. Swift, T. S. Molinski, and W. Lehn, "A fundamental approach to transformer thermal modeling: I. theory and equivalent circuit," *IEEE Transaction on Power Delivery*, vol. 16, no. 2, pp. 171–175, Apr. 2001.

[36] W. H. Tang, Q. H. Wu, and Z. J. Richardson, "Equivalent heat circuit based power transformer thermal model," *IEE Proceedings: Electric Power Applications*, vol. 149, no. 2, pp. 87–92, Mar. 2002.

[37] C. R. Soderberg, "Steady flow of heat in large turbine-generators," *AIEE Transactions*, vol. 50, pp. 787–802, Jan. 1931.

[38] I. J. Perez and J. G. Kassakian, "A stationary thermal model for smooth air-gap rotating electric machines," *Electric Machines and Electromechanics*, no. 3, pp. 285–303, 1979.

[39] Z. J. Liu, D. Howe, P. H. Mellor, and M. K. Jenkins, "Thermal analysis of permanent magnet machines," in *Proceedings of Electric Machines and Drives conference*, Oxford, UK, Sept. 1993, pp. 359 – 364.

[40] P. H. Mellor, D. Roberts, and D. R. Turner, "Lumped parameter thermal model for electrical machines of tefc design," *IEEE Proceedings-B*, vol. 138, no. 5, pp. 205–218, Sept. 1991.

[41] A. Boglietti, A. Cavagnino, A. Lazzari, and M. Pastorelli, "A simplified thermal model for variable-speed self-cooled industrial induction motor," *IEEE Transaction on Inductry Applications*, vol. 39, no. 4, pp. 945–952, Sept. 2003.

[42] J. F. Gieras and M. Wing, *Permanent magnet motor technology : design and applications*. New York, USA: Marcel Dekker, 2002.

[43] S. A. Nasar, *Handbook of electric machines*. London, UK: McGraw-Hill, 1987.

[44] A. Basak, *Permanent-magnet DC linear motors*. Oxford, UK: Clarendon Press, 1996.

[45] M. S. Bazaraa, H. D. Sherali, and C. M. Shetty, *Nonlinear programming, Theory and algorithms*. New York, USA: John Wiley & Sons, Inc., 1993.

[46] D. P. Bertsekas, *Nonlinear programming*. Belmont, USA: Athena Scientific, 1995.

[47] J. Yoo, "Modified method of topology optimization in magnetic fields," *IEEE Trans. Magn.*, vol. 40, no. 4, pp. 1796–1802, July 2004.

[48] N. Boules, "Design optimization of permanent magnet dc motors," *IEEE Transaction on industry applications*, vol. 26, no. 4, pp. 786–792, July 1990.

[49] J. Makarovic, J. C. Compter, and E. A. Lomonova, "Wire-bonder multiobjective optimization," in *Proceedings of 4th International Symposium on Linear Drives for Industry Applications*, Birmingham, UK, Sept. 2003, pp. 51–54.

[50] J. Makarovic, E. A. Lomonova, and J. C. Compter, "Constrained design optimization of voice coil actuator for light-weight positioning system," in *Proceedings of International Workshop on Optimization and Inverse Problems in Electromagnetism*, Grenoble, France, Sept. 2004.

[51] Raphson, *Analysis aequationum universalis*, London, UK, 1690.

[52] L. Encica, J. Makarovic, E. A. Lomonova, and A. J. A. Vandenput, "Space mapping optimization of a cylindrical voice coil actuator," in *IEEE International Conference on Electric Machines and Drives*, May 2005, pp. 831 – 1837.

[53] F. Sahin, "Design and development of a high-speed axial-flux permanent-magnet machine," Ph.D. dissertation, Technische Universiteit Eindhoven, 2001.

Summary

It is known that internal vibrations decrease the performance characteristics and life time of mechanisms, and in some cases they even may lead to mechanical failures. In motion systems used in precision technology (wafer scanners, scanners, pick-and-place machines for production of PCBs, wire-bonders etc.), internal vibrations limit the performance parameters. The vibrations are still a challenge for the generally accepted design approach at present time, which is heading towards higher system accuracy, speed and throughput.

Currently, the design approach to precision positioning applications places the dominant vibration frequencies of the mechanical parts several times higher than the required control bandwidth. However, these high mechanical frequencies are reached by constructing the mechanical parts with high stiffness, often at the cost of relatively high mass.

To eliminate the negative consequences of the classical methodology, another design philosophy is used in this thesis. A three-disciplinary lightweight positioning approach (control, mechanics and electromechanics) focuses on mass reduction of the moving parts of motion systems. For this purpose, a principle based on over-actuation is used, which allows designing a lighter overall kinematical structure (force-path).

In order to evaluate this approach on a general level, benchmarks for classical and lightweight positioning systems are proposed, namely, a so-called stiff beam system and a flexible beam system.

The main focus of the thesis is on the design and optimization of a novel Lorentz force actuator for a lightweight positioning system that can also be applied in other precision technology applications. The objective is to reach the maximum mass reduction of the flexible beam system.

In order to evaluate and design the novel actuator, a comprehensive static electromagnetic analysis of the actuator is elaborated. The resulting analytical model is based on a magnetic equivalent circuit, which has been identified by means of preliminary finite element calculations. The analytical model plays an essential role in the complete design. It is later used for the optimal dimensioning of the actuator for required performance specifications. Then, a numerical finite element model is built and the results are used to evaluate the accuracy of the analytical model and to identify parasitic forces and torques of the actuator.

Another important aspect that determines the operating conditions is the thermal behavior of the actuator. It is also described analytically by a thermal lumped parameter model. The suggested description of the heat transfer captures the static as well as the dynamic behavior.

To determine the optimal dimensions of the actuator an optimization approach, which uses the magnetic equivalent circuit and the thermal analytical model, is proposed. In terms of nonlinear programming, the problem statement consists of finding the dimensions of the actuator with minimal mass, where given force and torque are used as constraints. Because of the nonlinear nature of the problem the optimal solution is found numerically. The resulting optimal

actuator incorporating two degrees of freedom (DoF) has 22.2% less mass than two equivalent 1-DoF actuators.

It may be concluded, based on simulation and measurement results, that the proposed actuator can be analyzed with sufficient accuracy by the presented methods.

The invented short-stroke actuator uniquely combines two controlled degrees of freedom: translational and rotational. This combination ensures that the mass of the actuators used in the flexible beam system has been reduced compared to that in the stiff beam system. The actuators support the flexible beam system in a way that introduces less disturbances. Meanwhile, the controllability of higher order vibration modes and, consequently, the global performance are improved.

Two lightweight positioning systems were built, one with three 1-DoF actuators and the other with two novel Lorentz force actuators. In both setups the flexible beam has its mass reduced to 38.6% of that of the stiff beam. The total mass of the actuators in both cases is almost the same, but the setup with the innovative actuators allows to control the beam with two forces and two torques, while the setup with three 1-DoF actuators produces only three controlled forces.

Samenvatting

Het is bekend dat interne trillingen de prestaties en de levensduur van mechanische systemen verminderen. In sommige gevallen kunnen ze zelfs leiden tot een volledig mechanisch falen. In positioneringssystemen die in precisiesystemen worden toegepast (zoals in wafer scanners, scanners, pick-and-place machines voor het vervaardigen van PCBs, wire bonders, enz.) beperken de interne trillingen de prestaties. Deze prestaties zijn vaak toch al een uitdaging voor de algemeen aanvaarde ontwerpbenadering die naar hogere systeemnauwkeurigheid, snelheid en produktie streeft.

Momenteel verplaatst de ontwerpbenadering voor precisietoepassingen daarom de dominante trillingsfrekwenties van de mechanische delen naar een verscheidene keren hogere band dan de vereiste regelbandbreedte. Nochtans worden deze hoge mechanische frekwenties bereikt door de mechanische delen met een hoge stijfheid te construeren, wat vaak ten koste gaat van een vrij hoge massa.

Om de negatieve gevolgen van de klassieke methodologie te elimineren wordt een andere ontwerpfilosofie gebruikt in deze thesis. Een drie-disciplinaire (regeltechniek, mechanica en elektromechanica) lichtgewicht positioneringsbenadering concentreert zich op massavermindering van de bewegende delen van bewegingssystemen. Deze benadering berust op het principe van "niet vervormingsvrije aandrijving" en streeft naar het ontwerpen van een lichtere algemene kinematische structuur (kracht-weg).

Om deze benadering op een algemeen niveau te evalueren worden benchmarks voor zowel klassieke als voor lichtgewicht positioneringssystemen voorgesteld. Er wordt daarbij respectievelijk gebruik gemaakt van een zogenaamd rigide-balk systeem en een flexibele-balk systeem.

In deze thesis ligt de nadruk op het ontwerp en de optimalisering van een nieuwe Lorentzkracht actuator voor een lichtgewicht positioneringssysteem, dat ook in andere toepassingen, waar een hoge precisie vereist is, kan worden gebruikt. De doelstelling daarbij is de maximale massavermindering van een flexibele-balk systeem te bereiken.

Om de nieuwe actuator te evalueren en te ontwerpen wordt een uitvoerige statisch-elektromagnetische analyse van de actuator uitgewerkt. Het resulterende analytisch model is gebaseerd op een equivalent magnetisch circuit, dat door middel van preliminaire eindige elementen berekeningen is gedefinieerd. Dit analytisch model speelt een essentiële rol in het volledige ontwerp. Het wordt later gebruikt voor de optimale dimensionering van de actuator zodat de vereiste werkingsspecificaties worden gehaald. Dan wordt een numeriek eindige elementen model gebouwd en de daarmee verkregen resultaten worden gebruikt om de nauwkeurigheid van het analytisch model te evalueren en parasitaire krachten en koppels in de actuator te identificeren.

Een ander belangrijk aspect dat de bedrijfsvoorwaarden bepaalt, is het thermische gedrag van de actuator. Het wordt eveneens analytisch beschreven door een thermisch parameter model. De voorgestelde omschrijving van de warmteoverdracht omvat zowel het statische als het dynamis-

che gedrag.

Om de optimale afmetingen van de actuator te bepalen wordt een optimalisatie method-iek gevolgd waarin zowel het equivalent magnetisch circuit als het thermisch analytisch model wordt gebruikt. In termen van niet-lineaire programmering, bestaat het probleem uit het vinden van de afmetingen van de actuator met minimale massa, waarbij een gegeven kracht en koppel als randvoorwaarden worden gebruikt. Vanwege de niet-lineaire aard van het probleem wordt de optimale oplossing numeriek gevonden. De resulterende optimale actuator, die twee graden van vrijheid heeft, heeft een 22.2% lagere massa dan twee gelijkwaardige actuatoren met elk één vrijheidsgraad.

Op basis van simulaties en meetresultaten kan worden geconcludeerd dat de voorgestelde actuator met voldoende nauwkeurigheid kan worden geanalyseerd met behulp van de voorgestelde methodes.

De uitgevonden korte-slag actuator combineert op een unieke wijze twee gecontroleerde graden van vrijheid: een translatie en een rotatie. Deze combinatie zorgt ervoor dat de massa van de actuatoren die in een flexibele-balk systeem worden gebruikt, in vergelijking met die die in een rigide-balk systeem worden gebruikt, is verminderd. De actuatoren steunen het flexibele-balk systeem op een manier die minder storingen introduceert, en daarmee de controleerbaarheid van de hogere resonantiefrekwenties verhoogt, zodat de globale prestaties beter zijn.

Twee lichtgewicht positioneringssystemen werden gebouwd: één met drie actuatoren met elk één vrijheidsgraad en de andere met twee nieuwe Lorentz-kracht actuatoren. In beide opstellingen wordt de flexibele-balk massa tot 38.6% van die van de rigide-balk massa verminderd. De totale massa van de actuatoren is in beide gevallen bijna dezelfde, maar de opstelling met de innovatieve actuatoren staat het toe om de balk met twee krachten en twee koppels te controleren, terwijl de opstelling met drie actuatoren met elk één vrijheidsgraad slechts drie gecontroleerde krachten toestaat.

Curriculum Vitae

Juraj Makarovič was born in Košice (Slovakia) on January 13th in 1974. He studied electrical engineering at the Žilina University (Slovakia). His Master of Science thesis, *Traction drive control of a high speed elevator*, was finished in June 1997. Subsequently, he worked as a research assistant at the same university after which he started the Mechatronic Design Program of the Stan Ackermans Institute (Eindhoven University of Technology). The second year's project, *Linear motor for baggage handling system*, was carried out at VanDerLande Industries B.V. (Veghel) in 2001. In November 2001 he started the Ph.D. project that lead to this dissertation. Supervisors were prof. dr. ir. A.J.A. Vandenput from the Electromechanics and Power Electronics Group at the Electrical Engineering Department of the Eindhoven University of Technology and prof. dr. ir. J.C. Compter from Philips Applied Technologies.